POLITECNICO
MILANO 1863

SCUOLA DI INGEGNERIA INDUSTRIALE
E DELL'INFORMAZIONE

Transient Analysis on SUNRISE-LFR with an Updated Version of BELLA Plant Simulator

Tesi di Laurea Magistrale in
Nuclear Engineering - Ingegneria Nucleare

Author: **Alessandro Persico**

Student ID: 946215
Advisor: Prof. Antonio Cammi
Co-advisors: Prof. Janne Wallenius
Academic Year: 2020-21

Abstract

This thesis work is about the dynamical behavior of advanced nuclear systems, in particular lead-cooled fast reactors (LFRs). As they are currently under study and development, it is extremely important to provide accurate, though flexible and straightforward, computational tools to investigate their efficiency and safety under normal and off-normal conditions. This is done with reference to a demonstrator unit currently under design phase in Sweden, SUNRISE-LFR. Its primary circuit (reactor core, hot let, cold leg and cold pool) is modeled with a zero-dimensional plant simulator named BELLA, while a new model for the steam generator is built adopting the well-established moving boundary approach. The integrated code is adopted in MATLAB/Simulink® to perform safety analysis under four reference accidental scenarios: unprotected transient overpower (UTOP), unprotected loss of flow (ULOF), unprotected loss of heat sink (ULOHS) and station blackout (a combination of ULOF and ULOHS). The results obtained are physically reasonable and explainable in terms of causal relations between input and output variables. Moreover, they allow to critically discuss the design of SUNRISE-LFR with reference to the targeted safety margins to fuel melting and cladding creep rupture. In addition, they may constitute the basis and provide the means to further improve the codes, in particular working on the secondary side and on control strategies for such innovative nuclear systems.

Keywords: nuclear reactors, LFR, plant simulator, moving boundary approach, steam generator

Abstract in lingua italiana

Questo lavoro di tesi riguarda il comportamento dinamico di sistemi nucleari avanzati, in particolare reattori veloci refrigerati a piombo fuso. Durante il loro studio e sviluppo, è estremamente importante elaborare strumenti computazionali accurati, ma al tempo stesso semplici e flessibili, per indagare la loro efficienza e la loro sicurezza in condizioni di funzionamento normali ed anomale. Questo viene fatto rispetto ad un'unità dimostrativa attualmente in fase di progettazione in Svezia, di nome SUNRISE-LFR. Il circuito primario (nocciolo del reattore, gamba calda, gamba fredda e piscina fredda) viene modellato con un simulatore di impianto zero-dimensionale di nome BELLA, mentre per il generatore di vapore viene costruito un nuovo modello basato sul già dimostrato approccio alle frontiere mobili. Il codice integrato è scritto in MATLAB/Simulink® per eseguire analisi di sicurezza rispetto a quattro scenari incidentali di riferimento: *unprotected transient overpower* (UTOP), *unprotected loss of flow* (ULOF), *unprotected loss of heat sink* (ULOHS) e *station blackout* (una combinazione di ULOF e ULOHS). I risultati ottenuti sono fisicamente ragionevoli e spiegabili in termini delle relazioni causali tra le variabili di ingresso e di uscita. Inoltre, permettono di discutere criticamente le scelte di progettazione di SUNRISE-LFR rispetto ai margini di sicurezza prefissati. Per di più, possono costituire la base e fornire i mezzi per ulteriori miglioramenti del codice, lavorando in particolare sul circuito secondario e su strategie di controllo dell'impianto complessivo.

Parole chiave: reattori nucleari, LFR, simulatore di impianto, approccio alle frontiere mobili, generatore di vapore

Contents

Introduction

Toward a more sustainable world

On February 2nd, 2022 the European Commission (EC) published the Complementary Climate Delegated Act [1, 2] which includes certain nuclear activities in the "EU Taxonomy". It is classification system entered into force in European Union in 2020 which defines the activities that can be considered sustainable to meet EU's climate and energy targets for 2030 and to reach the objectives of the European Green Deal [3]. The EU Taxonomy is not intended as an instrument of energy policy, the Member States remain fully responsible and competent for deciding their own energy mix. But it is meant to be a guide for private investments toward activities that are needed to achieve climate neutrality, avoiding green washing.

This is only one of several times that an international institution recognizes the capability of nuclear power in fighting climate change, but it assumes an even greater importance because it is done by a governmental entity supported by the work of the scientific community, the Joint Research Center [4]. In this way, the European Union is going to include in the list of green activities both nuclear sector's existing technologies (Gen. III+) and advanced technologies (Gen. IV), provided that they respect strong and clear criteria related to safety, greenhouse gas emissions and nuclear waste disposals [1].

The EU Taxonomy is part of the European Green Deal, a plan which covers all sectors of the economy. Through its most important tool, the Climate Law, it writes into law the goal for Europe's economy and society to become climate-neutral by 2050. An intermediate step of reducing by 2030 net greenhouse gas emissions by at least 55% compared to 1990 levels − the Fit for 55 package [5] − is encompassed.
This is the European strategy to fully comply with the targets set out by the United Nations in the 2030 Agenda for Sustainable Development, an action program of the UN signed in 2015 which focuses on 17 sustainable development goals (SDGs). Later in the same year, 196 Parties negotiated the Paris Agreement at UNFCCC's COP21 which entered into force in 2016. Its goal is to limit global warming to well below 2, preferably to

1.5 °C, compared to pre-industrial levels [6]. The Paris Agreement and the 2030 Agenda together provide the foundation for sustainable, low-carbon and resilient development under a changing climate [7].

Why sustainable development? The role of sustainability in modern society has become more and more predominant after scientists have started studying climate change and its causes. Climate change refers to long-term shifts in temperature and weather patterns; although they may be natural, since 1800s human activities have been the main driver, primarily by burning fossil fuels which produce greenhouse gases (e.g., carbon dioxide and methane).

What is the meaning of sustainability? The scientific community agrees on the definition given by the Brundtland Report in 1987: sustainable is that development which "meets the needs of the present without compromising the ability of future generations to meet their own needs" [8]; something is sustainable when it does not waste resources, nor when it produces substances which harm people and environment in an irremediable way. However, every industrial process produces waste, also hazardous waste. Eventually, sustainability comes as an optimal balance between benefits and waste, which must be treated and confined in safety. As aforementioned, global warming is driven by greenhouse gases, they are the reference waste which must be reduced. Energy, industry, transport, buildings, agriculture and land use are the main emitters.

This is the whole picture where European Union is implementing the European Green Deal and the EU Taxonomy. Total use of energy corresponded to 75% of GHG emissions in EU in 2020 [1]. That is why power production has a special role in global warming and countermeasures need to be taken by all countries.

Power production and nuclear power plants

Power production is identified as the major contributor of GHG emissions [9], but at the same time as a necessary element of development and prosperity of society. From the beginning of History mankind has taken the path of progress and power is exactly what sustains this path. Power is necessary to have electricity for the industry, to transportation and to illuminate cities at night; it is necessary to let the hospitals work, to have hot water, to produce food. It is impossible to conceive this world without considering power.

Since the first Industrial Revolution, developed countries have found different resources to produce power: exploiting fossil fuels (coal, oil, natural gas), renewables (hydropower, solar power, wind, geothermal power, biomass conversion) or nuclear fuel. The huge

challenge for XXI century is to make it sustainable.

Nowadays several countries in the world have an unsustainable energy mix. China, Poland, Australia are only few examples of countries in which carbon occupies a dominant share in the electricity production mix. If humankind is willing to respect Paris Agreements promises and to avoid catastrophic consequences on Earth, it might be better to drive the energy mix toward a more sustainable path. What are the green solutions? According to studies conducted by the dedicated international organizations [10–13], a sustainable energy mix is renewables coupled with accumulation devices and with nuclear power as base load. Nuclear power is the reliable technology capable of guaranteeing electricity when intermittent renewables are unavailable. Moreover, according to a report by the World Energy Council [11] nuclear energy has the potential to contribute towards meeting 10 out of the 17 goals of the 2030 Agenda.

It is important to point out that renewable and sustainable are not synonyms: the first term refers to the availability of natural resources (sun, wind, water) once utilized, the second to the climate-altering substances − greenhouse gases − which are emitted by the resource itself when used. Solar (thermal or photovoltaic), wind and hydro are renewable resources and at the same time sustainable resources as their average greenhouse gases emissions are very low − within 50 gCO2 equivalent per kWh [14, 15]. On the other hand, biomass is an example of renewable resource which is not properly sustainable − 230 gCO2 equivalent per kWh [14, 15]. It should be mentioned that biomass might become carbon neutral when considering the whole life cycle of the plants: when growing they absorb circa the same amount of CO2 that is released when they are burned as biomass or as biofuel, making the evaluation of carbon emissions more complex [16]. Just to have in mind an order of magnitude, coal and natural gas emit 820 and 490 gCO2 equivalent per kWh respectively and thus they are totally unsustainable. It is worth to mention that these data are averages over all countries.

As far as nuclear is concerned, it is necessary to distinguish between two technologies: fission and fusion. Nuclear fission is the well-exploited nuclear reaction to produce electricity since 1940s, while nuclear fusion is the technology still under study and under experiment as no commercial nuclear fusion plant has already been built. This thesis deals with nuclear fission, thus when referring to nuclear, nuclear fuel and nuclear power plants (NPPs) here it is only in terms of nuclear fission.
Nuclear power is not renewable, but it is extremely sustainable: NPPs emit only 12 gCO2 equivalent per kWh [14, 15], making it the second-least carbon emitting resource, being the first one wind (offshore or onshore). This is because nuclear fission reaction releases energy without producing any greenhouse gas. Nevertheless, when considering the whole

nuclear power plant some CO2 emissions cannot be avoided in construction and transport phases, therefore the value is 12 gCO2 equivalent per kWh and not zero.

Moreover, nuclear power is extremely efficient and reliable: according to US Department of Energy [17] in 2019 NPPs had an average capacity factor equal to 93.5% which is 2.5 times hydropower or wind's average capacity factor and more than 3.5 times solar's average capacity factor. It means that 93.5% of time NPPs were providing their maximum electrical energy output. The remaining 6.5% of time could be due to different reasons: modulation of the power output in order to maximize renewables production, unavailability of the plant because of maintenance actions, external or internal problems. This capacity factor value is explained by nuclear power as a non-intermittent source of electricity, as opposed to some renewable resources − solar and wind. These are only some of many reasons which justify why nuclear power is considered one of the present and future technologies to lead the world toward a more sustainable life. Last but not least, the mortality rate: including the deaths from Fukushima and Chernobyl accidents, nuclear power is responsible for 0.07 deaths per TWh of energy production [15]. This value is extremely low and on the same order of magnitude of wind (0.04), solar (0.02) and hydropower (0.02), and it must be compared with coal (24.6), oil (18.4), natural gas (2.8) and biomass (4.6). In between there are circa two orders of magnitudes which make nuclear power among the safest sources of energy that we have, together with wind, solar and hydropower. Therefore, it becomes understandable why the European Commission decided to include nuclear activities in the green Taxonomy.

However, as any mean of power production, nuclear power has to deal with some problems which are deeply affecting its development. But although public opinion might think they are related to safety issues, especially after Fukushima accident in 2011, this is not the case. To prove it, it is sufficient to show once again the mortality rate which is comparable with the low rates of wind, solar and hydro. The problems connected to nuclear power can be divided into three categories.
Firstly, and maybe this is the most important issue in Western countries, it is management: budget and time overruns are characterizing some European projects − Olkiluoto 3 in Finland, Flamanville 3 in France and Hinkley Point C in UK − making NPPs even more difficult to deploy; this is not strictly related to the technology implemented (French EPR), but more in general to the difficulty of Western countries in dealing with the so called "mega-projects" within NPPs are included. China, Russia and South Korea construct reactors within time and budget schedule, thus demonstrating that nuclear power do not suffer from technological problems.
Second issue is nuclear proliferation. In order to ensure security in the world, IAEA and

the other national and international safeguards implement several programs consisting of inspections and cross-controls on nuclear materials with database of all nuclear sites (reactors, laboratories, companies, universities, etc.). It is extremely hard to work in the nuclear world without the supervision and the approval of the IAEA.
Third problem is public acceptance. This is very specific to each country and is caused by public ignorance in nuclear engineering field. Public acceptance has to do with radiation and nuclear waste, xthe byproduct of power production. Both must be treated with great attention and this has been done for decades. In fact, there are consolidated and under-research methods to reduce and confine radwaste. After its treatment, radwaste is isolated from the biosphere inside repositories. They are of two kinds: superficial where low-level waste (LLW) is stored until it reaches ambient radioactivity level − namely a few hundred years − and where intermediate-level waste (ILW) and high-level waste (HLW) are allocated only temporarily; geological disposals designed to be functional for hundreds of thousands of years where MLW and HLW can be safely stored. Another issue of public concern could be nuclear accidents, especially after Fukushima disaster. The accident occurred after the strongest earthquake ever registered in Japan which provoked a tsunami with waves 11 meters high; although the structures of the reactors resisted, they were totally disconnected from the electricity grid and the emergency cooling diesel generators were out of service due to the flooding of the bunker where they were located. However, according to the UNSCEAR Report 2019 [18] no casualties resulted from radiation expore, while more than 15000 people died from the earthquake and tsunami combined.

New reactor technologies try to overcome these three major issues of nuclear power.

Generation IV nuclear power plants

In the early 2000s the Generation IV International Forum (GIF) identified in six new reactors the future of fission technology [19]. They are: very-high temperature reactor (VHTR), molten salt reactor (MSR), supercritical-water-cooled reactor (SCWR), gas-cooled fast reactor (GFR), sodium-cooled fast reactor (SFR), lead-cooled fast reactor (LFR).

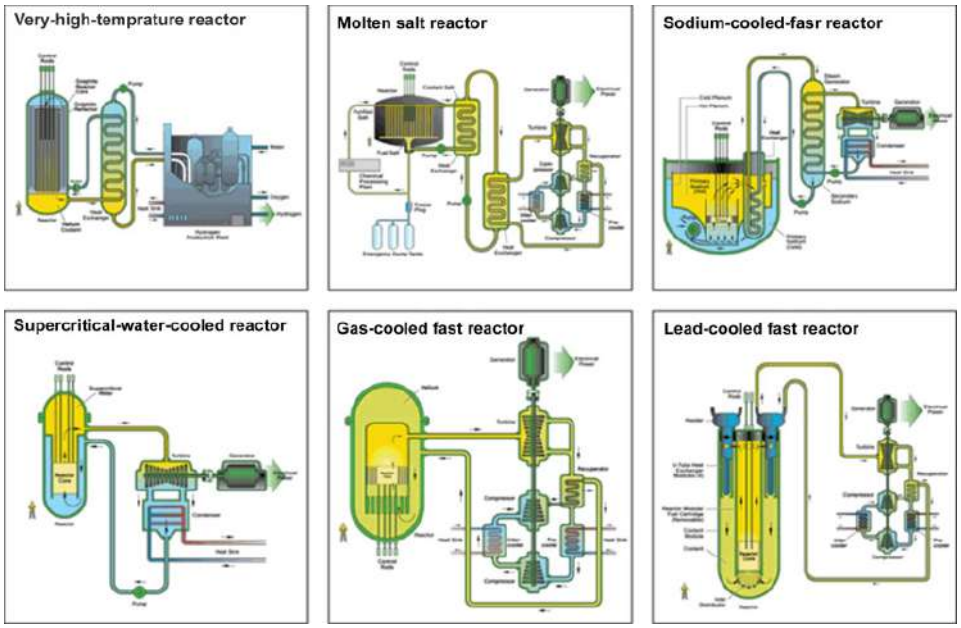

Figure 1: GIF Gen. IV nuclear reactors.

Gen. IV reactors are the novelty in nuclear power engineering and they will be available on the market in the 2030s. As for today, a lot of pivotal projects are under research and development in several countries all over the world. The claimed benefits include sustainability, safety and reliability, economic competitiveness, proliferation resistance and physical protection.

Sustainability is intended in the fuel cycle (resource utilization and waste) and it is the absolute novelty for Gen. IV reactors. Indeed, most of them are fast reactors, meaning that they exploit fast neutron spectrum to induce nuclear fission reactions on nuclear fuel. This has two consequences: first of all, it is possible to produce new fissile isotopes inside the reactor itself through the process of breeding starting from fertile nuclides, U-238 and Th-232. They are more abundant in nature than fissile nuclides but cannot be used alone in thermal reactors since they do not undergo fission at thermal energy - and this is why thermal reactors need fuel enrichment plants. By conversion of fertile isotopes, fast reactors will increase fuel utilization factor and improve front-end sustainability. These kinds of reactors go under the name of fast breeder reactors (FBRs). Second consequence is related to back-end sustainability: a fast neutron spectrum is able to transmute minor actinides (MAs) − among the most terrible radionuclides as they are long-lived alpha emitters − into fission products (FPs) which are beta emitters and whose half-life is a few orders of magnitude less. Eventually, fast reactors permit to exploit better the fuel cycle and to produce less radioactive waste, an important benefit both for public acceptance, non-proliferation and economic competitiveness.

Moreover, a lot of Gen. IV reactors are designed to be small and compact in order to exploit the advantages of SMRs (small modular reactors): modularity, economy of multiples, flexibility and coupling with renewables, safety [20]. The term "small" refers to the size of SMRs which is conventionally considered as below 300 MWe. Modularity refers to the ability to fabricate major components of the NPP in a factory environment and to ship them to the point of use. This implies simplicity of design, limited on-site preparation and largely reduces the lengthy construction times that are typical of larger units. Thus, from the financial point of view it can be even more convenient to build several units, one after the other, following the so called "economy of multiples". Additional modules can be incrementally added as demand for energy increases. Then, being so small, SMRs can be easily coupled with other power sources such as renewables: they will follow the load and cover that electricity demand which intermittent renewables cannot. SMRs can be exploited not only for electricity production, but also for cogeneration: district heating, desalination, hydrogen production, creating the so called "hybrid" electricity grid. Last but not least, SMRs will improve the already-strong safety of NPPs thanks to the adoption of passive safety systems, i.e. systems which do not need human action or even electricity to work because they rely only on intrinsic physical properties of the system.

Topics and goals of this work

Among the six families of Gen. IV nuclear systems, this manuscript refers to lead-cooled fast reactors. It is an advanced technology under development in several countries which aims at becoming a major player in the decarbonization process.

This manuscript serves to describe a seven months internship at Royal Institute of Technology (KTH), Stockholm, where a lot of work on LFRs has been done. In particular, the focus is on a general-purpose plant simulator named BELLA, adopted to simulate normal and off-normal conditions of a reference LFR under development in Sweden, called SUNRISE-LFR. To that end, this work improves BELLA in the primary system description, for which momentum and mass balance equations are rewritten, and develops a new model for the steam generator, a starting point for the plant secondary circuit. The ultimate goal is to provide an efficient but flexible code oriented to the dynamics and the control of LFRs.

Besides the general introduction concluded by this section, the manuscript is structured in six chapters. Each chapter is divided into sections and subsections and always ends with summarizing conclusions, both generic and specific.

Chapter 1 delineates the state-of-the-art of lead-cooled fast reactors. It begins with a

description of the technology, underlining the advantages and disadvantages in terms of coolant, fuel and structural materials. Then, the most interesting LFR projects all around the world are presented. After that, the chapter briefly introduces some benchmark codes and some developing tools used to simulate LFRs, including the one adopted in this work, BELLA. As last, it gives some general conclusions on LFRs.

Chapter 2 is about the reactor under study, SUNRISE-LFR. After mentioning the overall project, it describes the most updated layout of the reactor by means of figures and tables. The chapter ends with generic conclusions.

Chapter 3 describes the plant simulator BELLA in terms of its assumptions and equations. The new momentum and mass balance equations are presented. Then, the chapter shows BELLA's implementation in MATLAB/Simulink and discusses the simulation of some reference accidental scenarios, performed on SUNRISE-LFR. At the end, some conclusive remarks about the code, as well as about SUNRISE-LFR, are given.

Chapter 4 develops the new steam generator model and describes assumptions, limits and advantages of the chosen approach. Then, it shows how it is implemented in MATLAB/Simulink and discusses the simulation of some reference transients. Lastly, it gives a summary about the code performances and identifies possible ways of improvement.

Chapter 5 couples BELLA with the steam generator model in MATLAB/Simulink and carries out simulations of the reference accidental scenarios, adopting once again SUNRISE-LFR. The results are compared to the ones from Chapter 3 and, then, some specific conclusions about the coupling of the codes and about SUNRISE-LFR are highlighted.

Final Chapter 6 reassumes the entire work and tries to give overall conclusive remarks about the code developed, about the simulations carried out and about SUNRISE-LFR. It is done taking into account the original targets of the internship and the final accomplishments that are obtained.

The chapters are accompanied by four appendixes positioned after the bibliography. They integrate the work with specific topics. Appendix A lists the thermo-physical properties utilized in the work. Appendix B shows the derivation of the new momentum balance equation. Appendix C introduces the topic of two-phase flows. As last, Appendix D indicates Simulink settings adopted in all simulations.

1 | Lead-cooled fast reactors: a state-of-the-art

Lead-cooled fast reactors are one of the six technologies identified by the Generation IV International Forum (GIF) [19] as the future of nuclear power able to meet the objectives of the fourth generation of nuclear systems: sustainability, safety and reliability, economic competitiveness, proliferation resistance and physical protection. This chapter is entirely focused on LFRs and on the solutions under study or under implementation to achieve commercially deployable units in the 2030s.

In particular, Section 1.1 is dedicated to a general overview of LFR technology with specific references to coolant, fuel and structural materials. Section 1.2 goes through the most interesting projects currently under development all around the world. Section 1.3 gives a brief introduction to the codes that can be used to simulate lead-cooled fast reactors, mentioning also BELLA, the code used in this thesis work. As last, Section 1.4 tries to deduce some conclusions from the other sections on the state-of-the-art of LFRs.

1.1. LFR: the technology

First thing worth to mention is that this is a fast reactor, i.e. it adopts a fast neutron flux to fission nuclear fuel and produce thermal power. Thus, the choices regarding coolant, fuel and structural materials are first of all a consequence of having medium and high energy neutrons (keV-MeV range) inside the reactor. At the same time they must satisfy compatibility requirements in terms of chemical and physical interactions.
This section is about the general features of LFRs. It describes their advantages and disadvantages, as well as engineering solutions to the issues coming from the use of lead in the primary circuit. Three subsections addresses coolant, fuel and structural materials.

1.1.1. Coolant

In the Generation IV context, the coolant is required to:

- Effectively cool down the fuel and transport thermal power to the secondary system.
- Minimize neutron moderation to preserve a fast neutron spectrum.
- Minimize neutronic parasitic absorptions to keep a good neutron economy.

Gen. IV reactors have shifted from water solution to new coolants in the primary circuit. And the coolant choice is what distinguishes the six Gen. IV reactors one from another.

As contained in the name itself, lead-cooled fast reactors adopt lead as primary coolant. Two implementations are under development: pure lead and lead-bismuth eutectic (LBE). The first part of this subsection refers to the pure lead technology, while a few comments on LBE are given at the end.

Isotope	Isotopic abundance
^{203}Pb	1.4%
^{206}Pb	24.1%
^{207}Pb	22.1%
^{208}Pb	52.4%

Table 1.1: Natural lead isotopic composition (all stable isotopes).

Lead neutronic properties:

- High mass number (Table 1.1).
  It guarantees that lead neutron moderation power remains poor because, even though liquid lead has a very high density, scattering microscopic cross-section is extremely low. This allows to use lead in fast reactors, with all the benefits that follow: fuel breeding, MAs transmutation, no need of enrichment plants (sustainability, non-proliferation and economic competitiveness).
  In addition, high mass numbers strongly increase γ-rays absorption by lead, thus providing a very effective intrinsic shielding capability (higher safety). Consequently, it reduces the necessity of a thick reactor biological shield (economic competitiveness).
  Furthermore, lead good neutron reflection capability lowers leakages from the reactor core improving neutron economy.
- Low neutron absorption cross-section.
  First of all, this significantly improves neutron economy.
  Moreover, together with the low scattering cross-section, it has a very practical

consequence on core design: it allows to increase the coolant-to-fuel volume ratio by enlarging the fuel rods pitch and, subsequently, coolant flow area in the core. Considering the same mass flow rate, this reduces lead flow velocity in-core and, therefore, core pressure losses. Hence, requirements on pumping power level decrease (primary pump is asked to provide a lower pressure head) and primary fluid natural circulation can be achieved with great simplicity. Indeed, LFR projects usually rely on natural circulation of lead as an inherent cooling capability of the system, especially in case of loss of flow accidents.
Furthermore, less compact fuel rods bundles drastically enhance the safety against flow blockage.

- High capability of volatile FPs retention (lead can form compounds with iodine and cesium).
  This property, together with the excellent γ-rays absorption, reduces the source term in case of accident on the primary system (e.g., lead leakage). This not only increases the intrinsic safety properties of lead, but also improves economic competitiveness of LFRs because it reduces the emergency planning zones in case of accidental scenario.

Lead physical and chemical properties:

- High boiling point (1749 °C).
  Considering that the typical working conditions are in the range of 400-500 °C, it is present a sufficiently large margin to coolant boiling to claim that the core voiding reactivity risk is extremely low. This leads to simplification of the design of LFRs because pressurization of the primary system is not required.
  In addition, a high boiling point allows the reactor to work at relative high temperatures (limited on the other hand by corrosion issues) reaching increased thermal efficiencies (>40%) and enabling cogeneration (e.g., district heating, desalination, hydrogen production).

- Low vapor pressure (2.9 10^{-5} Pa at 400 °C).
  Again, this goes in favor of a primary system working at atmospheric pressure.

- High density (in the range of 10 tons/m^3).
  It favors the dispersion of breached fuel in case of accident.

- Good thermal expansion coefficient (1.22 10^{-4} K^{-1} at 500 °C).
  It improves natural circulation both in working conditions (increasing the buoyancy term) and under accidental transients (loss of flow accidents).

- Chemical compatibility with water and air.

It removes the necessity of an intermediate circuit, required conversely for sodium-cooled fast reactors (SFRs). This settles the conditions to develop pool-type reactors where all primary system components are integrated in the reactor vessel. The benefits are not only in design simplification and modularity, but also in safety: since lead flow is confined inside the primary vessel, no big penetrations of the vessel itself are needed. Hence, the reference large break LOCA (loss of coolant accident) is eliminated by design and the standard LOCA has a well decreased likelihood of occurring.

- Low potential energy stored.
  Since no hydrogen is in principle present inside the primary system, the likelihood of chemical explosions in the reactor vessel are drastically reduced (Fukushima alike event).

Disadvantages:

- High melting point (327.5 °C).
  It requires the system to work at higher temperatures, keeping a sufficient margin to coolant freezing. The reactor design must pay a careful attention on overcooling transients because a solidification of the coolant inside the primary vessel might compromise the reactor useful life.
  On the other hand, it provides a good resistance to lead spreading in case of vessel cracks and ruptures: lead would solidify almost immediately when in contact with air at ambient temperature.

- High density (around 10 tons/m^3).
  The main issue is related to erosion of structural materials by flowing lead. On the one side, this is counterbalanced by keeping lead flow velocity below a given value, usually 2 m/s [21]. On the other side, the research is studying and developing materials with strong resistance against lead erosion.
  Furthermore, high density provides a higher seismic risk for the plant. This explains why LFRs are usually of the pool-type configuration with a limit on the vessel height. It goes in the direction of a more compact system with a limited lead inventory.

- Heavy liquid metal corrosion (HLMC).
  This is the biggest challenge in developing LFRs because lead's attack on structural materials is quite strong, especially at high temperature due to the significant increase of Fe, Cr and Ni dissolution rates. The first countermeasure is to lower lead maximum temperature in the system: this is why LFRs usually keep lead temperatures below 550-600 °C.

Secondly, an active control of the oxygen concentration in the system must be taken over.
Then, most of the effort is done in new materials development and qualification to resist to HLMC, with the idea of coating metallic structures located in the most severe environments (fuel cladding, hot pools). The metals under study are alumina forming steels (AFA) and FeCrAl alloys, to which Subsection 1.1.3 gives a brief introduction.
In addition, strong coolant purification might help in reducing particulate that can attack metallic surfaces.

- Lead opacity.
  It has very practical consequences on the in-service inspection and monitoring of components inside the vessel and on fuel handling management. LFRs under development try to solve this problem in different, innovative ways, such as by extending fuel assemblies upper ends beyond lead free surface level (ALFRED, Subsection 1.2.1).

The other popular option for LFRs coolant is an eutectic between lead and bismuth [22, 23], with composition of 44.5 at.% in Pb and 55.5 at.% in Bi. The main reason to adopt it lies in the decreased melting point of the alloy: from 325.5 °C of pure lead to 123.5 °C of LBE, which significantly increases the margin to coolant freezing. While LBE shares with pure lead most of the other advantages (Bi is a heavy nuclide, with ^{209}Bi the only quasi-stable isotope), it exhibits some new issues:

- Bi is not abundant at all and, hence, very expensive (non nuclear-grade Bi costs around 6 USD/kg in 2019) [24, 25].
- After neutron radiative capture, bismuth is responsible of producing a non-negligible amount of ^{210}Po, among most radiotoxic nuclides (alpha emitter with specific activity of about 166 TBq/g) [26, 27].
- At the same temperature Bi is about 40 times more corrosive than Pb against Fe, Cr and Ni. Nevertheless, LBE does not require working temperatures as high as pure lead systems.

In general, pure lead systems are utilized for standard (fast) power reactors, while LBE is commonly adopted for partitioning and transmutation technologies. These are innovative nuclear systems specifically addressing nuclear waste incineration, and they consist of a high-power proton accelerator coupled to a subcritical nuclear reactor through a spallation

target. By impinging the proton beam against the high mass number target (tungsten, lead or, more commonly, LBE), neutrons are produced by spallation and criticality is achieved. In this way common nuclear fuel can be burned together with minor actinides, without compromising the safety characteristics of the system thanks to the sub-critical mode of operation, which intrinsically provides a SCRAM when the proton beam is shut down. These systems are also called accelerator-driven systems (ADS) and they are part of the Generation IV nuclear reactors.

1.1.2. Fuel

Advanced nuclear reactors need to consider innovative solutions for fuel in order to improve its performance and its safety. They are referred as accident-tolerant nuclear fuel (ATF) technologies and in their qualification process a special attention must be dedicated to cladding materials, which need to be chemically compatible with fuel and capable to resist fast reactors severe conditions.
Important prerequisites for optimal advanced nuclear fuels are high melting point (to reduce the melting risk), high thermal conductivity (to increase the safety margin to fuel melting by lowering the temperature difference across the fuel), high density (to decrease the volume needed to reach criticality conditions), good miscibility with actinides and capability of withstanding high burnup (to lower the fuel cycle costs and increase proliferation resistance).

For lead-cooled fast reactors the solutions at play are mainly two: oxides and nitrides. Also metallic fuels may be an option, with the great advantages of extremely high densities and thus maximizing the breeding ratio and minimizing the fissile core inventory, but only for low temperature operations. Main reference for this subsection is the state-of-the-art report on innovative fuels published by OECD Nuclear Energy Agency in 2014 [28].

The oxide technology has decades of experience from the very beginning of the nuclear era, as it has been adopted not only in LWRs (UO_2) but also in the first experimental fast reactors in the 1960s and 1970s when it comes to the mixed oxide $(U,Pu)O_2$ (MOX fuel). Several thousands of MOX fuel pins have been successfully irradiated worldwide in fast reactors under nominal and off-normal conditions. This provides a solid background of knowledge on oxide fuel's behavior and a large database for validation of models and fuel performance codes. This is the main reason why oxide fuels are contemplated as the already qualified, reference fuel in several fast reactors, LFRs included. It is valid in particular for the MOX configuration with allows to recycle plutonium from spent nuclear fuel and from the military sector (sustainability).

Despite having a low density and a poor thermal conductivity, MOX fuel shows a high melting point, excellent stability and an excellent behavior under irradiation (swelling rate is much lower than the other fuel kinds).

Nitride fuels have been mostly investigated in the uranium mononitride form (UN), but plutonium nitride and mixed variants continue to be studied. Compared to oxide fuels, the advantages of UN are higher fissile density (one HM atom per light atom), similar melting point but significantly enhanced thermal conductivity. Thus, large safety margins against fuel melting are obtained and fuel cladding temperature is in general kept to lower values. Nitride fuels support a hard spectrum, a requirement for efficient actinides fission. Both UN and PuN offer almost complete miscibility with the actinide nitrides, greatly relaxing a number of fabrication and operational concerns that exist in oxide and metallic fuel forms.
Besides being not qualified yet, a disadvantage of nitrides lies in ^{14}N: it is a strong neutron absorber which produces ^{14}C, deteriorating neutron economy and adding radioactive source to the fuel mixture. It is essential then to enrich nitrogen in its other stable isotope, ^{15}N, but the cost of supplying fresh ^{15}N is prohibitive on a large scale. Luckily, ^{15}N can be easily recovered from spent fuel and recycled, and this can be a very good strategy to make the process economically competitive.

More exotic fuel solutions, such as carbides and silicides, are under study in different countries, but they are not considered in this manuscript.

Fuel	**UO_2**	**UN**
Melting temperature (°C)	2850	2850
Density (ton/m^3)	10.9	13.4
Thermal conductivity (W/K·m)	3.5	20.1
Specific heat capacity (J/kg·K)	317	237

Table 1.2: Uranium dioxide and uranium mononitride main thermo-physical properties at comparison. Values are obtained using the correlations listed in Appendix A evaluated at 700 °C. For both the melting point is evaluated at 1 bar [28].

1.1.3. Structural materials

The previous subsections already posed the problem of finding structural materials capable of surviving LFRs severe environment: high temperature range, irradiation conditions and corrosion/erosion sharpen the list of candidates. In addition, at low temperatures

another phenomenon might compromise the integrity of structural materials: liquid metal embrittlement (LME).

Without entering into details, out of the scope of this work, it is worth to mention which are the most interesting candidate materials for lead-cooled fast reactors: among ferritic steels, the family of FeCrAl with different compositions seems to meet all requirements [29, 30]; on the other hand, alumina-forming austenitic (AFA) steels show very important corrosion resistance properties below 650 °C [31]. Both the two classes of steels have not been qualified yet for nuclear reactors and the process is very costly and time-consuming. This is the reason why they are usually coupled with already qualified materials, such as austenitic SS316L for pressure boundaries and 15-15Ti for fuel cladding [32]. It must be noted that metals adopted in fuel cladding need to satisfy an additional criterion: low neutron absorption cross-section to avoid significant parasitic captures and jeopardize neutron economy.

Section 1.2 and Chapter 2 contain specific references to solutions for cladding and structural materials.

1.2. Main projects currently under development

Lead-cooled reactors were historically associated to Soviet Union as they were used inside nuclear-powered attack submarines. They were seven Alfa class submarines built between 1960s and 1970s adopting a 155 MWth LBE reactor each. Thanks to the LBE technology, they were compact and therefore the fastest submarines in the world, but the program ended in 1996 with the decommission of all seven. In 1998 Russia declassified a lot of research information derived from its experience with submarine reactors and, as a consequence, Western countries' interest in using Pb or Pb-Bi for small reactors has increased.

Nowadays US, Europe, Japan, but also China, South Korea and Russia itself are the main actors in LFRs development. This section goes through the several reactors under study, deployment or operation in the world. Main reference here is the Lead Cooled Fast Reactor chapter on the Encyclopedia of Nuclear Energy [33] written in 2021 by A. Alemberti, Ansaldo Nucleare.
Regarding the conventional LFR technology, this section presents: ALFRED, ELFR, BREST, SSTAR, LFR-AS-200, CLFR and Westinghouse LFR.
Concerning the ADS concept, three projects are introduced: MYRRHA, SVBR-100 and CLEAR-I.

A particularly interesting projects is the Swedish SUNRISE [34]. It is not discussed in this section because, being it the reference LFR for this thesis manuscript, it has a wholly dedicated part (Chapter 2).

1.2.1. ALFRED

ALFRED (Advanced Lead-cooled Fast Reactor European Demonstrator) is the European demonstrator reactor for the liquid lead technology [35, 36]. It is one of the four ESNII (European Sustainable Nuclear Industrial Initiative) initiatives to develop a generation IV nuclear reactor in Europe, the others being MYRRHA (LBE-ADS prototype), ASTRID (SFR prototype) and ALLEGRO (GFR prototype). It leverages on the experience acquired with ELSY (European Lead SYstem) in 2006-2010 and has the target to demonstrate the LFR technology. Further step in the line will be the development of the first-of-a-kind industrial plant, named ELFR (European LFR). Final goal will be the deployment of commercial units in the time window 2035-2040.

In order to support it, the European Commission funds the LEADER (LEad-cooled Advanced DEmonstrator Reactor) projects, which involve 16 partners among which ENEA, RATEN-ICN, SCK-CEN, KTH, CEA, JRC, coordinated by the Italian private company Ansaldo Nucleare [37]. The commitment to the LFR development was formalized in 2013 through the formation of an unincorporated consortium, named FALCON (Fostering ALfred CONstruction). FALCON is aimed at managing the R&D strategic needs and securing the necessary funding for siting, licensing and construction. It also addresses the path to licensing through an innovative strategy in terms of R&D development, the so-called staged approach that foresees after the construction a progressive increase of operating temperature in order to qualify the structural materials and/or corrosion protection strategy in the lead coolant environment as well as prototypical irradiation conditions.

The reactor has a 300 MWth core, which turns into 125 MWe, and it is cooled by pure lead. The proposed secondary system is constituted by a steam-water cycle characterized by a turbine inlet pressure of 18 MPa, feed water entering at 335 °C and superheated steam exiting at 450 °C. This is exactly the same cycle that was used for the sodium fast reactor Superphénix and has an overall thermal efficiency greater than 40%.

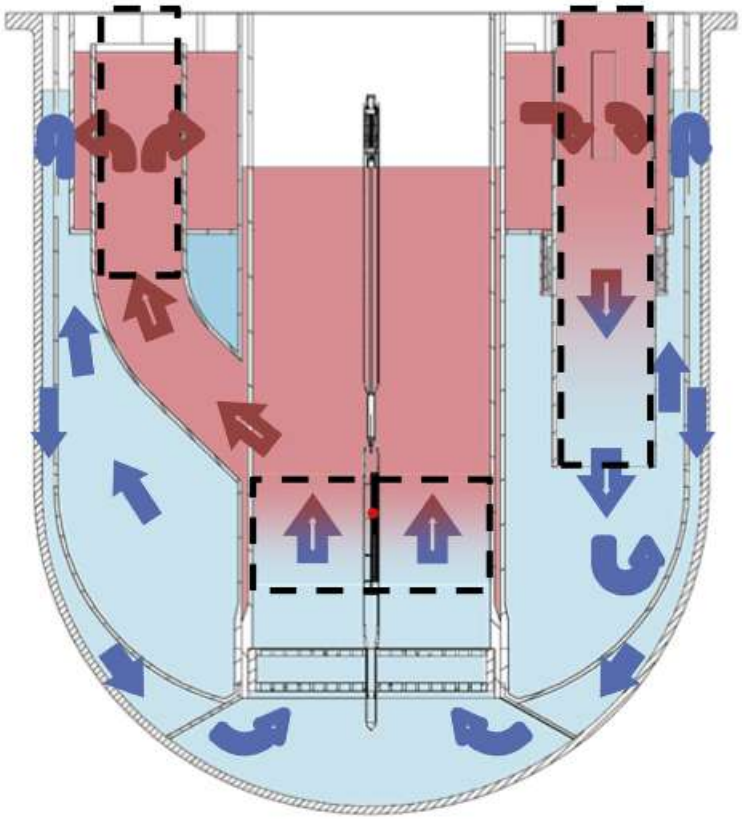

Figure 1.1: ALFRED primary system flow path [33]. In red hot regions and in light blue cold regions.

As most of the LFRs under demonstration, the primary system configuration is pool-type both to achieve modularity and compactness of the vessel and to prevent seismic impacts on the system. Thus, the reactor vessel (RV) contains all the primary coolant inventory, in principle eliminating by design the loss of coolant accident.
The reactor present a simple flow path (Figure 1.1), with a riser and a downcomer. The locations of the heat source (the core), below the riser, and of the heat sink (the steam generators, SGs), at the top of the downcomer, allow for an efficient natural circulation environment. The primary coolant flows from the core to the SG through the riser. The SG units are connected to the primary pumps (PPs), located at the entrance of the SGs, hence working in hot lead. After the steam generators, the flow continues along the downcomer reaching eventually the core, and then starts again the loop.
Inside the RV, the reactor core is supported by the so-called inner vessel (IV), while a steel layer covering the reactor pit constitutes the safety vessel (SV). The plenum between the primary coolant free levels and the reactor roof is filled by a cover gas. Figure 1.2 displays a vertical sketch of the reactor.

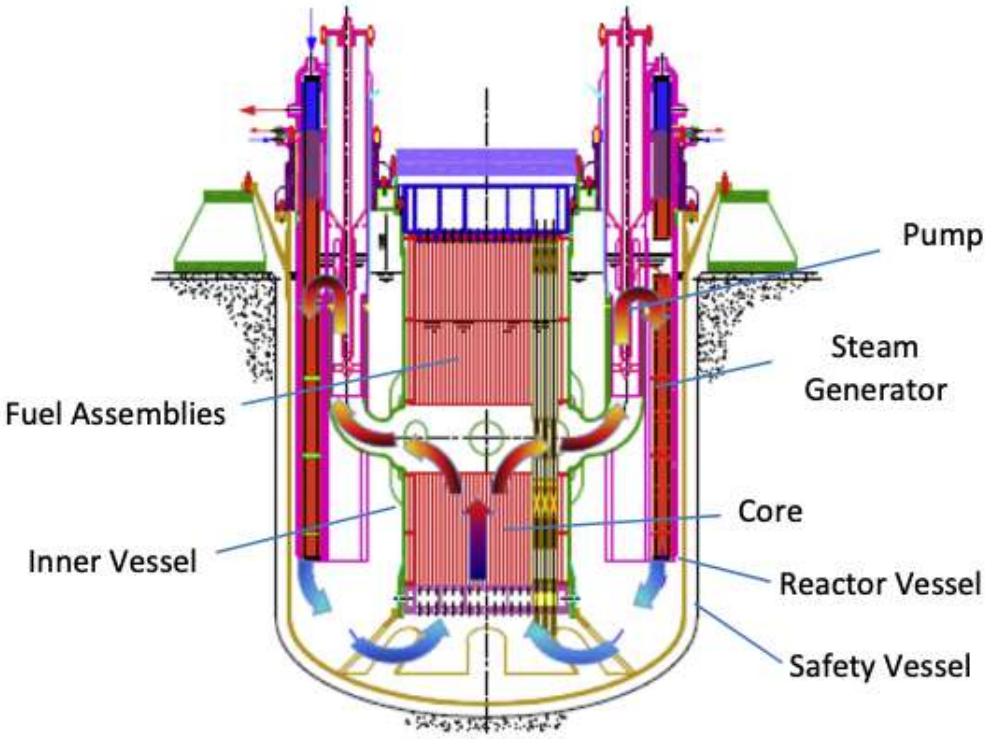

Figure 1.2: ALFRED primary system layout [33].

The function of the SV is to mitigate the consequences of through-wall cracks in the RV with leakage of lead. The dimension of the gap between the two vessels is designed in such a manner that, in case of lead leak from the RV, the resulting primary coolant always covers the SG inlet and the lead circulation flow path is indefinitely maintained.
The inner vessel has two targets: separation of cold lead from hot lead and fuel assemblies support.

As said, the steam generator and primary pump are integrated into a single vertical unit. The PP has its mechanical suction in the hot pool inside the IV and its motor above the reactor roof. The SG consists of a bundle of 542 bayonet tubes immersed in the RV pool for 6 m of their length. The configuration of the bayonet tubes, made of an external safety tube and an internal insulating layer composed of four concentric tubes, ensures that in case of external tube break the primary lead does not enter into contact with the secondary water. Moreover, a tube break can be easily detected by monitoring the pressure of the helium gap present in the insulating layer.

The core configuration (Figure 1.3) foresees 171 wrapped hexagonal fuel assemblies (FAs), 12 controls rods (CRs), 4 safety rods (SRs) surrounded by 108 dummy elements (ZrO_2-Y_2O_3) shielding the IV.

Each FA is about 8 m long and consists of 127 fuel pins. Fuel pellets are hollow and made by MOX fuel. The fuel rods are provided with upper elastic elements (cup springs) to prevent lifting induced by hydrodynamic loads and to accommodate axial thermal expansion. The FAs upper end extends beyond the lead free surface area in the cover gas to simplify their handling and inspection. This unique solution strongly characterizes ALFRED design and makes possible to refuel without the need of in-vessel machines.

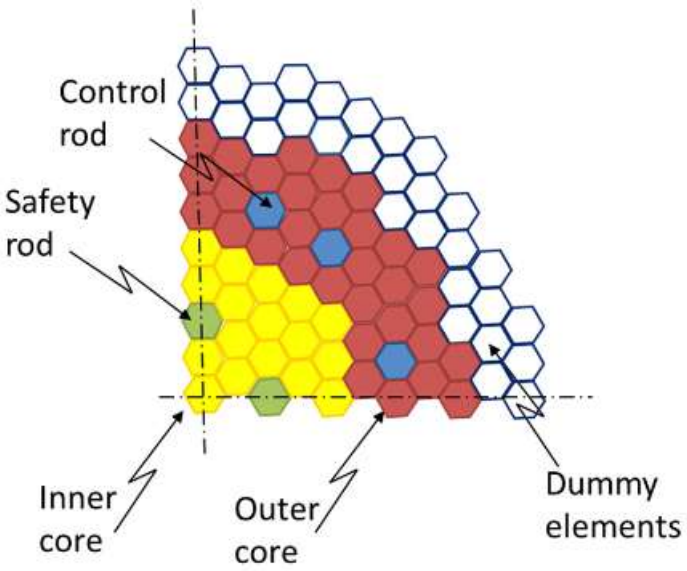

Figure 1.3: ALFRED core layout [33].

For what concerns the decay heat removal (DHR) system, ALFRED has two passive, redundant and independent systems, DHR1 and DHR2. They are both composed of 4 isolation condensers (ICs), immersed in water pools and connected to 4 SGs on the secondary side. The water inventory in each pool is enough to guarantee 3 days of decay heat removal operation. Three out of four ICs are sufficient to remove decay power and the total number of active ICs cannot exceeds four units in order to avoid excessive cooling of the primary coolant, leading to its solidification. In any case, anti-freezing systems are introduced to prevent lead to go below its melting point.

As of 2020, six experimental facilities and a coordination Hub are planned to be constructed in Romania, on the Institute for Nuclear Research (RATEN ICN) site, located in the Mioveni town. Each facility will address key aspects related to ALFRED reactor safety and licensing. They are:

- ATHENA, to test the behavior of full scale components in liquid lead, with a particular focus on the investigation of the steam generator tube rupture, the fluid-structure interaction, lead stratification and freezing in a pool configuration system.

- ChemLab, a laboratory specialized in the chemistry of lead and cover gas, to better understand oxygen and other impurities control and monitoring in both environments.
- HELENA2, a loop type installation, to test and demonstrate the thermal-hydraulic behavior in pure liquid lead of full scale ALFRED fuel assemblies and of the safety and control rods, in normal and forced flow regimes.
- ELF, a pure lead pool installation operated in natural or forced circulation mode, for endurance tests of the operation of components, equipment and systems to be used in by ALFRED demonstrator, as well as for the measurement of the reliability characteristics.
- Meltin'Pot, to investigate the phenomenology associated to severe accidents in a LFR reactor by studying fuel, cladding and coolant interactions, including fuel dispersion during a severe accident, fission products retention in pure lead, etc.
- HandsON, to test the handling of the full scale fuel assemblies and control rods of the ALFRED demonstrator, in operational conditions.

The Hub will coordinate the research activities in synergy with a network of additional facilities distributed in Europe, while the Centre of Excellence - Lead School, hosted by the HUB, will deliver world-class education and training to researchers, technicians and students, as well as lectures and dissemination events for the general public.

1.2.2. ELFR

The ELFR (European Lead-cooled Fast Reactor) is a modification of the earlier ELSY (European Lead SYstem) reactor concept while keeping the same power size (1500 MWth). It will be the foak industrial LFR in Europe and will open the road for commercial units.

It has a pool-type configuration with the reactor vessel kept as compact as possible to reduce the primary coolant inventory and, hence, the corresponding seismic loads, while sufficiently wide to accommodate the primary system components (Figure 1.4). They are 8 steam generators, 4 primary pumps and 8 decay heat dip-coolers. The hot pool of ELFR is enclosed by an inner vessel and is connected to he PPs through suction pipes.

Lead working conditions are 400 °C at core inlet and 480 °C at core outlet. Thanks to the low pressure losses in the primary circuit − 0.9 bar in core and 1.4 bar in total − and to the position of the heat source (the core) and the heat sinks (the steam generators), the system is able to provide efficient natural circulation of the coolant under emergency

shutdown conditions.
The decay heat removal is managed by two safety systems: they are characterized by passive operation, redundancy and diversity, while being completely independent of each other.

ELFR is intended to implement the so-called adiabatic reactor concept with closed fuel cycle and maintaining constant the quantity of plutonium. This strategy allows to achieve sustainability and proliferation resistance.

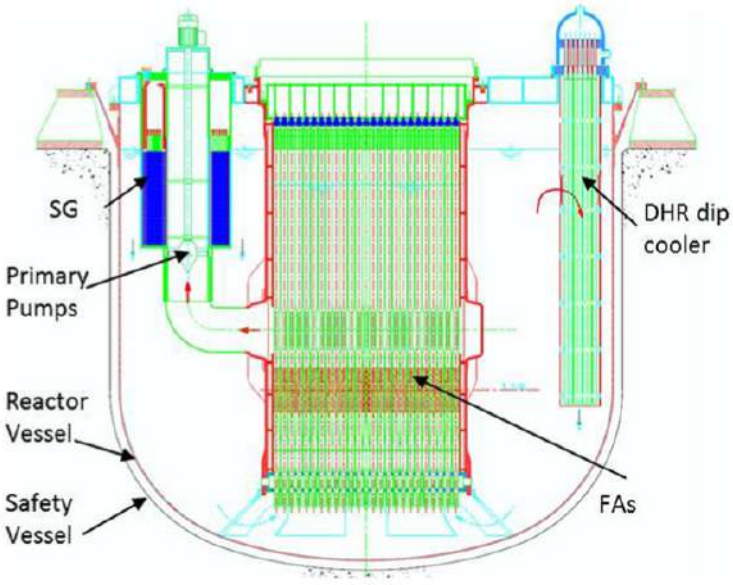

Figure 1.4: ELFR layout [33].

1.2.3. BREST

The BREST family is a series of reactors under study in Russia in the recents years. In particular, two units are envisaged: BREST-OD-300, a 300 MWe demonstrator, and BREST-1200 for commercial purposes in the long term.

The construction of BREST-300 was approved in 2016 and started in June 2021 in Seversk (near Tomsk). It employs a pool-type design which incorporates the core with reflector and control rods, steam generators and pumps, fuel reloading and management, safety and auxiliary systems, all within the primary vessel (Figure 1.5).

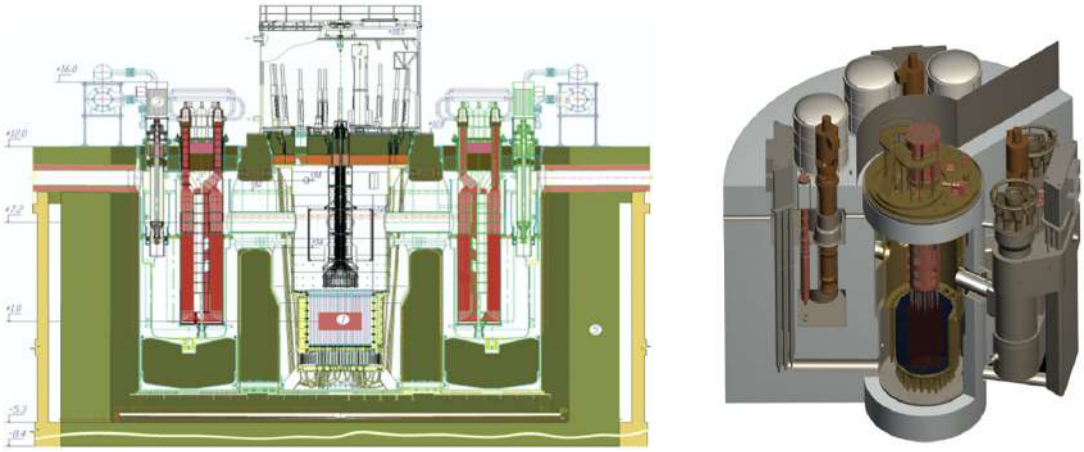

(a) Vertical section. (b) 3D representation.

Figure 1.5: BREST-OD-300 layout [33].

Primary thermal cycle is between 420 and 535 °C for a core thermal power of 700 MWth. On the secondary side, a conventional steam-water cycle reaching 505 °C at 17 MPa allows for a thermal efficiency of about 42%.

As other designs, the core is not provided with uranium blanket, replaced simply by lead reflector improving power distribution, providing negative density and void coefficients and ruling out the production of weapons-grade plutonium. Core's fuel lattice has a wide coolant flow area, resulting in low pressure losses and enabling the establishment of natural circulation for decay heat removal. For the first core loading, fuel type will be nitride of depleted uranium mixed with plutonium, coming from VVER's irradiated fuel after cooling and reprocessing. In this way it may be achieved a core breeding ratio equal to approximately 1 with fuel reprocessing limited to the removal of fission products. The reprocessing plant is co-located with the reactor, and this is a notable characteristic of BREST-300 which eliminates in principle any issue related to fuel transportation.

BREST decay heat removal system has the peculiarity of being passive and time-unlimited: through air-cooled heat exchangers, natural circulation of air removes power from the lead circuit. Heated air is then vented to the atmosphere.

1.2.4. SSTAR

SSTAR (Small, Sealed, Transportable, Autonomous Reactor) was a proposed small modular reactor developed in the United States at Lawrence Livermore National Laboratory. Although the project ended in 2015, it is still considered within GIF as representative concept of the small-size category of LFRs.

The reactor was designed to provide power to developing nations and remote communities without electrical grid connections, such as Hawaii, Alaska or island nations in the Pacific. This explains its most important features, including a small-size reactor vessel (12 m high) that can supply 45 MWth (20 MWe); reliance on natural circulation for both operational and shutdown heat removal; a very long core life without refueling (15-30 years) which imparts strong proliferation resistance; autonomous load following without control rod motion. A really innovative solution is the supercritical CO_2 (S-CO_2) Brayton cycle power conversion system.
The overall design incorporates inherent thermo-structural feedbacks which guarantee a high degree of passive safety.

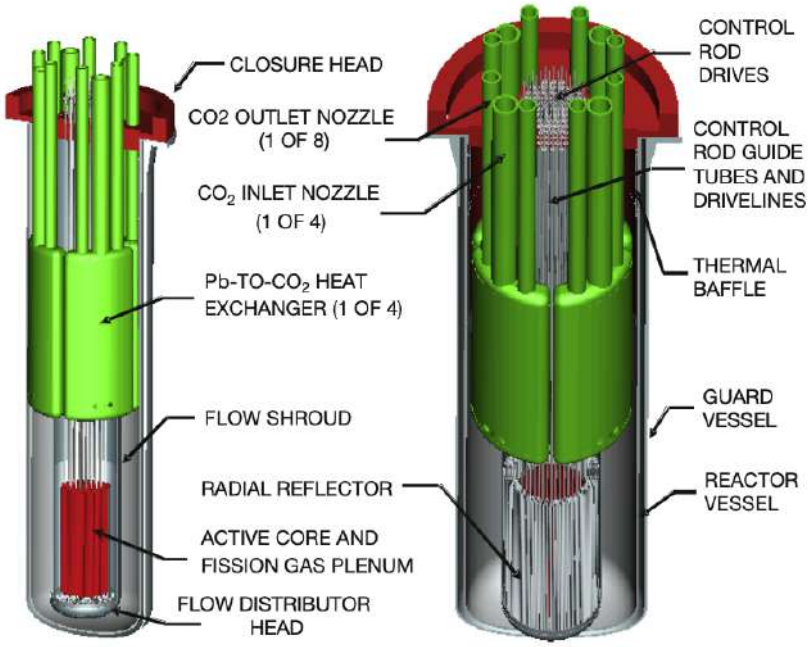

Figure 1.6: SSTAR layout [33].

1.2.5. LFR-AS-200

The LFR-AS-200 is an innovative SMR cooled by liquid lead currently under study by Hydromine Nuclear Energy S.à.r.l., Luxembourg. AS is the acronym for Amphora-Shaped, which refers to the shape of the inner vessel (IV), while 200 is the size of the reactor in MWe.

It is a pool-type lead-cooled fast reactor with all the primary system components integrated inside the reactor vessel (Figure 1.7). Among its peculiarities there are 6 innovative spiral-tube steam generators (STSGs), 6 mechanical pumps, reversed-flag-type controls rods, 3 + 3 dip-coolers belonging to passive, diversified, redundant decay heat removal

systems and the ASIV, large in the bottom part in order to dispense of shielding assemblies. The fuel assemblies are characterized by stems extending above lead free surface level with heads forming a self-sustaining core. Then, two rotating plugs and an ex-vessel refueling machine allow to perform refueling under visual control and sealed conditions.

The compactness of the reactor (less than 1 m^3/MWe) makes it competitive in the cost of kWh. This is also a consequence of the reduced need of in-service inspections, reached by the elimination of critical components such as in-vessel refueling machine, core strongback and above-core structures immersed in lead and, hence, submitted to thermal transients and fast neutron fluxes.

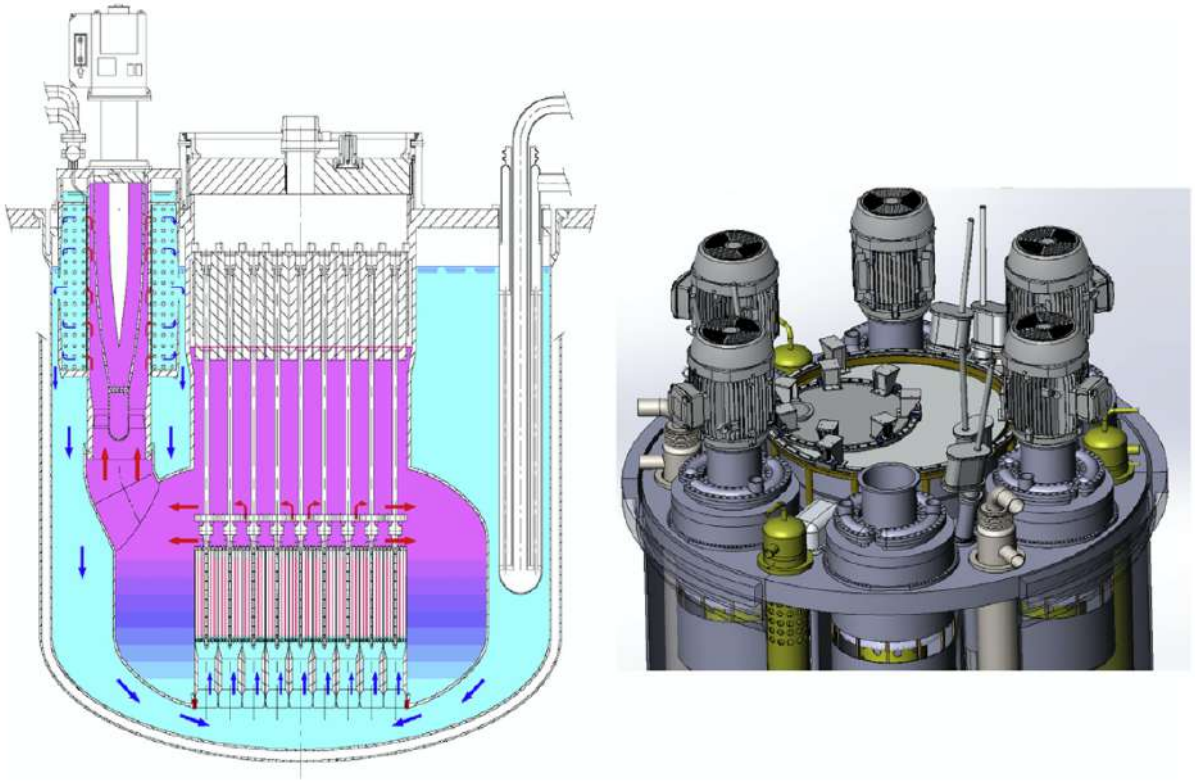

Figure 1.7: LFR-ASIV-200 layout [33].

1.2.6. CLFR

The CLFR series is developed by China Nuclear Power Technology Research Institute Co., Ltd. (CNPRI) as the next generation of commercial nuclear reactors of China General Nuclear Power Corporation (CGN). The series foresees two models: CLFR-100, a 100 MWe demonstrator for the heavy liquid metal technology with the target to be in operation by 2030; CLFR-300, a 300 MWe unit designed to demonstrate the economic competitiveness of the LFR technology relative to LWRs.

The CLFR series (Figure 1.8) introduces advanced design solutions like integral, modular arrangement and smart operation and maintenance. The reactor opted for the pool-type configuration with all primary components located inside the main vessel. This simplification of the design provides safety advantages for instance by eliminating main vessel penetrations, thus reducing the likelihood of loss of coolant accidents.

The CLFR series is developing an advanced safety concept named Natural-Driven Safety (NDS) to solve conflicting requirements of safety and economy. It aims at reactor safety systems entirely driven by physical laws without the use of any active system (including batteries or electronic devices). In particular, two mechanisms are under study: the Natural Driven Shutdown System (NDSS) and the Natural Driven Decay Heat Removal System (NDDHRS). The NDSS can virtually eliminate risks of unprotected accident, while the NDDHRS can virtually eliminate risks of core damage and large release of radioactivity.
These excellent safety features can help CLFR-300 to improve nuclear power safety and economic performances simultaneously and rule out the requirement of evacuation of the local population.

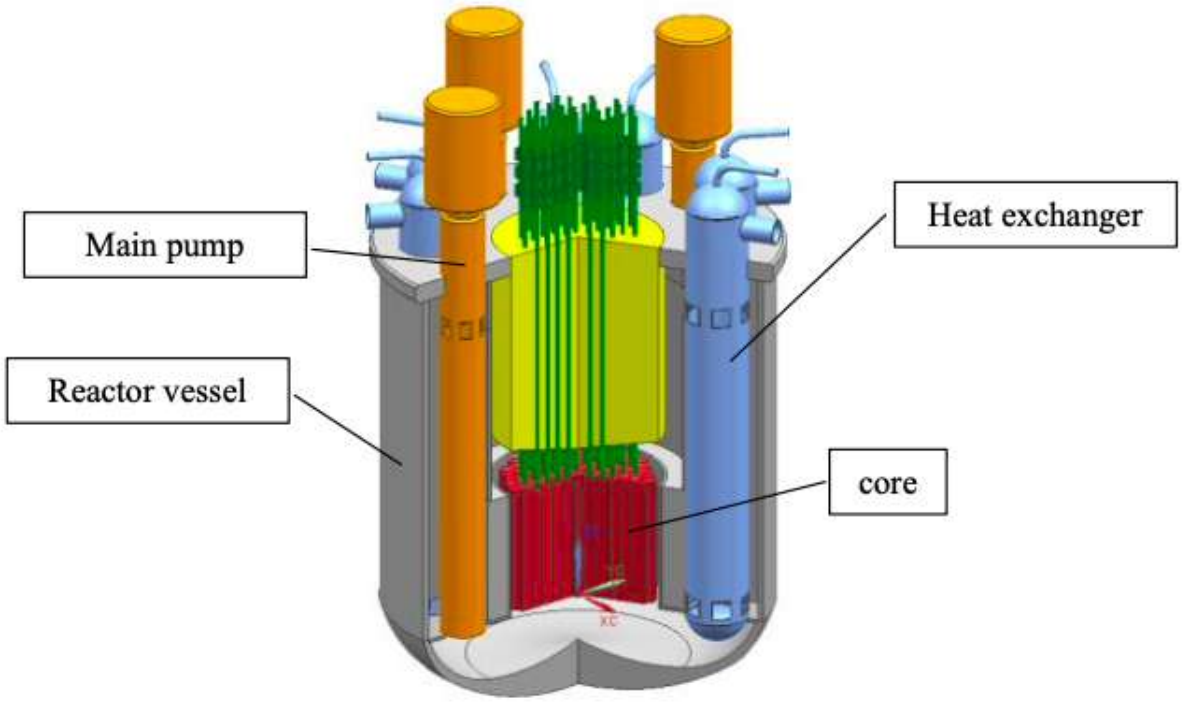

Figure 1.8: CLFR-300 general scheme [33].

1.2.7. Westinghouse LFR

The Westinghouse LFR is a medium-size (about 460 MWe), modular, lead-cooled nuclear reactor. It operates in pool configuration and is coupled with an air-cooled supercritical CO_2 (S-CO_2) secondary system. The primary plant mission is base load electricity production as well as load following, under competitive economics, versatility in future and diverse markets and high levels of safety at the same time. In fact, thanks to the medium-level power output the plant can be easily integrated into lower-capacity grids, while also being optimal for standard base load plant applications. Load leveling is achieved through an integrated energy storage system fully coupled with the balance of plant equipment, allowing to follow electricity demand without the necessity of core power variations. Moreover, being air-cooled, the plant does not require to be located in the vicinity of large water bodies, thus greatly expanding the list of options for plant siting.

The compactness of the reactor vessel is enhanced by the use of extremely robust, highly-compact hybrid microchannel-type primary heat exchangers and by the use of a water-assisted reactor vessel cooling system for emergency decay heat removal. In this way, in-vessel dip-coolers are eliminated because, in case of accidents, liquid lead natural circulation is simply driven by passive heat transfer through the reactor vessel and guard vessel to an outer annular water pool. When water inventory is depleted, natural convection with air circulating outside of the guard vessel is sufficient to remove the remaining decay power.

The scheme of the primary system is shown in Figure 1.9, while Figure 1.10 displays the plant layout.

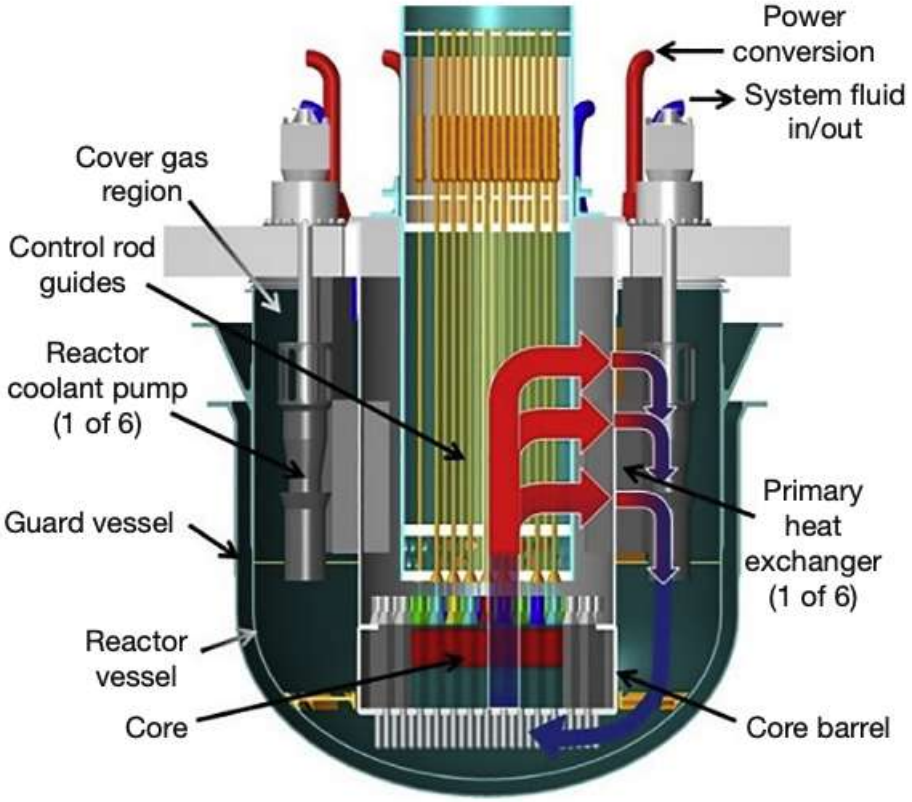

Figure 1.9: Westinghouse LFR primary system schematic sketch [33].

Figure 1.10: Westinghouse LFR plant layout [33].

1.2.8. MYRRHA

MYRRA (Multipurpose hYbrid Research Reactor for High-tech Applications) [38, 39] is an innovative research reactor planned for costruction at SCK-CEN's Mol site in northern Belgium. It aims at demonstrating the accelerator driven system (ADS) concept by coupling the high-power proton accelerator, the spallation target and the subcritical reactor (Figure 1.11). In addition, it permits the investigation of high-level waste (HLW) transmutation technology. Last but not least, since MYRRHA adopts lead-bismuth eutectic as coolant, it can also significantly contribute to lead fast reactors research.
The facility will be able to work both in subcritical mode and in critical mode, albeit with different performance characteristics. The two modes have their specific energy and flux distributions which allow to explore a wide range of applications: fuel development for innovative reactor systems, material study and testing for generation IV systems and fusion reactors, radioisotope production for medical and industrial purposes.

Figure 1.11: MYRRHA plant site sketch [39].

MYRRHA reactor is an integral pool-type concept (Figure 1.12). Among the in-vessel primary systems there are a diaphragm separating hot and cold plenum, 4 primary heat exchangers, 2 primary pumps, 2 in-vessel fuel handling machines and a core unit. The latter contains fuel assemblies, controls rods, safety rods, the spallation neutron target, instrumentation and experimental devices. The reactor pit features a liner as secondary containment in case of leakage or break from the primary vessel. Because of the structures above the core, fuel and reflector assemblies need to be loaded from underneath and, in this way, they do not need locking devices to hold them because they rely on buoyancy.

Decay heat is removed by a passive cooling system with quadruple redundancy. In case of a common cause failure, the diverse RVACS system can take over of the cooling function.

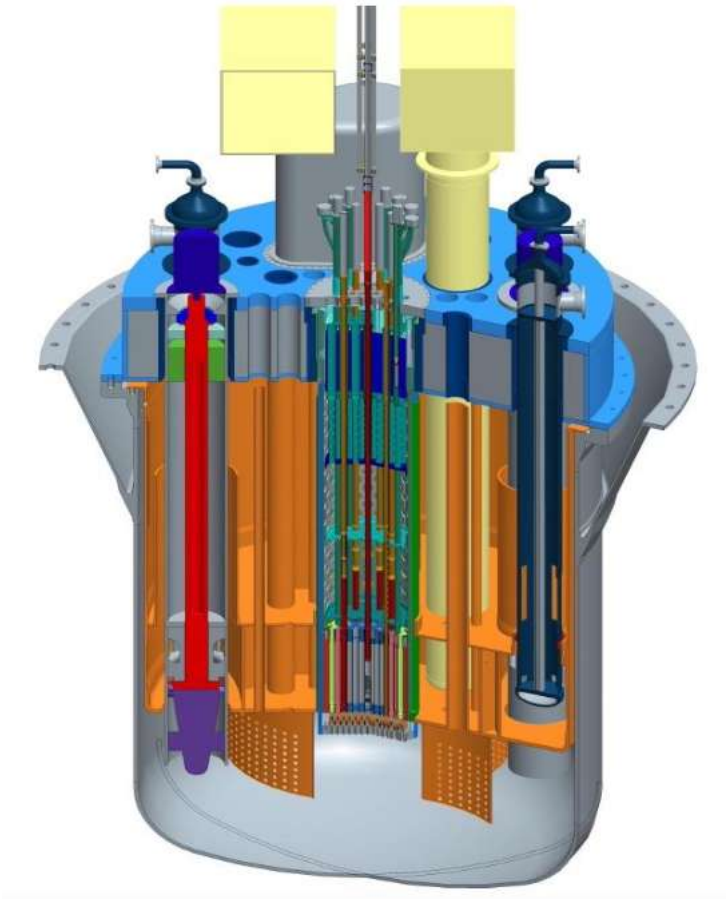

Figure 1.12: MYRRHA reactor 3D sketch.

At full power, the reactor operates at 100 MWth in critical mode or 65 MWth in subcritical mode. LBE temperature range is 270-352 °C with a mass flow rate of 13800 kg/s.

In 2018 Belgian Government supported the construction of MYRRHA in a phased approach. The first phase, called MINERVA, allocates budget for the accelerator up to 100 MeV including an isotope separator online and a proton target facility. It has to be finalized by 2026, and by then they plan to obtain all the necessary permits for the reactor construction.

1.2.9. SVBR-100

The SVBR-100 is a 280 MWth (100 MWe) multipurpose SMR cooled by LBE developed by AKME-engineering JSC together with SC Rosatom. The project leverages on the more than 80 reactor-years experience gained by Russian Federation in LBE technologies

adopted in nuclear submarines.
SVBR-100 can be used for regional scale grids, industrial heat and desalination systems. It is claimed to work without refueling for a period not less than 7-8 years.

The reactor features an integral layout where the entire primary circuit equipments − core, steam generators, circulation pumps, in-vessel radiation shielding − are contained within a robust vessel of the reactor mono-block (Figure 1.13). Inherent safety is guaranteed by negative void and temperature reactivity feedback coefficients. Natural circulation of the coolant is able to passively cool down the reactor for at least 72 hours preventing core temperature increase. Regarding the fuel, at a first stage it will use already qualified uranium dioxide (enrichment below 20%) providing a breeding ratio of 0.83. In case MOX fuel is adopted, the breeding ratio increases to approximately 1. Starting with UO_2, the closed fuel cycle can be realized in 15 years.

Thanks to the compactness of the reactor mono-block and to maximum factory readiness, SVBR-100 can be transported by railway and constructed in short time.

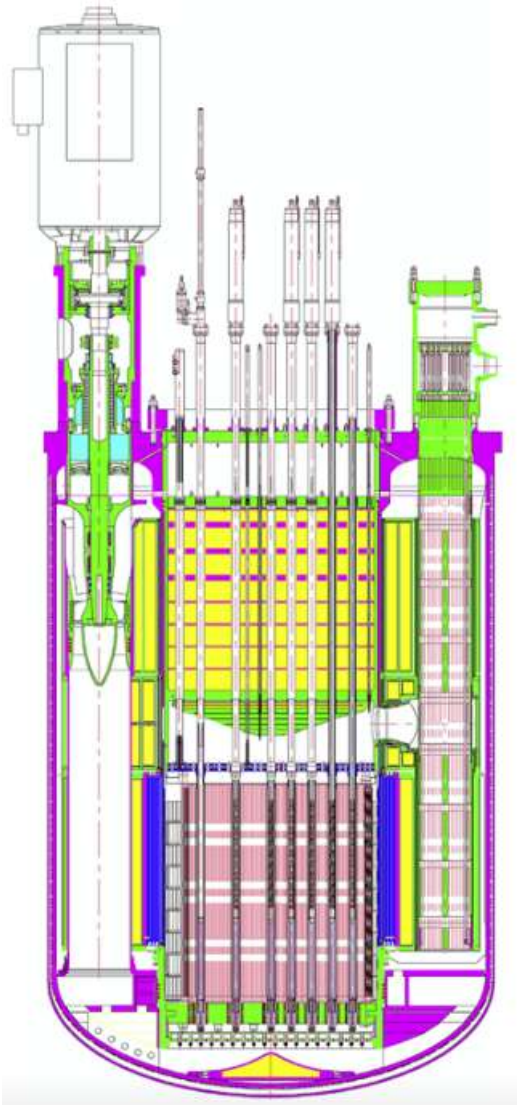

Figure 1.13: SVBR-100 reactor mono-block layout [33].

1.2.10. CLEAR-I

In 2011, the Chinese Academy of Sciences (CAS) launched an engineering project aimed at developing an accelerator driven system for nuclear waste transmutation. The CLEAR (China LEAd-based Reactor) proposed by the Institute of Nuclear Energy Safety Technology (INEST) was selected as the ADS reference concept.
The first step of the ADS deployment strategy is named CLEAR-I (Figure 1.14) and it is a 10 MWth pool-type fast reactor cooled by lead-bismuth eutectic, capable of being operated both in critical (to study LFR technology) and subcritical (for ADS technology validation) mode.

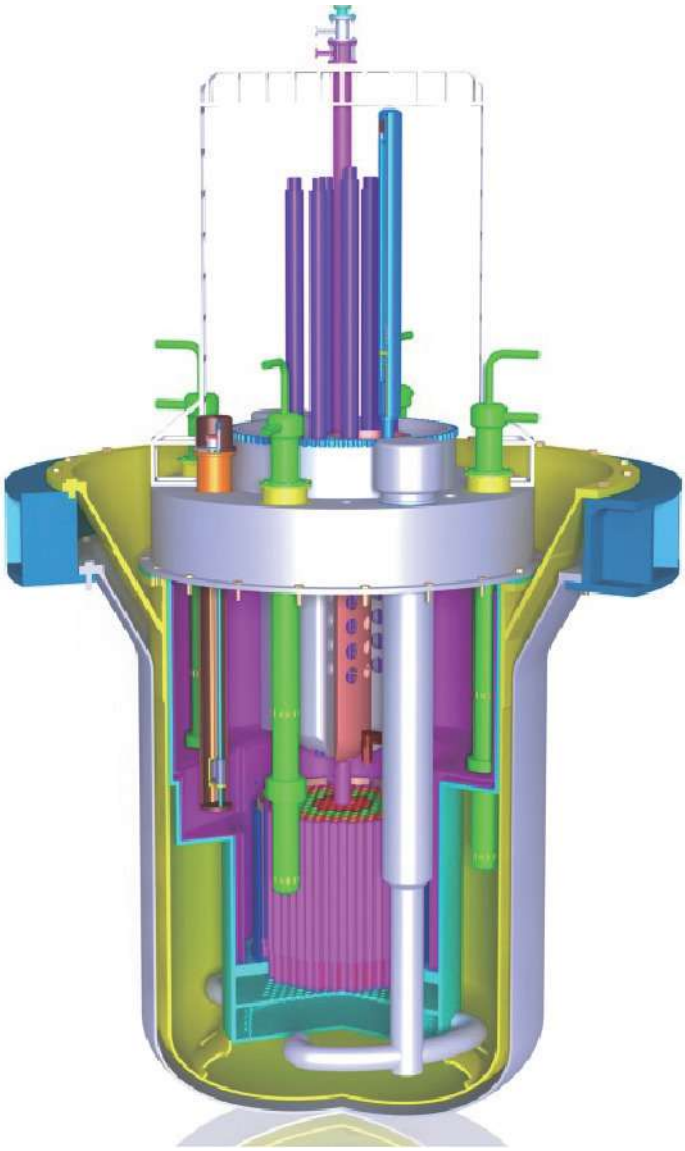

Figure 1.14: CLEAR-I nuclear reactor layout.

CLEAR-I features a core (Figure 1.15) composed of a variable (according to the operated mode) number of hexagonal wrapped fuel assemblies, each made of 61 fuel rods with triangular arrangement. For the first loading, the fuel pellet considered is UO_2 with enrichment of 19.75% and austenitic steel as fuel cladding (SS316Ti + SS316L). MOX fuel is the alternative. A vacuum bream tube is placed in the center of the core and lets a 250 MeV/10 mA proton beam enter from the top through the window and to the flowing LBE target. Double wall bayonet tubes for 4 primary heat exchangers are used as cooling system with 2 primary pumps vertically immersed in the cold pool. Decay heat is passively removed by the RVACS system in case of accidental conditions.

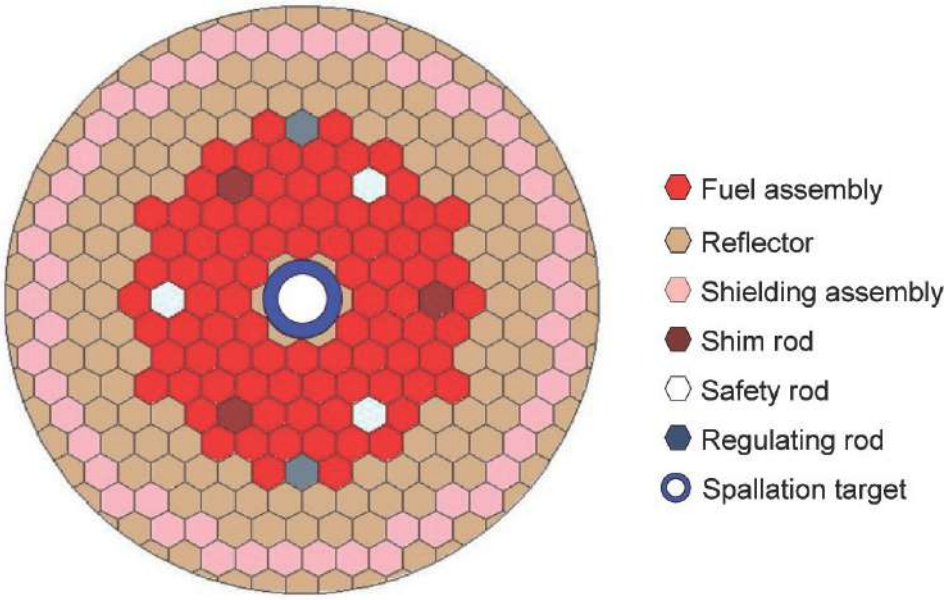

Figure 1.15: CLEAR-I core layout.

At present three integrated test facilities have been built at INEST to support CLEAR-I project and to validate its key components and operating regime. They are: CLEAR-S, a lead-based non-nuclear reactor, CLEAR-0, a lead-based zero power nuclear reactor, and CLEAR-V, the lead-based virtual reactor.

1.3. Short summary of codes for LFRs

The dynamical behavior of a complex industrial system is usually extremely difficult to experimentally assess and validate. This is true for nuclear systems as well. Therefore, it is necessary to have models of the system and softwares to run simulations.

Traditionally, liquid metal cooled reactors were studied adopting legacy system codes originally developed for safety analysis of sodium-cooled and/or light water reactors, such as SAS4A/SASSYS-1 [40, 41], APROS and RELAP. Although these codes were extended and validated on experimental data coming from SFRs, they need to be adapted by the user in various ways to be directly applicable to lead-cooled reactor systems. Another typical problem is related to the complexity of these codes after decades of modifications, extensions and applications, which makes further refinements to optimally include the study of LFRs really hard. Eventually, they appear as black boxes suitable only for the simulation of already existing LFRs. Other codes, such as SIM-LFR [35] and SIM-ADS, have been purpose-built for simulation of lead-cooled reactor systems, but have not been made available for public use.

From these reasons it emerges the necessity to write, verify and subsequently validate a new code totally tailored on LFRs. This has been done in the recent years by the Nuclear Engineering Division of Physics Department at KTH and the code goes under the name of Bortot's Elegant Liquid LFR Analysis tool (BELLA) [42–45]. BELLA is a general-purpose plant simulator oriented to the dynamics and control of lead-cooled fast reactors. It is based on a point-wise description of and coupling between the reactor core, primary coolant, steam generator and secondary system. Current capabilities include simulation of unprotected transient over-power (UTOP), loss-of-flow (ULOF) and loss-of-heat-sink (ULOHS) accidents, together with station blackout by combining ULOF and ULOHS. The code is currently available in different languages, namely Python, Matlab/Simulink, C++ and Mathematica [46–48].

What BELLA is currently missing in its most updated version is the correct implementation of fuel thermomechanics equations − in particular when adopting uranium nitride as fuel − and a model for the steam generator, among others. Indeed, one of the goals of this thesis work is the development of a functioning model for the steam generator module adopting an approach consistent with the rest of the code. To it, Chapter 4 is fully dedicated.

1.4. Conclusions

As advanced nuclear power systems, lead-cooled fast reactors propose an innovative technology to couple conventional power production with sustainability in the fuel cycle, both front-end (nuclear fuel breeding) and back-end (nuclear waste burning and recycling). This can be accomplished while keeping high safety standards thanks to passive safety systems (e.g., natural circulation, RVACS) and accident-tolerant fuels. New materials that can support the transition toward high-temperature fast reactors are under study and testing, as the qualification process needs time to be completed by safety authorities. Everything is done without jeopardize the economic competitiveness of such reactors which are meant to enter into the market in the 2030s. Several projects of all the possible sizes (micro, small, medium and large) are proceeding exactly in this direction.

In this work BELLA is adopted to propose transient analysis on lead-cooled fast reactors. This thesis goes also in the direction of improving the code by adding a new steam generator module. Everything is presented and discussed in Chapters 3, 4 and 5.

2 | SUNRISE-LFR

A particularly interesting program within the lead-cooled fast reactors environment is the Swedish SUNRISE (SUstainable Nuclear Research In SwEden) to which this thesis work refers. It is the first step towards building a research LFR in the country. The project partners are KTH, Luleå University of Technology and Uppsala University together with LeadCold Reactors and Uniper Sweden among other stakeholders. At present the program is in the early stages, but the aim is to construct the reactor within 2030 at Oskarshamn site in Sweden.

This chapter introduces the SUNRISE project and describes the layout of SUNRISE-LFR. In particular, Section 2.1 gives some background about the project. Section 2.2 describes the purposes of the demonstrator reactor and the safety margins that are targeted. Section 2.3 presents the layout of the reactor core, fuel and control rods. Section 2.4 is about the reactor vessel and the rest of the primary circuit. Section 2.5 gives some information about current and future ideas for the reactor secondary side. Lastly, Section 2.6 briefly delineates some conclusions about SUNRISE-LFR.

2.1. The SUNRISE center and correlated projects

In 2020 the Swedish Foundation for Strategic Research (SSF) announced a call for Research Centers on Future Advanced Technology for Sustainability in order to meet the UN 2030 Agenda's SDGs [49]. The SUNRISE center was formed as a response to that call with the ambition of designing an experimental lead-cooled fast reactor − SUNRISE-LFR − to be built in Sweden. The construction site is going to be Oskarshamn, where an already existing reactor is active providing about 10% of Swedish electricity need, while two older units are already decommissioned. They are all BWRs.

The plan is to have the demonstrator reactor operational by 2030 and, as an intermediate step, a conventional experimental facility will be built in the same site, starting in 2023 to have it operational by 2024. It will be a scaled-down (1:56) non-nuclear mockup which produces power through electrical heaters instead of nuclear fuel. It is meant to simulate

the reactor conditions and to study the behavior of structural materials, metals, steam generator and pump immersed in hot liquid lead flow. The name of this intermediate project, which has recently granted some fundings from the Swedish Energy Agency [50], is SOLSTICE and the name of the reactor SEALER-E [51].
After SOLSTICE and SUNRISE projects are successfully managed and after they demonstrate the capability of LFRs to contribute to safety, security and efficiency in a sustainable society, the further step will be the commercialization of the units. At present, it is probably too early to specifically address this topic, but LeadCold, among the industrial stakeholders in SUNRISE and SOLSTICE, is already developing ideas and solutions for the power reactors which will enter into the market in the 2030s. They plan to have two units: SEALER-55 (SwEdish Advanced LEad Reactor) of about 55 MWe and SEALER-Arctic (between 3 and 10 MWe) [52–54].

In the next sections SUNRISE-LFR is described.

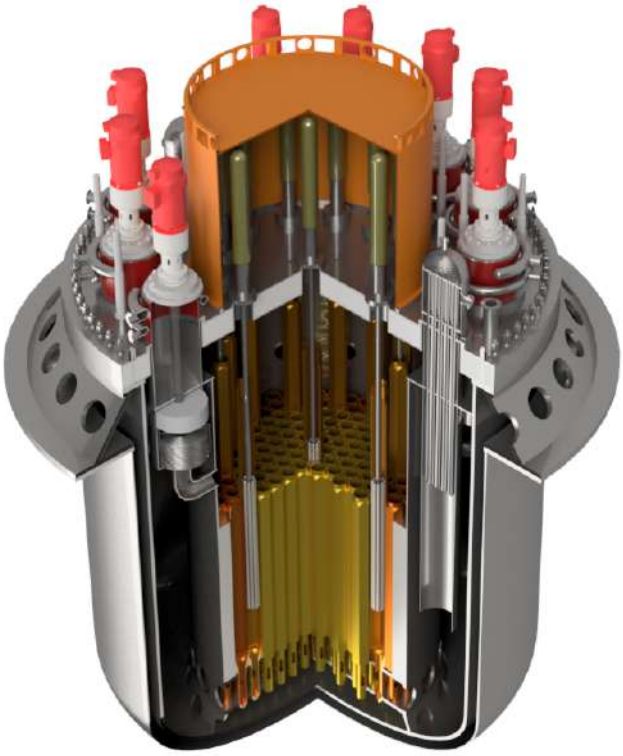

Figure 2.1: SEALER-55 graphical representation. Reproduced with the permission of LeadCold.

2.2. Purposes and safety margins

Before entering into the specifics of the SUNRISE demonstrator, it is worth to remember the goals of this reactor. As already stated, it does not target power production. It is intended as an experimental unit to demonstrate the applicability of LFRs for commercial purposes; to provide research opportunities for irradiation experiments in order to qualify new fuel types and to verify and validate computational tools and codes; to permit education of university students and training of commercial operators [48]. This implicitly requests safety margins larger than necessary, which allow to stress the reactor conditions with unprotected accidental scenarios to test its intrinsic capabilities to reach a safe, steady-state regime. During an unprotected transient human intervention is not envisaged (no reactor SCRAM by the plant operator).

SUNRISE-LFR has the general target of being able to withstand unprotected scenarios for seven days. This comes with specific safety requirements, both on fuel and cladding. First of all, it must be prevented by all means that fuel melting occurs in all scenarios, normal and off-normal. This would be the worst event in a nuclear reactor because it means that the system temperatures are extreme, all structural materials have already melted and fuel, mixing with coolant and primary system metals, escapes from the reactor vessel. System temperatures must be always very distant from fuel melting point, which is in any case very high (around 2700-2800 °C for oxides and nitrides).
The second criterion is preventing cladding tube rupture caused by thermal creep. This is a time-dependent, visco-elastic deformation of a metal tube that occurs at high temperatures (about 0.4-0.5 of melting point) and high stresses, eventually leading to rupture. The internal stress level is provided by the gap pressure. That in turn depends on the fission gas release (FGR), function of both temperature and burnup. The most conservative assumption is FGR=100% which leads to thermal creep rupture if $T > 763$ °C for seven days [48]. Adopting a recently published correlation for FGR on uranium nitride [55], the maximum FGR is less than 10% even at 1200 °C; in this case thermal creep rupture occurs if $T > 816$ °C for seven days [48]. However, these estimations account only for steady-state temperature behaviors neglecting the effects of short-interval high temperature peaks. Moreover, from a regulatory point of view, it might potentially not be acceptable to assume anything other than a 100% fission gas release. Therefore, in this work it is assumed the most conservative threshold for cladding creep failure after 7 days, which is 763 °C. The requirement for SUNRISE-LFR asks to prevent that fuel cladding consumes more than half of the margin to creep rupture after an unprotected transient. Because the hottest cladding position in the core is at 560 °C in nominal conditions (Sub-

section 3.4.1), half of the margin is at 662 °C: this is the first threshold in evaluating the cladding safety margin. Second threshold is at 763 °C.

2.3. Reactor core layout

The size of the reactor is 80 MWth. This choice comes after considerations [48] about the impact of a station blackout, which is a combination of ULOF (unprotected loss of flow) and ULOHS (unprotected loss of heat sink). All the pumps and the steam generators are supposed to completely fail and no other auxiliary system is supposed to successfully enter into action, leaving the system in hot conditions with stagnant lead. Although this is the worst-case scenario, the correct simulation of ULOF and ULOHS shows that some natural circulation is still present. But it is neglected, and a more conservative transient is assumed as the aim is just to give a quick a rough estimation of the size of the reactor.

Coolant maximum and minimum temperatures in the system are decided leveraging on lead characteristics. In order to limit the corrosion by flowing lead on structural materials, maximum temperature is fixed at 550 °C. This serves also in contrasting thermal creep on fuel cladding. Lead minimum temperature needs to be sufficiently distant from the melting point and needs to limit liquid metal embrittlement on metals: this is why it is fixed at 420 °C.

Coolant core inlet and outlet temperatures, together with core thermal power, set the mass flow rate: approximately 4243 kg/s.

Parameter	Value	Unit
Core thermal power	80	MW
Lead core inlet temperature	420	°C
Lead core outlet temperature	550	°C
Lead mass flow rate	4243	kg/s
No. fuel assemblies	54	-
No. fuel rods per assembly	217	-
No. control assemblies	2	-
No. control rods per assembly	7	-
No. shut-down assemblies	4	-
No. shut-down rods per assembly	7	-
No. reflector assemblies	60	-
No. reflector rods per assembly	37	-

Table 2.1: SUNRISE-LFR core main parameters.

A complete derivation and justification of the solutions adopted in the core layout and dimensioning can be found in a recent paper published by F. Dehlin from KTH [48]. It provides an analytical method that explains the rationale behind the design of SUNRISE-LFR. All the data here presented come from that article, as the author of this manuscript has closely collaborated with F. Dehlin and the other engineers from Nuclear Engineering Division at KTH.
This section continues with the description of the core layout.

The core is composed of 54 fuel assemblies containing each 217 fuel rods. The description of fuel and of fuel rods is addressed in Subsection 2.3.2.

Reactivity control is managed primarily by two independently operated control rod assemblies made of natural boron carbide (B_4C) welded with Fe-10Cr-4Al-RE cladding. Four shut-down assemblies organized into two independent banks with two assemblies per bank are envisaged for SCRAM. The two banks have a different composition in order to diversify the insertion mechanism: bank 1 adopts 96% ^{10}B enriched boron carbide which can be inserted by gravity having a higher density than lead, while bank 2 is made of 96% ^{10}B enriched tungsten diboride (WB_2) which will foresee another insertion strategy having a lower density than lead. It must be underlined that the control strategy is still under development and reactivity control rods may change in the near future.

In the periphery of the active core 60 reflector assemblies are foreseen to improve both the neutron economy and to lower the neutron damage dose absorbed by the core barrel.

The core layout is displayed in Figure 2.2. Main parameters of reactivity control rods, shut-down banks and reflector rods are summarized in Table 2.2.

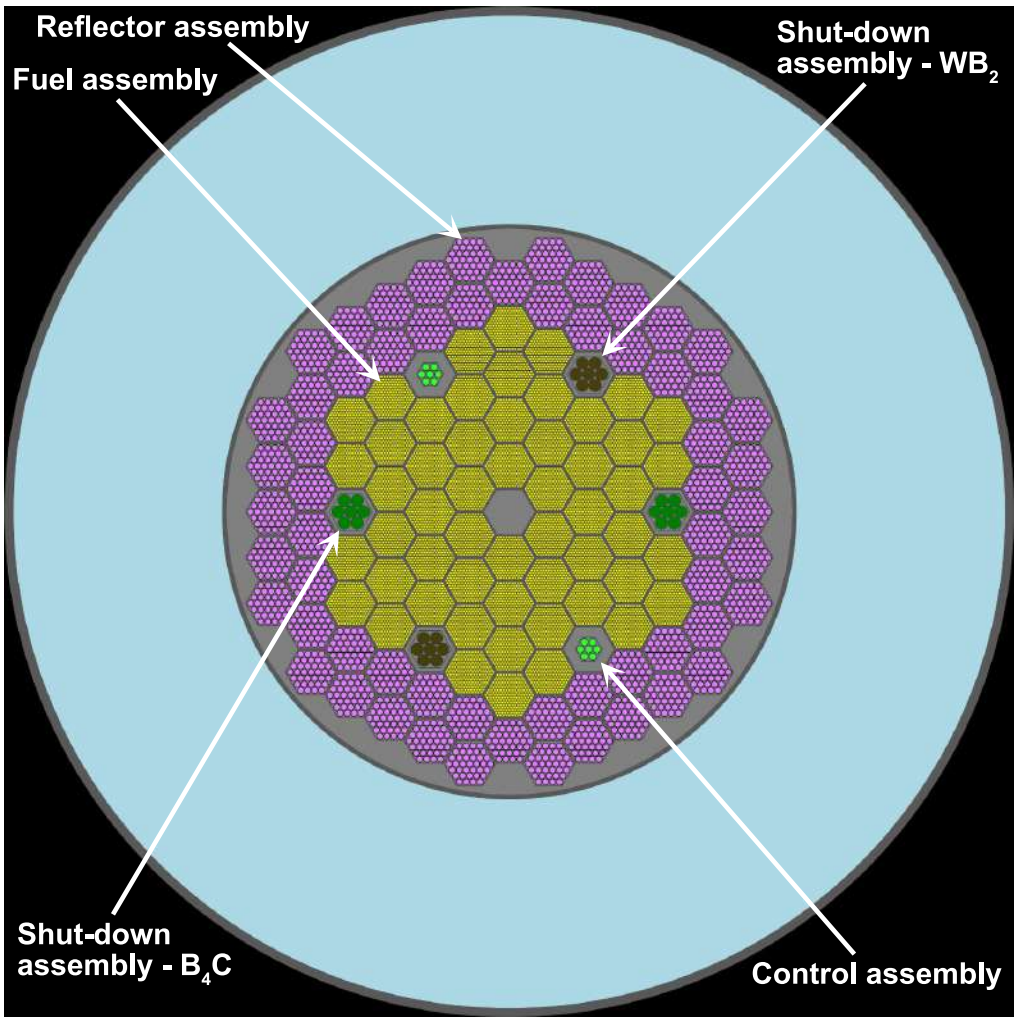

Figure 2.2: SUNRISE-LFR core layout [48].

Parameter	Value	Unit
Reactivity control pellet material	B_4C	-
B^{10} enrichment	Natural	at.%
Reactivity control pellet diameter	30.0	mm
Control assembly worth (at MoL)	257	pcm
Shut-down bank 1 pellet material	B_4C	-
Shut-down bank 1 worth (at MoL)	1236	pcm
Shut-down bank 2 pellet material	WB_2	-
Shut-down bank 2 worth (at MoL)	1167	pcm
B^{10} enrichment (both banks)	96	at.%
Shut-down pellet diameter	53.8	mm
Reflector pellet material	ZrO_2	-
Reflector pellet diameter	25.0	mm
Cladding material (all rods)	Fe-10Cr-4Al-RE	-
Inner duct material (all rods)	Fe-10Cr-4Al-RE	-

Table 2.2: SUNRISE-LFR reactivity control rods and reflector main parameters.

2.3.1. Fuel

One of the declared aims of Gen. IV nuclear reactors is to achieve sustainability in the fuel cycle, both in the front-end and in the back-end. The ultimate goal is to fully close the fuel cycle obtaining great benefits not only in efficiency (increase of conversion/breeding ratio and utilization factor), but also in energy cost (less fuel needs to be mined and enriched) and in proliferation resistance (plutonium and other fissile nuclides can be burned in the core).

In this sense, some Gen. IV demonstrators choose mixed uranium and plutonium oxides (MOX) as fuel. For instance, it is the case of the European ALFRED (Subsection 1.2.1).

For SUNRISE-LFR the fuel will be uranium nitride (UN) 12 at.% enrichment in ^{235}U. The reasons are many. First of all, it has a higher density (heavy-to-light-metal ratio is unity) which permits to reach criticality with a lower volume. Secondly, it has a higher thermal conductivity, thus fuel peak temperature is decreased (increasing safety margins). Then, it achieves a breeding ratio larger than one in a more compact way. Lastly, SUNRISE-LFR is designed with the target of minimizing the reactivity swing over the fuel cycle to

lower the need of control rods. With UN the reactivity reaches zero after approximately 16 EFPY (effective full power years), with a peak burnup of 59 GWd/ton-U and a peak damage dose of 106 dpa [48], which can be perfectly sustained by cladding material. Nitrogen will be enriched in ^{15}N through cryogenic distillation process.

At present UN is not qualified as nuclear fuel. This means that the near-term deployment of SUNRISE-LFR foresees a first core load with commercially available fuels, namely uranium dioxide (UO_2). Only at a later stage the reactor will transition to the novel, long-term operation uranium nitride, for which the experimental reactor serves as a qualification facility.

Although the author is aware that it is primarily important the study and the simulation of a uranium dioxide fueled core, this manuscript refers only to the long-term uranium nitride fueled core. To move from one core to the other, it is sufficient to change the set of correlations describing thermo-physical properties of fuel (Appendix A).

2.3.2. Fuel rods and fuel assemblies

The core contains 54 fuel assemblies each consisting of 217 fuel rods. Each fuel rod accounts primarily for the active region where UN pellets are located. The rest consists of two zirconium nitride (ZrN) insulators, one above and one below the fuel column; a boron carbide (B_4C) shield located below the lower insulator; a gas plenum filled with helium (He) located above the active zone; finally, two end-caps made out of alumina-forming-austenitic (AFA) stainless steel close the fuel rod at both ends. Figure 2.3 presents a sketch of the fuel rod and Table 2.4 lists its dimensions.

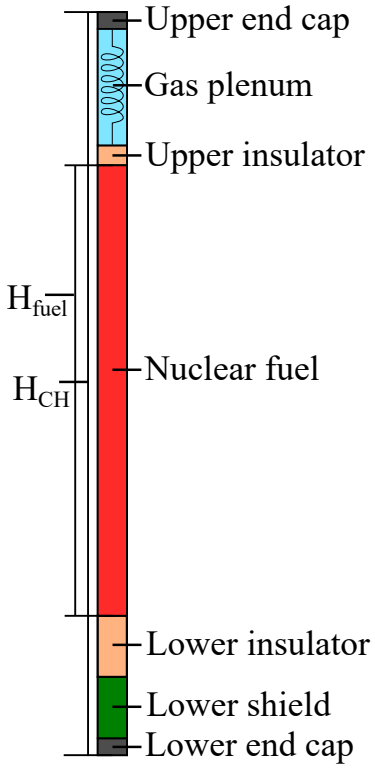

Figure 2.3: Fuel rod axial profile used in SUNRISE-LFR [48].

Fuel pellets and coolant are separated by cladding. Its choice is extremely delicate because of corrosion-erosion capabilities of molten lead. In the past, ideal candidates for fast reactors were ferritic-martensitic steels (T91) but because of their scarce resistance against creep at high temperatures they were discarded.
For SUNRISE-LFR the current idea is to adopt 15-15Ti-AIM1 as bulk material, due to its high radiation dose limit of circa 130 dpa and good creep resistance up to 650 °C, overlaid by a welded layer of Fe-10Cr-4Al-RE, a new metal alloy developed and studied at KTH which has demonstrated excellent capabilities against lead corrosion up to 800 °C [30, 31, 56, 57]. Its composition is shown is Table 2.3.
Due to low temperatures reached by the fuel pin, it must be avoided pellet-cladding interaction. This is why the thickness of the gap is a bit wider than standard fuel. Filling gas is helium (He).

Cr	Al	Si	C	RE	Fe
10.0	4.0	0.15	<0.05	Ti, Nb, Zr	Bal.

Table 2.3: Fe-10Cr-4Al-RE alloy composition (all values are given in wt%) [57]. RE stands for reactive elements.

Parameter	Value	Unit
Fuel rod diameter	11.8	mm
Fuel rod pitch	13.0	mm
Wire spacer diameter	1.2	mm
Fuel rod active height	1010	mm
Fuel rod total height	1750	mm
Pellet material	UN	-
Pellet enrichment	12	at.%
Pellet porosity	5	%
Pellet diameter	10.0	mm
Cladding material	15-15Ti AIM1	-
Cladding thickness	0.5	mm
Overlay-weld alloy material	Fe-10Cr-4Al-RE	-
Overlay-weld alloy thickness	0.2	mm
Gap filling gas	He	-
Pellet-cladding gap thickness	0.2	mm
Insulators material	ZrN	-
Upper insulator height	10	mm
Lower insulator height	100	mm
Plenum filling gas	He	-
Plenum height	460	mm
Shield material	B_4C	-
Shield height	100	mm
End cap material	AFA	-
Upper end cap height	20	mm
Lower end cap height	50	mm

Table 2.4: SUNRISE-LFR fuel rod layout.

The fuel rods are then inserted into hexagonal wire-wrapped tube bundles. The aim of the hexagonal can is to keep lead flow straight and prevent lead to cross-flow or to form

high turbulence regions which increase pressure losses and deteriorate removal power capabilities (local increase of temperature). The wire serves to keep a space between the rods and avoid any kind of oscillations (no spacer grids are present). The material is Fe-10Cr-4Al-RE. A simplified sketch of a generic hexagonal fuel assembly is portrayed in Figure 2.4a, while a sketch of the internal flow channel together with the wrapped wire is portrayed in Figure 2.4b. All dimensions of the hexagonal assembly can be found in Table 2.5.

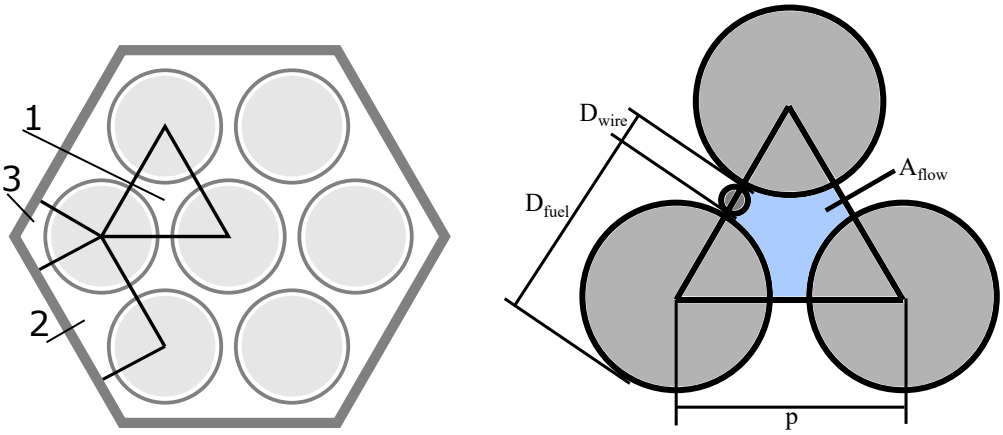

(a) Different kinds of channels [48]. (b) Internal flow channel [48].

Figure 2.4: Hexagonal assembly with a lower number of fuel rods.

Parameter	Value	Unit
Hex-can material	Fe-10Cr-4Al-RE	-
Hex-can inner flat-to-flat	196.0	mm
Hex-can outer flat-to-flat	202.0	mm
Hex-can pitch	204.2	mm

Table 2.5: SUNRISE-LFR hexagonal assembly layout.

2.4. Reactor vessel and primary circuit

SUNRISE-LFR is a pool-type reactor where all primary system is confined within the reactor vessel. On the one hand this allows the module to gain in simplicity of design, modularity in the deployment and overall safety (large break LOCA eliminated by design). But on the other hand it complicates the handling of the primary system components,

such as steam generators and pump, and the remote control of the fuel rods. Dedicated solutions have not been addressed yet, it will be subject of future work in SUNRISE.

The primary system (Figure 2.5) comprises the reactor core, hot leg, steam generator and pump module, cold leg and cold pool.
The core accommodates fuel which undergoes fission. It is cylindrically shaped and enclosed by the core barrels. The lead flows from the bottom to the top of it while being heated. Right above the core, lead is hot (550 °C in nominal conditions) and is flowing toward the heat exchanger: this region is called hot leg and has a free surface whose level changes according to lead thermal expansion. The remaining space above the hot leg is filled with an inert gas, probably argon (Ar). Then, molten lead flows radially from the central hot leg to the external cold leg passing through 10 steam generator units (Subsection 2.4.1). The cold leg is the annular part of the reactor and closed on top by a lid, patented by Wallenius and Szakalos in 2021 [58]. Through the cold leg, lead flows downward to the cold pool, which has spheroidal shape. This is the top bottom of the reactor and from it lead starts again the loop going through the core.

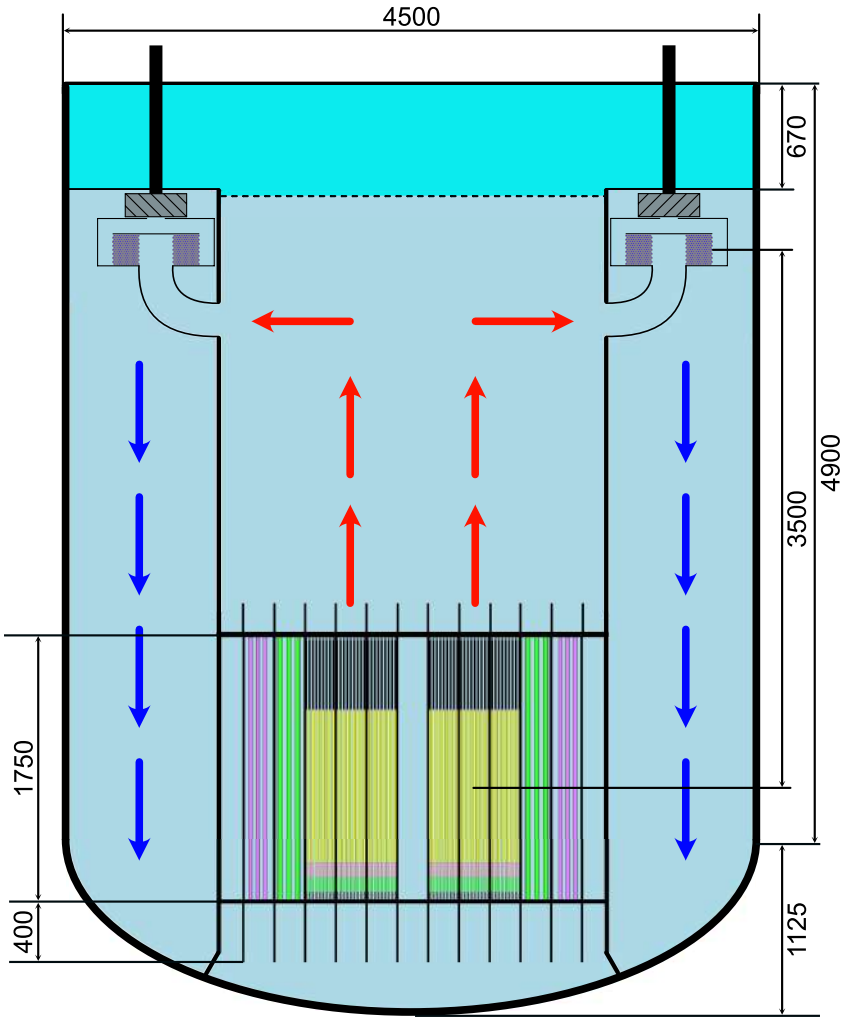

Figure 2.5: SUNRISE-LFR layout with dimensions (unit of measure is mm) [48].

The reactor vessel is surrounded by the guard vessel and the space in between is filled with argon (Ar). This is to provide an auxiliary, passive power removal system which enters into action only when the temperature of the system increases. In fact, due to argon poor thermal conductivity, all the heat is transferred from the reactor vessel to the guard vessel essentially by thermal radiation, which goes with the fourth power of temperature. This means that until primary system is working in nominal conditions (low lead and reactor vessel temperatures) the heat losses are about few hundreds kW, while when a sudden rise in lead temperature occurs, for instance after an unprotected transient overpower (UTOP) accident, power removed by thermal radiation almost doubles. In turn, the guard vessel

exchanges power with the surrounding ambient through radiation and natural convection. This system is called RVACS (reactor vessel auxiliary cooling system).
Another practical reason explains the existence of the guard vessel: it serves as a lead catcher in case the primary vessel is fractured. In fact, it must be guaranteed that the fuel is always covered by lead and this conditions sets the gap between the two vessels.

The primary vessel foresees to have a bulk of nuclear-grade SS316L stainless steel, already qualified to preserve the integrity of pressure boundary, with an overlay weld of AFA steel [31] on the lead exposed surfaces to form a boundary layer between the corrosive lead and the corrosion susceptive SS316L. AFA steels are very convenient to be welded on SS316L by conventional procedures; in principle, it is possible to adopt Fe-10Cr-4Al-RE as overlay, but it would be unreasonable to laser-weld it over such a wide surface. At present, AFA steels alone cannot be used to construct the vessel, because they need to go under the costly and time-consuming process of qualification as a nuclear-grade steel, and this is not the plan for SUNRISE-LFR.
Core barrel is made of Fe-10Cr-4Al-RE, while guard vessel adopts SS316L.

The position of the heat exchanger is crucial in maximizing buoyancy forces in natural circulation. Not only this is beneficial in case of ULOF accident, but also reduces the pump pressure injection in nominal conditions because it contributes in contrasting pressure losses. In particular, the higher is the distance between the two thermal centers, located at the midpoint of the core (heating region) and at the midpoint of the SG (cooling region), the stronger natural circulation becomes. This is the reason behind the choice of 3.5 m.

All the dimensions of the primary circuit components and of the vessels are listed in Table 2.6.

Parameter	Value	Unit
Core height	1.750	m
Core barrel material	Fe-10Cr-4Al-RE	-
Core barrel inner diameter	2.520	m
Core barrel outer diameter	2.560	m
Primary vessel material	SS316L	-
Primary vessel overlay-weld alloy	Fe-10Cr-4Al-RE	-
Primary vessel inner diameter	4.420	m
Primary vessel outer diameter	4.500	m
Guard vessel material	SS316L	-
Guard vessel inner diameter	4.700	m
Guard vessel outer diameter	4.800	m
Core and SG thermal centers distance	3.500	m
Cold pool spheroid radius	2.250	m
Cold pool spheroid height	1.125	m
Vessel height (cylindrical part)	4.900	m

Table 2.6: SUNRISE-LFR primary system design main parameters.

2.4.1. Steam generators and pumps

Primary circuit heat exchanger is composed of ten steam generator (SG) modules, patented by L. Cinotti in 2013 [59]. They are in charge of the thermal power removal in the 80 MWth reactor, which means that each unit removes 8 MWth by heating up the secondary fluid, water. A single module comprises both the actual steam generator and a pump, located at the outlet of the module, in cold lead, to increase longevity. The steam generator is made of 15 identical, spirally-coiled tubes stacked one above the other in a staggered way (Figure 2.6). Water is flowing inside the tube bundles from the periphery to the central part, while lead flows radially in the shell from the inner part to the periphery. In each single SG lead enters at 550 °C and exits at 420 °C with a mass flow rate equal to 424.3 kg/s. In the secondary side, subcooled water enters at 340 °C and exits in superheated conditions at 530 °C. It is at 16.5 MPa and has a total mass flow rate equal to 4.46 kg/s.

The material adopted in the steam generator is once again Fe-10Cr-4Al-RE since it deals with hot lead. In Table 2.8 all dimensions regarding the steam generator are listed.

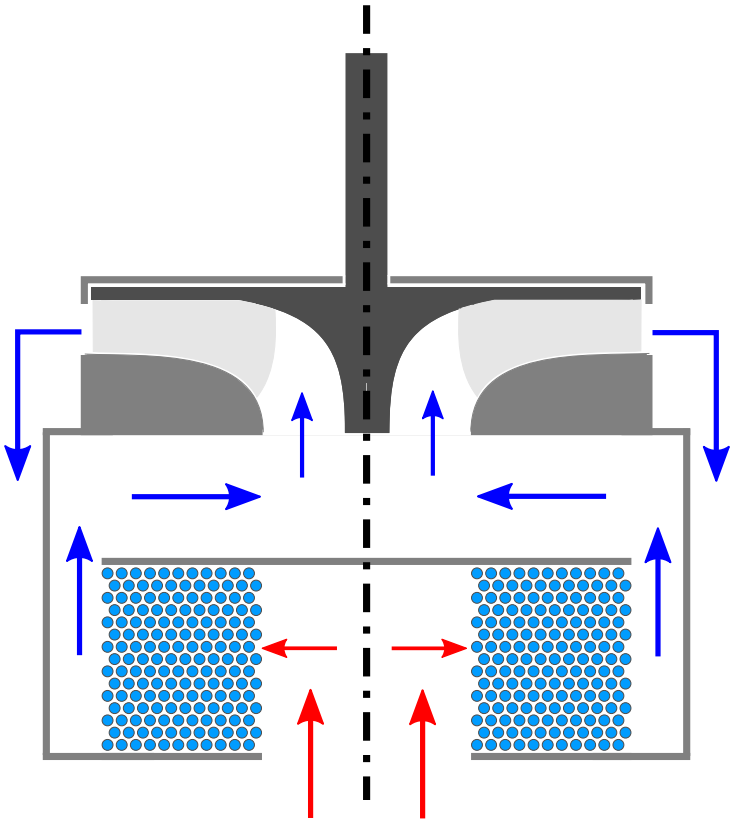

Figure 2.6: SG and pump module. The arrows denote hot (red) and cold (blue) lead flow [48].

Parameter	Value	Unit
Power removed	8	MW
Water inlet temperature	340	°C
Water outlet temperature	530	°C
Water pressure	16.5	MPa
Water mass flow rate	4.46	kg/s
Lead inlet temperature	550	°C
Lead outlet temperature	420	°C
Lead mass flow rate	424.3	kg/s

Table 2.7: SUNRISE-LFR steam generator nominal conditions.

Parameter	Value	Unit
No. units	10	-
No. spiral tubes per unit	15	-
Tubes material	Fe-10Cr-4Al-RE	-
Tubes internal diameter	10.7	mm
Tubes external diameter	12.7	mm
Tubes pitch	15.2	mm
No. spirals of the tubes	11	-
First spiral radius	0.112	m
Last spiral radius	0.280	m
SG elevation from the top of the core	2.47	m
SG tubes stack height	0.200	m

Table 2.8: SUNRISE-LFR steam generator and pump module main parameters.

This component is one of the main subjects of the overall work presented in this manuscript. Chapter 4 introduces and goes into details of the assumptions and the approach of the steam generator model.

Anyway, it must be remembered that the steam generators are not the only power removal mechanism adopted in SUNRISE-LFR. First of all, the RVACS system mentioned before is always present are ready to enter into play in case of temperatures increase. At present its modeling does not include natural convection with the ambient but only thermal radiation. Secondly, two passive dip-coolers will be introduced to dissipate heat in the event of complete loss of secondary system (ULOF and ULOHS combined). They are not modeled yet, but will consist of two empty tanks that can be filled with subcooled water whenever the secondary system stops removing power; through the evaporation of water, heat is removed from the primary circuit, thus leading to safe, steady-state conditions. Both these auxiliary systems are intended to be passive.

2.5. Secondary side

The steam generator modules connect primary with secondary circuit, where water flows and is heated reaching a very high superheating degree. What use can hot steam have? Swedish nuclear regulator SSM prevents research reactors from being connected to the electricity grid for profit purposes. This is the reason why a conventional Rankine cycle

is not envisaged for SUNRISE-LFR. Instead, unconventional solutions are at study, being the most probable just the use of high quality steam for industrial processes. Its selling allows to finance the operation of the reactor itself without power production. In any case, a detailed secondary system design will be studied and published at a later stage.

2.6. Conclusions

This chapter presented SUNRISE-LFR together with the research center formed among the academic and industrial partners. The primary system and the core layout are described with specific references to materials and dimensions. Also fuel and cladding are properly commented, also with references to Gen. IV reactors. SUNRISE-LFR's operating conditions and safety systems are mentioned. In the next Chapters 3, 4 and 5 the reactor's capability of withstanding unprotected accidental scenarios without compromising its targeted safety requirements is tested.

3 | Core and primary system modeling and simulations

The necessity of a new code able to simulate the behavior of a lead-cooled fast reactor under accidental scenarios comes after the fact that at present no software has been purpose-built for studying specifically LFRs and kept open to the public. This led to BELLA (Bortot's Elegant Liquid LFR Analysis tool) [42–45], a computational tool developed at KTH and intended for use in safety informed, pre-conceptual design of LFRs, as well as for education and training purposes. It is a plant simulator oriented to the dynamics and control of lead-cooled fast reactors and provides a non-linear solution for the coupled neutron kinetics and thermal-hydraulics of primary and secondary systems. It is based on the use of point kinetics and balance equations for mass, energy and momentum, which are in general applied to all the primary system components, namely core, steam generator and pool volumes, such as hot and cold legs.

This chapter is dedicated to the description of BELLA and to its use in some transient analysis. In particular, Sections 3.1 and 3.2 address the modeling of neutronics and thermal-hydraulics, respectively. Then, Section 3.3 shows how the different modules are implemented and coupled in MATLAB/Simulink. Section 3.4 presents simulations and discusses results of SUNRISE-LFR under four accidental scenarios: UTOP, ULOF, ULOHS and ULOF-ULOHS combined. Lastly, Section 3.5 delineates the conclusions of this chapter mentioning the major accomplishments, limits and future work both on BELLA, on the simulated transients and on the reference SUNRISE-LFR.

3.1. Neutronics

The modeling of neutrons behavior inside a finite, multiplying material can be approached in different ways, according to the desired accuracy and targets. The starting point is the neutron transport equation:

$$\frac{\partial n(\vec{r},t)}{\partial t} = S(\vec{r},t) - \Sigma_a(\vec{r})\phi(\vec{r},t) - \nabla \cdot \vec{J}(\vec{r},t) \tag{3.1}$$

where neutron density n is both space and time dependent. Without entering into details, the right-hand side contains three terms: in order, the source term, the loss term due to absorption and the loss term due to leakage from the system.
A common approximation that relates neutron current density $\vec{J}$ with neutron density n is given by Fick's law in diffusion theory:

$$\vec{J} = -D\nabla\phi \tag{3.2}$$

which, recalling neutron flux $\phi = nv$, leads to the diffusion equation:

$$\frac{1}{v}\frac{\partial\phi}{\partial t} = S - \Sigma_a\phi + D\nabla^2\phi \tag{3.3}$$

All the hypotheses and physical interpretations of diffusion approximation are well explained in Lamarsh' book [60]. This is the typical approach to study neutron flux changes in space and time adopting an analytically-derived equation. It can be extremely useful when reactor core studies are aimed by the user or when specific regions inside the reactor core are of interest.

However, the goal of BELLA is to give a fast but accurate representation of the whole reactor together with the primary and the secondary circuit. There is no need to investigate the spacial dependence of the neutron flux inside the reactor core. Instead, it is preferable to adopt a zero-dimensional model which accounts for all neutrons in the reactor core without taking care about their position. Neutron point kinetics is perfectly suited to that end. This is what BELLA utilizes as neutronics module.

3.1.1. Neutron point kinetics

This is a zero-dimensional model which focuses only on the time-dependent term of neutronic population. Its validity holds if the system is approaching the critical state and if there are no large localized perturbations. It is reasonable to assume that the conditions are met in all the transients modeled and studied in this work.

In point kinetics formulation, neutron population is split into two contributions: prompt neutrons, which are assumed to be emitted instantaneously with fission and which occupy more than 99% of the fraction of total neutronic emissions, and delayed neutrons, which are the result of fission products (FPs) decay and, therefore, have way larger time constants. Those FPs emitting neutrons while decaying are called neutron precursors.

Neutron population varies over time according to:

$$\frac{dn}{dt} = (\text{ext source}) + (\text{prompt n}) + (\text{delayed n}) - (\text{losses}) \tag{3.4}$$

where n is the total neutron density (cm^{-3}) and losses are due to neutrons absorption and leakage from the system. Apart from reactor startup, external source term is always neglected due to both its smaller value and a very practical reason: a neutron source would be totally consumed by the reactor nominal neutron flux very quickly, so it is simply removed after the fission chain reaction has been initiated.
On the other hand, delayed neutrons are emitted after the decay of neutron precursors and, because they are many and with different properties, they are commonly divided into some groups. For thermal reactors a good approximation is 6 groups of neutron precursors, while for fast reactor it can be even more (typically 8 or 10). For SUNRISE-LFR 8 groups of neutron precursors are envisaged. The time variation of i-th group density C_i (cm^{-3}) is:

$$\frac{dC_i}{dt} = (\text{production}) - (\text{decay}) \tag{3.5}$$

Starting from diffusion equation (Eq. 3.3) and following Lamarsh' book [60], Eq.s (3.4) and (3.5) can be manipulated to obtain the point kinetic model:

$$\frac{dn(t)}{dt} = \frac{\rho(t) - \beta_{\text{eff}}}{\Lambda_{\text{eff}}} n(t) + \sum_{i=1}^{8} \lambda_i C_i(t) \tag{3.6}$$

$$\frac{dC_i(t)}{dt} = \frac{\beta_i}{\Lambda_{\text{eff}}} n(t) - \lambda_i C_i(t) \tag{3.7}$$

where $\rho(t)$ is the time-dependent reactivity, β_{eff} is the effective delayed neutron fraction, Λ_{eff} is the effective neutron reproduction time, β_i and λ_i are the effective delayed neutron fraction and decay rate for the i-th precursor group.

The effective delayed neutron fraction β_{eff} is the sum over each precursor effective delayed neutron yield

$$\beta_{\text{eff}} = \sum_{i=1}^{8} \beta_i \tag{3.8}$$

and the equilibrium precursor concentration for group i can be obtained as:

$$C_i^{eq} = \frac{\beta_i}{\Lambda_{\text{eff}} \lambda_i} n_i^{eq} \tag{3.9}$$

All the aforementioned parameters are calculated with the Monte Carlo software Serpent2

by F. Dehlin and in [48] some information can be retrieved. Their values are listed in Tables 3.1 and 3.2.

Group	β_i (pcm)	λ_i (1/s)
1	15.9	0.0125
2	92.1	0.0283
3	50.4	0.0425
4	117.1	0.133
5	205.1	0.292
6	84.6	0.666
7	67.8	1.63
8	32.2	3.55

Table 3.1: SUNRISE-LFR point kinetics parameters for all neutron precursors. They are calculated at MoL [48].

Parameter	Value	Unit
β_{eff}	665.2	pcm
λ_{eff}	0.089	1/s
Λ_{eff}	0.88	μs

Table 3.2: SUNRISE-LFR point kinetics main effective parameters. They are calculated at MoL [48].

It might seem a linear model but it is not, being reactivity $\rho(t)$ time-dependent.

3.1.2. Decay power

Current version of BELLA incorporates the capability to estimate the decay heat resulting from radioactive decay of unstable fission products. The model is based on the 1994 American National Standard (ANS) for decay heat power in LWRs [61] but, since the purpose in BELLA is to provide a rough estimation rather than a precise calculation, several simplifications are made.

Among all decay heat precursors only ^{235}U is considered and its decay curves (23 groups are described) are derived from thermal fission data. This is because the ANS report

was originally developed for LWRs, thus it does not contain any information on decay heat fractions for fast reactors. Furthermore, the model does not account for the heat source that arises from fission products undergoing neutron capture reactions after reactor shutdown.

On this basis, the work of Paulsen et al. [62] was used as a guide in writing the decay heat equations:

$$\frac{dh_j(t)}{dt} = \frac{\beta_j}{\varepsilon_{fiss}} n(t) - \lambda_j h_j(t) \tag{3.10}$$

where h_j is defined as the decay power released by group j relative to the power generated from fission under steady-state conditions. Recall that $n(t)$ refers to the normalized, time-dependent neutron population; β_j (MeV/s) and λ_j are the decay power fraction and the decay constant for group j, respectively; ε_{fiss} is the energy released per fission event in units of MeV, which averages around 200 MeV for ^{235}U. Steady-state solution is:

$$h_j(0) = \frac{\beta_j}{\varepsilon_{fiss}\lambda_j} n(0) \tag{3.11}$$

In this way, reactor thermal power can be computed as a sum of neutron population (fission reactions) and ^{235}U fission products decay source:

$$\dot{Q}_{th}(t) = \frac{\dot{Q}_{th}(0)}{n(0) + \sum_{j=1}^{23} h_j(0)} \left[n(t) + \sum_{j=1}^{23} h_j(t) \right] \tag{3.12}$$

Values of the decay power fractions and decay constants of all 23 fission products groups are listed in Table 3.3.

Group	β_j (MeV/s)	λ_j (1/s)
1	$5.28{\cdot}10^{-4}$	$2.72{\cdot}10^{0}$
2	$6.86{\cdot}10^{-1}$	$1.03{\cdot}10^{0}$
3	$4.08{\cdot}10^{-1}$	$3.14{\cdot}10^{-1}$
4	$2.19{\cdot}10^{-1}$	$1.18{\cdot}10^{-1}$
5	$5.77{\cdot}10^{-2}$	$3.44{\cdot}10^{-2}$
6	$2.25{\cdot}10^{-2}$	$1.18{\cdot}10^{-2}$
7	$3.34{\cdot}10^{-3}$	$3.61{\cdot}10^{-3}$
8	$9.37{\cdot}10^{-4}$	$1.40{\cdot}10^{-3}$
9	$8.09{\cdot}10^{-4}$	$6.26{\cdot}10^{-4}$
10	$1.96{\cdot}10^{-4}$	$1.89{\cdot}10^{-4}$
11	$3.26{\cdot}10^{-5}$	$5.51{\cdot}10^{-5}$
12	$7.58{\cdot}10^{-6}$	$2.10{\cdot}10^{-5}$
13	$2.52{\cdot}10^{-6}$	$9.99{\cdot}10^{-6}$
14	$4.98{\cdot}10^{-7}$	$2.54{\cdot}10^{-6}$
15	$1.85{\cdot}10^{-7}$	$6.63{\cdot}10^{-7}$
16	$2.66{\cdot}10^{-8}$	$1.23{\cdot}10^{-7}$
17	$2.24{\cdot}10^{-9}$	$2.72{\cdot}10^{-8}$
18	$8.96{\cdot}10^{-12}$	$3.30{\cdot}10^{-9}$
19	$8.60{\cdot}10^{-11}$	$7.42{\cdot}10^{-10}$
20	$2.11{\cdot}10^{-14}$	$2.47{\cdot}10^{-10}$
21	$7.12{\cdot}10^{-16}$	$1.56{\cdot}10^{-13}$
22	$8.11{\cdot}10^{-17}$	$2.26{\cdot}10^{-14}$
23	$9.47{\cdot}10^{-17}$	$2.05{\cdot}10^{-14}$

Table 3.3: Parameters for ^{235}U fission products decay power adopted in SUNRISE-LFR.

3.1.3. Reactivity feedback

Reactivity is the parameter which links neutronics to external control of the reactor (control rods, neutron poisons, etc.) and to thermal-hydraulic quantities. It is defined as:

$$\rho = \frac{k_{\text{eff}} - 1}{k_{\text{eff}}} \tag{3.13}$$

where k_{eff} is the effective multiplication factor, namely the total number of neutrons produced, prompt or latent, per neutron lost in the system. It can be calculated starting from the diffusion equation and it allows to express reactivity ρ as a function of neutron cross-sections and other microscopic parameters. However, there is no necessity to deepen the knowledge about k_{eff} in this work, also because reactivity ρ is here expressed in terms of thermal-hydraulic quantities.

According to the value of ρ, or of k_{eff}, a system can be defined:

$$\begin{cases} \text{critical} & \rho = 0 \quad \text{or} \quad k_{\text{eff}} = 1 \\ \text{supercritical} & \rho > 0 \quad \text{or} \quad k_{\text{eff}} > 1 \\ \text{subcritical} & \rho < 0 \quad \text{or} \quad k_{\text{eff}} < 1 \end{cases} \tag{3.14}$$

A critical system has a constant neutron population (thus power) over time. A supercritical (subcritical) system has an increasing (decreasing) neutron population over time.

As stated, reactivity ρ connects point kinetics to thermal-hydraulics and external control of the reactor. In particular, it expresses the influence of the system temperatures variation and of position of control rods (no neutron poison is modeled in BELLA at present) on neutron population, thus on power. In fact, a feedback loop between neutronics and the thermal-hydraulic block is present: neutrons fission produces power, which acts on temperatures of the system (fuel, cladding, coolant), which in turn give a contribution to reactivity, which is present in neutron density's derivative.

BELLA considers only the most important terms: Doppler effect, fuel thermal expansion, lead thermal expansion, fuel assembly diagrid radial expansion. They are incorporated in the reactivity feedback coefficients, calculated by neutronic codes (Serpent2 in this case [48]) and assumed to be independent of temperature.
The influence of control rods position on reactivity is present in the external contribution $\Delta\rho_{ext}$, treated as an input of the model.

Therefore, a variation in time-dependent reactivity $\Delta\rho(t)$ is calculated in BELLA as:

$$\Delta\rho(t) = K_D \ \ln\left[\frac{\overline{T}_f(t)}{\overline{T}_f(0)}\right] + \alpha_{ax} \ \Delta\overline{T}_f(t) + \alpha_{Pb} \ \Delta\overline{T}_{Pb}(t) + \alpha_{rad} \ \Delta T^{in}_{Pb}(t) + \Delta\rho_{ext} \tag{3.15}$$

Here, $\overline{T}_f$ and $\overline{T}_{Pb}$ are the average temperatures of fuel and coolant in the core, and T^{in}_{Pb} is the temperature of the coolant in the inlet plenum, governing the radial expansion of the fuel assembly diagrid. K_D is the Doppler constant of the fuel. Fuel axial expansion, coolant thermal expansion and assembly diagrid radial expansion temperature coefficients are denoted by α_{ax}, α_{Pb} and α_{rad}, respectively.

All terms are linear to temperature variations except for Doppler effect: this is because for fast reactors k_{eff} temperature dependence goes as $\frac{1}{T}$ [63]. After the integration of the differential multiplication factor, the obtained dependence is logarithmic.

Table 3.4 lists the feedback coefficients at the middle of life (MoL) of SUNRISE-LFR.

Parameter	Value	Unit
K_D	-530	pcm
α_{ax}	-0.15	pcm/K
α_{Pb}	-0.66	pcm/K
α_{rad}	0.03	pcm/K

Table 3.4: SUNRISE-LFR point kinetics main effective parameters. They are calculated at MoL [48].

It is worth to point out that the value of K_D must not be compared to the others. Firstly and simply because they have different units of measure (pcm against pcm/K); secondly, and as already underlined above, because Doppler term has a logarithmic dependence on temperature which has always a lower absolute value than the linear temperature dependence of all the other contributions. Later on in this chapter, the simulated transients show that all terms in reactivity feedback have comparable orders of magnitude.

3.2. Thermal-hydraulics

This section addresses the calculation of temperatures of the system, mass flow rate in the primary circuit and free surface level of the hot leg, exploiting energy balance equations, momentum balance equation and mass balance equation, respectively. It is divided into four subsections.

3.2.1. Core energy balance

In BELLA, the heat transfer from fuel to coolant is modeled by writing the set of energy balance equations for fuel, fuel-cladding gap, cladding and coolant. In order to be consistent with the assumptions of point kinetics, the approach is zero-dimensional. However, because the reactor safety margins are calculated with respect to fuel and cladding temperature, it is wise to divide radially the fuel rod into different parts, each characterized by a given temperature, mass and radii. In particular, each fuel pellet is divided into cen-

tral, middle and outer part, while cladding into inner, middle and outer part. In this way it is possible to investigate the most severe conditions, which are in the pellet centerline for fuel and in proximity of the gap for cladding.
Table 3.5 summarizes the characteristics of each part and Figure 3.1 represents the radial nodalization of fuel rods.

Part	Inner radius	Outer radius	Mass	Temperature
Fuel center	0	R_{fuel}^{center}	m_{fuel}^{center}	T_{fuel}^{center}
Fuel middle	R_{fuel}^{center}	R_{fuel}^{mid}	m_{fuel}^{mid}	T_{fuel}^{mid}
Fuel outer	R_{fuel}^{mid}	R_{fuel}^{out}	m_{fuel}^{out}	T_{fuel}^{out}
Cladding inner	R_{clad}^{in}	$\overline{R}_{clad}^{in}$	m_{clad}^{in}	T_{clad}^{in}
Cladding middle	$\overline{R}_{clad}^{in}$	$\overline{R}_{clad}^{out}$	m_{clad}^{mid}	T_{clad}^{mid}
Cladding outer	$\overline{R}_{clad}^{out}$	R_{clad}^{out}	m_{clad}^{out}	T_{clad}^{out}

Table 3.5: SUNRISE-LFR fuel rod nodalization main characteristics.

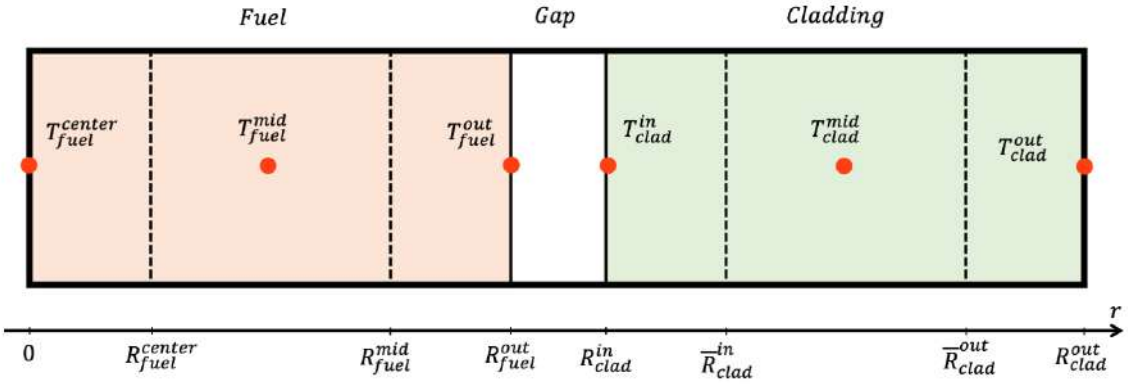

Figure 3.1: SUNRISE-LFR radial nodalization of fuel rods (not in scale).

For what concerns the coolant, it is used only one radial node with mass m_{Pb}^{core}.
Only one axial node is considered and its length is equal to the active height (H_{active}) of the fuel.

Energy balance equations are:

$$m_{fuel}^{center} c_{fuel} \frac{dT_{fuel}^{center}}{dt} = \dot{Q}_{fuel}^{center} - h_{fuel}^{center}(T_{fuel}^{center} - T_{fuel}^{mid}) \quad (3.16)$$

$$m_{fuel}^{mid} c_{fuel} \frac{dT_{fuel}^{mid}}{dt} = \dot{Q}_{fuel}^{mid} + h_{fuel}^{center}(T_{fuel}^{center} - T_{fuel}^{mid}) - h_{fuel}^{mid}(T_{fuel}^{mid} - T_{fuel}^{out}) \quad (3.17)$$

$$m_{fuel}^{out} c_{fuel} \frac{dT_{fuel}^{out}}{dt} = \dot{Q}_{fuel}^{out} + h_{fuel}^{mid}(T_{fuel}^{mid} - T_{fuel}^{out}) - h_{gap}(T_{fuel}^{out} - T_{clad}^{in}) - \dot{Q}_{rad} \quad (3.18)$$

$$m_{clad}^{in} c_{clad} \frac{dT_{clad}^{in}}{dt} = h_{gap}(T_{fuel}^{out} - T_{clad}^{in}) - h_{clad}^{in}(T_{clad}^{in} - T_{clad}^{mid}) + \dot{Q}_{rad} \quad (3.19)$$

$$m_{clad}^{mid} c_{clad} \frac{dT_{clad}^{mid}}{dt} = h_{clad}^{in}(T_{clad}^{in} - T_{clad}^{mid}) - h_{clad}^{out}(T_{clad}^{mid} - T_{clad}^{out}) \quad (3.20)$$

$$m_{clad}^{out} c_{clad} \frac{dT_{clad}^{out}}{dt} = h_{clad}^{out}(T_{clad}^{mid} - T_{clad}^{out}) - h_{Pb}(T_{clad}^{out} - \overline{T}_{Pb}^{core}) \quad (3.21)$$

$$m_{Pb}^{core} c_{Pb} \frac{d\overline{T}_{Pb}^{core}}{dt} = h_{Pb}(T_{clad}^{out} - \overline{T}_{Pb}^{core}) - \dot{m}_{Pb} c_{Pb} \Delta T_{Pb}^{core} = \quad (3.22)$$

$$= h_{Pb}(T_{clad}^{out} - \overline{T}_{Pb}^{core}) - 2\dot{m}_{Pb} c_{Pb}(\overline{T}_{Pb}^{core} - T_{Pb}^{core,in})$$

$$T_{Pb}^{core,out} = 2\overline{T}_{Pb}^{core} - T_{Pb}^{core,in} \quad (3.23)$$

being:

$$\dot{Q}_{fuel}^{center} = \dot{Q}_{fuel,tot} \frac{(R_{fuel}^{center})^2}{(R_{fuel}^{out})^2} \quad (3.24)$$

$$\dot{Q}_{fuel}^{mid} = \dot{Q}_{fuel,tot} \frac{(R_{fuel}^{mid})^2 - (R_{fuel}^{center})^2}{(R_{fuel}^{out})^2} \quad (3.25)$$

$$\dot{Q}_{fuel}^{out} = \dot{Q}_{fuel,tot} \frac{(R_{fuel}^{out})^2 - (R_{fuel}^{mid})^2}{(R_{fuel}^{out})^2} \quad (3.26)$$

$$\Delta T_{Pb}^{core} = T_{Pb}^{core,out} - T_{Pb}^{core,in} \quad (3.27)$$

$$\dot{Q}_{rad} = 2\pi R_{fuel}^{out} H_{active} N_{pins} \frac{\sigma}{\frac{1}{\varepsilon_f} + \frac{1}{\varepsilon_c} - 1} \left[(T_{fuel}^{out})^4 - (T_{clad}^{in})^4 \right] \quad (3.28)$$

The generalized conductive heat transfer coefficients h (in W/K) are given by

$$h_{fuel}^{center} = \frac{4\pi k_{fuel}^{c-m} R_{fuel}^{center} N_{pins} H_{active}}{R_{fuel}^{out}} \tag{3.29}$$

$$h_{fuel}^{mid} = \frac{4\pi k_{fuel}^{m-o} R_{fuel}^{mid} N_{pins} H_{active}}{R_{fuel}^{out}} \tag{3.30}$$

$$h_{gap} = \frac{2\pi k_{He} N_{pins} H_{active}}{\ln\left(R_{clad}^{in}/R_{fuel}^{out}\right)} \tag{3.31}$$

$$h_{clad}^{in} = \frac{4\pi k_{clad}^{m} \overline{R}_{clad}^{in} N_{pins} H_{active}}{\delta_c} \tag{3.32}$$

$$h_{clad}^{out} = \frac{4\pi k_{clad}^{m} \overline{R}_{clad}^{out} N_{pins} H_{active}}{\delta_c} \tag{3.33}$$

$$h_{Pb} = 2\pi k_{Pb}^{core} R_{clad}^{out} N_{pins} H_{fuel} \frac{\mathrm{Nu}_{Pb}^{core}}{D_h^{core}} \tag{3.34}$$

where $\delta_c = R_{clad}^{out} - R_{clad}^{in}$ is the cladding thickness, D_h^{core} is the hydraulic diameter of the core and Nu_{Pb}^{core} is lead Nusselt number in the core. For the latter BELLA applies the Mikityuk correlation [64]:

$$\mathrm{Nu} = 0.047\left\{1 - \exp\left[-3.8\left(\frac{P_{pin}}{2R_{clad}^{out}} - 1\right)\right]\right\}\left(\mathrm{Pe}^{0.77} + 250\right) \tag{3.35}$$

where P_{pin} is the fuel pin pitch and Pe the Peclet number defined as

$$\mathrm{Pe} = \mathrm{RePr} \tag{3.36}$$

In the above equations, the thermal conductivity k_{fuel}^{i-j} at the interface of two adjacent fuel nodes i and j is evaluated at their average temperature. As for the cladding, its node-to-node changes in temperature are of the order of 5 K, thus its thermal conductivity is calculated at the cladding mid-point and assumed equal for all nodes.
Fuel and cladding heat capacities c_i are evaluated at average fuel temperature and at cladding mid-point temperature, respectively. Average fuel temperature and average

cladding temperature are:

$$\begin{aligned}\overline{T}_{fuel} &= T_{fuel}^{center}\left[\frac{(R_{fuel}^{center})^2}{(R_{fuel}^{out})^2}\right] + T_{fuel}^{mid}\left[\frac{(R_{fuel}^{mid})^2-(R_{fuel}^{center})^2}{(R_{fuel}^{out})^2}\right] + \\ &+ T_{fuel}^{out}\left[\frac{(R_{fuel}^{out})^2-(R_{fuel}^{mid})^2}{(R_{fuel}^{out})^2}\right] \end{aligned} \tag{3.37}$$

$$\begin{aligned}\overline{T}_{clad} &= T_{clad}^{in}\left[\frac{(\overline{R}_{clad}^{in})^2-(R_{clad}^{in})^2}{(R_{clad}^{out})^2-(R_{clad}^{in})^2}\right] + T_{clad}^{mid}\left[\frac{(\overline{R}_{clad}^{out})^2-(\overline{R}_{clad}^{in})^2}{(R_{clad}^{out})^2-(R_{clad}^{in})^2}\right] + \\ &+ T_{clad}^{out}\left[\frac{(R_{clad}^{out})^2-(\overline{R}_{clad}^{out})^2}{(R_{clad}^{out})^2-(R_{clad}^{in})^2}\right] \end{aligned} \tag{3.38}$$

Coolant specific heat capacity, thermal conductivity, and Nusselt number are evaluated at the average core coolant temperature $\overline{T}_{Pb}^{core}$ and velocity v_{Pb}^{core}, the second determined as:

$$\overline{v}_{Pb}^{core} = \frac{\dot{m}_{Pb}}{A_{Pb}^{core}\overline{\rho}_{Pb}^{core}} \tag{3.39}$$

Coolant mass flow rate $\dot{m}_{Pb}$ is retrieved from the mass transfer block related to momentum balance equation. It is discussed in Subsection 3.2.3.

As more than once stated, the aim of BELLA is to inform the user about the safety margins of the reactor, calculated with respect to fuel melting and cladding tube creep rupture (Section 2.2). Therefore, it is of absolute importance to keep track of fuel and cladding hottest positions inside the reactor. The radial profile is correctly taken into account by radial nodes of fuel rods.
However, BELLA does not discretize the axial direction which needs to be considered in some other way. For this purpose, the spacial profile of volumetric power q''' (almost proportional to neutron flux ϕ) is introduced. Assuming to have a homogeneous, non reflected, cylindrical core (large number of fuel assemblies and small heterogeneities) of radius R and height H (with extrapolated dimensions R_{ex} and H_{ex}), and separating radial dependence from axial dependence, diffusion equation (Eq. (3.3)) has solution:

$$q'''(\vec{r}) = q'''(r,z) = q'''_{max} J_0\left(\frac{2.4048\ r}{R_{ex}}\right) cos\left(\frac{\pi z}{H_{ex}}\right) \tag{3.40}$$

where J_0 is the Bessel function of first kind, zero order. Reference system is $r \in [-R_{core}/2, R_{core}/2]$ in radial direction and $z \in [-H_{active}/2, H_{active}/2]$ in axial direction. q'''_{max} is the maximum volumetric power and is computed after the average volumetric power q'''_{avg} through the

peak factors (F_A axial and F_R radial are calculated by means of Serpent2 [48] adopting the real core geometry):

$$q'''_{max} = q'''_{avg} F_A F_R = \frac{\dot{Q}_{fuel,tot}}{N_{pins} A_{pin} H_{active}} F_A F_R \tag{3.41}$$

The worst conditions are in the peak assembly (PA), i.e. $r = 0$, both for fuel and cladding. There, the axial power profile is:

$$q'''(0,z) = q'''(z) = q'''_{max} cos\left(\frac{\pi z}{H_{ex}}\right) \tag{3.42}$$

Now the linear power and the heat flux calculated at a given radial position $R \neq 0$ can be introduced:

$$q'(z) = q'''(z) \cdot A_{pin} \tag{3.43}$$

$$q'(z) = q''(z)|_R \cdot 2\pi R \tag{3.44}$$

Starting from the coolant and imposing the energy balance in steady-state conditions, temperatures axial profiles are obtained:

$$T_{Pb}(z) = T_{Pb,in} + \frac{q'_{max} H_{ex} N_{pins,ass}}{\pi \dot{m}^{PA}_{Pb} c_{Pb}} \left[sin\left(\frac{\pi z}{H_{ex}}\right) + sin\left(\frac{\pi H_{active}}{2H_{ex}}\right)\right] \tag{3.45}$$

$$T^{out}_{clad}(z) = T_{Pb}(z) + \frac{q'_{max}}{2\pi R^{out}_{clad} h_{Pb}} cos\left(\frac{\pi z}{H_{ex}}\right) \tag{3.46}$$

$$T^{in}_{clad}(z) = T^{out}_{clad}(z) + \frac{q'_{max}}{2\pi k_{clad}} \ln\left(\frac{R^{out}_{clad}}{R^{in}_{clad}}\right) cos\left(\frac{\pi z}{H_{ex}}\right) \tag{3.47}$$

$$T^{out}_{fuel}(z) = T^{in}_{clad}(z) + \frac{q'_{max}}{2\pi k_{gap}} \ln\left(\frac{R^{in}_{clad}}{R^{out}_{fuel}}\right) cos\left(\frac{\pi z}{H_{ex}}\right) \tag{3.48}$$

$$T^{center}_{fuel}(z) = \left[T^{out}_{fuel}(z)^{1.361} + 0.0581 q'_{max} e^{2.14P} cos\left(\frac{\pi z}{H_{ex}}\right)\right]^{\frac{1}{1.361}} \tag{3.49}$$

where $N_{pins,ass}$ is the number of pins per fuel assembly and $\dot{m}^{PA}_{Pb}$ is lead mass flow rate in the peak assembly (look at Subsection 3.2.3 for its calculation).
Since fuel thermal conductivity has a strong dependence on temperature, the energy balance equation cannot be simplified as in the other cases. This is the reason why Eq. (3.49) has a different shape. It is derived considering the conductivity integral and the correlation for fuel thermal conductivity [48]. P is the porosity of the fuel (assumed constant).

By plotting Eq.s (3.45−3.49) in Figure 3.2 it is clear that cladding worst position is at the core outlet (or better, at $z = H_{active}/2$) while for fuel it is slightly above the midplane. These two are the positions where cladding and fuel temperature are tracked before and after a transient to check the compliance with safety criteria.

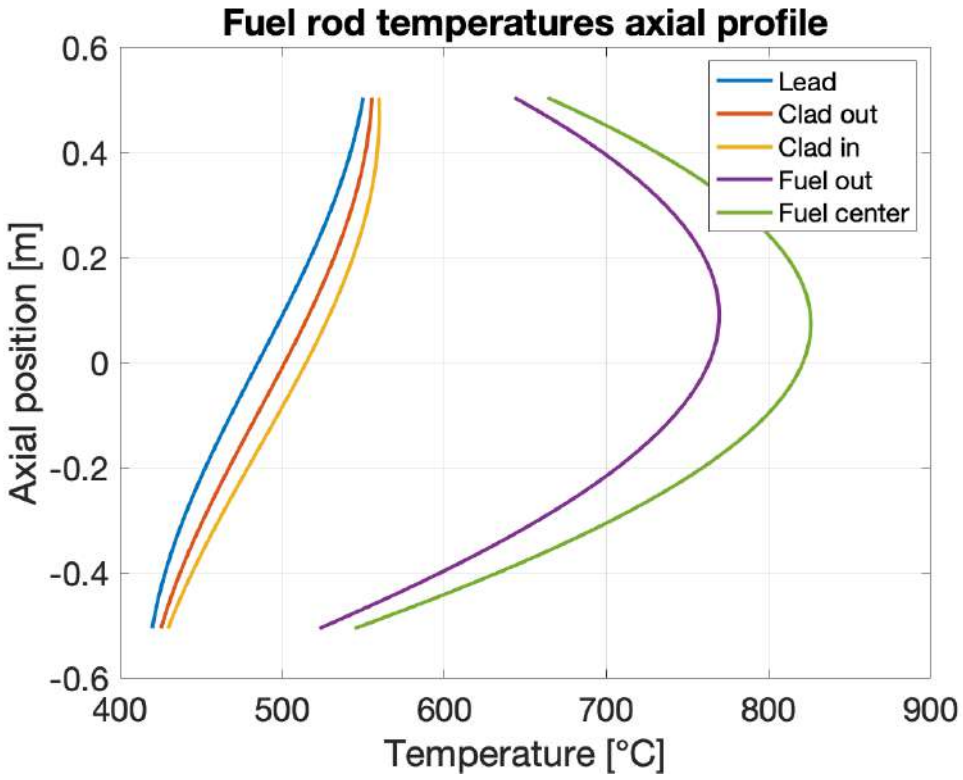

Figure 3.2: SUNRISE-LFR fuel rod temperatures axial profile in nominal conditions.

It must be underlined that Eq.s (3.45−3.49) are valid only in steady-state conditions (before and after a transient) because they do not take into account the correct time behavior of fuel, cladding and lead. In fact, those are algebraic equations where the time dependence is present only in $T_{Pb,in}$ and in q'''_{max} and where fuel, cladding and lead's time constants are neglected. But this is not correct: fuel, cladding and lead should have finite time constants properly accounted by differential equations such as Eq. (3.16). However, Eq.s (3.45−3.49) are still correct in steady-state conditions and, therefore, they are not used with the intent of tracking the whole transient but with the idea of checking only initial and final values.

Another assumption is implicitly made: Eq. (3.40) is derived considering one-group diffusion in a homogeneous, non reflected, finite cylinder. Although the peak factors are calculated adopting the real core geometry, the temperature axial profile is estimated using the cosine shape for q'''. In any case, this is not a strong approximation and it is

totally within the scope of BELLA.

Parameter	Value	Unit
Radial peak factor	1.53	-
Axial peak factor	1.31	-

Table 3.6: SUNRISE-LFR's core peak factors [48].

3.2.2. Primary circuit energy balance

In BELLA, the heat transfer from the core to the rest of the primary system components – hot leg (HL), steam generator (SG), cold leg (CL), cold pool (CP) – is approximated by the following set of energy balance equations:

$$m_{Pb}^{HL} c_{Pb} \frac{d\overline{T}_{Pb}^{HL}}{dt} = \dot{m}_{Pb} c_{Pb} \left(T_{Pb}^{core,out} - \overline{T}_{Pb}^{HL} \right) \tag{3.50}$$

$$T_{Pb}^{SG,in} = \overline{T}_{Pb}^{HL} \tag{3.51}$$

$$T_{Pb}^{SG,out} = F(\dot{m}_{Pb}^{SG}, T_{Pb}^{SG,in}, \dot{m}_{H_2O}^{SG}, T_{H_2O}^{SG,in}, P_{H_2O}^{SG}) \tag{3.52}$$

$$m_{Pb}^{CL} c_{Pb} \frac{d\overline{T}_{Pb}^{CL}}{dt} = \dot{m}_{Pb} c_{Pb} \left(T_{Pb}^{SG,out} - \overline{T}_{Pb}^{CL} \right) - h_{Pb}^{RV} (\overline{T}_{Pb}^{CL} - \overline{T}_{RV}) \tag{3.53}$$

$$m_{RV} c_{RV} \frac{d\overline{T}_{RV}}{dt} = h_{Pb}^{RV} (\overline{T}_{Pb}^{CL} - \overline{T}_{RV}) - \frac{A_{RV} \sigma_{SB}}{\frac{1}{\varepsilon_{RV}} + \frac{1}{\varepsilon_{GV}} - 1} (\overline{T}_{RV}^4 - \overline{T}_{GV}^4) \tag{3.54}$$

$$m_{GV} c_{GV} \frac{d\overline{T}_{GV}}{dt} = \frac{A_{RV} \sigma_{SB}}{\frac{1}{\varepsilon_{RV}} + \frac{1}{\varepsilon_{GV}} - 1} (\overline{T}_{RV}^4 - \overline{T}_{GV}^4) - \frac{A_{GV} \sigma_{SB}}{\frac{1}{\varepsilon_{GV}} + \frac{1}{\varepsilon_a} - 1} (\overline{T}_{GV}^4 - T_{amb}^4) \tag{3.55}$$

$$m_{Pb}^{CP} c_{Pb} \frac{d\overline{T}_{Pb}^{CP}}{dt} = \dot{m}_{Pb} c_{Pb} \left(\overline{T}_{Pb}^{CL} - \overline{T}_{Pb}^{CP} \right) \tag{3.56}$$

$$T_{Pb}^{core,in} = \overline{T}_{Pb}^{CP} \tag{3.57}$$

$\overline{T}_{Pb}^{HL}$, $\overline{T}_{Pb}^{CL}$, $\overline{T}_{RV}$ and $\overline{T}_{GV}$ are, respectively, the average temperature of lead in the hot leg, in the cold leg, the average temperature of the primary vessel or reactor vessel (RV) wall and guard vessel (GV) wall. ε_{RV}, ε_{GV} and ε_a denote the RV, GV and ambient emissivities (the ambient is assumed to be an infinite sink with constant temperature $T_{amb} = 20$ °C), respectively.

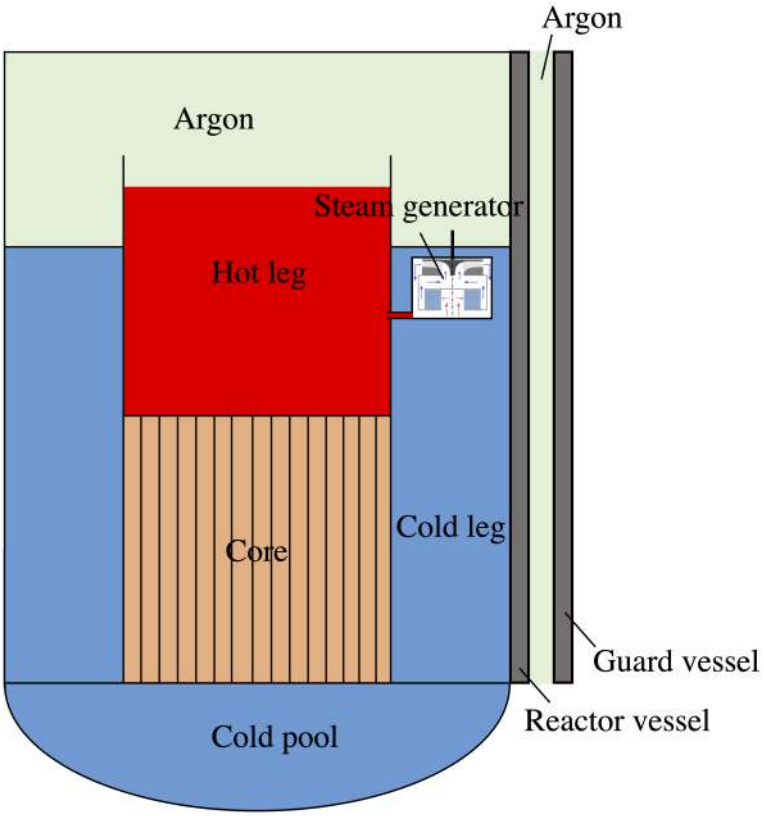

Figure 3.3: SUNRISE-LFR primary system simplified sketch in BELLA (not in scale).

Coolant mass in the HL and in the CL can be computed as:

$$m_{Pb}^{HL} = A_{Pb}^{HL}\, Z_{Pb}^{HL}\, \overline{\rho}_{Pb}^{HL} \tag{3.58}$$

$$m_{Pb}^{CL} = A_{Pb}^{CL}\, Z_{Pb}^{CL}\, \overline{\rho}_{Pb}^{CL} \tag{3.59}$$

being A_{Pb}^{i} the flow area of region i, Z_{Pb}^{HL} the time-dependent elevation of the HL free surface relative to the outlet of the core and Z_{Pb}^{CL} the fixed CL height (from the inlet of the core to the CL inner lid).

Reference BELLA code accounts also for the fraction of heat which is dissipated and eventually transferred to the primary vessel (RV and GV) as the coolant flows through the CL. Its convective heat transfer coefficient is calculated using Seban and Shimazachi's correlation [65] for Nusselt number:

$$h_{Pb}^{RV} = \pi D_{in}^{RV}\, Z_{Pb}^{CL} \left[5 + 0.0025(\mathrm{Pe}_{Pb}^{CL})^{0.8}\right] \frac{k_{Pb}^{CL}}{D_{h}^{CL}} \tag{3.60}$$

where D_{in}^{RV} is the internal diameter of the reactor vessel and Pe_{Pb}^{CL} is the Peclet number

relative to lead inside the CL. Thermal conductivity k_{Pb}^{CL} is evaluated at the average CL temperature.
At the same time, the primary reactor vessel radiates heat from its outer surface A_{RV} to the guard vessel (space in between is filled with a stagnant inert gas, typically argon, for which thermal conductivity is negligible). In turn, the guard vessel exchanges thermal power with the ambient through radiation only from its outer surface A_{GV}. Natural convection is supposed to be modeled at a later stage.
An approximation whose validity has not been investigated in deep is the negligibility of RV and GV's thermal conductivity in the heat transfer across the walls: Eq.s (3.54) and (3.55) assume a unique node at uniform temperature both for reactor vessel and for guard vessel. Thermal conductivity should have an influence but, since the dynamics of radiative heat transfer is extremely low (it can be observed in later simulations), it should not be evident at all. This is the main reason why thermal conduction across the wall is not considered.

Regarding the steam generator, the heat transfer from primary side (lead) to secondary side (water) is modeled using a general function F dependent on lead mass flow rate and temperature, and water mass flow rate, temperature and pressure. The simplest version of BELLA provides two different approaches: imposing any user-defined function for either power removal $\dot{Q}_{SG}$ or temperature difference between the inlet and the outlet ΔT_{Pb}^{SG}. Thus, equations are:

$$T_{Pb}^{SG,out} = T_{Pb}^{SG,in} - \Delta T_{Pb}^{SG} \tag{3.61}$$

$$T_{Pb}^{SG,out} = T_{Pb}^{SG,in} - \frac{\dot{Q}_{SG}}{\dot{m}_{Pb}^{SG} c_{Pb}} \tag{3.62}$$

This is how BELLA addressed the SG module before a new version has been developed and to which Chapter 4 is dedicated. The older version − Eq.s (3.61) and (3.62) − does not even consider secondary side properties and working conditions. The SG is only a constant sink of power or a block which lowers lead temperature by a constant amount, whatever are the working conditions in the primary circuit. This approach has strong limits, especially in simulating accidental scenarios. But it is fast, simple and it works correctly in case of ULOHS transient (since SG module completely fails, there is no need to demand for any complex model). Because of that, in this chapter (Section 3.3) simulations adopting the simplest version for the SG are presented and discussed. In particular, the author chose to model the SG adopting Eq. (3.62) and a few reasons explain why: firstly, through reactivity feedbacks the SG module is capable of stabilizing the thermal power generated by the core (SUNRISE-LFR is designed to produce 80 MWth constantly);

secondly and most importantly, it allows the system to be affected by lead mass flow rate changes and this is crucial in ULOF scenario: when $\dot{m}_{Pb}$ decreases as a consequence of pump failure, the system responds by increasing the ΔT_{Pb} across the SG (thus across the core) in order to keep the power produced by the core and the power removed by the SG equal and constant. This is exactly what simulations with the newly developed SG module show, at least on a general level, in Chapter 5.

Coming back to the whole primary circuit model, steady-state temperatures are obtained by setting to zero all time derivatives and by solving the resulting system of linear equations.

3.2.3. Primary circuit momentum balance

This subsection proposes a new equation to compute the derivative of coolant mass flow rate through the entire primary circuit. Based on Todreas and Kazimi's book [66], Appendix B contains its full derivation starting from momentum balance. The final result is:

$$\frac{d\dot{m}_{Pb}}{dt} = \frac{\Delta P_{buoyancy} - \Delta P_{friction} + \Delta P_{pump}}{\sum_k \frac{L_k}{A_k}} \tag{3.63}$$

where $\dot{m}_{Pb}$ is lead mass flow rate in the system, $\Delta P_{buoyancy}$ is the buoyancy term, $\Delta P_{friction}$ are the friction pressure losses and ΔP_{pump} the pressure head given by the ten variable speed reactor coolant pumps. Last term can be considered as an input of the model but usually it is kept fixed at the value needed to balance the other pressure terms in steady-state nominal conditions:

$$\Delta P_{pump}(t) = \Delta P_{pump}(0) = \Delta P_{friction}(0) - \Delta P_{buoyancy}(0) \tag{3.64}$$

The buoyancy term is the result of the gravitational contributions in the momentum balance equation:

$$\Delta P_{buoyancy} = \overline{\rho}^{CL} g(H^{core} + Z^{SG} + H^{SG}) - \overline{\rho}^{core} g H^{core} - \overline{\rho}^{HL} g Z^{SG} - \overline{\rho}^{SG} g H^{SG} \tag{3.65}$$

Assuming that $\overline{T}^{core} = \overline{T}^{SG} = \frac{\overline{T}^{HL} + \overline{T}^{CL}}{2}$ it can be simplified to

$$\Delta P_{buoyancy} = g(\overline{\rho}^{CL} - \overline{\rho}^{HL}) H_{th,centers} = g\beta(\overline{T}^{HL} - \overline{T}^{CL}) H_{th,centers} \tag{3.66}$$

where $\beta = -\frac{\partial \rho}{\partial T}$ (lead thermo-physical properties are listed in Appendix A) and $H_{th} = \frac{1}{2}H^{core} + Z^{SG} + \frac{1}{2}H^{SG}$ (distance between core and SG thermal centers).

Frictional pressure losses are computed for all regions in the primary circuit:

$$\Delta P_{friction} = \Delta P_{fr}^{core} + \Delta P_{fr}^{SG} + \Delta P_{fr}^{HL} + \Delta P_{fr}^{CL} + \Delta P_{fr}^{pump} + 2\Delta P_{fr}^{annular} \tag{3.67}$$

Each term is typically splitted into distributed and concentrated contributions:

$$\Delta P_{fr} = \Delta P_{fr,distr} + \Delta P_{fr,conc} \tag{3.68}$$

In most of the cases (core, HL, CL), distributed pressure losses are calculated adopting Darcy-Weisbach equation:

$$\Delta P_{fr,distr} = \left(f \frac{H}{D_h} \right) \frac{\dot{m}|\dot{m}|}{2\rho A^2} \tag{3.69}$$

where f is Darcy friction factor, D_h hydraulic diameter, H height or length of the region, ρ density of lead, A flow area of the region. The absolute value notation with $\dot{m}$ accounts for the friction force change in direction depending on lead flow direction. The friction factor is usually calculated adopting empirical correlations. One of the most utilized and simple for its mathematical expression is Blasius correlation [67]:

$$f = \frac{A}{\mathrm{Re}^B} \tag{3.70}$$

where A and B are empirically-fitted coefficients, typically equal to 0.316 and 0.25 when Reynolds number is within [2300, 20'000], to 0.184 and 0.20 when Reynolds number is larger than 20'000. For the reactor core a better correlation would be the one proposed by Chen and Todreas [68] which is derived for hexagonal wire-wrapped tube bundles (used in SUNRISE-LFR). In order to keep the simplicity of Blasius together with the accuracy of Chen-Todreas, Dehlin and Wallenius fitted the second correlation with a Blasius-shaped curve and found as coefficients $A = 0.406$ and $B = 0.272$ [48]. For HL and CL standard values for Blasius are implemented.

Concentrated pressure losses are due to specific obstructions, restrictions of the flow induced by deflecting fittings (bends or elbows) etc., and their expressions typically consist in experimentally-derived coefficients which multiply the kinetic part. The best manual for concentrated pressure losses coefficient is given by I.E. Idelchick in 1960 [69].

SUNRISE-LFR's core includes neither valves nor deflecting fittings, thus concentrated

pressure losses are offered solely by geometry changes in the fuel assembly:

$$\Delta P^{core}_{fr,conc} = K_{core,geom} \cdot \dot{m}|\dot{m}| \tag{3.71}$$

where $K_{core,geom}$ is the sum of eight contributions:

$$\begin{aligned} K_{core,geom} &= K_{foot,inlet} + K_{foot} + K_{hex,section,in} + K_{rail} + K_{rod,bundle,out} + \\ &+ K_{hex,section,out} + K_{head} + K_{grip} \end{aligned} \tag{3.72}$$

They are calculated as follows:

$$K_{foot,inlet} = \mathrm{C}_{\mathrm{foot,inlet,resistance}} \frac{1}{2\ \rho_{Pb}^{PA,in}\ A^2_{foot,inlet}} \tag{3.73}$$

$$K_{foot} = \left(1 - \frac{A_{Pb,foot}}{A_{hexcan,in}}\right)^2 \frac{1}{2\ \rho_{Pb}^{PA,in}\ A^2_{Pb,foot}} \tag{3.74}$$

$$K_{hex,section,in} = \frac{1}{2}\left(1 - \frac{A_{Pb,rail}}{A_{hexcan,in}}\right) \frac{1}{2\ \rho_{Pb}^{PA,in}\ A^2_{Pb,rail}} \tag{3.75}$$

$$K_{rail} = \frac{1}{2}\left(1 - \frac{A_{Pb,PA}}{A_{Pb,rail}}\right) \frac{1}{2\ \rho_{Pb}^{PA,in}\ A^2_{Pb,PA}} \tag{3.76}$$

$$K_{rod,bundle,out} = \left(1 - \frac{A_{Pb,PA}}{A_{hexcan,in}}\right)^2 \frac{1}{2\ \rho_{Pb}^{PA,out}\ A^2_{Pb,PA}} \tag{3.77}$$

$$K_{hex,section,out} = \frac{1}{2}\left(1 - \frac{A_{Pb,head}}{A_{hexcan,in}}\right) \frac{1}{2\ \rho_{Pb}^{PA,out}\ A^2_{Pb,head}} \tag{3.78}$$

$$K_{head} = \frac{1}{2}\left(1 - \frac{A_{Pb,PA,out}}{A_{Pb,head}}\right) \frac{1}{2\ \rho_{Pb}^{PA,out}\ A^2_{Pb,PA,out}} \tag{3.79}$$

$$K_{grip} = \left(1 - \frac{A_{Pb,PA,out}}{A_{HL,PA}}\right)^2 \frac{1}{2\ \rho_{Pb}^{PA,out}\ A^2_{Pb,PA,out}} \tag{3.80}$$

where $\mathrm{C}_{\mathrm{foot,inlet,resistance}}$ is a coefficient equal to 1.5.
In both distributed and concentrated pressure losses equations for the core the mass flow rate $\dot{m}$ is calculated in the peak assembly (PA). The reason comes from the core outlet temperature profile: in order to gain efficiency in the heat power extraction, coolant temperature profile at the outlet of the core should be as flat as possible. This is because mixing lead flows at different temperatures can establish strong instabilities in the overall coolant motion (counter-flows, vortices, etc.) which deeply affect the general functioning of the reactor and can even cause thermal fatigue to fuel elements and structural materials. However, due to the radial profile in the linear power rate (Bessel-shaped), it is impossible to keep a flat temperature profile unless some compensation strategy is implemented. At

present SUNRISE-LFR envisages to introduce orifices at the core inlet in order to increase pressure losses in the core outer rings. There, coolant mass flow rate decreases and higher temperatures are reached, eventually flattening the coolant temperature radial profile. Because of this reason, only the peak channel is not touched by the orificing and there frictional pressure losses can be calculated by Eq. (3.71) using the PA mass flow rate $\dot{m} = \dot{m}_{Pb}^{PA}$ evaluated as:

$$\dot{m}_{Pb}^{PA} = \frac{\dot{Q}_{fuel}^{PA}}{c_{Pb}\Delta T_{Pb}^{core,PA}} \tag{3.81}$$

$\dot{Q}_{fuel}^{PA}$ is the thermal power of the PA which is determined from the reactor power level and the radial peak factor F_R as

$$\dot{Q}_{fuel}^{PA} = F_R \frac{\dot{Q}_{fuel,tot}}{N_{ass}} \tag{3.82}$$

being N_{ass} the number of fuel assemblies.
$\Delta T_{Pb}^{core,PA}$ is the coolant temperature difference across the peak assembly and it is not explicitly calculated in BELLA, which assumes that it is equal to the temperature difference across the average channel in the core. The target for SUNRISE-LFR is indeed to have temperature profile at core outlet as flat as possible, hence $\Delta T_{Pb}^{core,PA} = \Delta T_{Pb}^{core,avg}$ is considered to be an acceptable approximation for the moment. A detailed spacial representation of the core will be done at a later stage adopting CFD softwares.

Hot leg and cold leg do not have specific elements which give concentrated pressure losses. They enter in the momentum balance equation just with the distributed pressure losses using Eq. (3.69), even though their value is totally negligible ($< 1\ Pa$).

The steam generator of the reactor is based on the spiral heat exchanger tube design patented by Cinotti [59]. The hot coolant is delivered from the HL into the annular plenum inside the steam generator. Then, due to the hydrostatic pressure caused by the top plate at the end of the plenum, the coolant is forced to flow radially through the spiral tube stack, transferring heat to the secondary side. The resistance offered to coolant cross-flow by staggered layers of planar spiral tubes with diameter D and pitch P cannot be described in terms of the Darcy-Weisbach equation. Therefore, a correlation proposed by Idelchik [69] is used to compute the distributed frictional pressure drops across the

steam generator:

$$\Delta P^{SG}_{fr,distr} = \frac{R_{in}^{-0.73} - R_{out}^{-0.73}}{R_{out} - R_{in}} \left(15.6 - 8.35\frac{P}{D}\right) \frac{N_{tubes} + 1}{1.46\rho} \left(\frac{\mu}{D}\right)^{0.27} \left[\frac{\dot{m}^{SG}_{Pb}}{2\pi H_{shell}} \frac{P}{P - D}\right]^{1.73} \tag{3.83}$$

where N_{tubes} is the number of staggered layers per steam generator, R_{in} and R_{out} are the spiral initial and terminal radius respectively, ρ is the coolant density and μ is the coolant dynamic viscosity both evaluated at the average temperature of the SG, H_{shell} is the height of the spiral tube stack and $\dot{m}^{SG}_{Pb} = \dot{m}_{Pb}/10$ stands for the mass flow rate in a single SG.
Concentrated pressure losses for the SG have yet to be considered.

Lastly, concentrated pressure losses related to the motion of lead from central region (core and HL) to the annular part (CL) and viceversa have yet to be investigated. Probably the correct coefficients can be found once again on Idelchik [69].

3.2.4. Primary circuit mass balance

SUNRISE-LFR is planned to have a hot leg right above the core with a surface level Z^{HL} able to change over time in such a way to adapt to density variations of lead (thermal expansion). On the contrary, and differently than previous versions of the reactor, cold leg has a fixed level Z^{CL} covered by a metallic lid, patented by LeadCold [58], through which the shaft of the pump-SG module passes.
This subsection proposes a new method to estimate the time-dependent HL free surface level leveraging on mass balance equation.

A first dimensioning of Z^{HL} can be done in hot shut-down (SD) just considering a mechanical equilibrium in the cold pool:

$$P_{hydr,center} = P_{hydr,annular} \tag{3.84}$$

where

$$P_{hydr,center} = P^{core}_{hydr} + P^{HL}_{hydr} = \left(H^{core}\rho^{core} + Z^{HL}\rho^{HL}\right)g \tag{3.85}$$

$$P_{hydr,annular} = P^{CL}_{hydr} = Z^{CL}\rho^{CL}g \tag{3.86}$$

Solving for HL free surface level

$$Z^{HL}_{SD} = \frac{Z^{CL}\rho^{CL} - H^{core}\rho^{core}}{\rho^{HL}} = Z^{CL} - H^{core} \tag{3.87}$$

since in hot shut-down all system temperatures are equal to 420 °C, differently than cold shut-down (all system temperatures are at 350 °C). This is the correct formula to calculate Z^{HL} in stationary SD conditions, without the action of the pump. It allows to calculate total lead mass in the system and, in turn, the time-dependent $Z^{HL}(t)$ by applying total lead mass conservation equation:

$$\begin{aligned} M_{SD} &= M_{SD}^{core} + M_{SD}^{HL} + M_{SD}^{CL} + M_{SD}^{CP} = \\ &= \left(A^{core}H^{core} + A^{HL}Z^{HL} + A^{CL}Z^{CL} + V^{CP}\right)\rho_{SD} \end{aligned} \tag{3.88}$$

$$Z^{HL}(t) = \frac{M_{SD} - A^{core}H^{core}\rho^{core} - A^{CL}Z^{CL}\rho^{CL} - V^{CP}\rho^{CP}}{A^{HL}\rho^{HL}} \tag{3.89}$$

where M_{SD} is the lead total mass in hot shut-down, i.e. total lead mass in the system in all conditions. SG and pump are not included in the equations since CAD calculations of their volume have yet to be provided. Nevertheless, they account just for a second order contribution which is negligible at present.

3.3. Simulink implementation

The software utilized throughout all the dynamical simulations in this work is MATLAB® (MATtrix LABoratory) developed by MathWork® [70, 71]. In particular, due to its strong reliability and efficiency in simulating complex dynamical systems, all simulations are performed by Simulink®, a MATLAB tool [72]. This is valid for all simulations presented in this and subsequent chapters.

Simulink primary interface is a graphical block diagramming tool and a customizable set of block libraries. It is optimized to solve explicit systems of differential equations where input and output variables are well identified (causal approach). Therefore, an optimal way to implement BELLA in Simulink is by grouping its equations into subsystems and coupling them through flow signals.

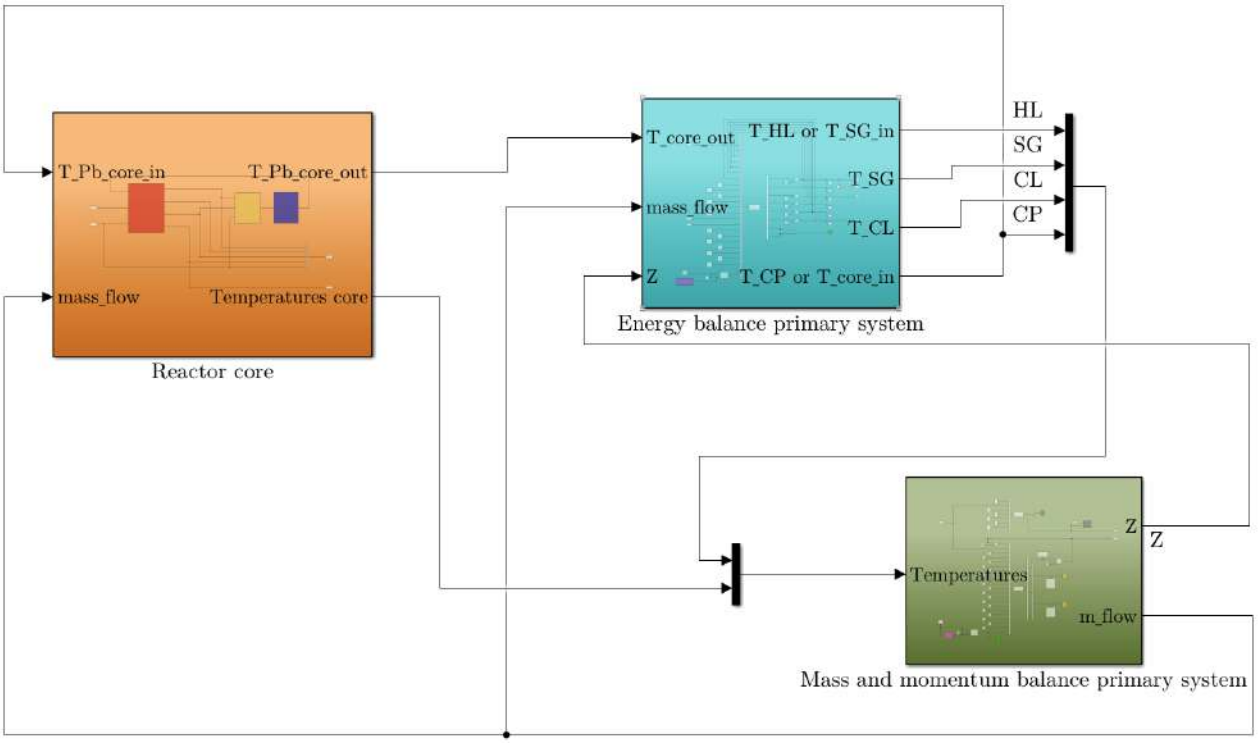

Figure 3.4: BELLA implementation in Simulink. Three main subsystems represent: reactor core (orange), primary circuit energy balance (light blue) and primary circuit momentum and mass balance (green).

The whole code is divided into three main subsystems (Figure 3.4). The first subsystem (orange) models the reactor core and contains three other sub-subsystem: core energy balance, point kinetics and reactivity feedbacks (Figure 3.5); its outputs are core temperatures in general and, in particular, lead temperature at the outlet of the core. The second subsystem (light blue) is the energy balance of the rest of the primary system and it calculates lead temperatures in HL, CL, SG and CP. Third and final subsystem (green) models the momentum and mass balance of the primary circuit providing as outputs lead mass flow rate and HL free surface level.

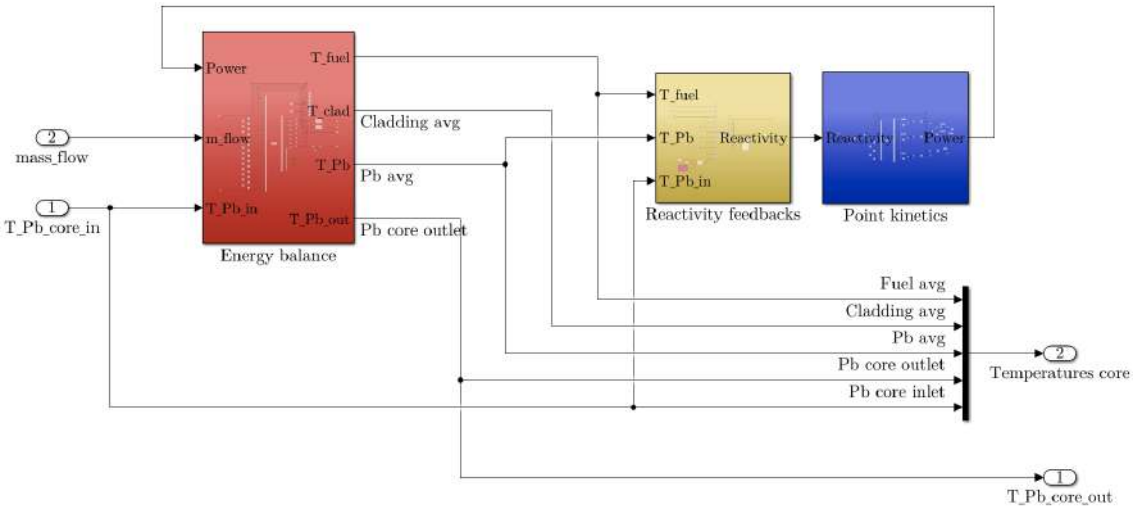

Figure 3.5: Reactor core implementation in Simulink. The three subsystems represent: core energy balance (red), reactivity feedbacks (yellow) and point kinetics (blue).

Each subsystem is built systematically utilizing MATLAB Function blocks, which relate inputs and output variables through equations, and Integrator blocks to solve the ordinary differential equations (e.g., Figure 3.6 shows the primary system energy balance). All blocks are taken from the Simulink Library Browser.

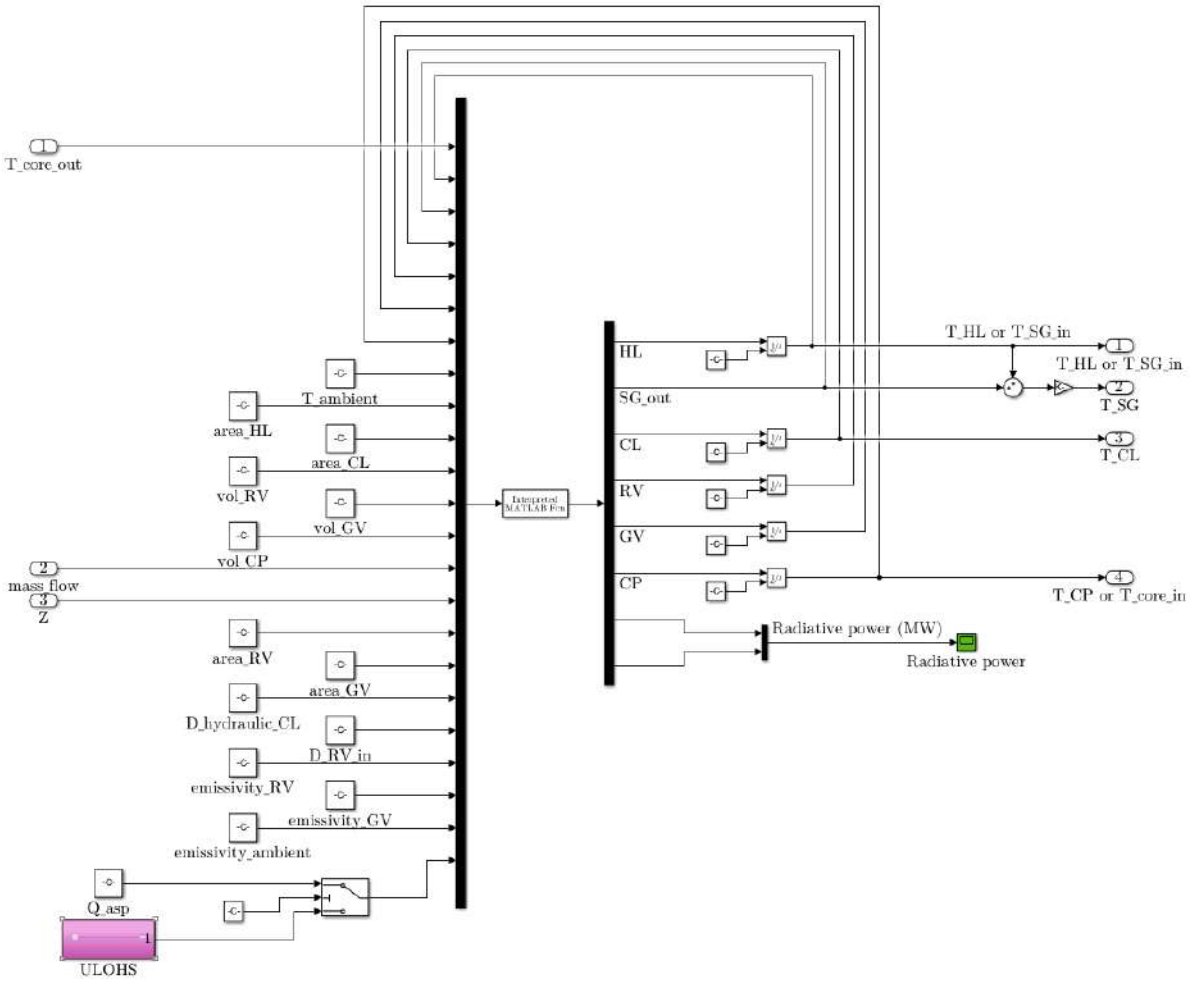

Figure 3.6: Primary system energy balance implementation in Simulink. Magenta sub-subsystem contains the modeling of ULOHS accidental scenario.

Table 3.7 lists the input and the output variables of each subsystem.

Subsystem	Inputs	Outputs
Reactor core	$T_{Pb}^{core,in}$, $\dot{m}_{Pb}$	T_{fuel}, T_{clad}, $T_{Pb}^{core,avg}$, $T_{Pb}^{core,out}$
Core energy balance	$\dot{Q}_{fuel}$, $T_{Pb}^{core,in}$, $\dot{m}_{Pb}$	T_{fuel}, T_{clad}, $T_{Pb}^{core,avg}$, $T_{Pb}^{core,out}$
Reactivity feedbacks	T_{fuel}, $T_{Pb}^{core,avg}$, $T_{Pb}^{core,in}$	$\Delta\rho_{fb}$
Point kinetics	$\Delta\rho_{fb}$, $\Delta\rho_{ext}$	$\dot{Q}_{fuel}$
Primary system energy balance	$T_{Pb}^{core,out}$, $\dot{m}_{Pb}$, Z^{HL}, $\dot{Q}_{SG}$	T_{Pb}^{HL}, T_{Pb}^{SG}, T_{Pb}^{CL}, $T_{Pb}^{core,in}$
Primary system momentum and mass balance	All primary system temperatures, ΔP_{pump}	$\dot{m}_{Pb}$, Z^{HL}

Table 3.7: Simulink subsystems input and output variables in BELLA.

Figures 3.4 and 3.5 do not show some inputs: $\Delta\rho_{ext}$, ΔP_{pump} and $\dot{Q}_{SG}$. They are the controlled variables which trigger accidental scenarios. For this reason, they are incorporated in special magenta sub-subsystems named after the accidental transient (UTOP, ULOF, ULOHS). They can be found in point kinetics subsystem, primary system mass and momentum balance subsystem and primary system energy balance subsystem (e.g., Figure 3.6), respectively.

3.4. Simulations

A computational tool intended for use in safety informed, pre-conceptual design of lead-cooled reactor systems is required to be capable of simulating the system under normal and off-normal conditions. Indeed, BELLA current capabilities include simulation of unprotected transient over-power (UTOP), loss-of-flow (ULOF), loss-of-heat-sink (ULOHS) scenarios and a combination of ULOF and ULOHS (station blackout). This section is entirely dedicated to BELLA's simulation of transients on SUNRISE-LFR. It serves both to test the code and to verify safety margins of the demonstrator reactor under accidental scenarios.
This section starts with steady-state conditions of SUNRISE-LFR and then it proceeds by showing simulation results in UTOP, ULOF, ULOHS and ULOF-ULOHS combined.

The general Simulink settings adopted in these transients are briefly discussed in Appendix D.

3.4.1. Steady-state conditions

BELLA perfectly sustains steady-state conditions. They are set by the total power of the reactor, the core inlet temperature of lead, lead mass flow rate and total amount of lead inside the primary system. Besides showing the results of the simulations through plots − which is done only for thermal power and reactor core temperatures (fuel, cladding and lead) in Figure 3.7 −, the most important values of SUNRISE-LFR working conditions are listed in Table 3.8.

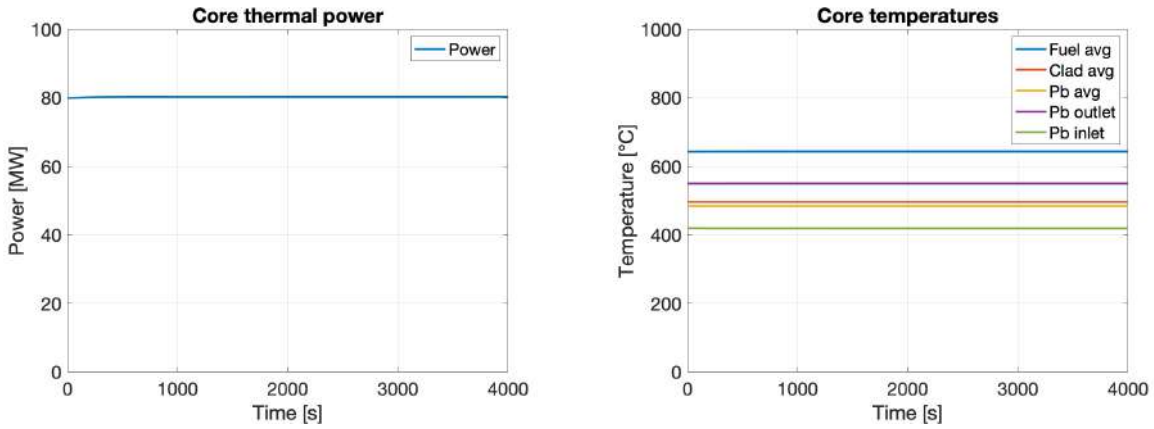

(a) Constant core thermal power.

(b) Constant main core temperatures.

Figure 3.7: Simulation results adopting BELLA in steady-state conditions.

Quantity	Value	Unit
Core thermal power	80.33	MW
Fuel average temperature*	643.9	°C
Fuel max temperature**	867.9	°C
Clad average temperature*	496.3	°C
Clad max temperature**	559.8	°C
Lead core average temperature	484.8	°C
Lead core inlet temperature	419.5	°C
Lead core outlet temperature	550.1	°C
Lead mass flow rate	4243.4	kg/s
HL free surface level	2.947	m
SG thermal power removal	80	MW
Radiative power losses from the RV***	328	kW

Table 3.8: BELLA steady-state values for the most important quantities.

Some notes to Table 3.8:

* : fuel and cladding average temperatures are calculating using Eq.s (3.38) and (3.39), respectively. Therefore, they consider the average temperature in radial direction in the average channel at core midplane.

** : fuel and cladding maximum temperatures are calculating using Eq.s (3.49) and (3.47), respectively. Therefore, they consider the innermost node temperature in the peak channel at the hottest axial position.

*** : global energy balance is not perfectly respected. This is totally understandable because the dynamics of the radiative power removed from the reactor vessel is extremely poor. Even though the simulation time is not low (4000 s), an equilibrium between power lost (SG removal and RV losses) and power produced (fissions) has yet to be reached.

3.4.2. UTOP

UTOP (unprotected transient overpower) is the first reference accidental scenario that is examined. It is modeled as a sudden (step-wise) insertion of a positive reactivity through the external contribution $\Delta\rho_{ext}$. Its value is 0.2 \$ which corresponds to 133 pcm. The

rationale behind it is here explained: a sudden injection of positive reactivity can happen because of unexpected control rod extraction; the most critical moment when UTOP can occur is the one which exhibits maximum control rods insertion, which is at middle of life (MoL). In fact, considering the reactivity swing curve (Figure 3.8), after reactor startup the internal reactivity increases due to fuel breeding until around the 8th year when it starts to decrease because of both fissile fuel burning, neutron poisoning and fuel axial swelling. At MoL control rods must be inserted up to an amount corresponding to 210 pcm to achieve criticality, which means 105 pcm per control rod. This is the most critical moment for UTOP to occur. Then it is decided that UTOP simulates the sudden extraction of one control rod (105 pcm), plus some extra margin: in this way, 130 pcm are obtained, rounded up to 0.2 $.

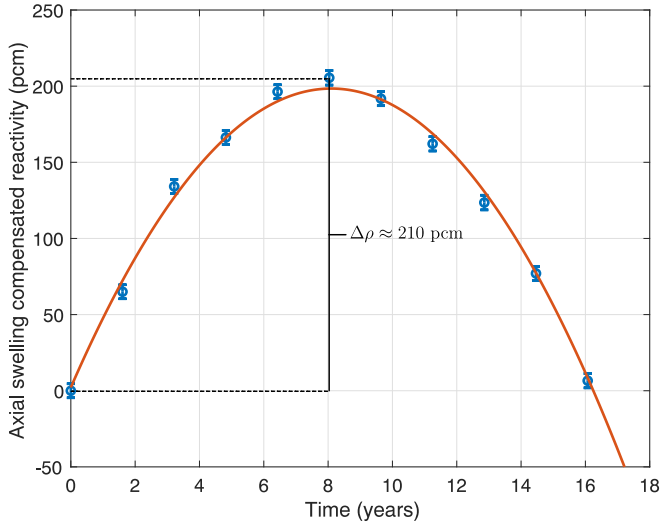

Figure 3.8: SUNRISE-LFR reactivity swing during the fuel cycle [48]. Blue markers are results obtained with Serpent2 and the red line is a fitted quadratic function.

By setting the simulation time to 2000 s and triggering UTOP after 500 s, the major quantities of interest are plotted in Figure 3.9.

The insertion of 0.2 $ of reactivity disturbs the established steady-state conditions. $\Delta\rho_{ext}$ acts immediately on neutronics and, in particular, on neutron population (almost proportional to core thermal power) with a step increase of its derivative. It can be noticed because the first parameter to vary in the simulation is the core thermal power. Subsequently, all core temperatures start to increase according to their time constants: fuel is the fastest because it is directly influenced by thermal power, but then cladding and lead follow. At this point two things occur at the same time, even though with different time scales: reactivity feedbacks and propagation of events in the primary circuit.

Reactivity feedbacks act together with the increase of core temperatures. They are regulated by an algebraic equation, meaning that, as soon as fuel temperature increases, for instance, Doppler effect and fuel axial expansion counterbalance the power increase by removing reactivity due to their coefficients negative sign. In Figure 3.9b they appear to be the first to assume non-zero values, although with different amplitudes. After about 50 s, and following the slower dynamics of lead, coolant thermal expansion and fuel assembly diagrid radial expansion enter into play (lead thermal expansion has a very low feedback on reactivity when compared to the others and it is simply motivated by the one-order-of-magnitude lower feedback coefficient). Doppler effect and diagrid radial thermal expansion exhibit a strong feedback response capable of reducing reactivity and, eventually, to bring it to zero, restoring neutronics steady-state conditions.
At the same time, the temperature increase of lead in the core has consequences on the rest of the primary circuit: all pools show increased temperatures which, due to lead thermal expansion, lead to an increased volume of lead inventory in the circuit. This volume increase is managed by the hot leg which enhances its free surface level by approximately 20 cm (+6.7%). Primary circuit temperatures variation influences also lead mass flow rate: both buoyancy term and frictional pressure losses change during the transient in such a way that the mass flow initially increases and after a while achieves stable conditions. Lead flow velocity never overcomes 0.90 m/s inside the core (the most critical region due to the small area of flow channels), keeping a good margin to erosion.

What seems to be unexpected in this simulation is displayed in Figure 3.9a: even after injecting 0.2 $ in the system, power returns back to initial value of 80 MW after a peak just below 150 MW. Considering how the system is modeled, it is not weird at all: due to the overall energy balance in the primary system, at steady-state conditions all sources of power need to be balanced by sinks, which are the SG and the RV thermal radiation (Eq. (3.90)). Since radiation from the RV never increases beyond 1 MW (starting from about 330 kW, peak value in the simulation is approximately 805 kW), the sinks are dominated in amplitude by the constant SG which removes 80 MW independently of the conditions of the system. This is the reason why core thermal power is restored at a value very close to the initial one. The only slight difference is due to a variation in the thermal power losses through the reactor vessel.

$$\dot{Q}_{fuel,tot} = \dot{Q}_{SG} + \dot{Q}_{radiation} \tag{3.90}$$

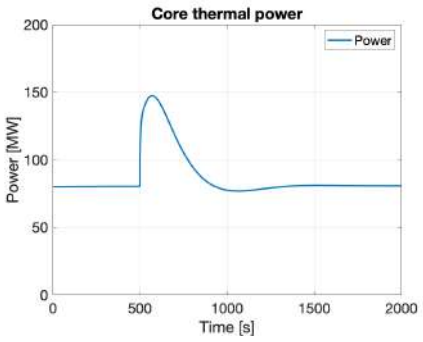

(a) Core thermal power.

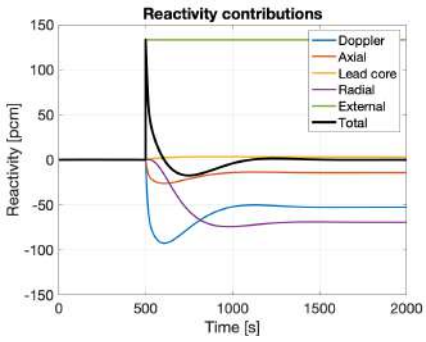

(b) Reactivity contributions.

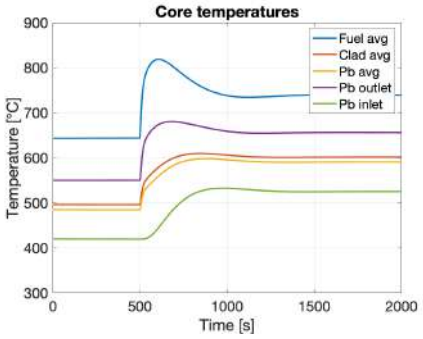

(c) Core temperatures.

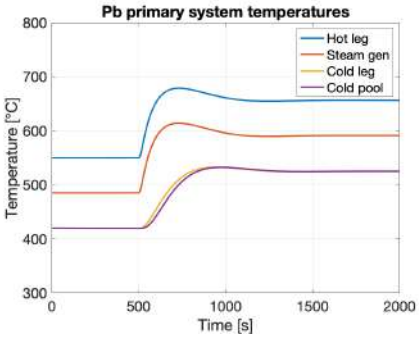

(d) Primary system temperatures.

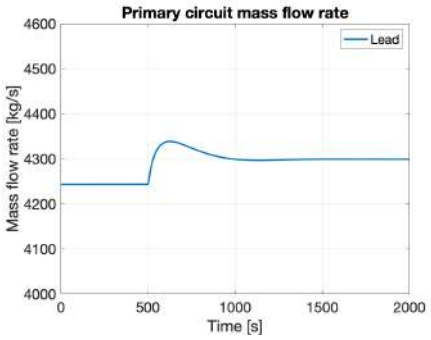

(e) Lead mass flow rate.

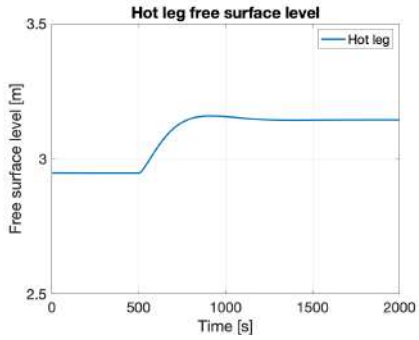

(f) HL free surface level.

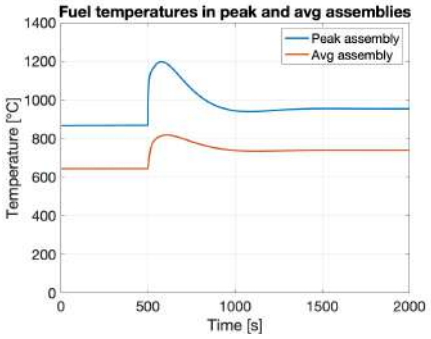

(g) Fuel temperature in the peak** and average* assemblies.

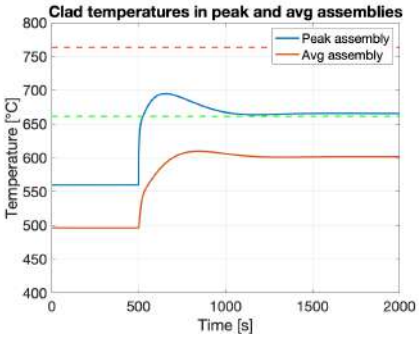

(h) Cladding temperature in the peak** and average* assemblies.

Figure 3.9: Main plots resulting from UTOP simulation. For the starred parameters look at the notes after Table 3.8.

Coming to the last two plots (Figures 3.9g and 3.9h), they show the behavior of fuel and cladding in the peak assembly (innermost node at the worst axial position) and in the average assembly (average node at the midplane). This is the meaning of the legend present in the two plots which remains valid for all the other simulations.
Fuel undergoes a significant temperature increase, but it stays well distant from the melting point (2850 °C). On the contrary, in the peak assembly cladding temperature overcomes the 662 °C threshold, even though by only 3.5 °C, while the average assembly remains about 60 °C below it. In any case, the second threshold at 763 °C is never reached.

Although it is worth to remember that the likelihood of such an event (full expulsion of one control rod without plant operator intervention) remains extremely low, this transient requires to be further investigated because cladding in the peak assembly consumes half of the margin to creep failure. Perhaps a different code that employs 1-dimensional (or even 2 and 3-dimensional) simulations of the whole core can check the results of the lumped tool BELLA.

Table 3.9 lists the value of the main variables of interest after UTOP simulation.

Quantity	Value	Variation (%)	Unit
Core thermal power	80.74	+0.5%	MW
Fuel average temperature*	739.0	+14.8%	°C
Fuel max temperature**	953.5	+9.9%	°C
Clad average temperature*	601.6	+21.2%	°C
Clad max temperature**	665.6	+18.9%	°C
Lead core average temperature	590.6	+21.8%	°C
Lead core inlet temperature	525.0	+25.1%	°C
Lead core outlet temperature	656.3	+19.3%	°C
Lead mass flow rate	4299.0	+1.3%	kg/s
HL free surface level	3.144	+6.7%	m
SG thermal power removal	80	+0.0%	MW
Radiative power losses from the RV***	731	+130.9%	kW

Table 3.9: Values of the most important quantities simulated with BELLA after UTOP. For the starred parameters look at the notes after Table 3.8.

3.4.3. ULOF

ULOF (unprotected loss of flow) transient is the second reference accidental scenario that BELLA is capable of simulating. It is initiated by a complete failure of all the pumps in the system and modeled by an exponential decrease of the pump pressure head ΔP_{pump} from nominal value to zero with a time constant equal to 10 s (Figure 3.10). The system continues to work only if it is capable of sustaining natural circulation by relying on buoyancy forces to compensate for frictional pressure losses.

By setting the simulation time to 3000 s and triggering ULOF after 500 s, the major quantities of interest are plotted in Figure 3.11.

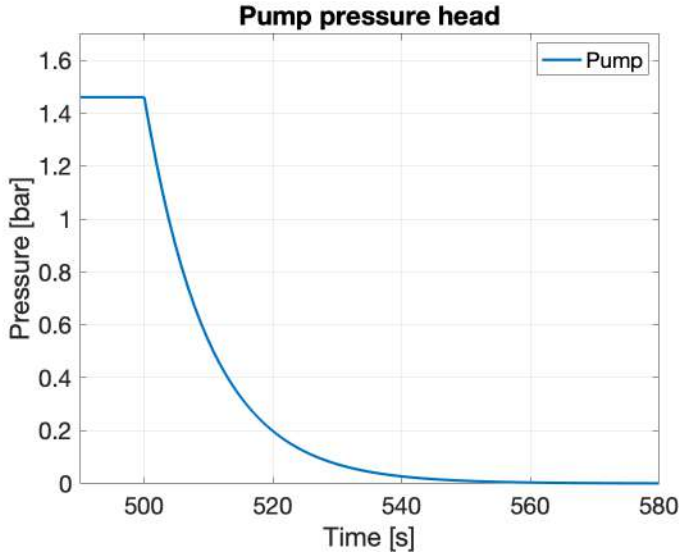

Figure 3.10: Pump failure: exponential decrease of pressure head.

The failure of the pumps affects immediately lead mass flow rate: following Eq. (3.63), time derivative of $\dot{m}_{Pb}$ loses the main positive contribution and, thus, begins a steep decrease which stops only when natural circulation has established, i.e. when $\Delta P_{buoyancy} = \Delta P_{friction}$. This is possible because frictional pressure losses are proportional to some power of the mass flow rate, meaning that as $\dot{m}_{Pb}$ decreases, $\Delta P_{friction}$ follows. When natural circulation conditions are met, $\dot{m}_{Pb} = 1314$ kg/s, about 31% of nominal value.
The strong decrease in the mass flow rate influences at first core temperatures (fuel, cladding and lead at the outlet), which tend to increase. Then, because the steam generator continues to remove fixed power, the temperature difference across the SG (and across the core) is enhanced. The following equation explains it:

$$\dot{Q} = \dot{m} c_p \Delta T \tag{3.91}$$

When $\dot{m}$ decreases but $\dot{Q}$ remains constant, ΔT has to increase (c_p variations are not significant). Therefore, if temperatures in the core and in the hot leg increase, lead temperatures in CL, CP and at core inlet decrease. After that, some slow oscillations raise up caused by reactivity feedbacks: due to Doppler effect and lead thermal expansion in core, initially reactivity becomes negative and core thermal power decreases; consequently core temperatures (fuel, cladding and lead) reach the peak and then decrease, lowering their contribution in reactivity. After a while, because the constant SG power removal remains higher than core thermal power, lead temperature at the core inlet decreases and, due to the negative sign of the diagrid radial feedback coefficient, it injects positive reactivity into the system (violet line in Figure 3.11b) which counterbalances fuel and core lead negative contributions and sets the conditions for very slow oscillations. The poor oscillation velocity is mainly motivated by the large thermal inertia of lead. After a couple of oscillations the system reaches the steady-state. As already explained for UTOP, core thermal power comes back to 80 MW following the reactivity trend with some delay.
On a global view, after the transient primary system temperatures have increased in the core and in the HL, decreased elsewhere. Because of the larger volumes of CL and CP, the net contribution to lead thermal expansion is slightly negative and, therefore, HL free surface level have slightly decreased.

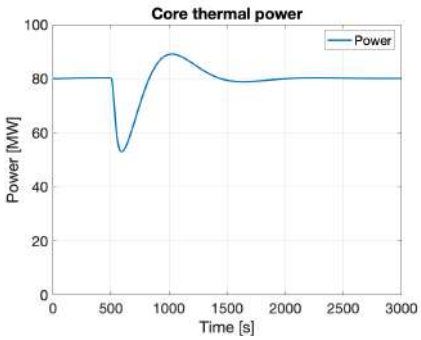

(a) Core thermal power.

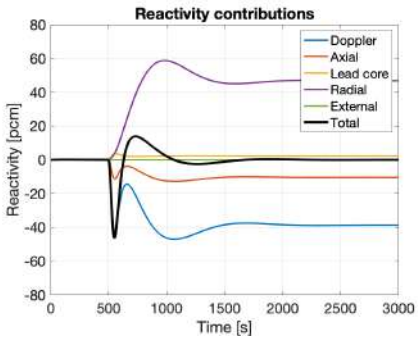

(b) Reactivity contributions.

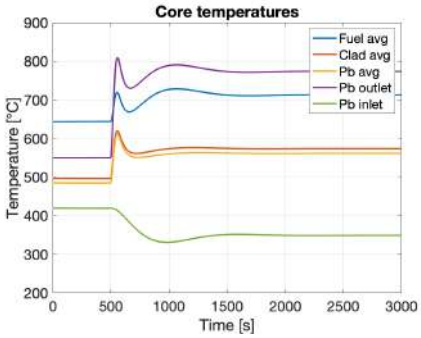

(c) Core temperatures.

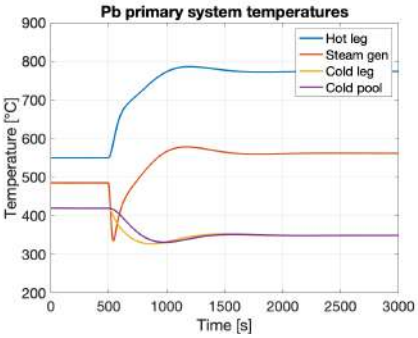

(d) Primary system temperatures.

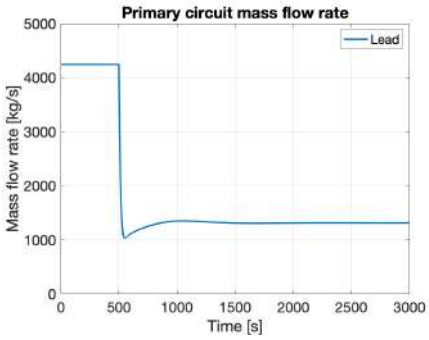

(e) Lead mass flow rate.

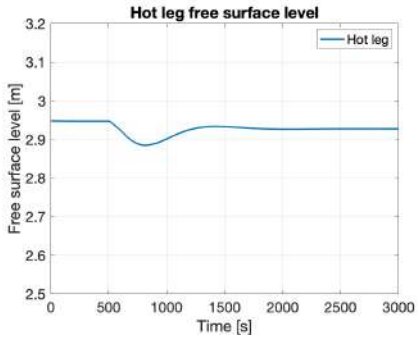

(f) HL free surface level.

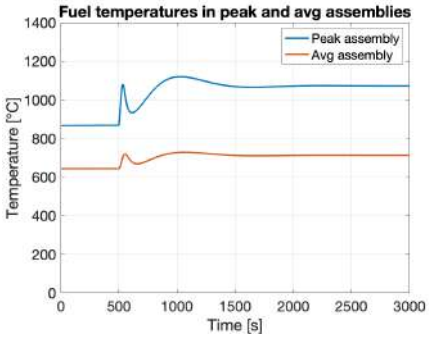

(g) Fuel temperature in the peak** and average* assemblies.

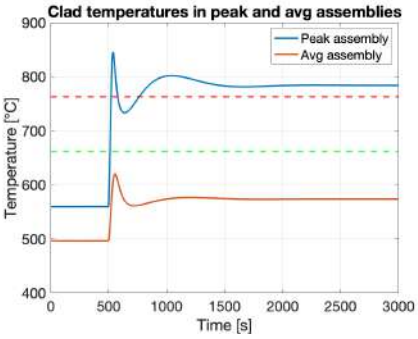

(h) Cladding temperature in the peak** and average* assemblies.

Figure 3.11: Main plots resulting from ULOF simulation. For the starred parameters look at the notes after Table 3.8.

If on the one hand the system is capable of driving toward stable conditions, the temperatures after transient are not satisfactory at all.
In particular, around $t = 900\ s$ coolant temperature at core inlet (or in CL and CP) equalizes lead melting point, and for the rest of the transient it remains about only 25 °C above it. This is problematic in two senses: first of all because of coolant solidification risk; secondly, because of liquid metal embrittlement (LME), particularly strong at low temperatures.
Moreover, Figure 3.11h shows cladding average temperature in the average channel always below the first threshold at 662 °C, but its maximum temperature in the peak assembly above the second threshold of 763 °C at final steady-state conditions. This is a bad behavior of the system and requires a better investigation through more advanced 1-dimensional (or 2 or 3-dimensional) codes to correctly simulate the transient in all core assemblies and to check cladding integrity at high temperature.
For what concerns fuel pellets, they preserve a strong safety margin against melting both in the peak and in the average assemblies.

However, it must be remembered that this transient is simulated with the strong hypothesis of constant SG power removal capacity, which cannot be assumed to be realistic. Chapter 5 simulates ULOF in the presence of a time-depended SG module and some differences appear. Additional comments are given at the end of this chapter, in Section 3.5.

Table 3.10 lists the value of the main variables of interest after ULOF simulation.

Quantity	Value	Variation (%)	Unit
Core thermal power	80.13	-0.3%	MW
Fuel average temperature*	712.8	+10.7%	°C
Fuel max temperature**	1072.4	+23.6%	°C
Clad average temperature*	573.7	+15.6%	°C
Clad max temperature**	784.0	+40.1%	°C
Lead core average temperature	561.5	+15.8%	°C
Lead core inlet temperature	349.1	-16.8%	°C
Lead core outlet temperature	773.8	+40.7%	°C
Lead mass flow rate	1313.8	-69.0%	kg/s
HL free surface level	2.927	-0.7%	m
SG thermal power removal	80	+0.0%	MW
Radiative power losses from the RV***	152	-52.0%	kW

Table 3.10: Values of the most important quantities simulated with BELLA after ULOF. For the starred parameters look at the notes after Table 3.8.

3.4.4. ULOHS

ULOHS (unprotected loss of heat sink) is the third reference transient for BELLA. It is caused by a failure of all SG units at the same time and it is modeled as a step-wise decrease of SG power removal from nominal 80 MW to zero.

This accidental scenario is simulated adopting two simulation times, 4000 s (about 1.1 hours) and 1000000 s (about 278 hours or 11.6 days), because of the very slow dynamics, dominated entirely by the only thermal power sink left in the system, thermal radiation from the reactor vessel. In the first simulation (Figures 3.12 and 3.13) it is possible to notice the short-term events (steep decrease of core power and subsequent collapse of system temperatures into a unique curve), while the second simulation (Figures 3.15 and 3.16) shows the long-term behavior of the reactor, characterized by a general decrease of the temperatures.

As soon as SG modules fail, the system loses its main power sink: SG average temperature reaches immediately 550 °C and, hereafter, all the rest of the primary system pools (CL, CP and core) start to increase their temperatures. Hence, hotter lead in the core activates the first reactivity feedbacks: diagrid radial thermal expansion negative feedback (violet line in Figure 3.12b) totally dominates lead thermal expansion positive feedback (yellow

line again in Figure 3.12b) and, then, reactivity becomes negative. Subsequently, core thermal power reduces and the same does fuel temperature. Even though that activates Doppler effect and fuel axial expansion inserting positive reactivity into the system, diagrid radial expansion continues to set the overall behavior of reactivity: its very strong contribution is a consequence of both its feedback coefficient absolute value (more than four times fuel axial feedback coefficient, for instance) and the large temperature excursion that lead at core inlet has already undergone. This is the mechanism that links the loss of SG and the strong decrease in fission power. In about 30 minutes, only decay power is left, which is only a fraction of the nominal 80 MW but remains for a very long time.

Due to the low value of decay power (just above 1 MW), all temperatures collapse into a unique line (tiny differences are still present, though) and slightly increase. In fact, decay power remains larger than the only power sink left, thermal radiation from the reactor vessel, at least until the end of the first simulation (Figure 3.13b). And it is true even though thermal radiation immediately increases above 1 MW as a consequence of the rising in RV temperature, in contact with hot lead (Figure 3.13c).

Due to the general temperature increment in the primary system, HL free surface level grows to accommodate lead thermal expansion. Coolant mass flow rate decreases because buoyancy term lowers as a consequence of the smaller ΔT across the system.

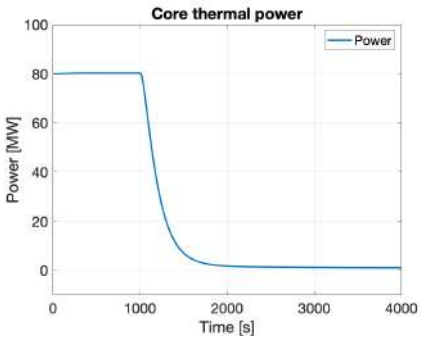

(a) Core thermal power.

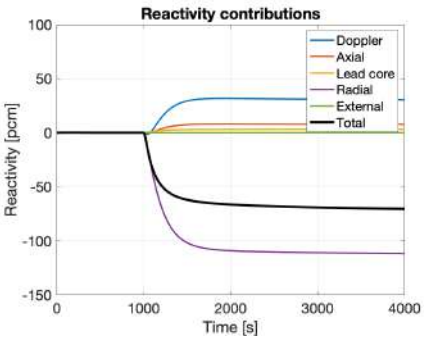

(b) Reactivity contributions.

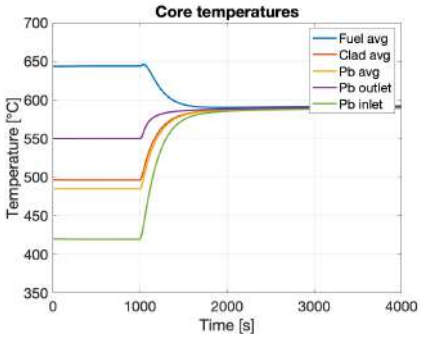

(c) Core temperatures.

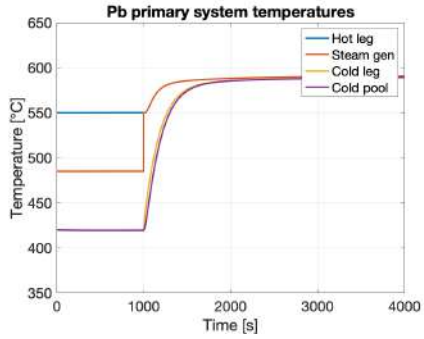

(d) Primary system temperatures.

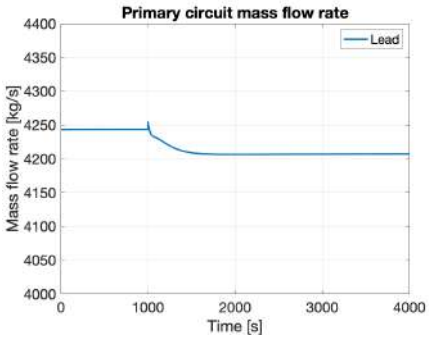

(e) Lead mass flow rate.

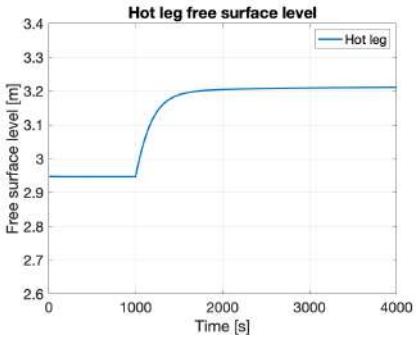

(f) HL free surface level.

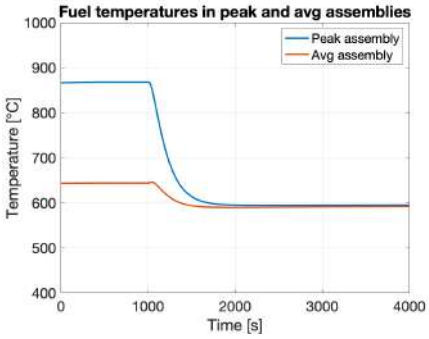

(g) Fuel temperature in the peak** and average* assemblies.

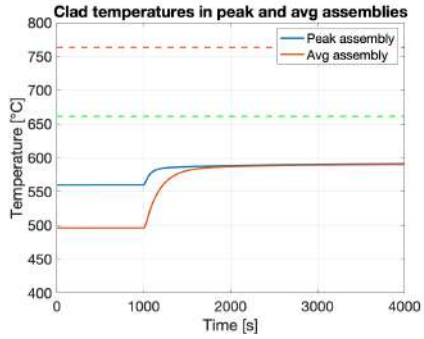

(h) Cladding temperature in the peak** and average* assemblies.

Figure 3.12: Main plots resulting from ULOHS simulation with simulation time equal to 4000 s (1.1 hours). For the starred parameters look at the notes after Table 3.8.

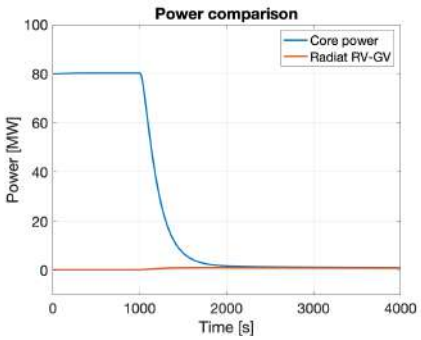

(a) Decay and radiation power.

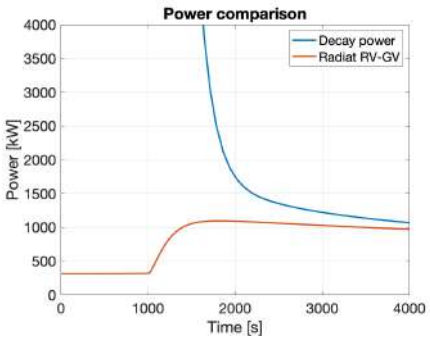

(b) Zoom on decay and radiation power.

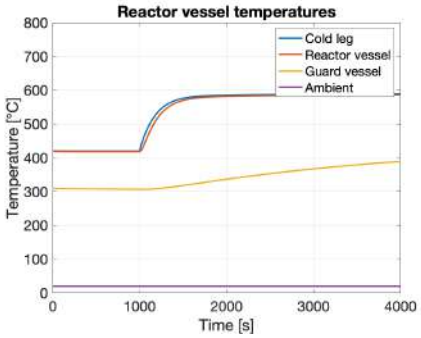

(c) Vessel temperatures.

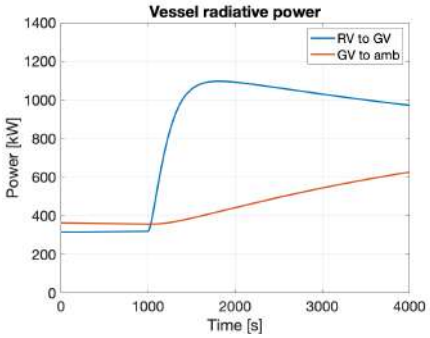

(d) Radiative power (losses).

Figure 3.13: Additional plots resulting from ULOHS simulation with simulation time equal to 4000 s (1.1 hours).

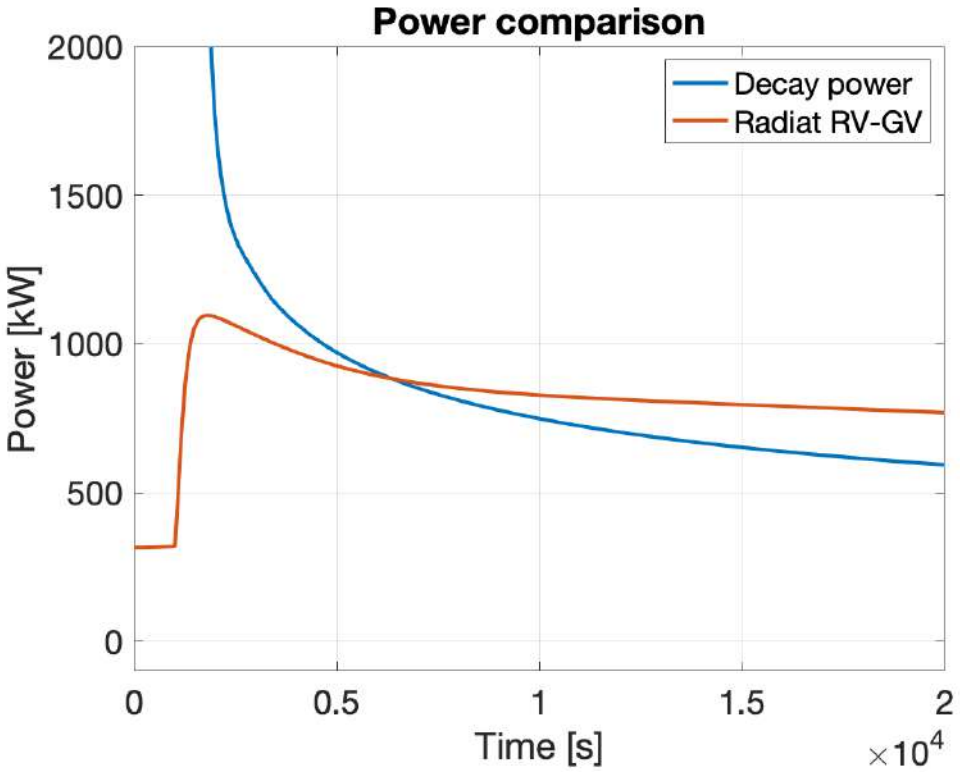

Figure 3.14: Zoom on the moment when radiation power losses overcome core decay power.

Figure 3.14 shows the instant in which thermal losses from RV overcome decay power: approximately 1.6 hours after ULOHS is triggered. From that moment on the reactor is effectively cooled down by the RVACS system (passive safety). This is extremely beneficial because drives the system toward steady-state, safe conditions, but eventually it may lead to solidification of the coolant if the system temperature goes below lead melting point (327.5 °C). However, the dynamics of the transient is extremely low because dominated by radiation heat transfer, giving in principle sufficient time to the plant operators to intervene and restore working conditions. In fact, LFRs projects under development described in Chapter 1 usually foresee 72 hours as a time reference before human intervention and ULOHS simulation shows that even after 11.6 days some margin to lead solidification is still present.
In Figure 3.15b reactivity feedbacks are positive and continue to increase. They do not have any influence on thermal power because neutron population is null at this point. Thermal power is entirely controlled by fission products decay power.
Due to primary system temperatures decrease, lead density grows and HL free surface level decreases. Lead mass flow rate exhibits only a mild decrement in this transient.

Regarding the safety margins to fuel melting and cladding tube creep rupture, this transient is not a concern at all because the system is effectively cooled down. Safety margins are always well respected. However, it must be noted that the dynamics of RVACS cooling action is here underestimated because it does not include natural convection by external air. That should increase the cooling rate of the system lowering the time needed to reach coolant solidification. In this case, a delayed intervention of the plant operator could lead to some troubles.

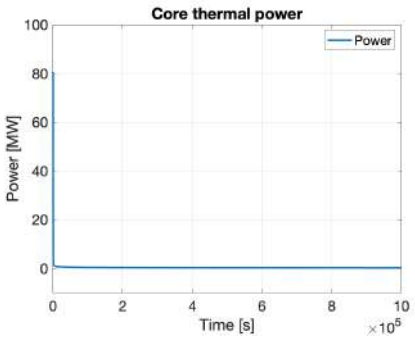

(a) Core thermal power.

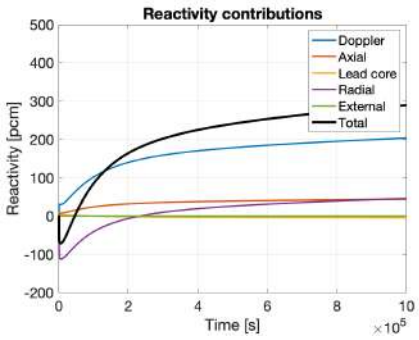

(b) Reactivity contributions.

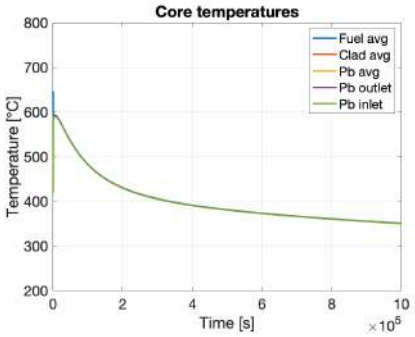

(c) Core temperatures.

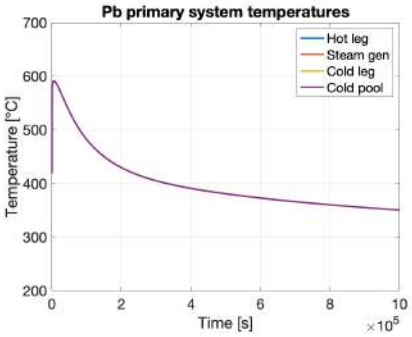

(d) Primary system temperatures.

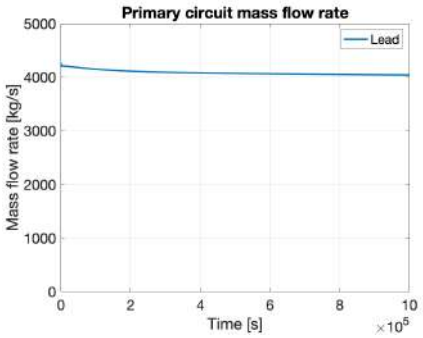

(e) Lead mass flow rate.

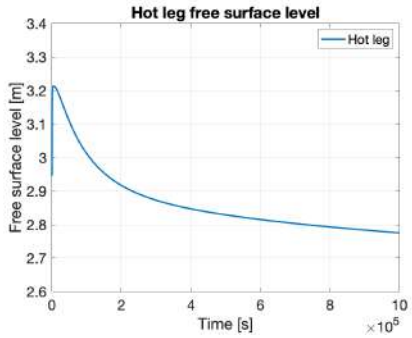

(f) HL free surface level.

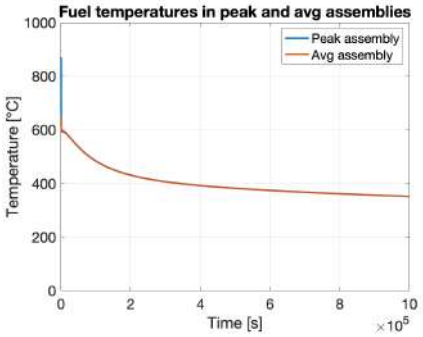

(g) Fuel temperature in the peak** and average* assemblies.

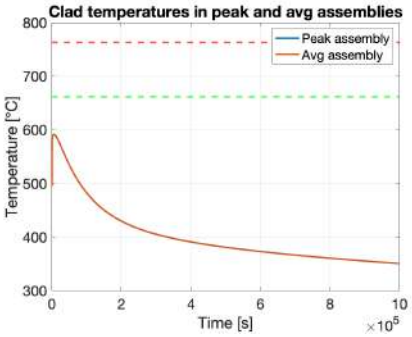

(h) Cladding temperature in the peak** and average* assemblies.

Figure 3.15: Main plots resulting from ULOHS simulation with simulation time equal to 1000000 s (278 hours or 11.6 days). For the starred parameters look at the notes after Table 3.8.

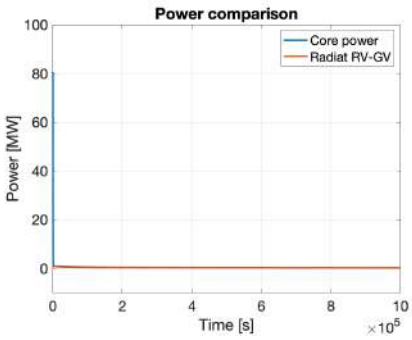

(a) Decay and radiation power.

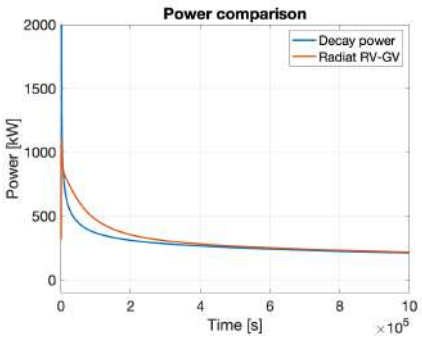

(b) Zoom on decay and radiation power.

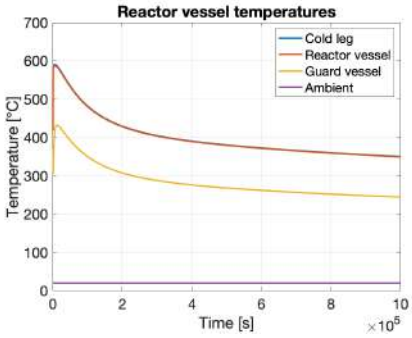

(c) Vessel temperatures.

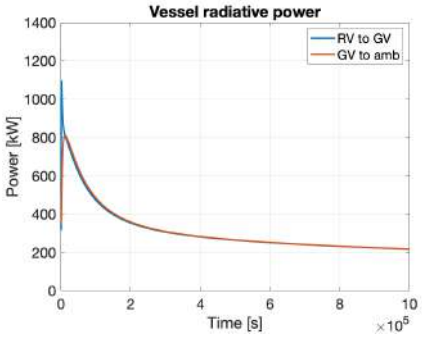

(d) Radiative power (losses).

Figure 3.16: Additional plots resulting from ULOHS simulation with simulation time equal to 1000000 s (278 hours or 11.6 days).

Table 3.11 lists the value of the main variables of interest after ULOHS simulation.

Quantity (unit)	Value (1.1 h)	Variation (1.1 h)	Value (11.6 d)	Variation (11.6 d)
Core thermal power (kW)	1069	-98.7%	211	-99.7%
Fuel average temperature* (°C)	592.1	-8.0%	350.9	-45.5%
Fuel max temperature** (°C)	595.2	-31.4%	351.6	-59.5%
Clad average temperature* (°C)	590.2	+18.9%	350.4	-29.4%
Clad max temperature** (°C)	591.1	+5.6%	350.6	-37.4%
Lead core average temperature (°C)	590.1	+21.7%	350.4	-27.7%
Lead core inlet temperature (°C)	589.2	+40.4%	350.2	-16.5%
Lead core outlet temperature (°C)	590.9	+7.4%	350.6	-36.3%
Lead mass flow rate (kg/s)	4207.2	-0.9%	4042.0	-4.8%
HL free surface level (m)	3.212	+9.0%	2.776	-5.8%
SG thermal power removal (MW)	0	-100%	0	-100%
Radiative power losses from the RV*** (kW)	972	+204.6%	217	-31.9%

Table 3.11: Values of the most important quantities simulated with BELLA after ULOHS. For the starred parameters look at the notes after Table 3.8.

3.4.5. ULOF and ULOHS

Last accidental scenario considered as a reference in BELLA is a combination of ULOF and ULOHS. It is supposed to model station blackout: all primary system components that rely on external conditions − primary pumps and steam generators − fail at the same time. Pump module follows once again an exponential decay with time constant equal to 10 s; SG module goes to zero as a step function starting from its nominal value.

This scenario is simulated by triggering at $t = 1000$ s both ULOF and ULOHS events. Considering once again two simulation times equal to 4000 s (about 1.1 hours) and 1000000 s (about 278 hours or 11.6 days), the trend of the main variables of interest is displayed in Figures 3.17, 3.18, 3.19 and 3.20.

In this complex scenario two major events occurs: pump does not provide anymore pressure head and SG power removal goes instantaneously to zero. In the previous subsections the two transients are analyzed separately, while here they must be coupled. It is not

trivial to distinguish between the consequences of one failure and the other, especially because this is a strongly non-linear system. Nevertheless, some comments can be pointed out.

Although the instantaneous SG failure provokes an immediate surge in the SG temperature, the effects on the rest of the system take slightly more time because of the large lead thermal inertia. On the other hand, even though the rate of failure of the pump is finite (about 50 s to complete), its effects take place very quickly: lead mass flow rate strongly decreases and, as a consequence, core temperatures (fuel, cladding and lead) grows. Differently than ULOF alone, here SG power removal capacity has gone and hot lead coming out of the core is not cooled down effectively. This induces an increase of CL, CP and core inlet lead temperatures.
To understand what happens to core thermal power, reactivity feedbacks need to be taken into account (Figure 3.17b): initially, Doppler effect and fuel axial expansion inject negative reactivity into the system causing a decrease in core power (lead thermal expansion is not significant); consequently, core temperatures stop their increment and start decreasing, partially removing the negative reactivity inserted (Doppler and axial expansion become even positive after 4 minutes); at the same time, hot lead at core inlet activates diagrid radial expansion which slowly adds more negative reactivity. The total reactivity remains always negative because diagrid expansion dominates; thus, core power continues to decrease until neutron population is set to zero, remaining only with FPs decay contribution, almost entirely removed from the system by thermal radiation through the reactor vessel (Figure 3.18b).

Eventually, the system temperatures converge toward 600 °C without collapsing on it (Figures 3.17c and 3.17d), differently than ULOHS only. This is simply because here both $\dot{Q}_{SG}$ and $\dot{m}_{Pb}$ decrease. In fact, considering Eq. (3.92), since core power decrease (almost -99%) is larger than mass flow rate decrease (-93%), ΔT lowers but remains finite.

$$\dot{Q} = \dot{m} c_p \Delta T \tag{3.92}$$

Coolant mass flow rate is still present because sustained by natural circulation.

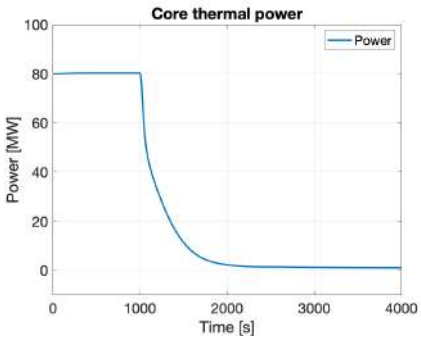

(a) Core thermal power.

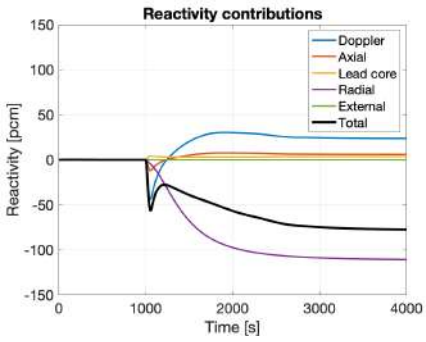

(b) Reactivity contributions.

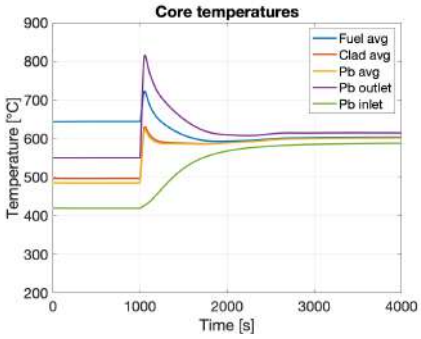

(c) Core temperatures.

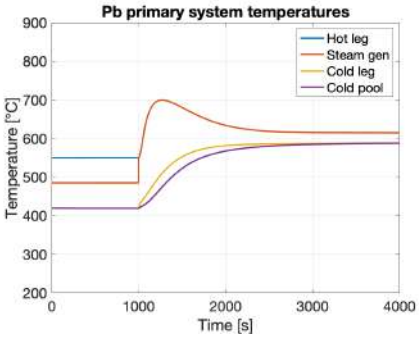

(d) Primary system temperatures.

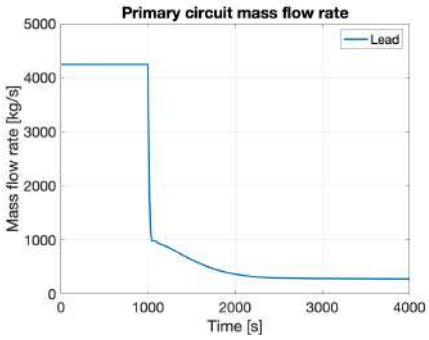

(e) Lead mass flow rate.

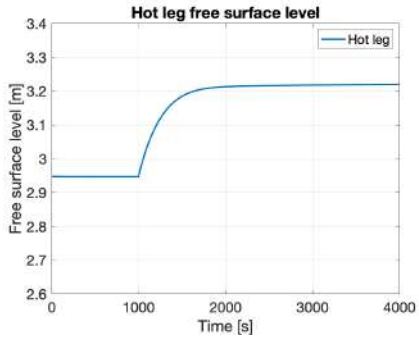

(f) HL free surface level.

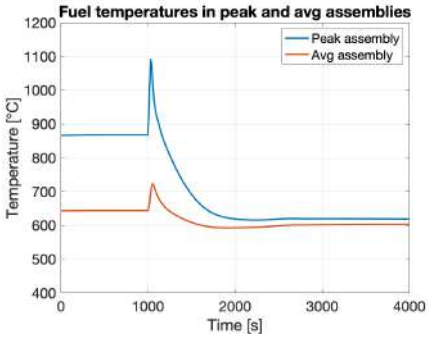

(g) Fuel temperature in the peak** and average* assemblies.

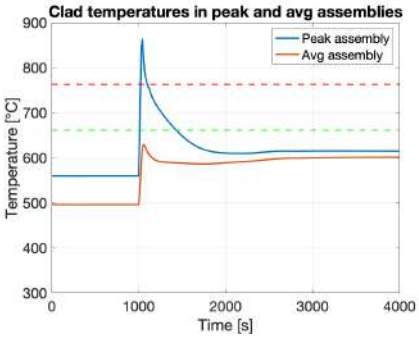

(h) Cladding temperature in the peak** and average* assemblies.

Figure 3.17: Main plots resulting from ULOF-ULOHS combined simulation with simulation time equal to 4000 s (1.1 hours). For the starred parameters look at the notes after Table 3.8.

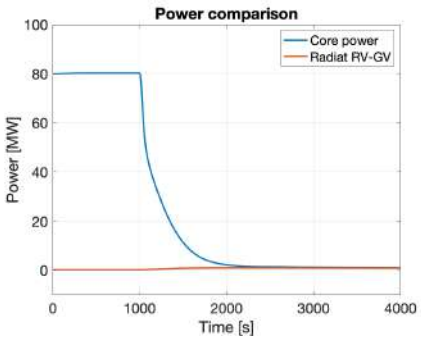

(a) Decay and radiation power.

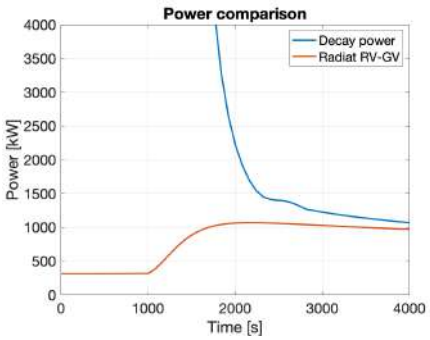

(b) Zoom on decay and radiation power.

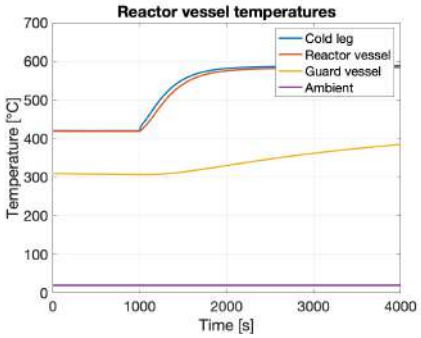

(c) Vessel temperatures.

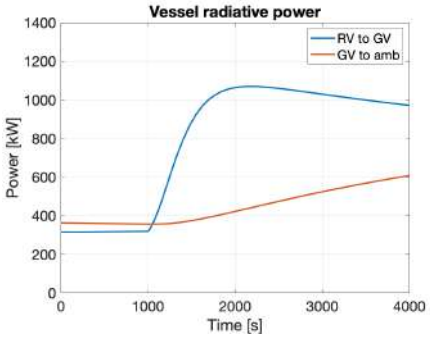

(d) Radiative power (losses).

Figure 3.18: Additional plots resulting from ULOF-ULOHS combined simulation with simulation time equal to 4000 s (1.1 hours).

Thermal radiation from the reactor vessel overcomes decay power about 1.6 hours after the accident is triggered. From that time on, the reactor is effectively cooled down by the passive RVACS system and led to safe conditions. In general, all the comments already given about ULOHS are still valid here: the behavior of the system is optimal but some attention must be paid over solidification of the coolant, which would compromise the further utilization of the reactor. Anyway, thanks to the very slow dynamics dominated by radiative heat transfer, human intervention taking place within 10 days can take full control of the system avoiding any lead freezing. At the end of the simulation (11.6 days) lead temperature in the cold pool (approximately 350 °C) is still higher than the melting point. Nevertheless, thermal radiation alone underestimates the real cooling capability of the RVACS, which would significantly enhance if external natural convection is modeled. Due to primary system temperatures lowering, eventually HL free surface level decreases.

Regarding the safety margins to fuel melting and cladding tube creep rupture, this transient is not a concern at all because the system is effectively cooled down. This is true even

though cladding temperature in peak assembly (blue curve in Figure 3.17h) undergoes a steep increase beyond the second threshold at 763 °C. In fact, it must be remembered that fuel and cladding temperatures in the peak assembly are calculated through algebraic equations neglecting their own dynamics (Subsection 3.2.1). This conservative assumption does not represent correctly the transient; only the steady-state values are correct. Also, it has to be reminded that thermal creep is a time-dependent phenomenon: cladding temperature above the second thresholds for a short time interval should not give any problem. Nevertheless, the overcoming of the second threshold is surely a general indicator that needs further analysis.

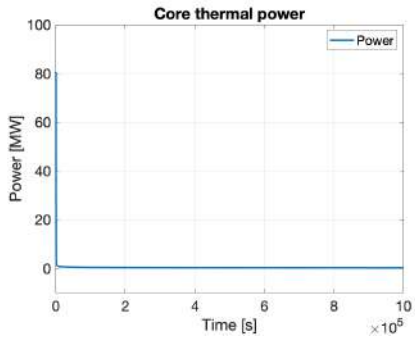

(a) Core thermal power.

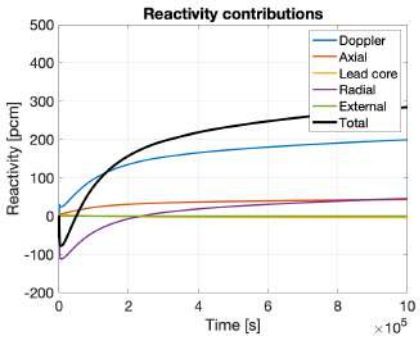

(b) Reactivity contributions.

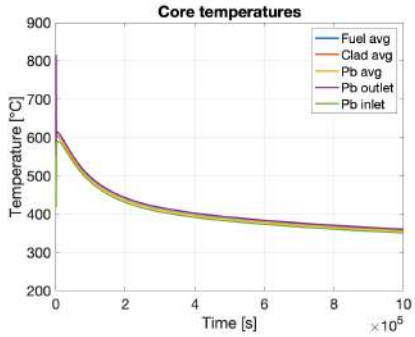

(c) Core temperatures.

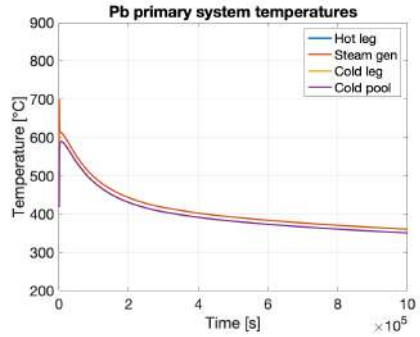

(d) Primary system temperatures.

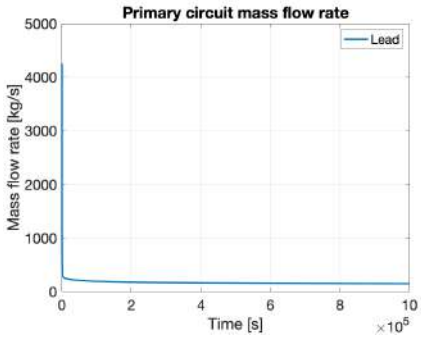

(e) Lead mass flow rate.

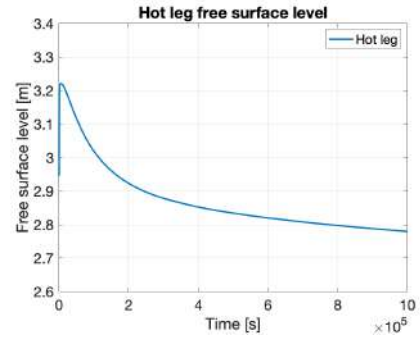

(f) HL free surface level.

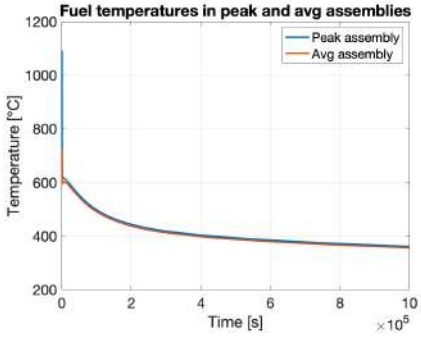

(g) Fuel temperature in the peak** and average* assemblies.

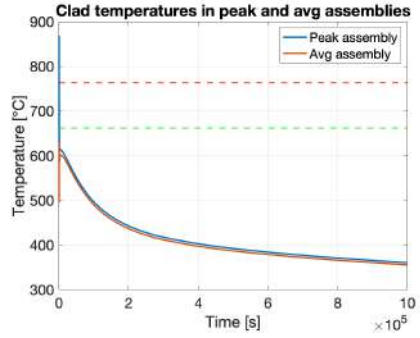

(h) Cladding temperature in the peak** and average* assemblies.

Figure 3.19: Main plots resulting from ULOF-ULOHS combined simulation with simulation time equal to 1000000 s (278 hours or 11.6 days).

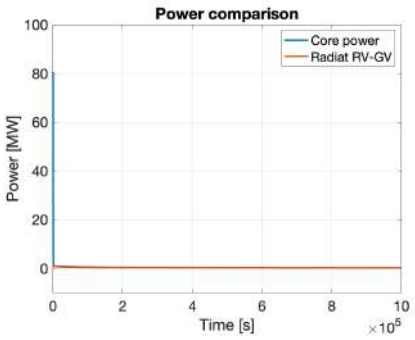

(a) Decay and radiation power.

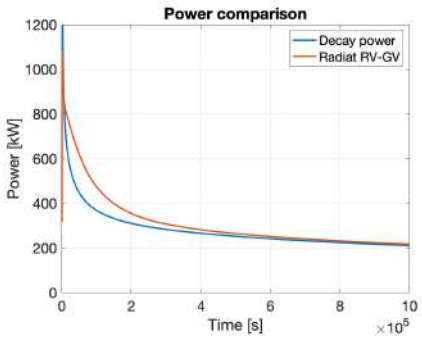

(b) Zoom on decay and radiation power.

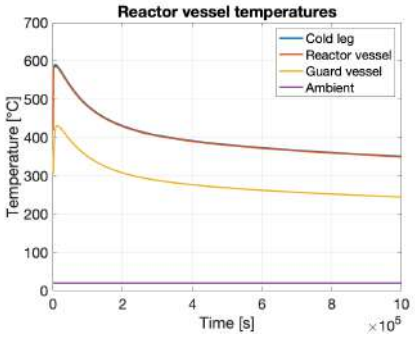

(c) Vessel temperatures.

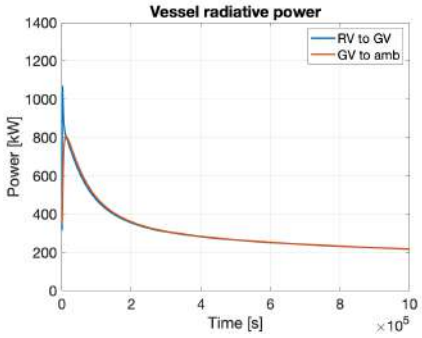

(d) Radiative power (losses).

Figure 3.20: Additional plots resulting from ULOF-ULOHS combined simulation with simulation time equal to 1000000 s (278 hours or 11.6 days).

Table 3.12 lists the value of the main variables of interest after ULOF-ULOHS simulation.

Quantity (unit)	Value (1.1 h)	Variation (1.1 h)	Value (11.6 d)	Variation (11.6 d)
Core thermal power (kW)	1070	-98.7%	211	-99.7%
Fuel average temperature* (°C)	603.3	-6.3%	356.1	-44.7%
Fuel max temperature** (°C)	618.9	-28.7%	361.4	-58.4%
Clad average temperature* (°C)	601.4	+21.2%	355.6	-28.4%
Clad max temperature** (°C)	614.8	+9.8%	360.3	-35.6%
Lead core average temperature (°C)	601.2	+24.0%	355.5	-26.7%
Lead core inlet temperature (°C)	587.8	+40.1%	350.8	-16.4%
Lead core outlet temperature (°C)	614.9	+11.8%	360.4	-34.5%
Lead mass flow rate (kg/s)	278.4	-93.4%	149.8	-96.5%
HL free surface level (m)	3.220	+9.3%	2.780	-5.7%
SG thermal power removal (MW)	0	-100%	0	-100%
Radiative power losses from the RV*** (kW)	971	+204.3%	217	-32.1%

Table 3.12: Values of the most important quantities simulated with BELLA after ULOF-ULOHS combined. For the starred parameters look at the notes after Table 3.8.

3.5. Conclusions

This chapter has focused on the modeling of the reactor core and of the rest of the primary system. A lumped code, namely BELLA, is presented and discussed in depth. The basic assumptions are listed and explained not only from the theoretical point of view but also while describing the simulations of SUNRISE-LFR: in this way it is perhaps easier to the reader to better understand the implications of the rationale behind BELLA.

Four accidental scenarios are simulated and discussed by means of plots and tables in the dedicated subsections. This conclusive section is not meant to give specific comments about those transient because that is already done, but general considerations about the code and the design of the reference reactor.

As a general overview, BELLA is capable of correctly sustaining steady-state conditions of an LFR and of simulating severe accidental transients. Each simulation seems to

have physically reasonable results and explanations of the complex relations between the variables of interest. This is clearly a first important goal of this chapter.

Some improvements of BELLA to simulate even more realistic and accurate conditions can be implemented. For instance, even though 8 groups of neutron precursors are a very good approximation of neutronics, more groups can be considered to achieve a better resolution of neutron spectrum. Again in neutronics, fission products groups used to calculate the decay power come from thermal reactors database; considering parameters coming from fast reactor, as well as fission products of other fissionable nuclides besides ^{235}U, can surely increase the accuracy of the decay power.
In thermal-hydraulics the improvements can go in different directions. Cladding can be modeled considering both 15-15Ti and Fe-10Cr-4Al-RE layers. Primary circuit pressure losses should include additional terms, such as concentrated pressure losses in the steam generator or due to lead flow from the central hot leg to the annular cold leg (and viceversa). Moreover, RVACS needs to incorporate also natural convection, which speeds up the dynamics and gives a new contribution in passive reactor cooling (but also in thermal losses).
However, the two most important contributions might come from including a thermomechanical module of the fuel, which accounts for both thermal effects and fuel burn-up affecting several properties of the fuel rods (thermal conductivity, swelling, fuel gap composition, etc.), and a model of the secondary circuit starting from the steam generator module, at present represented by a couple of extremely simplified algebraic equations. Fuel thermomechanical module is currently being developed at KTH and has the ambition to be finished and operative by August 2022. For what concerns the secondary side, a major topic of this manuscript, it is developed and discussed in depth in Chapter 4.

Coming back to BELLA, not only the general code can be improved, but also the accidental scenarios can be modeled differently: for instance, UTOP, ULOF and ULOHS can be coupled in various ways, even without assuming the worst conditions in the failure of components (e.g., 0.1 $ reactivity insertion with partial ULOHS). Furthermore, both in ULOF and ULOHS additional pressure losses can be included as a consequence of failure of pumps and SGs.

Last comments are devoted to the general results of the simulations and to SUNRISE-LFR capability of maintaining safe conditions. As said, the dedicated subsections goes into details of the scenarios results. SUNRISE-LFR shows important capacity of resisting to severe accidents. This is in particular true when fuel melting is taking as a reference: excellent properties of uranium nitride and passive safety mechanisms (natural circulation and RVACS) give to the system a high degree of inherent safety which keeps the margin

to the melting point always very large.
A more complex situation comes up when fuel cladding safety margin is monitored. On the one hand, ULOHS and ULOF-ULOHS do not show any problem in the long-term cladding temperature, below the first threshold (662 °C) in both cases; in ULOF-ULOHS the two thresholds are overcome by peak assembly cladding temperature right after the accident is triggered, but, as said, out of steady-state conditions the equations implemented are not physically correct (they neglect cladding time constant) and, also, thermal creep rupture takes place only when cladding stays at high temperature for a long time (days as an order of magnitude). On the other hand, UTOP and ULOF show some bad behavior. The first is characterized by a cladding temperature in the peak assembly which overcomes the first threshold and it remains there after the transient is finished; this should not be a big issue for thermal creep, but for sure a better investigation both on thermal creep at lower temperatures and on power and temperatures spacial profile (1, 2 or 3-dimensional) may be suggested. ULOF represents the most problematic transient: cladding temperature in the peak assembly results to be larger than the second threshold (763 °C) for almost the whole simulation time and, in particular, at the final steady-state conditions. This is a major concern because it may compromise the integrity of the fuel pins in the peak assembly. In addition, ULOF calculates that the cold lead inside the system approaches the melting point and stabilizes to no more than 30 °C above it: this second problem is again of big concern. Without any doubt, ULOF transient requires a deep investigation adopting accurate reference codes.

Anyway, it has to be remembered that these transients are simulated adopting strong hypotheses that in some scenarios may be unrealistic, especially when it comes to thermal creep thresholds (Section 2.2) or to the assumed constant power removal by the steam generator. Regarding the latter, Chapter 5 allows to understand the differences when the SG module is explicitly modeled.
As a last remark, these are severe accidental scenarios whose likelihood of occurring is regarded to be extremely low. They assume the failure of all ten steam generators or all ten primary pumps, or even the two together, without conceiving human intervention nor automatic control action of the reactor, whose conditions are thus stressed as much as possible. But this is exactly what design basis accidents are supposed to be and their simulation is extremely important in understanding the behavior of the nuclear system under low-probable but severe scenarios.

4 | Steam generator modeling and simulations

Among the goals of this thesis work, the improvement of BELLA by means of a more realistic model for the steam generator (SG) is envisaged. It is part of the larger target of modeling the whole secondary system of lead-cooled fast reactors and here it is done with reference to SUNRISE-LFR.

This chapter is composed of six sections. Section 4.1 recaps the layout of the SG foreseen in SUNRISE-LFR. Section 4.2 discusses different ways of approaching two-phase flows in SGs. Section 4.3 is dedicated to the moving boundary approach, chosen for this work; it discusses assumptions and derives equations. Section 4.4 shows the implementation of the model in Simulink. Section 4.5 presents some reference simulations to test the SG module standalone. Lastly, Section 4.6 delineates some conclusions.

4.1. Real SG module

SUNRISE-LFR features ten steam generator modules, patented by L. Cinotti in 2013 [59]. They are in charge of the thermal power removal in the 80 MWth reactor, which means that each unit removes 8 MWth by heating up the secondary fluid, water. A single module comprises both the actual steam generator and a pump, located in cold lead at the outlet of the SG, to increase longevity. The steam generator is made of 15 identical, spirally-coiled tubes stacked one above the other in a staggered way (Figures 4.1a and 4.1b). Water is flowing inside the tube bundles from the periphery to the central part, while lead flows radially in the shell from the inner part to the periphery (Figure 4.2a illustrates the flow scheme).
In each single SG lead enters at 550 °C and exits at 420 °C with a mass flow rate equal to 424.3 kg/s. In the secondary side, subcooled water enters at 340 °C and exits in superheated conditions at 530 °C. It is at 16.5 MPa and has a total mass flow rate equal to 4.46 kg/s.

The material adopted in the steam generator is Fe-10Cr-4Al-RE in order to cope with corrosion issues. In Table 4.2 all dimensions regarding the steam generator are listed.

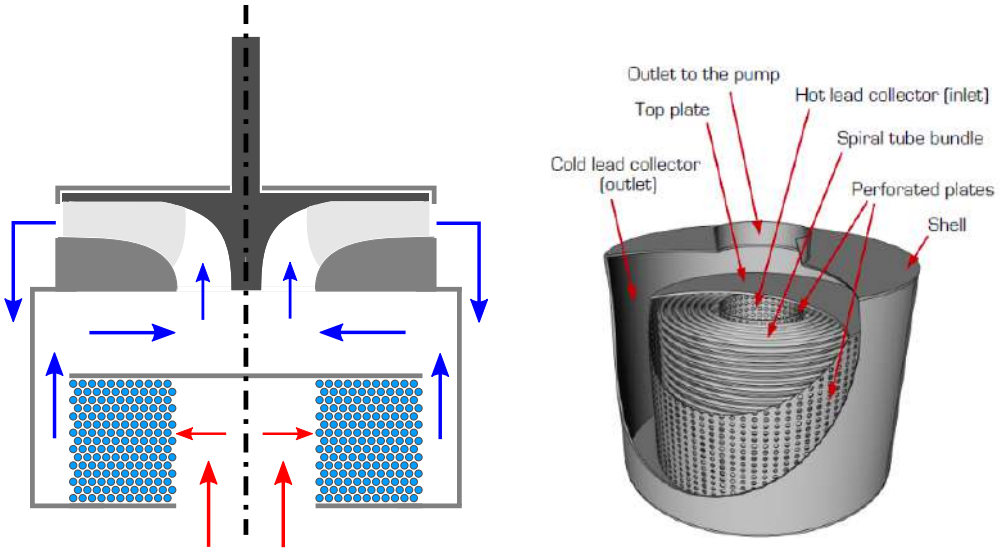

(a) Vertical section [48].

(b) 3D representation. Reproduced with the permission of LeadCold.

Figure 4.1: SG and pump module.

Parameter	Value	Unit
Power removed	8	MW
Water inlet temperature	340	°C
Water outlet temperature	530	°C
Water pressure	16.5	MPa
Water mass flow rate	4.46	kg/s
Lead inlet temperature	550	°C
Lead outlet temperature	420	°C
Lead mass flow rate	424.3	kg/s

Table 4.1: SUNRISE-LFR steam generator nominal conditions.

Parameter	Value	Unit
No. units	10	-
No. spiral tubes per unit	15	-
Tubes material	Fe-10Cr-4Al-RE	-
Tubes internal diameter	10.7	mm
Tubes external diameter	12.7	mm
Tubes pitch	15.2	mm
No. spirals of the tubes	11	-
First spiral radius	0.112	m
Last spiral radius	0.280	m
SG elevation from the top of the core	2.47	m
SG tubes stack height	0.200	m

Table 4.2: SUNRISE-LFR steam generator and pump module main parameters.

4.2. Notes on modeling approaches

As described in Chapter 3, BELLA current version incorporates a very simplified SG model. It implements two mutually exclusive equations, which assume either constant temperature difference or constant power removal:

$$T_{Pb}^{SG,out} = T_{Pb}^{SG,in} - \Delta T_{Pb}^{SG} \tag{4.1}$$

$$T_{Pb}^{SG,out} = T_{Pb}^{SG,in} - \frac{\dot{Q}_{SG}}{\dot{m}_{Pb}^{SG} c_{Pb}} \tag{4.2}$$

As a consequence, the SG is a static component totally independent of the conditions of the reactor primary system.

The large limits of this approach may be overcome in different ways according to the level of accuracy, and subsequent computational load, desired. Due to the complex geometry of the spiral tubes and of the cross-flow pattern between the two fluids, only a 3-dimensional approach can respect the configuration of the real component. For instance, CFD (computational fluid dynamics) investigates the physical phenomena in a 3-dimensional mesh with high spacial resolution. The computational cost is intense, but a complete simulation of the SG dynamics can be achieved. However, the final goal is to integrate the SG model within BELLA, a high-speed lumped code, and, hence, it would be senseless to develop a

3-D, low-speed CFD code.

In order to build a model compatible with BELLA, a simplification of the SG geometry must be carried out. First of all, spirally-coiled tubes are reduced to straight, concentric tubes with water flowing inside and lead outside. Then, the complex 3-D cross-flow pattern is replaced by a 1-D counter-current flow configuration (Figure 4.2). The latter is preferred over co-current flow configuration because of the general direction of the two fluids in the real component: lead is flowing toward the periphery while water is flowing toward the central part, thus making the counter-current option more suitable.

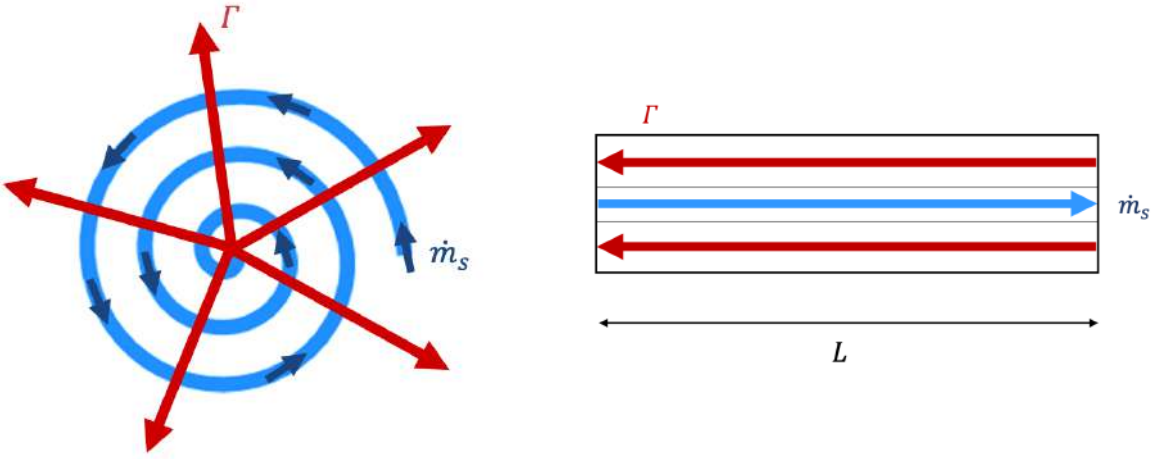

(a) Real (spiral) tube. (b) Approximated (straight) tube.

Figure 4.2: Lead (red) and water (blue) flow pattern for the real and the approximated SG at comparison.

Tubes inner and outer diameters are kept equal to those of the real SG, thus maintaining the same values for water flow area and wall thickness. On the other hand, lead flow area is more difficult to assess, also because in the real component it increases along radial direction (cylindrical area is proportional to the radius), while in the approximated straight tubes it is uniform along the flow axis. Although an average value between the 11 spirals cylindrical areas could be used, in this work lead flow area is not derived from geometrical parameters but from the erosion constraint: in order to keep some margin from it, nominal lead flow velocity inside the tubes is fixed at a value slightly lower than 1.5 m/s and then the flow area is calculated from lead mass flow rate and density. The

following equations show how flow areas for a single tube are computed:

$$A_s = \frac{\pi D_{in}^2}{4} \quad \text{(water)} \tag{4.3}$$

$$A_w = \frac{\pi (D_{out}^2 - D_{in}^2)}{4} \quad \text{(wall)} \tag{4.4}$$

$$A_p = f(r) = \frac{\dot{m}_{Pb}^{SG}}{N_{tubes} \rho_{Pb} v_{Pb}} \quad \text{(lead)} \tag{4.5}$$

A better calculation of the average lead flow area can be derived after the CAD model of the SG is developed.

As a modeling approach, this 1-dimensional system can be described in terms of distributed-parameter methods. They divide the axial length in slices (1-D mesh) and apply conservation equations in each slice, solved by finite difference methods for instance. Then, fluids conditions are computed and the boundaries between the three SG regions (subcooled, saturated and superheated) are identified. Some complexity may rise when the boundary between two regions is exactly in the middle of one slice, but this can be coped by increasing the mesh resolution.
However, it is not convenient to increase the spacial resolution of the SG to achieve high-level accuracy in single-phase regions temperature profile while the rest of the code (reactor primary system) is kept zero-dimensional. In fact, in order to be as consistent as possible to BELLA, it is preferable to implement a lumped-parameter method which is still capable of simulating the dynamics of the three regions. These considerations led to the moving boundary approach, a zero-dimensional model which allows to track the time-dependent lengths of the SG three regions. It permits to easily simulate accidental conditions while monitoring the amount of water and steam inside the SG. Moreover, literature claims that it is numerically faster compared to discretized models and very robust to sudden changes in the boundary conditions [73]. Section 4.3 describes it in detail by deriving the equations.

But before addressing the moving boundary model, a couple of additional considerations need to be discussed.
First of all, in SUNRISE-LFR ten steam generators are present with 15 tubes each. Here it is decided to neglect any possible difference among the 10 steam generators and among the 15 tubes in order to model a unique once-through tube assumed to be in the average conditions. Thus, power removed and fluids mass flow rates are referred to a single tube and then have values equal to 1/15 of the SG ones. Table 4.3 summarizes the single tube working conditions. Inlet and outlet temperatures do not change.

Quantity	Reactor	Single SG	Single tube
Removed power (MW)	80	8	0.533
Water mass flow rate (kg/s)	4243	424.3	28.29
Lead mass flow rate (kg/s)	44.61	4.46	0.297

Table 4.3: SUNRISE-LFR steam generator nominal conditions. Last column (Single tube) is adopted in the model.

A second important consideration is about the modeling of the saturated region, where liquid water and steam are present at the same time. Appendix C discusses possible approaches to it. In this work a homogenous equilibrium model (HEM) is considered where the average (volumetric) void fraction $\overline{\gamma}$ is calculated starting from the saturated density ratio η as:

$$\overline{\gamma} = (1+\eta)\left[1-\eta\,\ln\left(1+\frac{1}{\eta}\right)\right] \tag{4.6}$$

$$\eta = \frac{\rho_{s,g}}{\rho_{s,l}-\rho_{s,g}} \tag{4.7}$$

being $\rho_{s,g}$ and $\rho_{s,l}$ the density of saturated vapor and of saturated liquid water, respectively.

As a conclusive remark of this section, the author is aware of the approximations that are introduced hereabove, although their effects have not been quantified. It could be an interesting future work that can be done together with the code verification against some benchmarks (e.g., RELAP) and with its validation by testing the real SG in an experimental facility (among the scope of the SOLSTICE project, Section 2.1).

4.3. Moving boundary approach

The moving boundary model [47, 63, 73] is the choice for the dynamical simulation of the steam generator in BELLA. It consists in a lumped-parameter approach where three regions of length L_1, L_2 and L_3 and same cross-section A are characterized by uniform thermodynamic conditions. Each region corresponds to each phase of water: subcooled (1), saturated (2) and superheated (3).
The model utilizes mass and energy conservation, together with Leibniz' rule to approximate PDEs with ODEs, to derive all dynamical equations for water, lead and wall. In this way, wall and fluids temperatures and water mass flow rate are calculated in every region.

Momentum balance equation is not encompassed and neither are pressure drops; pressure is only determined by the outlet water mass flow rate and a valve admission coefficient. Since the valve is always kept open, pressure is constant.

The method leverages on some basics assumptions, besides the ones already discussed in Section 4.2. They are all here summarized:

- Simplification of the geometry.
- Lumped-parameter approach: uniform temperature and average thermo-physical properties in each region.
- One-dimensional flow in axial direction z.
- Uniform flow in the cross-section perpendicular to axial direction.
- Homogeneous and equilibrium model (HEM) for the two-phase flow (Appendix C).
- Constant and uniform pressure P.
- Instantaneous dynamics for $T_{w,p}$ and $T_{w,s}$ temperatures (steady-state energy balance).
- Adiabatic or frozen-mode approximation for some fluid properties (e.g., lead and wall densities and specific heat capacities, water average void fraction): they are in general time-dependent but their time derivative is not explicitly accounted.

Before showing the equations, some notation. All temperatures are denoted by subscripts: firstly a letter to indicate the substance (s for water, p for lead and w for wall), then a number to indicate the region in the SG (1 for subcooled, 2 for saturated and 3 for superheated). To avoid confusion, lead mass flow rate is renamed in this context $\Gamma = \frac{\dot{m}_{Pb}^{SG}}{N_{tubes}}$, while $\dot{m}_s$ or $\dot{m}$ is adopted for water mass flow rate. Figure 4.3 helps in understanding the configuration.

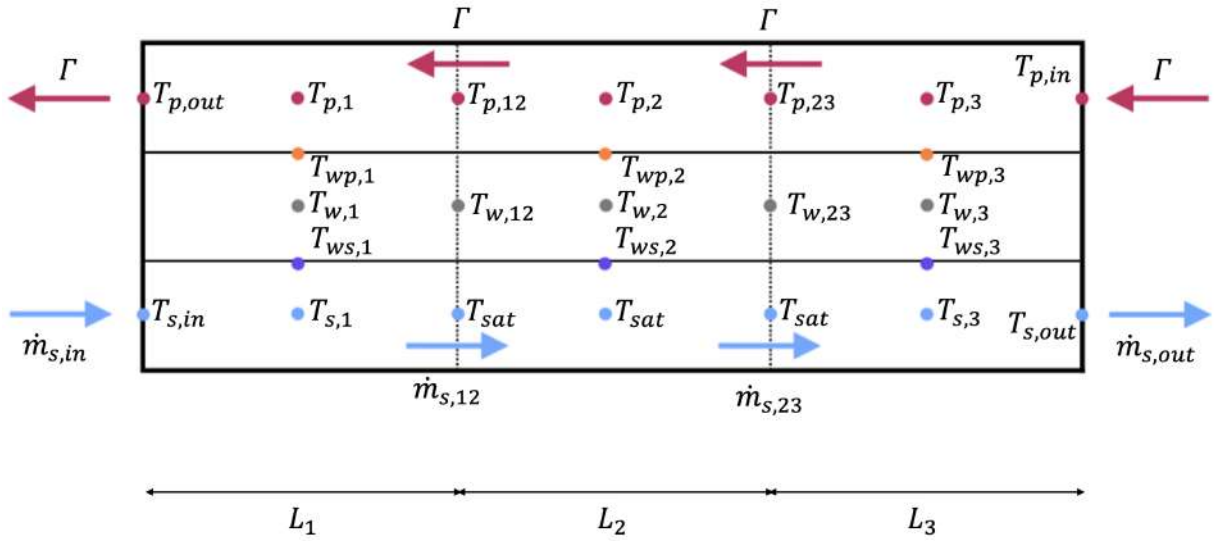

Figure 4.3: Scheme of the regions and of the notation for the SG moving boundary model. Blue is water, red is lead and gray is wall; violet and orange are wall in contact with water and with lead, respectively.

Each region is identified by the average temperature (e.g., $T_{p,1}$) and by the boundary temperatures (e.g., $T_{p,in}$ and $T_{p1,2}$).

At this point, equations. The model is derived from first principle mass and energy balance:

$$\frac{\partial \rho}{\partial t} + \nabla \cdot (\rho \vec{u}) = 0 \tag{4.8}$$

$$\frac{\partial \rho h}{\partial t} + \nabla \cdot (\rho h \vec{u}) = -\nabla \cdot \vec{q''} - q''' + \frac{DP}{Dt} + \phi \tag{4.9}$$

which, for a 1-dimensional system and separating water, lead and wall, reduce to:

$$\frac{\partial A\rho}{\partial t} + \frac{\partial \dot{m}}{\partial z} = 0 \tag{4.10}$$

$$A_s \frac{\partial(\rho h - P)}{\partial t} + \frac{\partial \dot{m} h}{\partial z} = \pi D_{in} \alpha_s (T_w - T_s) \tag{4.11}$$

$$A_p \frac{\partial(\rho_p c_p T_p)}{\partial t} + \Gamma \frac{\partial(c_p T_p)}{\partial z} = -\pi D_{out} \alpha_p (T_p - T_w) \tag{4.12}$$

$$A_w \rho_w c_w \frac{\partial T_w}{\partial t} = \pi D_{out} \alpha_p (T_p - T_w) - \pi D_{in} \alpha_s (T_w - T_s) \tag{4.13}$$

being h enthalpy $\left(\frac{J}{kg}\right)$, ρ density $\left(\frac{kg}{m^3}\right)$, c specific heat capacity $\left(\frac{J}{kg \cdot K}\right)$, α heat transfer coefficient $\left(\frac{W}{m^2 \cdot K}\right)$.

In order to move from PDEs (both time t and length z derivatives) to ODEs (only time t derivative) Leibniz' rule is utilized:

$$\frac{d}{dt}\int_{z_1}^{z_2} f(z,t)dz = f(z_2,t)\frac{dz_2}{dt} - f(z_1,t)\frac{dz_1}{dt} + \int_{z_1}^{z_2}\frac{\partial}{\partial t}f(z,t)dz \tag{4.14}$$

which, applied to Eq.s (4.10, 4.11, 4.12, 4.13), eventually leads to:

$$A_s\left[\frac{d}{dt}\big(\overline{\rho}(z_2-z_1)\big) + \rho(z_1,t)\frac{dz_1}{dt} - \rho(z_2,t)\frac{dz_2}{dt}\right] = \dot{m}(z_1,t) - \dot{m}(z_2,t) \tag{4.15}$$

$$\begin{aligned} &A_s\left[\frac{d}{dt}\big(\overline{\rho h}(z_2-z_1)\big) + \rho(z_1,t)h(z_1,t)\frac{dz_1}{dt} - \rho(z_2,t)h(z_2,t)\frac{dz_2}{dt} - (z_2-z_1)\frac{dP}{dt}\right] = \\ &= \dot{m}(z_1,t)h(z_1,t) - \dot{m}(z_2,t)h(z_2,t) + \pi D_{in}(z_2-z_1)\overline{\alpha}_s(\overline{T}_{ws} - \overline{T}_s) \end{aligned} \tag{4.16}$$

$$\begin{aligned} &A_p\overline{\rho}_p\overline{c}_p\left[\frac{d}{dt}\big(\overline{T}_p(z_2-z_1)\big) + T_p(z_1,t)\frac{dz_1}{dt} - T_p(z_2,t)\frac{dz_2}{dt}\right] = \\ &= \Gamma\overline{c}_p\big(T_p(z_2,t) - T_p(z_1,t)\big) - \pi D_{out}(z_2-z_1)\overline{\alpha}_p(\overline{T}_p - \overline{T}_{wp}) \end{aligned} \tag{4.17}$$

$$\begin{aligned} &A_w\overline{\rho}_w\overline{c}_w\left[\frac{d}{dt}\big(\overline{T}_w(z_2-z_1)\big) + T_w(z_1,t)\frac{dz_1}{dt} - T_w(z_2,t)\frac{dz_2}{dt}\right] = \\ &= \pi D_{out}(z_2-z_1)\overline{\alpha}_p(\overline{T}_p - \overline{T}_{wp}) - \pi D_{in}(z_2-z_1)\overline{\alpha}_s(\overline{T}_{ws} - \overline{T}_s) \end{aligned} \tag{4.18}$$

In the previous passage the adiabatic or frozen-mode approximation has been exploited on ρ_p, c_p, ρ_w and c_w, assuming that those properties are time-dependent but with a negligible time-derivative with respect to the other terms. To check the validity of the approximation, the relative variation rates of those properties need to be compared to the relative variation rates of their corresponding temperatures, and they need to satisfy:

$$\frac{1}{\overline{\rho}_p}\frac{d\overline{\rho}_p}{dt}\ ,\quad \frac{1}{\overline{c}_p}\frac{d\overline{c}_p}{dt} \quad \ll \quad \frac{1}{\overline{T}_p}\frac{d\overline{T}_p}{dt} \tag{4.19}$$

$$\frac{1}{\overline{\rho}_w}\frac{d\overline{\rho}_w}{dt}\ ,\quad \frac{1}{\overline{c}_w}\frac{d\overline{c}_w}{dt} \quad \ll \quad \frac{1}{\overline{T}_w}\frac{d\overline{T}_w}{dt} \tag{4.20}$$

The results of simulations are in general accordance with this approximation, especially when it comes to lead properties. However, although wall properties variation rates are almost always lower than wall temperature variations rates, they are in the same order of magnitude. Figures 4.4a and 4.4b show the general trend for lead properties and wall properties.

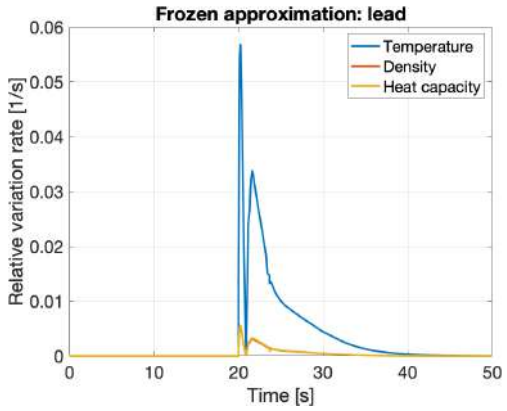

(a) Lead well satisfies the frozen-mode approximation.

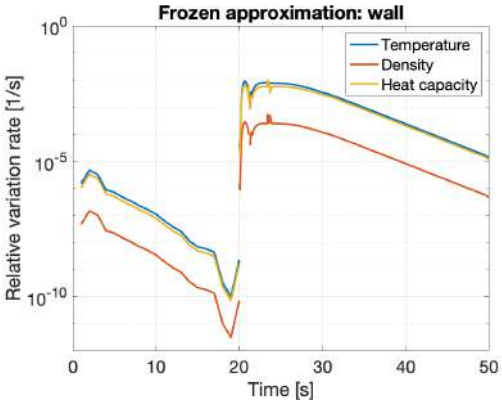

(b) Wall thermal heat capacity has a boundary behavior (note that y axis is logarithmic).

Figure 4.4: Relative variations rates for lead and wall properties in saturated region under a transient in which $T_{p,in}$ increases by 20%.

Then, the approximation must be considered with some caution.

Next subsections show the equations implemented in water, lead and wall sides.

4.3.1. Water side

A water thermodynamic state is defined by two thermodynamic quantities, e.g. P and h_s or P and T_s. In saturated conditions, the state is defined only by pressure P. The three regions equations are hereafter derived starting from Eq.s (4.10) and (4.11).

Subcooled region

Mass and energy balance equations:

$$A_s \left[\frac{d}{dt}(\rho_{s1} L_1) - \rho_{s,l} \frac{dL_1}{dt} \right] = \dot{m}_{in} - \dot{m}_{1,2} \tag{4.21}$$

$$\begin{aligned} A_s \left[\frac{d}{dt}(\rho_{s1} h_{s1} L_1) - \rho_{s,l} h_{s,l} \frac{dL_1}{dt} - L_1 \frac{dP}{dt} \right] &= \dot{m}_{in} h_{s,in} - \dot{m}_{1,2} h_{s,l} + \\ &+ \pi D_{in} L_1 \alpha_{s1} (T_{w,s1} - T_{s1}) \end{aligned} \tag{4.22}$$

Separating all terms:

$$A_s\left[(\rho_{s1}-\rho_{s,l})\frac{dL_1}{dt}+L_1\frac{d\rho_{s1}}{dt}\right] = \dot{m}_{in}-\dot{m}_{1,2} \tag{4.23}$$

$$A_s\left[(\rho_{s1}h_{s1}-\rho_{s,l}h_{s,l})\frac{dL_1}{dt}+L_1h_{s1}\frac{d\rho_{s1}}{dt}+\rho_{s1}L_1\frac{dh_{s1}}{dt}-L_1\frac{dP}{dt}\right] = \tag{4.24}$$
$$= \dot{m}_{in}h_{s,in}-\dot{m}_{1,2}h_{s,l}+\pi D_{in}L_1\alpha_{s1}(T_{w,s1}-T_{s1})$$

and considering that:

$$h_{s1} = \frac{h_{s,in}+h_{s,l}}{2} \tag{4.25}$$

$$\rho_{s1} = \rho(h_{s1},P) \tag{4.26}$$

$$h_{s,l} = h(P) \tag{4.27}$$

the equations become:

$$A_s\left[(\rho_{s1}-\rho_{s,l})\frac{dL_1}{dt}+\frac{1}{2}L_1\frac{\partial\rho_{s1}}{\partial h}\bigg|_P\frac{dh_{s,in}}{dt}+L_1\left(\frac{1}{2}\frac{\partial\rho_{s1}}{\partial h}\bigg|_P\frac{\partial h_{s,l}}{\partial P}+\frac{\partial\rho_{s1}}{\partial P}\bigg|_h\right)\frac{dP}{dt}\right] = \tag{4.28}$$
$$= \dot{m}_{in}-\dot{m}_{1,2}$$

$$A_s\Bigg\{(\rho_{s1}h_{s1}-\rho_{s,l}h_{s,l})\frac{dL_1}{dt}+\frac{1}{2}L_1\left(h_{s1}\frac{\partial\rho_{s1}}{\partial h}\bigg|_P+\rho_{s1}\right)\frac{dh_{s,in}}{dt}+ \tag{4.29}$$
$$+L_1\left[\frac{1}{2}\left(h_{s1}\frac{\partial\rho_{s1}}{\partial h}\bigg|_P+\rho_{s1}\right)\frac{\partial h_{s,l}}{\partial P}+h_{s1}\frac{\partial\rho_{s1}}{\partial P}\bigg|_h-1\right]\frac{dP}{dt}\Bigg\} =$$
$$= \dot{m}_{in}h_{s,in}-\dot{m}_{1,2}h_{s,l}+\pi D_{in}L_1\alpha_{s1}(T_{w,s1}-T_{s1})$$

Saturated region

Mass and energy balance equations:

$$A_s\left[\frac{d}{dt}(\rho_{s2}L_2)+\rho_{s,l}\frac{dL_1}{dt}-\rho_{s,g}\frac{d(L_1+L_2)}{dt}\right] = \dot{m}_{1,2}-\dot{m}_{2,3} \tag{4.30}$$

$$A_s\left[\frac{d}{dt}(\overline{\rho h}L_2)+\rho_{s,l}h_{s,l}\frac{dL_1}{dt}-\rho_{s,g}h_{s,g}\frac{d(L_1+L_2)}{dt}-L_2\frac{dP}{dt}\right] = \tag{4.31}$$
$$= \dot{m}_{1,2}h_{s,l}-\dot{m}_{2,3}h_{s,g} + \pi D_{in}L_2\alpha_{s2}(T_{w,s2}-T_{s2})$$

Separating all terms:

$$A_s\left[(\rho_{s,l}-\rho_{s,g})\frac{dL_1}{dt}+(\rho_{s2}-\rho_{s,g})\frac{dL_2}{dt}+L_2\frac{d\rho_{s2}}{dt}\right] = \dot{m}_{1,2}-\dot{m}_{2,3} \tag{4.32}$$

$$A_s\left[(\rho_{s,l}h_{s,l}-\rho_{s,g}h_{s,g})\frac{dL_1}{dt}+(\overline{\rho h}-\rho_{s,g}h_{s,g})\frac{dL_2}{dt}+L_2\frac{d\overline{\rho h}}{dt}-L_2\frac{dP}{dt}\right] = \dot{m}_{1,2}h_{s,l}-\dot{m}_{2,3}h_{s,g}+\pi D_{in}L_2\alpha_{s2}(T_{w,s2}-T_{s2}) \tag{4.33}$$

and considering that:

$$\rho_{s2} = \frac{1}{L_2}\int_{L_1}^{L_2}\rho dz=\overline{\gamma}\rho_{s,g}+(1-\overline{\gamma})\rho_{s,l} \tag{4.34}$$

$$\overline{\rho h} = \frac{1}{L_2}\int_{L_1}^{L_2}\rho h dz=\overline{\gamma}\rho_{s,g}h_{s,g}+(1-\overline{\gamma})\rho_{s,l}h_{s,l} \tag{4.35}$$

$$\rho_{s,g},\ \rho_{s2},\ \rho_{s,l},\ h_{s,g},\ h_{s,l},\ \overline{\gamma}=f(P) \tag{4.36}$$

with the average void fraction $\overline{\gamma}$ as in Eq. 4.6 (HEM) and assumed to have a negligible time-derivative (frozen-mode approximation is perfectly satisfied since pressure P in always constant), the equations become:

$$A_s\left[(\rho_{s,l}-\rho_{s,g})\frac{dL_1}{dt}+(1-\overline{\gamma})(\rho_{s,l}-\rho_{s,g})\frac{dL_2}{dt}+L_2\left(\overline{\gamma}\frac{\partial\rho_{s,g}}{\partial P}+(1-\overline{\gamma})\frac{\partial\rho_{s,l}}{\partial P}\right)\frac{dP}{dt}\right] = \dot{m}_{1,2}-\dot{m}_{2,3} \tag{4.37}$$

$$A_s\left[(\rho_{s,l}h_{s,l}-\rho_{s,g}h_{s,g})\frac{dL_1}{dt}+(1-\overline{\gamma})(\rho_{s,l}h_{s,l}-\rho_{s,g}h_{s,g})\frac{dL_2}{dt}+\right.$$
$$\left.+L_2\left(\overline{\gamma}h_{s,g}\frac{\partial\rho_{s,g}}{\partial P}+\overline{\gamma}\rho_{s,g}\frac{\partial h_{s,g}}{\partial P}+(1-\overline{\gamma})h_{s,l}\frac{\partial\rho_{s,l}}{\partial P}+(1-\overline{\gamma})\rho_{s,l}\frac{\partial h_{s,l}}{\partial P}-1\right)\frac{dP}{dt}\right] = \dot{m}_{1,2}h_{s,l}-\dot{m}_{2,3}h_{s,g}+\pi D_{in}L_2\alpha_{s2}(T_{w,s2}-T_{s2}) \tag{4.38}$$

Superheated region

Instead of modeling the superheated region into a unique zone as for subcooled and saturated regions, the choice is to divide it into $n_{zones}=2$ sub-regions (Figure 4.5). Two main reasons explain why:

- Considering the working conditions of the reference SG, the superheated region has a very large length L_3 (16 times L_1 and almost 3 times L_2). Average properties poorly represent real conditions over such an extended region. To gain in accuracy, it is suggested to increase the number of regions.

- In some scenarios, it happened that $T_{s,out}$ was larger than $T_{p,in}$, physically impossible. This is in principle allowed by the model because these are boundary temperatures not controlled by the energy balance equations which, instead, contain heat transfer between the average temperatures. In particular, giving the large value of L_3, this happened in scenarios of 20-30% increase of $T_{p,in}$. By considering one additional region this problem is solved.

The increased number of regions does not compromise or change the overall method, which remains consistent with a lumped-parameter approach.
In principle one could even extend n_{zones} beyond 2 to gain further in accuracy. This has not been done in the proposed model although it may be considered as a future direction of improvement. Section 4.6 gives further comments about it.

The two regions in superheated conditions are named region 3 and region 4. They are equally spaced with length named $L_{3i} = L_3/2$ and treated exactly as before starting from Eq.s (4.10) and (4.11).

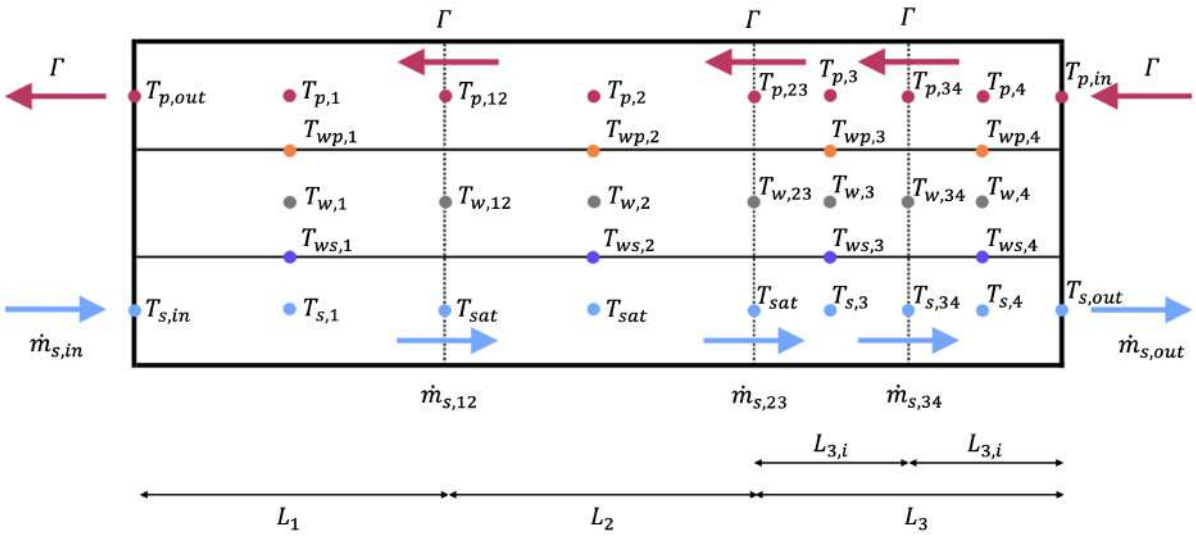

Figure 4.5: Scheme of the regions and of the notation for the SG moving boundary model, employing 2 superheated regions.

Region 3

Mass and energy balance equations:

$$A_s\left[\frac{d}{dt}(\rho_{s3}L_{3,i})+\rho_{s2,3}\frac{d(L_1+L_2)}{dt}-\rho_{s3,4}\frac{d(L_1+L_2+L_{3,i})}{dt}\right] = \dot{m}_{2,3}-\dot{m}_{3,4} \tag{4.39}$$

$$A_s\left[\frac{d}{dt}(\rho_{s3}h_{s3}L_{3,i})+\rho_{s2,3}h_{s2,3}\frac{d(L_1+L_2)}{dt}-\rho_{s3,4}h_{s3,4}\frac{d(L_1+L_2+L_{3,i})}{dt}-L_{3,i}\frac{dP}{dt}\right] = \dot{m}_{2,3}h_{s2,3}-\dot{m}_{3,4}h_{s3,4}+\pi D_{in}L_{3,i}\alpha_{s3}(T_{w,s3}-T_{s3}) \tag{4.40}$$

Separating all terms:

$$A_s\left[(\rho_{s,g}-\rho_{s3,4})\left(\frac{dL_1}{dt}+\frac{dL_2}{dt}\right)+(\rho_{s3}-\rho_{s3,4})\frac{dL_{3,i}}{dt}+L_{3,i}\frac{d\rho_{s3}}{dt}\right] = \dot{m}_{2,3}-\dot{m}_{3,4} \tag{4.41}$$

$$A_s\left[(\rho_{s,g}h_{s,g}-\rho_{s3,4}h_{s3,4})\left(\frac{dL_1}{dt}+\frac{dL_2}{dt}\right)+(\rho_{s3}h_{s3}-\rho_{s3,4}h_{s3,4})\frac{L_{3,i}}{dt}+ +L_{3,i}h_{s3}\frac{d\rho_{s3}}{dt}+L_{3,i}\rho_{s3}\frac{dh_{s3}}{dt}-L_{3,i}\frac{dP}{dt}\right] = \dot{m}_{2,3}h_{s,g}-\dot{m}_{3,4}h_{s3,4}+\pi D_{in}L_{3,i}\alpha_{s3}(T_{w,s3}-T_{s3}) \tag{4.42}$$

and considering that:

$$h_{s3} = \frac{h_{s,g}+h_{s3,4}}{2} \tag{4.43}$$

$$\rho_{s3} = \rho(h_{s3},P) \tag{4.44}$$

$$h_{s,g} = h(P) \tag{4.45}$$

$$L = L_1+L_2+2L_{3,i} \tag{4.46}$$

$$\frac{dL_{3,i}}{dt} = -\frac{1}{2}\left(\frac{dL_1}{dt}+\frac{dL_2}{dt}\right) \tag{4.47}$$

the equations become:

$$A_s\Bigg[(\rho_{s,g}-\rho_{s3,4})\left(\frac{dL_1}{dt}+\frac{dL_2}{dt}\right)+(\rho_{s3}-\rho_{s3,4})\frac{dL_{3,i}}{dt}+\frac{1}{2}L_{3,i}\frac{\partial\rho_{s3}}{\partial h}\bigg|_P\frac{dh_{s3,4}}{dt} \quad + \quad (4.48)$$
$$+L_{3,i}\left(\frac{1}{2}\frac{\partial\rho_{s3}}{\partial h}\bigg|_P\frac{\partial h_{s,g}}{\partial P}+\frac{\partial\rho_{s3}}{\partial P}\bigg|_h\right)\frac{dP}{dt}\Bigg] \quad = \quad \dot{m}_{2,3}-\dot{m}_{3,4}$$

$$A_s\Bigg\{(\rho_{s,g}h_{s,g}-\rho_{s3,4}h_{s3,4})\left(\frac{dL_1}{dt}+\frac{dL_2}{dt}\right)+(\rho_{s3}h_{s3}-\rho_{s3,4}h_{s3,4})\frac{L_{3,i}}{dt} \quad + \quad (4.49)$$
$$+\frac{1}{2}L_{3,i}\left(h_{s3}\frac{\partial\rho_{s3}}{\partial h}\bigg|_P+\rho_{s3}\right)\frac{dh_{s3,4}}{dt} \quad +$$
$$+L_{3,i}\left[\frac{1}{2}\left(h_{s3}\frac{\partial\rho_{s3}}{\partial h}\bigg|_P+\rho_{s3}\right)\frac{\partial h_{s,g}}{\partial P}+h_{s3}\frac{\partial\rho_{s3}}{\partial P}\bigg|_h-1\right]\frac{dP}{dt}\Bigg\} \quad =$$
$$= \quad \dot{m}_{2,3}h_{s,g}-\dot{m}_{3,4}h_{3,4}+\pi D_{in}L_{3,i}\alpha_{s3}(T_{w,s3}-T_{s3})$$

Region 4

Mass and energy balance equations:

$$A_s\left[\frac{d}{dt}(\rho_{s4}L_{3,i})+\rho_{s3,4}\frac{d(L_1+L_2+L_{3,i})}{dt}\right] \quad = \quad \dot{m}_{3,4}-\dot{m}_{out} \quad (4.50)$$

$$A_s\left[\frac{d}{dt}(\rho_{s4}h_{s4}L_{3,i})+\rho_{s3,4}h_{s3,4}\frac{d(L_1+L_2+L_{3,i})}{dt}-L_{3,i}\frac{dP}{dt}\right] \quad = \quad (4.51)$$
$$= \quad \dot{m}_{3,4}h_{s3,4}-\dot{m}_{out}h_{s,out}+\pi D_{in}L_{3,i}\alpha_{s4}(T_{w,s4}-T_{s4})$$

Separating all terms:

$$A_s\left[(\rho_{s3,4}-\rho_{s,out})\left(\frac{dL_1}{dt}+\frac{dL_2}{dt}\right)+(\rho_{s3,4}+\rho_{s4}-2\rho_{s,out})\frac{dL_{3,i}}{dt}+L_{3,i}\frac{d\rho_{s4}}{dt}\right] \quad = \quad (4.52)$$
$$= \quad \dot{m}_{3,4}-\dot{m}_{,out}$$

$$A_s\Bigg[(\rho_{s3,4}h_{s3,4}-\rho_{s,out}h_{s,out})\left(\frac{dL_1}{dt}+\frac{dL_2}{dt}\right)+(\rho_{s4}h_{s4}+\rho_{s3,4}h_{s3,4}-2\rho_{s,out}h_{s,out})\frac{dL_{3,i}}{dt}+ \quad (4.53)$$
$$+L_{3,i}h_{s4}\frac{d\rho_{s4}}{dt}+L_{3,i}\rho_{s4}\frac{dh_{s4}}{dt}-L_{3,i}\frac{dP}{dt}\Bigg] \quad =$$
$$= \quad \dot{m}_{3,4}h_{s3,4}-\dot{m}_{out}h_{s,out}+\pi D_{in}L_{3,i}\alpha_{s4}(T_{w,s4}-T_{s4})$$

and considering that:

$$h_{s4} \quad = \quad \frac{h_{s3,4}+h_{s,out}}{2} \quad (4.54)$$

$$\rho_{s4} \quad = \quad \rho(h_{s4},P) \quad (4.55)$$

the equations become:

$$A_s\Bigg[(\rho_{s3,4}-\rho_{s,out})\left(\frac{dL_1}{dt}+\frac{dL_2}{dt}\right)+(\rho_{s3,4}+\rho_{s4}-2\rho_{s,out})\frac{dL_{3,i}}{dt}+ \tag{4.56}$$
$$+\frac{1}{2}L_{3,i}\frac{\partial\rho_{s4}}{\partial h}\bigg|_P\left(\frac{dh_{s3,4}}{dt}+\frac{dh_{s,out}}{dt}\right)+L_{3,i}\frac{\partial\rho_{s4}}{\partial P}\bigg|_h\frac{dP}{dt}\Bigg] = \dot{m}_{3,4}-\dot{m}_{out}$$
$$A_s\Bigg[(\rho_{s3,4}h_{s3,4}-\rho_{s,out}h_{s,out})\left(\frac{dL_1}{dt}+\frac{dL_2}{dt}\right)+(\rho_{s4}h_{s4}+\rho_{s3,4}h_{s3,4}-2\rho_{s,out}h_{s,out})\frac{dL_{3,i}}{dt}+ \tag{4.57}$$
$$+\frac{1}{2}L_{3,i}\left(h_{s4}\frac{\partial\rho_{s4}}{\partial h}\bigg|_P+\rho_{s4}\right)\left(\frac{dh_{s3,4}}{dt}+\frac{dh_{s,out}}{dt}\right)+L_{3,i}\left(h_{s4}\frac{\partial\rho_{s4}}{\partial P}\bigg|_h-1\right)\frac{dP}{dt}\Bigg] =$$
$$= \dot{m}_{3,4}h_{s3,4}-\dot{m}_{out}h_{s,out}+\pi D_{in}L_{3,i}\alpha_{s4}(T_{w,s4}-T_{s4})$$

4.3.2. Lead side

Lead thermodynamic states are univocally identified by temperatures T_p. The four regions equations are derived starting from Eq (4.12):

$$A_p\rho_{p1}c_{p1}\left[\frac{d}{dt}(T_{p1}L_1)-T_{p1,2}\frac{dL_1}{dt}\right] = \tag{4.58}$$
$$= \Gamma c_{p1}(T_{p1,2}-T_{p,out})-\pi D_{out}L_1\alpha_{p1}(T_{p1}-T_{w,p1})$$
$$A_p\rho_{p2}c_{p2}\left[\frac{d}{dt}(T_{p2}L_2)+T_{p1,2}\frac{dL_1}{dt}-T_{p2,3}\frac{d(L_1+L_2)}{dt}\right] = \tag{4.59}$$
$$= \Gamma c_{p2}(T_{p2,3}-T_{p1,2})-\pi D_{out}L_2\alpha_{p2}(T_{p2}-T_{w,p2})$$
$$A_p\rho_{p3}c_{p3}\left[\frac{d}{dt}(T_{p3}L_{3,i})+T_{p2,3}\frac{d(L_1+L_2)}{dt}-T_{p3,4}\frac{d(L_1+L_2+L_{3,i})}{dt}\right] = \tag{4.60}$$
$$= \Gamma c_{p3}(T_{p3,4}-T_{p2,3})-\pi D_{out}L_{3,i}\alpha_{p3}(T_{p3}-T_{w,p3})$$
$$A_p\rho_{p4}c_{p4}\left[\frac{d}{dt}(T_{p4}L_{3,i})+T_{p3,4}\frac{d(L_1+L_2+L_{3,i})}{dt}\right] = \tag{4.61}$$
$$= \Gamma c_{p4}(T_{p,in}-T_{p3,4})-\pi D_{out}L_{3,i}\alpha_{p4}(T_{p4}-T_{w,p4})$$

Separating all terms the equations become:

$$A_p\rho_{p1}c_{p1}\left[L_1\frac{dT_{p1}}{dt}+(T_{p1}-T_{p1,2})\frac{dL_1}{dt}\right] = \tag{4.62}$$
$$= \Gamma c_{p1}(T_{p1,2}-T_{p,out})-\pi D_{out}L_1\alpha_{p1}(T_{p1}-T_{w,p1})$$
$$A_p\rho_{p2}c_{p2}\left[L_2\frac{dT_{p2}}{dt}+(T_{p1,2}-T_{p2,3})\frac{dL_1}{dt}+(T_{p2}-T_{p2,3})\frac{dL_2}{dt}\right] = \tag{4.63}$$
$$= \Gamma c_{p2}(T_{p2,3}-T_{p1,2})-\pi D_{out}L_2\alpha_{p2}(T_{p2}-T_{w,p2})$$
$$A_p\rho_{p3}c_{p3}\left[(T_{p2,3}-T_{p3,4})\left(\frac{dL_1}{dt}+\frac{dL_2}{dt}\right)+(T_{p3}-T_{p3,4})\frac{dL_{3,i}}{dt}+L_{3,i}\frac{dT_{p3}}{dt}\right] = \tag{4.64}$$
$$= \Gamma c_{p3}(T_{p3,4}-T_{p2,3})-\pi D_{out}L_{3,i}\alpha_{p3}(T_{p3}-T_{w,p3})$$
$$A_p\rho_{p4}c_{p4}\left[(T_{p3,4}-T_{p,in})\left(\frac{dL_1}{dt}+\frac{dL_2}{dt}\right)+(T_{p4}+T_{p3,4}-2T_{p,in})\frac{dL_{3,i}}{dt}+L_{3,i}\frac{dT_{p4}}{dt}\right] =$$
$$= \Gamma c_{p4}(T_{p,in}-T_{p3,4})-\pi D_{out}L_{3,i}\alpha_{p4}(T_{p4}-T_{w,p4}) \tag{4.65}$$

The average temperatures are calculated as:

$$T_{p1} = \frac{T_{p,out}+T_{p1,2}}{2} \tag{4.66}$$
$$T_{p2} = \frac{T_{p1,2}+T_{p2,3}}{2} \tag{4.67}$$
$$T_{p3} = \frac{T_{p2,3}+T_{p3,4}}{2} \tag{4.68}$$
$$T_{p4} = \frac{T_{p3,4}+T_{p,in}}{2} \tag{4.69}$$

4.3.3. Wall side

Wall thermodynamic states are univocally identified by temperatures T_w. The four regions equations are derived starting from Eq (4.13):

$$A_w\rho_{w1}c_{w1}\left[\frac{d}{dt}(T_{w1}L_1) - T_{w1,2}\frac{dL_1}{dt}\right] = \tag{4.70}$$
$$= \pi D_{out}L_1\alpha_{p1}(T_{p1} - T_{w,p1}) - \pi D_{in}L_1\alpha_{s1}(T_{w,s1} - T_{s1})$$
$$A_w\rho_{w2}c_{w2}\left[\frac{d}{dt}(T_{w2}L_2) + T_{w1,2}\frac{dL_1}{dt} - T_{w2,3}\frac{d(L_1+L_2)}{dt}\right] = \tag{4.71}$$
$$= \pi D_{out}L_2\alpha_{p2}(T_{p2} - T_{w,p2}) - \pi D_{in}L_2\alpha_{s2}(T_{w,s2} - T_{s2})$$
$$A_w\rho_{w3}c_{w3}\left[\frac{d}{dt}(T_{w3}L_{3,i}) + T_{w2,3}\frac{d(L_1+L_2)}{dt} - T_{w3,4}\frac{d(L_1+L_2+L_{3,i})}{dt}\right] = \tag{4.72}$$
$$= \pi D_{out}L_{3,i}\alpha_{p3}(T_{p3} - T_{w,p3}) - \pi D_{in}L_{3,i}\alpha_{s3}(T_{w,s3} - T_{s3})$$
$$A_w\rho_{w4}c_{w4}\left[\frac{d}{dt}(T_{w4}L_{3,i}) + T_{w3,4}\frac{d(L_1+L_2+L_{3,i})}{dt}\right] = \tag{4.73}$$
$$= \pi D_{out}L_{3,i}\alpha_{p4}(T_{p4} - T_{w,p4}) - \pi D_{in}L_{3,i}\alpha_{s4}(T_{w,s4} - T_{s4})$$

Separating all terms the equations become:

$$A_w\rho_{w1}c_{w1}\left[L_1\frac{dT_{w1}}{dt} + (T_{w1} - T_{w1,2})\frac{dL_1}{dt}\right] = \tag{4.74}$$
$$= \pi D_{out}L_1\alpha_{p1}(T_{p1} - T_{w,p1}) - \pi D_{in}L_1\alpha_{s1}(T_{w,s1} - T_{s1})$$
$$A_w\rho_{w2}c_{w2}\left[L_2\frac{dT_{w2}}{dt} + (T_{w1,2} - T_{w2,3})\frac{dL_1}{dt} + (T_{w2} - T_{w2,3})\frac{dL_2}{dt}\right] = \tag{4.75}$$
$$= \pi D_{out}L_2\alpha_{p2}(T_{p2} - T_{w,p2}) - \pi D_{in}L_2\alpha_{s2}(T_{w,s2} - T_{s2})$$
$$A_w\rho_{w3}c_{w3}\left[L_{3,i}\frac{dT_{w3}}{dt} + (T_{w2,3} - T_{w3,4})\left(\frac{dL_1}{dt} + \frac{dL_2}{dt}\right) + (T_{w3} - T_{w3,4})\frac{dL_{3,i}}{dt}\right] = \tag{4.76}$$
$$= \pi D_{out}L_{3,i}\alpha_{p3}(T_{p3} - T_{w,p3}) - \pi D_{in}L_{3,i}\alpha_{s3}(T_{w,s3} - T_{s3})$$
$$A_w\rho_{w4}c_{w4}\left[L_{3,i}\frac{dT_{w4}}{dt} + T_{w3,4}\left(\frac{dL_1}{dt} + \frac{dL_2}{dt}\right) + (T_{w4} + T_{w3,4})\frac{dL_{3,i}}{dt}\right] = \tag{4.77}$$
$$= \pi D_{out}L_{3,i}\alpha_{p4}(T_{p4} - T_{w,p4}) - \pi D_{in}L_{3,i}\alpha_{s4}(T_{w,s4} - T_{s4})$$

4.3.4. Properties and correlations

Thermo-physical properties of water are obtained through the well-known X Steam tool [74] in MATLAB, which is a full implementation of the International Association for Properties of Water and Steam Industrial Formulation 1997 (IAPWS IF-97) [75, 76]. Thermo-physical properties of lead and of wall are listed in Appendix A. It is important to specify that, although the metallic alloy utilized in the SG will be Fe-10Cr-4Al-RE,

at present a set of correlations for a different metal has been employed. This alloy is T91, a ferritic-martensitic steel that was originally considered among the options for structural materials in Gen. IV reactors but then discarded because of bad behavior at high temperatures, especially in terms of creep. New properties for FeCrAl steels will be integrated once available at a later stage.

Water convective heat transfer coefficients

For single-phase convection Dittus-Boelter correlation [60] is considered:

$$\mathrm{Nu}_{DB} = 0.023\ \mathrm{Re}^{0.8}\mathrm{Pr}^{0.4} \tag{4.78}$$

where Nu_{DB}, Re and Pr are the Nusselt, Reynolds and Prandtl numbers respectively:

$$\mathrm{Nu}_{DB} = \frac{\alpha_{DB} L_c}{k} \tag{4.79}$$

$$\mathrm{Re} = \frac{v \rho L_c}{\mu} \tag{4.80}$$

$$\mathrm{Pr} = \frac{c_p \mu}{k} \tag{4.81}$$

with α_{DB} heat transfer coefficient and L_c characteristic length (hydraulic diameter). Its validity range is $\mathrm{Re} > 10000$ and $0.6 \leq \mathrm{Pr} \leq 160$.

For two-phase region Kandlikar correlation [77] is adopted:

$$\alpha_{Ka} = (C_1 Co^{C_2} (25\ \mathrm{Fr}_{lo})^{C_5} + C_3 Bo^{C_4} F_{fluid}) \cdot \alpha_{DB} \tag{4.82}$$

where C_1, C_2, C_3, C_4 and C_5 are experimentally derived constants, Fr_{lo} is the Froude number in "liquid only" conditions, F_{fluid} is a fluid-dependent parameter (equal to 1 in case of water) and α_{DB} is the single-phase heat transfer coefficient for the subcooled region. Co and Bo are the convection number and the boiling number.

$$\mathrm{Fr}_{lo} = \frac{v_{lo}}{\sqrt{g L_c}} \tag{4.83}$$

$$Co = \left(\frac{1-\overline{x}}{\overline{x}}\right)^{0.8} \left(\frac{\rho_g}{\rho_l}\right)^{0.5} \tag{4.84}$$

$$Bo = \frac{Q''}{G(h_g - h_l)} \tag{4.85}$$

being $\overline{x}$ the dryness fraction, Q'' the heat flux $\left(\frac{W}{m^2}\right)$ and G the mass flux $\left(\frac{kg}{m^2 \cdot s}\right)$:

$$\overline{x} = \frac{1}{1 + \frac{\rho_L}{\rho_g}\frac{1-\overline{\gamma}}{\overline{\gamma}}} \tag{4.86}$$

$$Q'' = \frac{\dot{Q}}{A_{lat}} \tag{4.87}$$

$$G = \frac{\dot{m}}{A_s} \tag{4.88}$$

$$A_{lat} = \pi D L \tag{4.89}$$

Lead convective heat transfer coefficients

For lead Žukauskas correlation [78, 79] for staggered tubes with $S_T/S_L < 2$ and in transition regime ($10^3 < \mathrm{Re} < 2 \times 10^5$) is used:

$$\mathrm{Nu}_{Zu} = 0.35\left(\frac{S_T}{S_L}\right)^{0.2} \mathrm{Re}^{0.60}\mathrm{Pr}^{0.36}\left(\frac{\mathrm{Pr}}{\mathrm{Pr}_s}\right)^{0.25} \tag{4.90}$$

with S_T and S_L transverse pitch and longitudinal pitch respectively (Figure 4.6), and Pr_s Prandtl number evaluated at tube-wall temperature. Out of that validity range other versions of the same correlation exist.

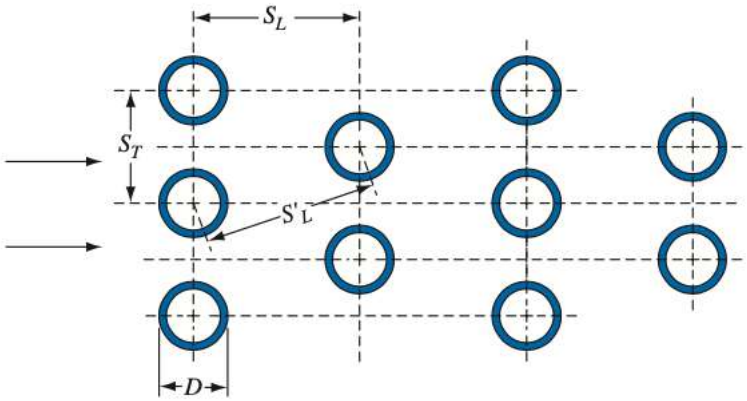

Figure 4.6: Sketch illustrating nomenclature for staggered tube arrangements used in Žukauskas correlation [78].

Table 4.4 summarizes the correlations adopted for water and lead heat transfer coefficients and lists their values in nominal conditions.

Region	Water correlations	Value $\left(\frac{kW}{m^2 \cdot K}\right)$	Lead correlations	Value $\left(\frac{kW}{m^2 \cdot K}\right)$
Subcooled (1)	Dittus-Boelter	40	Žukauskas	211
Saturated (2)	Kandlikar	350	Žukauskas	216
Superheated (3)	Dittus-Boelter	19	Žukauskas	227
Superheated (4)	Dittus-Boelter	13	Žukauskas	233

Table 4.4: SG heat transfer coefficients values in nominal conditions.

4.4. Simulink implementation

The software utilized throughout all the dynamical simulations is Simulink®, a MATLAB® tool. It is optimized to solve explicit systems of differential equations where input and output variables are well identified (causal approach). Thus, it is appropriate to re-write all moving boundary SG equations in explicit form.

Water

Input variables: $T_{s,in},\ \dot{m}_{in},\ K,\ \frac{dh_{s,in}}{dt},\ T_{w1},\ T_{w2},\ T_{w3},\ T_{w4}$.
State variables: $L_1,\ L_2,\ h_{s3,4},\ h_{s,out}$.
Output variables: $\dot{m}_{1,2},\ \dot{m}_{2,3},\ \dot{m}_{3,4},\ \dot{m}_{out},\ T_{s1},\ T_{s2},\ T_{s3},\ T_{s4},\ T_{s,out},\ L_1,\ L_2,\ L_3,\ \frac{dL_i}{dt}$, $\dot{Q}_{s1},\ \dot{Q}_{s2},\ \dot{Q}_{s3},\ \dot{Q}_{s4}$.

Mass flow rates are obtained from mass balance equations, while regions lengths and water enthalpies from energy balance equations:

$$\begin{aligned} \dot{m}_{1,2} &= \dot{m}_{in} - A_s\left[(\rho_{s1}-\rho_{s,l})\frac{dL_1}{dt} + \frac{1}{2}L_1\frac{\partial\rho_{s1}}{\partial h}\bigg|_P\frac{dh_{s,in}}{dt} + \right. \\ &+ \left. L_1\left(\frac{1}{2}\frac{\partial\rho_{s1}}{\partial h}\bigg|_P\frac{\partial h_{s,l}}{\partial P} + \frac{\partial\rho_{s1}}{\partial P}\bigg|_h\right)\frac{dP}{dt}\right] \end{aligned} \tag{4.91}$$

$$\begin{aligned} \frac{dL_1}{dt} &= \frac{1}{\rho_{s1}h_{s1}-\rho_{s,l}h_{s,l}}\left\{-\frac{1}{2}L_1\left(h_{s1}\frac{\partial\rho_{s1}}{\partial h}\bigg|_P + \rho_{s1}\right)\frac{dh_{s,in}}{dt} + \right. \\ &- L_1\left[\frac{1}{2}\left(h_{s1}\frac{\partial\rho_{s1}}{\partial h}\bigg|_P + \rho_{s1}\right)\frac{\partial h_{s,l}}{\partial P} + h_{s1}\frac{\partial\rho_{s1}}{\partial P}\bigg|_h - 1\right]\frac{dP}{dt} + \frac{\dot{m}_{in}h_{s,in} - \dot{m}_{1,2}h_{s,l}}{A_s} + \\ &+ \left.\frac{\pi D_{in}L_1\alpha_{s1}}{A_s}(T_{w,s1}-T_{s1})\right\} \end{aligned} \tag{4.92}$$

$$\dot{m}_{2,3} = \dot{m}_{1,2} - A_s\Bigg[(\rho_{s,l}-\rho_{s,g})\frac{dL_1}{dt} + (1-\overline{\gamma})(\rho_{s,l}-\rho_{s,g})\frac{dL_2}{dt} + \tag{4.93}$$
$$+ \; L_2\left(\overline{\gamma}\frac{\partial\rho_{s,g}}{\partial P} + (1-\overline{\gamma})\frac{\partial\rho_{s,l}}{\partial P}\right)\frac{dP}{dt}\Bigg]$$

$$\frac{dL_2}{dt} = \frac{1}{(1-\overline{\gamma})(\rho_{s,l}h_{s,l}-\rho_{s,g}h_{s,g})}\Bigg\{-(\rho_{s,l}h_{s,l}-\rho_{s,g}h_{s,g})\frac{dL_1}{dt} + \tag{4.94}$$
$$- \; L_2\left(\overline{\gamma}h_{s,g}\frac{\partial\rho_{s,g}}{\partial P} + \overline{\gamma}\rho_{s,g}\frac{\partial h_{s,g}}{\partial P} + (1-\overline{\gamma})h_{s,l}\frac{\partial\rho_{s,l}}{\partial P} + (1-\overline{\gamma})\rho_{s,l}\frac{\partial h_{s,l}}{\partial P} - 1\right)\frac{dP}{dt} +$$
$$+ \; \frac{\dot{m}_{1,2}h_{s,l}-\dot{m}_{2,3}h_{s,g}}{A_s} + \frac{\pi D_{in}L_2\alpha_{s2}}{A_s}(T_{w,s2}-T_{s2})\Bigg\}$$

$$\dot{m}_{3,4} = \dot{m}_{2,3} - A_s\Bigg[(\rho_{s,g}-\rho_{s3,4})\left(\frac{dL_1}{dt}+\frac{dL_2}{dt}\right) + (\rho_{s3}-\rho_{s3,4})\frac{dL_{3,i}}{dt} + \tag{4.95}$$
$$+ \; \frac{1}{2}L_{3,i}\frac{\partial\rho_{s3}}{\partial h}\bigg|_P\frac{dh_{s3,4}}{dt} + L_{3,i}\left(\frac{1}{2}\frac{\partial\rho_{s3}}{\partial h}\bigg|_P\frac{\partial h_{s,g}}{\partial P} + \frac{\partial\rho_{s3}}{\partial P}\bigg|_h\right)\frac{dP}{dt}\Bigg]$$

$$\frac{dh_{s3,4}}{dt} = \frac{1}{\frac{1}{2}L_{3,i}\left(\rho_{s3}+h_{s3}\frac{\partial\rho_{s3}}{\partial h}\big|_P\right)}\Bigg\}-(\rho_{s,g}h_{s,g}-\rho_{s3,4}h_{s3,4})\left(\frac{dL_1}{dt}+\frac{dL_2}{dt}\right) + \tag{4.96}$$
$$- \; (\rho_{s3}h_{s3}-\rho_{s3,4}h_{s3,4})\frac{L_{3,i}}{dt} - L_{3,i}\left[\frac{1}{2}\left(h_{s3}\frac{\partial\rho_{s3}}{\partial h}\bigg|_P+\rho_{s3}\right)\frac{\partial h_{s,g}}{\partial P} + h_{s3}\frac{\partial\rho_{s3}}{\partial P}\bigg|_h - 1\right]\frac{dP}{dt} +$$
$$+ \; \frac{\dot{m}_{2,3}h_{s,g}-\dot{m}_{3,4}h_{3,4}}{A_s} + \frac{\pi D_{in}L_{3,i}\alpha_{s3}}{A_s}(T_{w,s3}-T_{s3})\Bigg\}$$

$$\dot{m}_{out} = \dot{m}_{3,4} - A_s\Bigg[(\rho_{s3,4}-\rho_{s,out})\left(\frac{dL_1}{dt}+\frac{dL_2}{dt}\right) + (\rho_{s3,4}+\rho_{s4}-2\rho_{s,out})\frac{dL_{3,i}}{dt} + \tag{4.97}$$
$$+ \; \frac{1}{2}L_{3,i}\frac{\partial\rho_{s4}}{\partial h}\bigg|_P\left(\frac{dh_{s3,4}}{dt}+\frac{dh_{s,out}}{dt}\right) + L_{3,i}\frac{\partial\rho_{s4}}{\partial P}\bigg|_h\frac{dP}{dt}\Bigg]$$

$$\frac{dh_{s,out}}{dt} = -\frac{dh_{s3,4}}{dt} + \frac{1}{\frac{1}{2}L_{3,i}\left(\rho_{s4}+h_{s4}\frac{\partial\rho_{s4}}{\partial h}\big|_P\right)}\Bigg[-(\rho_{s3,4}h_{s3,4}-\rho_{s,out}h_{s,out})\left(\frac{dL_1}{dt}+\frac{dL_2}{dt}\right) +$$
$$- \; (\rho_{s4}h_{s4}+\rho_{s3,4}h_{s3,4}-2\rho_{s,out}h_{s,out})\frac{dL_{3,i}}{dt} - L_{3,i}\left(h_{s4}\frac{\partial\rho_{s4}}{\partial P}\bigg|_h - 1\right)\frac{dP}{dt} + \tag{4.98}$$
$$+ \; \frac{\dot{m}_{3,4}h_{s3,4}-\dot{m}_{out}h_{s,out}}{A_s} + \frac{\pi D_{in}L_{3,i}\alpha_{s4}}{A_s}(T_{w,s4}-T_{s4})\Bigg]$$

Lead

Input variables: $L_1,\ L_2,\ L_3,\ T_{p,in},\ T_{w1},\ T_{w2},\ T_{w3},\ T_{w4},\ \frac{dL_i}{dt},\ \Gamma,\ \frac{dT_{p,in}}{dt}$.
State variables: $T_{p1,2},\ T_{p2,3},\ T_{p3,4},\ T_{p,out}$.
Output variables: $T_{p1,2},\ T_{p2.3},\ T_{p3,4},\ T_{p,out},\ T_{p1},\ T_{p2},\ T_{p3},\ T_{p4},\ \dot{Q}_{p1},\ \dot{Q}_{p2},\ \dot{Q}_{p3},\ \dot{Q}_{p4}$.

$$\frac{dT_{p3,4}}{dt} = \frac{2(T_{p,in}-T_{p3,4})}{L_{3,i}}\left(\frac{dL_1}{dt}+\frac{dL_2}{dt}\right)+\frac{2(2T_{p,in}-T_{p4}-T_{p3,4})}{L_{3,i}}\frac{dL_{3,i}}{dt}+ \quad (4.99)$$
$$+ \frac{2\Gamma}{A_p\rho_{p4}L_{3,i}}(T_{p,in}-T_{p3,4})-\frac{2\pi D_{out}\alpha_{p4}}{A_p\rho_{p4}c_{p4}}(T_{p4}-T_{w,p4})-\frac{dT_{p,in}}{dt}$$

$$\frac{dT_{p2,3}}{dt} = \frac{2(T_{p3,4}-T_{p2,3})}{L_{3,i}}\left(\frac{dL_1}{dt}+\frac{dL_2}{dt}\right)+\frac{2(T_{p3,4}-T_{p3})}{L_{3,i}}\frac{dL_{3,i}}{dt}+ \quad (4.100)$$
$$+ \frac{2\Gamma}{A_p\rho_{p3}L_{3,i}}(T_{p3,4}-T_{p2,3})-\frac{2\pi D_{out}\alpha_{p3}}{A_p\rho_{p3}c_{p3}}(T_{p3}-T_{w,p3})-\frac{dT_{p3,4}}{dt}$$

$$\frac{dT_{p1,2}}{dt} = \frac{2(T_{p2,3}-T_{p1,2})}{L_2}\frac{dL_1}{dt}+\frac{2(T_{p2,3}-T_{p2})}{L_2}\frac{dL_2}{dt}+ \quad (4.101)$$
$$+ \frac{2\Gamma}{A_p\rho_{p2}L_2}(T_{p2,3}-T_{p1,2})-\frac{2\pi D_{out}\alpha_{p2}}{A_p\rho_{p2}c_{p2}}(T_{p2}-T_{w,p2})-\frac{dT_{p2,3}}{dt}$$

$$\frac{dT_{p,out}}{dt} = \frac{2(T_{p1,2}-T_{p1})}{L_1}\frac{dL_1}{dt}+\frac{2\Gamma}{A_p\rho_{p1}L_1}(T_{p1,2}-T_{p,out})+ \quad (4.102)$$
$$- \frac{2\pi D_{out}\alpha_{p1}}{A_p\rho_{p1}c_{p1}}(T_{p1}-T_{w,p1})-\frac{dT_{p1,2}}{dt}$$

where

$$T_{p1} = \frac{T_{p,out}+T_{p1,2}}{2} \quad (4.103)$$
$$T_{p2} = \frac{T_{p1,2}+T_{p2,3}}{2} \quad (4.104)$$
$$T_{p3} = \frac{T_{p2,3}+T_{p3,4}}{2} \quad (4.105)$$
$$T_{p4} = \frac{T_{p3,4}+T_{p,in}}{2} \quad (4.106)$$

Wall

Input variables: $L_1,\ L_2,\ L_3,\ \dot{Q}_{s1},\ \dot{Q}_{s2},\ \dot{Q}_{s3},\ \dot{Q}_{s4},\ \dot{Q}_{p1},\ \dot{Q}_{p2},\ \dot{Q}_{p3},\ \dot{Q}_{p4},\ \frac{dL_i}{dt}$.
State variables: $T_{w1},\ T_{w2},\ T_{w3},\ T_{w4}$.
Output variables: $T_{w1},\ T_{w2},\ T_{w3},\ T_{w4}$.

$$\frac{dT_{w1}}{dt} = \frac{T_{w1,2}-T_{w1}}{L_1}\frac{dL_1}{dt} + \frac{\pi D_{out}\alpha_{p1}}{A_w\rho_{w1}c_{w1}}(T_{p1}-T_{w,p1}) - \frac{\pi D_{in}\alpha_{s1}}{A_w\rho_{w1}c_{w1}}(T_{w,s1}-T_{s1}) \quad (4.107)$$

$$\frac{dT_{w2}}{dt} = \frac{T_{w2,3}-T_{w1,2}}{L_2}\frac{dL_1}{dt} + \frac{T_{w2,3}-T_{w2}}{L_2}\frac{dL_2}{dt} + \frac{\pi D_{out}\alpha_{p2}}{A_w\rho_{w2}c_{w2}}(T_{p2}-T_{w,p2}) + \quad (4.108)$$

$$- \frac{\pi D_{in}\alpha_{s2}}{A_w\rho_{w2}c_{w2}}(T_{w,s2}-T_{s2})$$

$$\frac{dT_{w3}}{dt} = \frac{T_{w3,4}-T_{w2,3}}{L_{3,i}}\left(\frac{dL_1}{dt}+\frac{dL_2}{dt}\right) + \frac{T_{w3,4}-T_{w3}}{L_{3,i}}\frac{dL_{3,i}}{dt} + \quad (4.109)$$

$$+ \frac{\pi D_{out}\alpha_{p3}}{A_w\rho_{w3}c_{w3}}(T_{p3}-T_{w,p3}) - \frac{\pi D_{in}\alpha_{s3}}{A_w\rho_{w3}c_{w3}}(T_{w,s3}-T_{s3})$$

$$\frac{dT_{w4}}{dt} = \frac{T_{w3,4}-T_{w4}}{L_{3,i}}\frac{dL_{3,i}}{dt} + \frac{\pi D_{out}\alpha_{p4}}{A_w\rho_{w4}c_{w4}}(T_{p4}-T_{w,p4}) - \frac{\pi D_{in}\alpha_{s4}}{A_w\rho_{w4}c_{w4}}(T_{w,s4}-T_{s4}) \quad (4.110)$$

Closure equations

Some equations to close the problem and compute all needed quantities must be considered.

First of all, secondary side pressure P is calculated as:

$$P = P_{out} + \frac{\dot{m}_{out}}{K} \quad (4.111)$$

where P_{out} is the pressure at the outlet of the SG and K is the valve admission coefficient. Since the valve is always open, $K \to \infty$ and hence $P \to P_{out}$.

Secondly, temperatures of wall in contact with water ($T_{w,s}$) and with lead ($T_{w,p}$). They

are calculated assuming an instantaneous dynamics (negligible time constants) as:

$$T_{w,s1} = T_{w1} - \frac{\ln\left(\frac{R_{avg}}{R_{in}}\right)}{2\pi k_{w1} L_1}\dot{Q}_{s1} \tag{4.112}$$

$$T_{w,s2} = T_{w2} - \frac{\ln\left(\frac{R_{avg}}{R_{in}}\right)}{2\pi k_{w2} L_2}\dot{Q}_{s2} \tag{4.113}$$

$$T_{w,s3} = T_{w3} - \frac{\ln\left(\frac{R_{avg}}{R_{in}}\right)}{2\pi k_{w3} L_{3,i}}\dot{Q}_{s3} \tag{4.114}$$

$$T_{w,s4} = T_{w4} - \frac{\ln\left(\frac{R_{avg}}{R_{in}}\right)}{2\pi k_{w4} L_{3,i}}\dot{Q}_{s4} \tag{4.115}$$

$$T_{w,p1} = T_{w1} + \frac{\ln\left(\frac{R_{out}}{R_{avg}}\right)}{2\pi k_{w1} L_1}\dot{Q}_{p1} \tag{4.116}$$

$$T_{w,p2} = T_{w2} + \frac{\ln\left(\frac{R_{out}}{R_{avg}}\right)}{2\pi k_{w2} L_2}\dot{Q}_{p2} \tag{4.117}$$

$$T_{w,p3} = T_{w3} + \frac{\ln\left(\frac{R_{out}}{R_{avg}}\right)}{2\pi k_{w3} L_{3,i}}\dot{Q}_{p3} \tag{4.118}$$

$$T_{w,p4} = T_{w4} + \frac{\ln\left(\frac{R_{out}}{R_{avg}}\right)}{2\pi k_{w4} L_{3,i}}\dot{Q}_{p4} \tag{4.119}$$

where k_w is wall thermal conductivity $\left(\frac{W}{m \cdot K}\right)$, and $\dot{Q}_s$ and $\dot{Q}_p$ are thermal power exchanged from water side and lead side, respectively. The latter are calculated as:

$$\dot{Q}_{s1} = \pi D_{in} L_1 \alpha_{s1}(T_{w,s1} - T_{s1}) > 0 \tag{4.120}$$

$$\dot{Q}_{s2} = \pi D_{in} L_2 \alpha_{s2}(T_{w,s2} - T_{s2}) > 0 \tag{4.121}$$

$$\dot{Q}_{s3} = \pi D_{in} L_{3i} \alpha_{s3}(T_{w,s3} - T_{s3}) > 0 \tag{4.122}$$

$$\dot{Q}_{s4} = \pi D_{in} L_{3i} \alpha_{s4}(T_{w,s4} - T_{s4}) > 0 \tag{4.123}$$

$$\dot{Q}_{p1} = \pi D_{out} L_1 \alpha_{p1}(T_{p1} - T_{w,p1}) > 0 \tag{4.124}$$

$$\dot{Q}_{p2} = \pi D_{out} L_2 \alpha_{p2}(T_{p2} - T_{w,p2}) > 0 \tag{4.125}$$

$$\dot{Q}_{p3} = \pi D_{out} L_{3i} \alpha_{p3}(T_{p3} - T_{w,p3}) > 0 \tag{4.126}$$

$$\dot{Q}_{p4} = \pi D_{out} L_{3i} \alpha_{p4}(T_{p4} - T_{w,p4}) > 0 \tag{4.127}$$

Lastly, wall temperatures at the regions boundaries are simply evaluated looking at the

derivatives of the regions lengths as suggested in [73]:

$$T_{w1,2} = \begin{cases} T_{w2} & \frac{dL_1}{dt} > 0 \\ T_{w1} & \frac{dL_1}{dt} \leq 0 \end{cases} \tag{4.128}$$

$$T_{w2,3} = \begin{cases} T_{w3} & \frac{dL_2}{dt} > 0 \\ T_{w2} & \frac{dL_2}{dt} \leq 0 \end{cases} \tag{4.129}$$

$$T_{w3,4} = \begin{cases} T_{w4} & \frac{dL_{3,i}}{dt} > 0 \\ T_{w3} & \frac{dL_{3,i}}{dt} \leq 0 \end{cases} \tag{4.130}$$

This approach leads to some discontinuities in their values, but it does not affect the good behavior of state variables T_{w1}, T_{w2}, T_{w3}, T_{w4}, as it is shown by simulations in the next section.

As it was done in Chapter 3, the optimal way to implement the SG model in Simulink is by grouping its equations into subsystems and coupling them through flow signals.

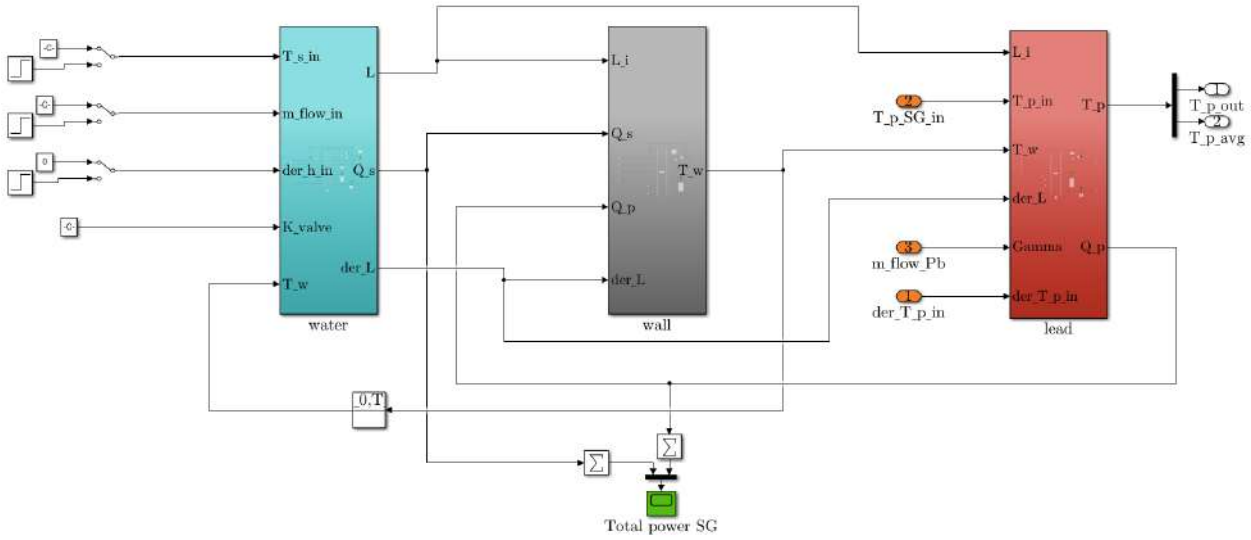

Figure 4.7: SG implementation in Simulink. Three main subsystems represent: water side (light blue), wall (gray) and lead side (red).

The whole code is divided into three main subsystems (Figure 4.7), each representing one side of the SG. The first subsystem (light blue) models water side, the second subsystem (gray) is the wall interface, the third subsystem (red) models the lead side. They all contain a MATLAB Function block, which calculates properties and differential equations, Integrator blocks and input/output signals. All blocks are taken from the Simulink Library

Browser. For instance, Figure 4.8 represents water side subsystem.

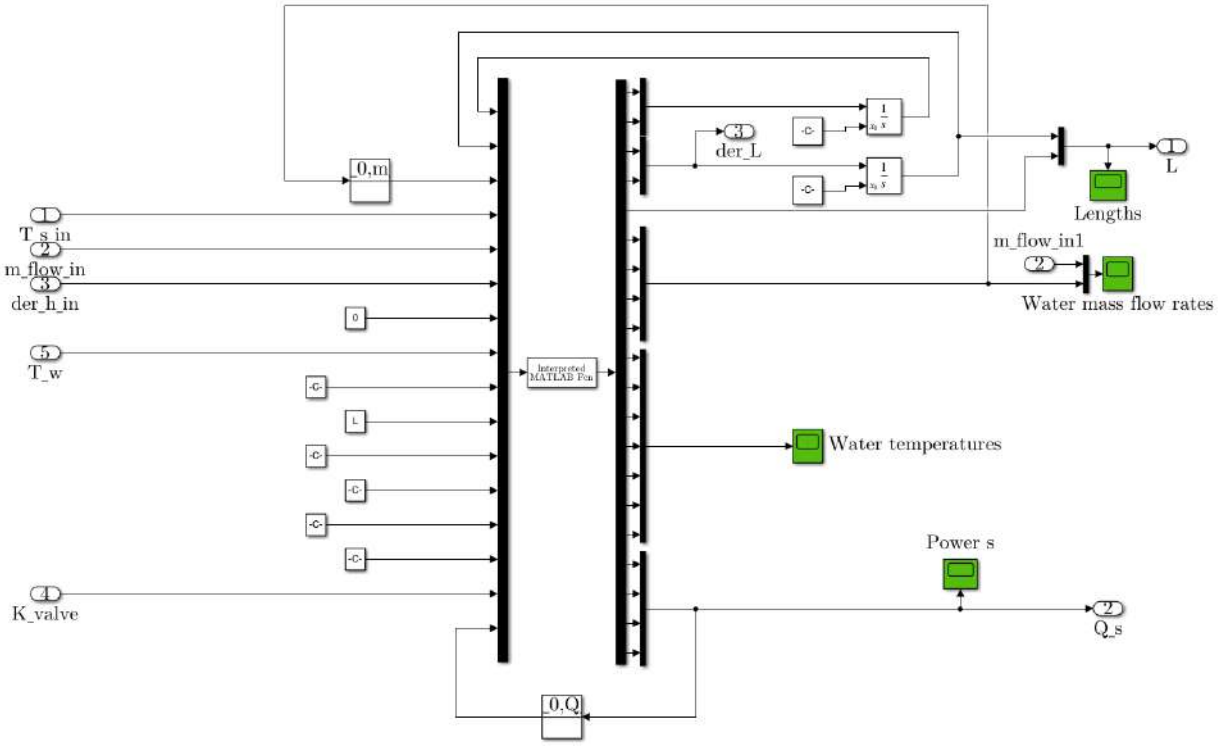

Figure 4.8: Water side implementation in Simulink.

Table 4.5 lists the input and the output variables of each subsystem.

Subsystem	Inputs	Outputs
Whole SG model	$T_{p,in}$, $\frac{dT_{p,in}}{dt}$, Γ, $T_{s,in}$, $\frac{dh_{s,in}}{dt}$, $\dot{m}_{in}$	$T_{Pb}^{SG,avg}$, $T_{Pb}^{SG,out}$
Water side	$T_{s,in}$, $\frac{dh_{s,in}}{dt}$, $\dot{m}_{in}$, K, T_w^i	L_i, $\frac{dL_i}{dt}$, $\dot{Q}_s^i$
Wall	L_i, $\frac{dL_i}{dt}$, $\dot{Q}_s^i$, $\dot{Q}_p^i$	T_w^i
Lead side	$T_{p,in}$, $\frac{dT_{p,in}}{dt}$, Γ, L_i, $\frac{dL_i}{dt}$, T_w^i	$\dot{Q}_p^i$, $T_{Pb}^{SG,avg}$, $T_{Pb}^{SG,out}$

Table 4.5: Simulink subsystems input and output variables in moving boundary SG.

The outputs of the whole model are lead temperature at the outlet of the SG ($T_{p,out} = T_{Pb}^{SG,out}$) and lead average temperature in the SG ($T_{Pb}^{SG,avg}$). Their role is better clarified in the next Chapter 5, when the SG model is integrated within BELLA.

4.5. Simulations

The model requires to be tested against some reference scenarios. They correspond to possible transients caused by variations on primary side (lead) or secondary side (water) conditions, namely on inlet temperature and mass flow rate. This section is entirely dedicated to these transients. They are:

- 20% increase of $T_{p,in}$
- 65% decrease of Γ
- 20% decrease of $T_{s,in}$
- 20% decrease of $\dot{m}_{s,in}$

Before doing that, steady-state conditions of the moving boundary SG are computed.

The general Simulink settings adopted in these transients are briefly discussed in Appendix D.

4.5.1. Steady-state conditions

The moving boundary SG model perfectly sustains steady-state conditions. They are used to calculate the total length L of the once-through tube on the condition that it needs to be capable of removing 0.533 MW of power from lead by flowing water. Once this value is found, it is kept fixed for all the remaining simulations.

Due to the absence of any transient, only regions lengths and total power removed by the SG are plotted (Figure 4.9). The values of the most important parameters of the SG in nominal conditions are listed in Table 4.6.

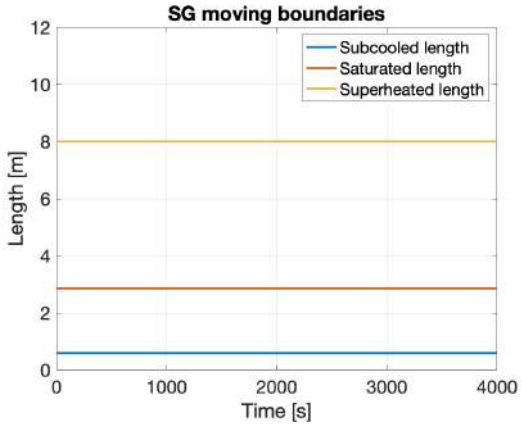

(a) SG regions lengths.

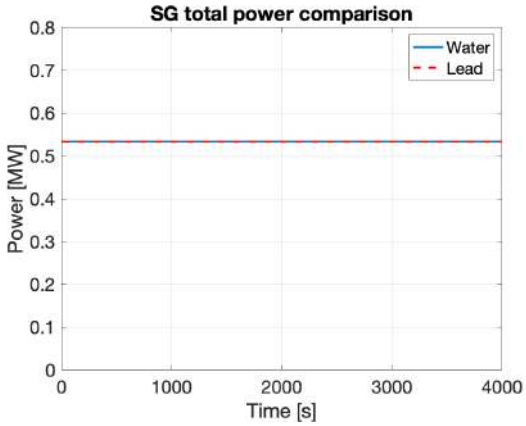

(b) SG power exchanged between the fluids.

Figure 4.9: Simulation results adopting the moving boundary SG in steady-state conditions.

Quantity	Value	Unit
Subcooled region length	0.592	m
Saturated region length	2.855	m
Superheated region length	8.006	m
Total thermal power	0.533	MW
Lead inlet temperature	550.0	°C
Lead outlet temperature	420.0	°C
Lead mass flow rate	14.14	kg/s
Water inlet temperature	340.0	°C
Water outlet temperature	530.0	°C
Water mass flow rate	0.297	kg/s

Table 4.6: SG steady-state values for the most important quantities.

Total length results in $L = 11.453$ m. Although the geometry is different, this value is considered as a first estimation of the real SG spiral tubes length.
Now all the other transients can be simulated.

4.5.2. Lead inlet temperature surge

This transient can be interpreted as a preliminary test of the SG model to the UTOP scenario, where indeed all temperatures of the primary system, and especially lead temperature at the SG inlet, increase.

In Simulink the temperature surge is modeled as a step-wise increase of $T_{p,in}$ by 20% at time $t = 10$ s. Total simulation time is 50 s, sufficient to let the SG dynamics conclude. The trend of the main variables of interest is displayed in Figure 4.10.

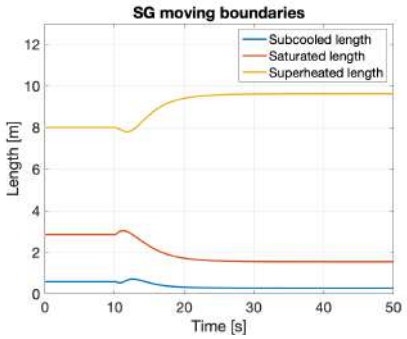

(a) SG regions lengths.

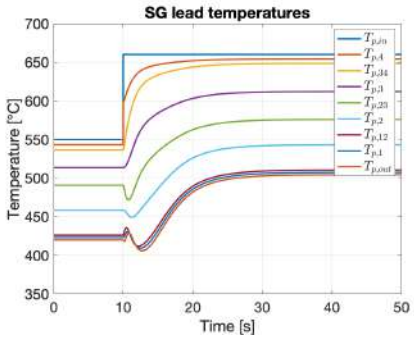

(b) Lead temperatures.

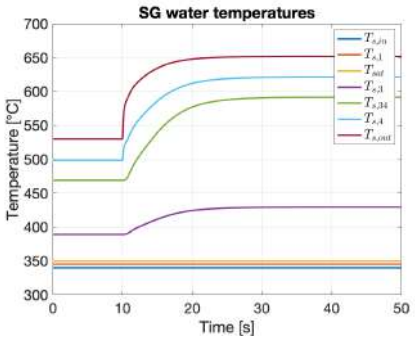

(c) Water temperatures.

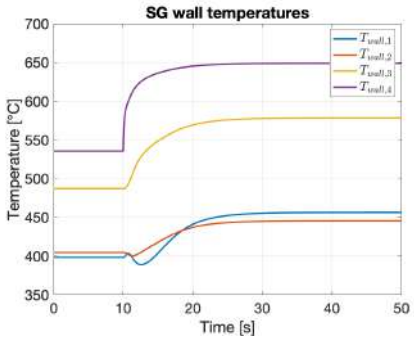

(d) Wall temperatures.

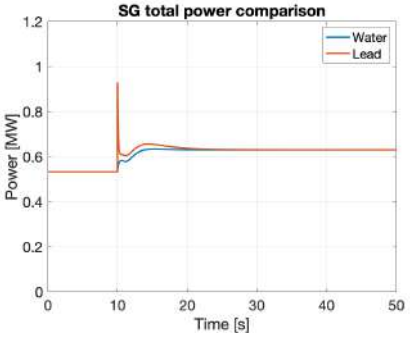

(e) Total power exchanged.

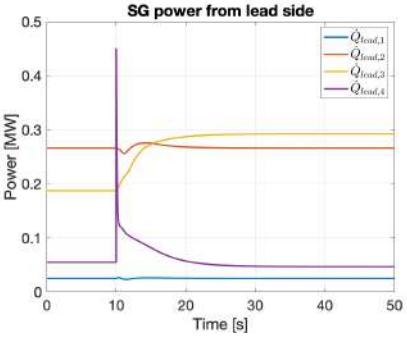

(f) SG power from lead side in regions.

Figure 4.10: Main plots resulting from $T_{p,in}$ surge simulation.

Since this is the first simulated transient adopting the SG model, it is taken as a reference for some very general comments about the behavior of the main quantities which are not repeated in the next subsections.

Following the instantaneous increase of $T_{p,in}$, all lead temperatures in the system grow. In Figure 4.10b it is possible to notice some weird oscillations in the colder lead regions: this does not seem to be a physically reasonable trend, but it is clear that it is caused by the last term in Eq.s (4.99, 4.100, 4.101, 4.102). One could decide to remove those terms to simplify the equations and, as a consequence, eliminate the oscillations. Although it has been tried, in this work the preferred choice is to keep them − they come after a correct mathematical derivation of the equations − and just ignore the oscillatory behavior (additional comments are given in Section 4.6). $T_{p3,4}$ does not suffer from these oscillations because the inlet lead temperature surge is instantaneous and no derivative is accounted $\left(\frac{dT_{p,in}}{dt} = 0\right)$.

The increase in lead temperatures implies a general grow of the system temperatures, both for water and for wall.
Water temperatures in subcooled and saturated regions do not change because inlet temperature $T_{s,in}$ and pressure P are constant throughout the transient. Superheating degree increases significantly and, hence, the extension of superheated region rises too. As a consequence, both subcooled and saturated regions decrease in length. Their oscillatory behavior is caused by the oscillations in lead temperatures.

Regarding wall temperatures, T_{w1} overcomes T_{w2} around $t = 50$ s (Figure 4.10d). Although this might seem strange, it is perfectly justified by the conditions of the transient: since wall is positioned between water and lead, $T_s < T_w < T_p$ is always valid for each region. T_w is closer to lead or to water temperature according to their thermal conductance, whose difference is mostly determined by the convective heat transfer coefficient of the fluids (wall thermal conductivity is about the same on both sides). Focusing on region 1, due to the poor heat transfer capability of subcooled water, T_{w1} is closer to T_{p1} rather than to T_{s1}. Conversely, since in saturated region two-phase flow has very good heat transfer properties, T_{w2} is almost equidistant from T_{p1} and T_{s1} (heat transfer coefficients in SG nominal conditions are listed Table 4.4). To understand what happens in the transient, Figure 4.11 is considered. Due to the system temperatures increase and due to the subsequent variations in regions lengths and power exchanged, water heat transfer coefficient in region 1 remains about the same while in region 2 increases by approximately 50%. On the other hand, heat transfer coefficients on lead side equally increase by around 8%. This suggests that T_{w1} increases more than T_{w2} and that, at some point, overcomes it.

Figure 4.10e explains the increase of system temperatures from another point of view: total power delivered to the system by lead is larger than total power removed by water for the most part of the transient. Due to the conservation of energy, the difference is stored inside the system by increasing the temperature. The initial spike in the power exchanged by lead is determined by region 4 contribution (Figure 4.10f) and it is caused by the algebraic relation to calculate Q_{p4} – look at Eq. (4.127) – and by the step-wise increase of $T_{p,in}$.

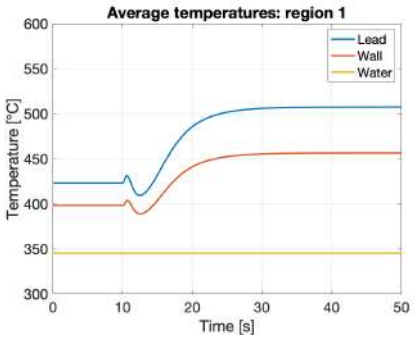

(a) Subcooled region average temperatures.

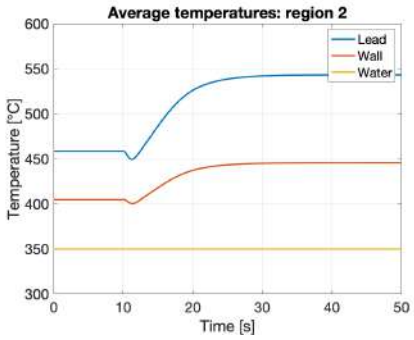

(b) Saturated region average temperatures.

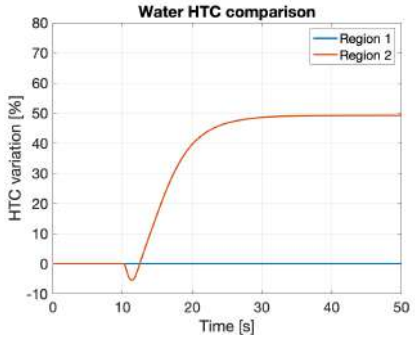

(c) Water heat transfer coefficients (HTCs) in region 1 and 2.

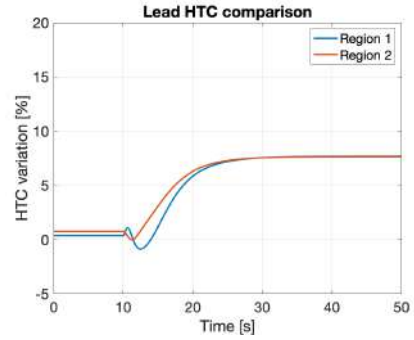

(d) Lead heat transfer coefficients (HTCs) in region 1 and 2.

Figure 4.11: Additional plots resulting from $T_{p,in}$ 20% surge simulation.

4.5.3. Lead mass flow rate decrease

This is a very interesting scenario for two reasons. First of all, it allows to stress the SG model with external conditions similar to ULOF transient (where lead mass flow rate decreases by 69% according to Subsection 3.4.3). Second of all, it is representative of the biggest limit of the current approach: in transients where power strongly decreases and water does not fully evaporate, the SG model fails. The following discussion, with the help of Figure 4.13, explains why.

In Simulink this scenario is modeled by a step-wise decrease of Γ by 65% at time $t = 20$ s. Total simulation time is extended to 100 s in order to let the dynamics finish.

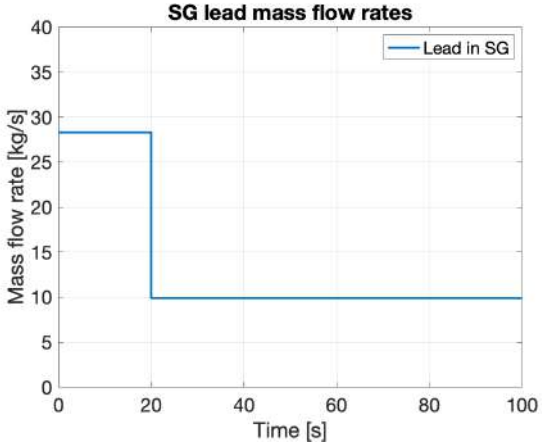

Figure 4.12: Lead mass flow rate.

The immediate consequence of the strong, instantaneous fall of lead mass flow rate Γ (Figure 4.12) is a sudden decrease in total power exchanged by lead, easily understandable from:

$$\dot{Q}_p = \Gamma c_p \Delta T_p \tag{4.131}$$

That is initially true for all SG regions, but then each region behaves in a different way. Subcooled and saturated regions eventually come back to their nominal power levels because, no matter what happens to lead side, water conditions at SG inlet never change and water flow continues to evaporate absorbing the same amount of power. This implies no variations of water temperatures, while lead temperature difference across subcooled and saturated regions increases, explained once again by Eq. (4.131): if Γ decreases with Q_p constant, ΔT_p has to rise up (c_p variation is not significant).
Instead, superheated regions account for the whole power losses, so intense that Q_{p3} and Q_{p4} continue to decrease down to very low values (less than 40 kW each). Eventually, in superheated regions lead is not cooled down effectively and there its temperatures grow toward $T_{p,in}$ (550 °C), while water is not heated up properly and its temperatures approach the saturation point (350 °C). As a consequence, L_3 greatly decreases, while L_1 and L_2 increase.

Power removed by water follows power exchanged by lead (Figure 4.13e).
L_1 and L_2 compensate for L_3 decrease, whose final steady-state value obviously depends on the amount of Γ decrease. With a 65% decrement, saturated region becomes very small (less than 8 cm).

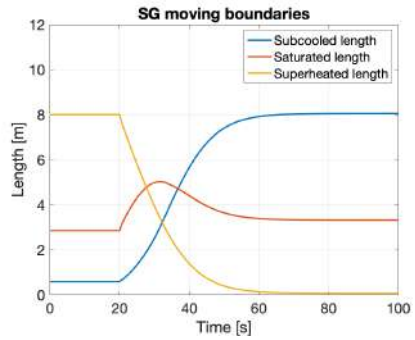

(a) SG regions lengths.

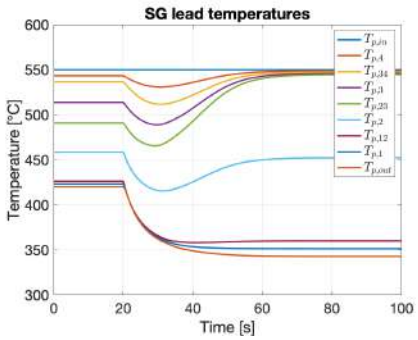

(b) Lead temperatures.

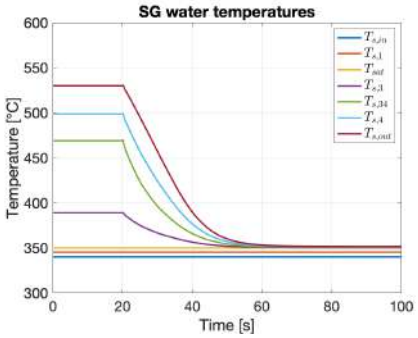

(c) Water temperatures.

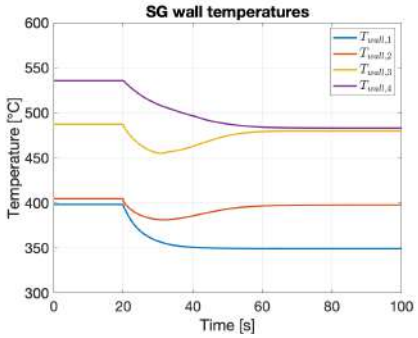

(d) Wall temperatures.

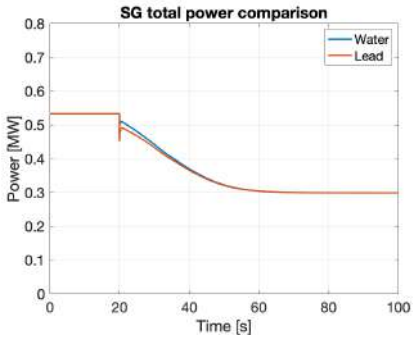

(e) Total power exchanged.

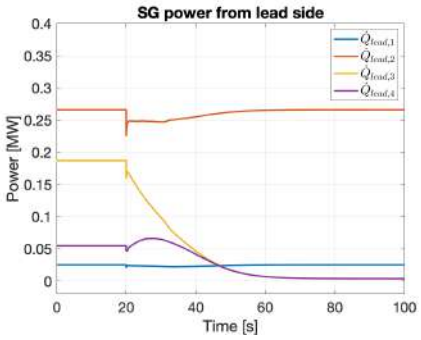

(f) SG power from lead side in regions.

Figure 4.13: Main plots resulting from Γ 65% decrease simulation.

The simulation of lead flow losses even more severe (>65%) is not possible. The moving boundary SG model presented here assumes that the three regions (subcooled, saturated, superheated) always exist with positive, finite lengths L_1, L_2 and L_3. None of them can ever become zero or negative. Thus, there is a minimum amount of power that the system always requires to exchange, and it is the one needed by the water flow to fully evaporate:

$$\dot{Q}_{s,min} = \dot{m}_s(h_{s,g} - h_{s,in}) = 0.291 \text{ MW} \tag{4.132}$$

A 65% decrease of lead mass flow rate is very close to that threshold: $\dot{Q}_{s,tot} = 0.299$ MW and $L_3 = 7.6$ cm. A further decrement of Γ would cause an error because water does not evaporate entirely and L_3 tries to become null and negative. This is the biggest limit in the current SG model and, in order to be capable of simulating more severe scenarios, the model requires some improvements. A few hints are given in Section 4.6.

Moreover, this limit of the moving boundary model may result in some issues when simulating ULOF scenario. In Subsection 3.4.3 it is calculated that with the old, static SG model natural circulation sets a value for Γ decreased by 69%. That is not promising. Chapter 5 correctly simulates ULOF with BELLA fully coupled to the moving boundary SG.

4.5.4. Inlet water temperature decrease

The remaining two subsections present the transients caused by sudden variations of water working conditions. They are intended to represent failures on the secondary side of the SG.

Here at $t = 10$ s, a step-wise 20% decrease of water inlet temperature is considered. Total simulation time is 40 s. The trend of the main variables of interest is displayed in Figure 4.14.

The impact of $T_{s,in}$ decrease is first of all on subcooled region: due to a higher subcooling degree, L_1 starts to increase immediately.
At the same time, $\dot{m}_{1,2}$ strongly decreases to about 1/3 of its nominal value (Figure 4.14f). This is explained by the first term inside square brackets in Eq. (4.91): ρ_{s1} suddenly increases because water at SG inlet becomes colder, $\frac{dL_1}{dt}$ is positive and, thus, because of the negative sign in front of the square brackets, $\dot{m}_{1,2}$ decreases. The decrement is instantaneous because Eq. (4.91) is algebraic. The other mass flow rates follow.

Both these effects have consequences on the rest of the system, which exhibits quick variations at the beginning of the transient. Since $\dot{m}_{in}$ is constant, all the other water mass flow rates come back almost immediately to their nominal value.

At the end of the transient, subcooled region has extended by 3.8 times, L_2 is about the initial value, while L_3 has decreased by 26% . Thermal power exchanged in region 1 increments by more than 4.5 times (due to the larger subcooling degree) and overcomes the decrease of thermal power in the other regions. As a consequence, total thermal power exchanged increases (Figure 4.14e).

Water temperatures show an overall decrease, especially in (and caused by) subcooled

region. Due to the larger total thermal power exchanged, the temperature difference of lead across the SG increases.

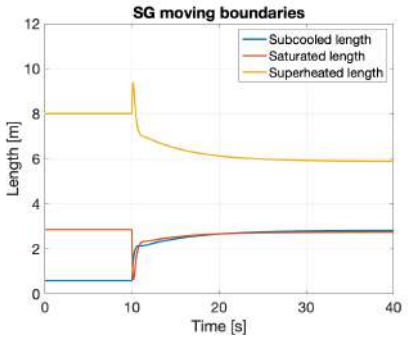

(a) SG regions lengths.

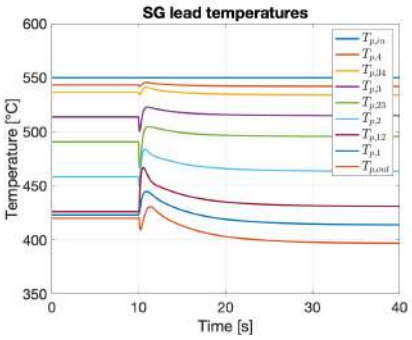

(b) Lead temperatures.

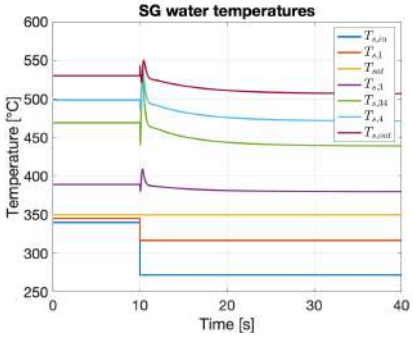

(c) Water temperatures.

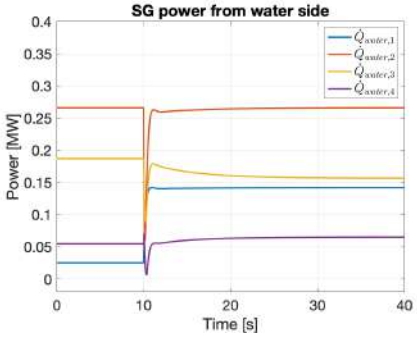

(d) SG power from water side in regions.

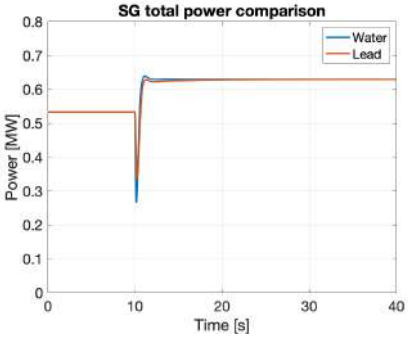

(e) Total power exchanged.

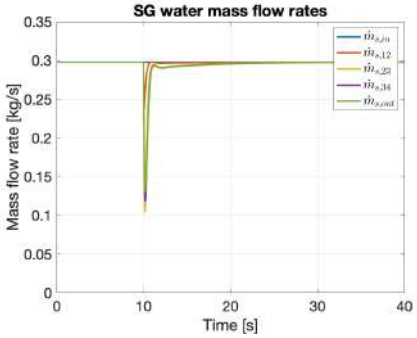

(f) Water mass flow rates.

Figure 4.14: Main plots resulting from $T_{s,in}$ 20% decrease simulation.

4.5.5. Water mass flow rate decrease

This is the last transient presented in this chapter. It tests the response of the SG after a sudden decrease of the water mass flow rate by 20%. This scenario is supposed to simulate a loss of flow accident on the secondary fluid.

In Simulink, a step-wise decrease of $\dot{m}_{in}$ is triggered at $t = 10$ s and the total simulation

time is 40 s. The trend of the main variables of interest is displayed in Figure 4.15.

Together with $\dot{m}_{in}$, all the other water mass flow rates instantaneously decrease as well, since they are related by algebraic equations. The same happens to power removed by water and, subsequently, to power exchanged by lead (Figure 4.15e). This worsens the cooling capabilities of the system and hence lead temperatures increase.
Although the power exchanged in all regions has decreased, due to the lower $\dot{m}_s$, also water temperatures increase reaching a higher superheating degree (Figure 4.15c). Consequently, superheated regions gets larger (Figure 4.15a).

From Figure 4.15d, the region characterized by the largest power loss is the saturated one.

As a general comment, the SG model reacts to a loss of flow in the secondary circuit by decreasing the total exchanged power and by increasing the temperatures of the system.

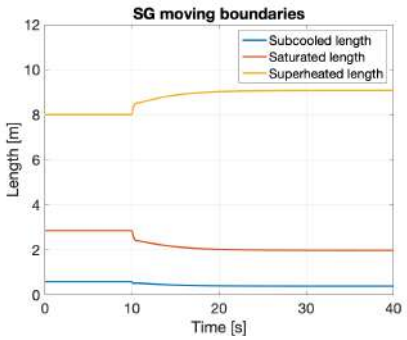

(a) SG regions lengths.

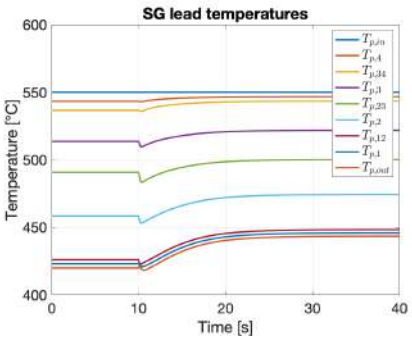

(b) Lead temperatures.

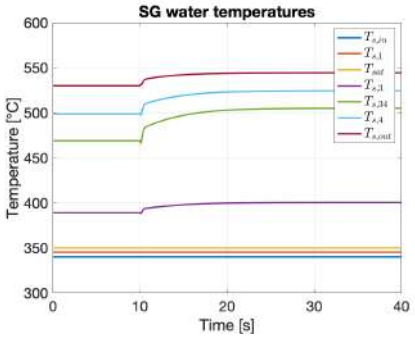

(c) Water temperatures.

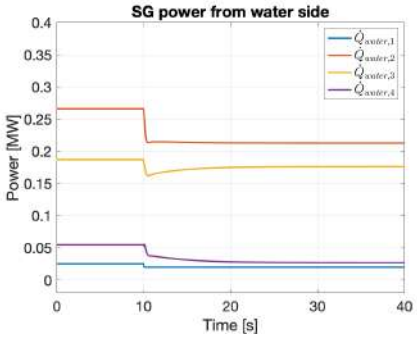

(d) SG power from water side in regions.

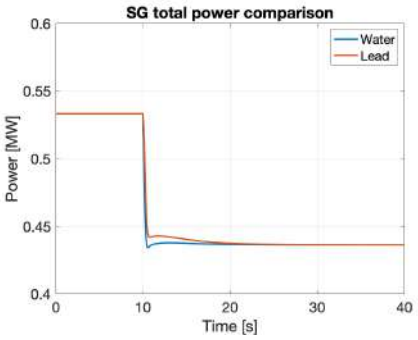

(e) Total power exchanged.

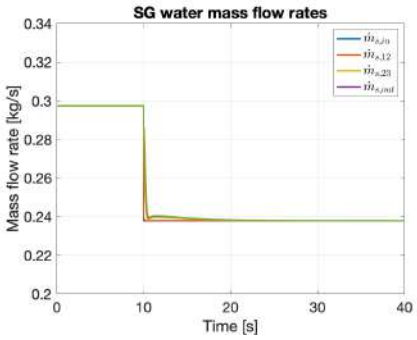

(f) Water mass flow rates.

Figure 4.15: Main plots resulting from $\dot{m}_{in}$ 20% decrease simulation.

4.6. Conclusions

This chapter focused on steam generator modeling adopting the specific layout of the SG modules foreseen in SUNRISE-LFR. Different approaches are presented and discussed, and the rationale behind the implemented choice is explained. It is the moving boundary approach, whose equations are step-by-step derived in Section 4.3. A little modification to the standard method is applied: superheated region is divided into two parts to improve accuracy and avoid unphysical behavior of the system. After building the model, it is

implemented in Simulink and utilized to simulate four accidental scenarios. They serve to test it as well as to prepare the ground for the next chapter, where it is integrated within BELLA.

This conclusive section is meant to give some general considerations about the code and to indicate possible directions to improve it.

As a general overview, the moving boundary SG is capable of correctly sustaining steady-state conditions and of simulating some reference accidental transients. The results seem to have physical sense as they can be explained in terms of relations between the input and output variables. That is the very first goal of this chapter.

Although with different intensities, all scenarios present some oscillations in lead temperatures which were labeled as "weird" in Subsection 4.5.2. On a more profound way, they are a consequence of parabolic equations (heat equations) which imply an infinite velocity for disturbances propagation: as soon as $T_{p,in}$ increases, all the dominion is affected. This is embodied in the system transfer function by the presence of some positive zeros, the real causes of the oscillatory behavior. In a certain way, the oscillations set to avoid violation of physics. This is an expected behavior because no transport equation is implemented: it would solve the issue and account for a finite velocity in heat propagation. However, that is not considered here.

In developing the model and discussing the simulations, some limits of the approach have already risen up.
First of all, this thesis lacks of a verification of the code against well-proved benchmarks. The author is aware of this limit and is open to future works where appropriate time can be dedicated to it. A reliable code which can be adopted in the verification procedure is RELAP [80]. Connected to this, a subsequent validation of the code against experimental data is of extreme interest to check the correctness and the accuracy of the model. Indeed, in parallel with the SUNRISE project, the SOLSTICE project (Section 2.1) aims at constructing an electrically-heated mockup where components and materials for SUNRISE-LFR will be tested. This is the environment where both the SG module and the moving boundary code are going to be validated.

Then, strictly speaking about the code, a lot of improvements can be pursued. Once available, correlations for Fe-10Cr-4Al-RE might substitute those of T91 steel to enhance the adherence to the real component. Different approaches for the two-phase flow can be explored (Appendix C), even though they can increase the number of equations and, thus, the complexity of the model. Also, momentum balance equation can be included in the moving boundary approach to calculate pressure drops along the SG and introduce a

more realistic time dependence on pressure.

Although all these are interesting ways to refine the newly built SG model, two additional strategies might lead to even larger improvements. They are discussed as follows.
It is absolutely necessary to expand the validity of the model also to those scenarios (or systems) characterized by low exchanged power and incomplete water evaporation. As already mentioned in Subsection 4.5.3, when the exchanged power decreases below a minimum value (necessary to evaporate all water), superheated region length tries to become negative and, thus, the SG model fails. It happens because the model is built to always have subcooled, saturated and superheated regions with positive, finite lengths. One way to cope with this limit is by constructing three sub-models A, B and C and by coupling them with simple conditional clauses. Model A has all three regions (subcooled, saturated and superheated), model B has only two regions (subcooled and saturated), while model C has only a single region (subcooled). Conditional clauses are based on the power $\dot{Q}$ exchanged by the fluids. The logical structure of the model is presented in Algorithm 4.1.

Algorithm 4.1 SG moving boundary sub-models logic.

if $\dot{Q} > \dot{m}_s(h_{s,g} - h_{s,in})$ **then**
    Model A
else if $\dot{m}_s(h_{s,l} - h_{s,in}) < \dot{Q} \leq \dot{m}_s(h_{s,g} - h_{s,in})$ **then**
    Model B
else
    Model C
end if

If the conceptual part is not difficult to understand, the practical development may face some annoying intricacies.

The second strategy to improve the code aims at gaining in the overall accuracy. As already done in Section 4.3, by increasing the total number of regions the spacial resolution of the module increases and the same does the accuracy. This does not compromise the nature of the approach, which remains lumped and moving boundary, but can potentially lead to benefits without largely increasing the computational effort. In this sense the idea is to divide both the subcooled and the superheated regions into smaller parts that can be called "zones" (Figure 4.16). The number of zones, which can be different in the two regions, can be user-defined according to the level of accuracy desired (e.g., more zones where gradients ∇T are high). This allows to have a versatile SG code which can be

tailored on the real module working conditions. For instance, a SG with a very large subcooling degree and a lower superheating degree might benefit from a large number of subcooled zones and a low number of superheated zones. The situation is the opposite for the SG envisaged for SUNRISE-LFR. One could also think about discretizing the saturated region, even though the benefits may not be significant. The general advantage in having an adaptive SG model can be enormous.

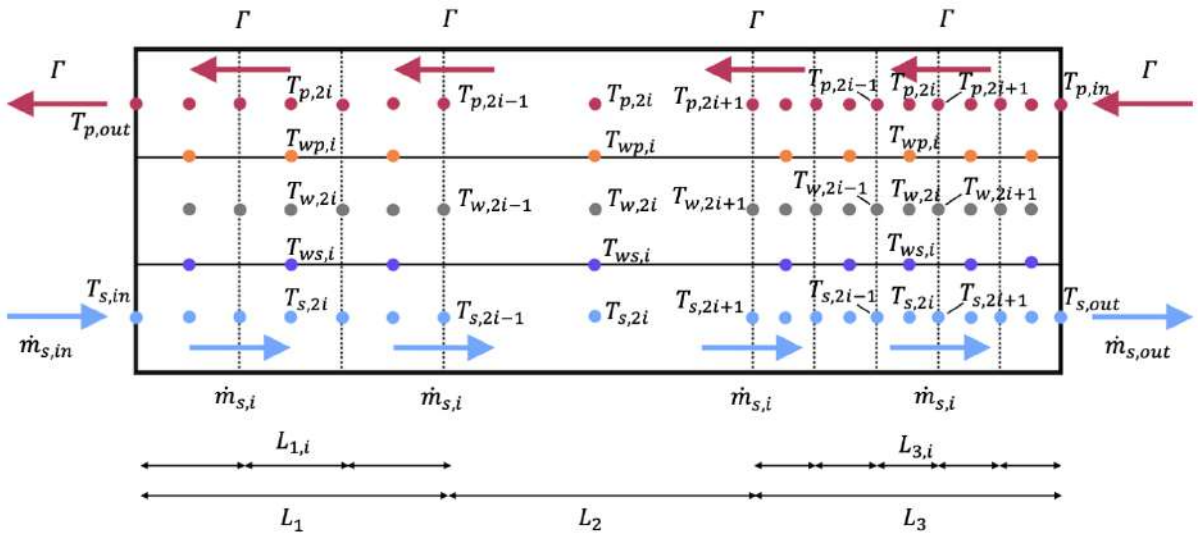

Figure 4.16: Scheme of the SG moving boundary model with user-defined zones for subcooled (3 zones) and superheated (5 zones) regions.

Moreover, the two strategies can be coupled, so that the obtained code is extremely powerful.

Both directions have been investigated by the author of this manuscript. The equations are derived and the Simulink codes are written. However, due to the aforementioned unexpected intricacies, an insufficient amount of useful and reasonable results has been obtained so far. Thus, that part is not included in this thesis. It would be interesting to dedicate more time to both in a future project.

As mentioned at the beginning of this chapter, the moving boundary SG is developed with the aim of coupling it with BELLA to overcome its oversimplified SG module. This is the topic of Chapter 5.

5 | Primary circuit and SG coupling

The ultimate goal of this thesis is to developed an improved version of BELLA able to represent lead-cooled fast reactors more realistically. The focus has been on the component connecting primary and secondary circuits − the steam generator −, developed in Chapter 4. The last chapter before conclusions completes the work by integrating the moving boundary SG within BELLA and by simulating the reference accidental scenarios UTOP and ULOF. Conversely, ULOHS and ULOF-ULOHS combined are not considered here because they are not affected by the new SG model. In fact, after the SG goes instantaneously from 100% power removal to 0 (ULOHS scenario), the module is disconnected from the primary system and does not influence it anymore.

This chapter is divided into three sections. Section 5.1 shows how Simulink allows to couple the newly developed SG model to BELLA. Section 5.2 presents the simulated transients underlying the differences between the old static SG and the new SG model. Lastly, Section 5.3 summarizes and concludes the chapter.

5.1. Simulink implementation

The compatibility between BELLA and the new SG code is on different levels. Firstly, they share the zero-dimensional approach to describe the physical system. Secondly, they are very (BELLA) or quite (SG model) fast in computing the simultions. Thirdly, both codes are developed within MATLAB/Simulink® and so they are written as explicit systems of differential and algebraic equations (DAE) visualized in terms of subsystems with input and output variables, very easy to connect. This really facilitates the procedure.

In SUNRISE-LFR's primary circuit the SG interacts only with the hot leg and the cold leg. Therefore, without aiming at great aesthetics of the resulting graphical interface, but focusing only on the efficiency and practical simplicity of the blocks manipulation, the SG subsystem (blue block) is collocated within the primary system energy balance subsystem

(Figure 5.1). It receives as inputs lead temperature at SG inlet, its derivative and lead mass flow rate, while computes as outputs for BELLA lead temperature at SG outlet and lead average temperature in SG.

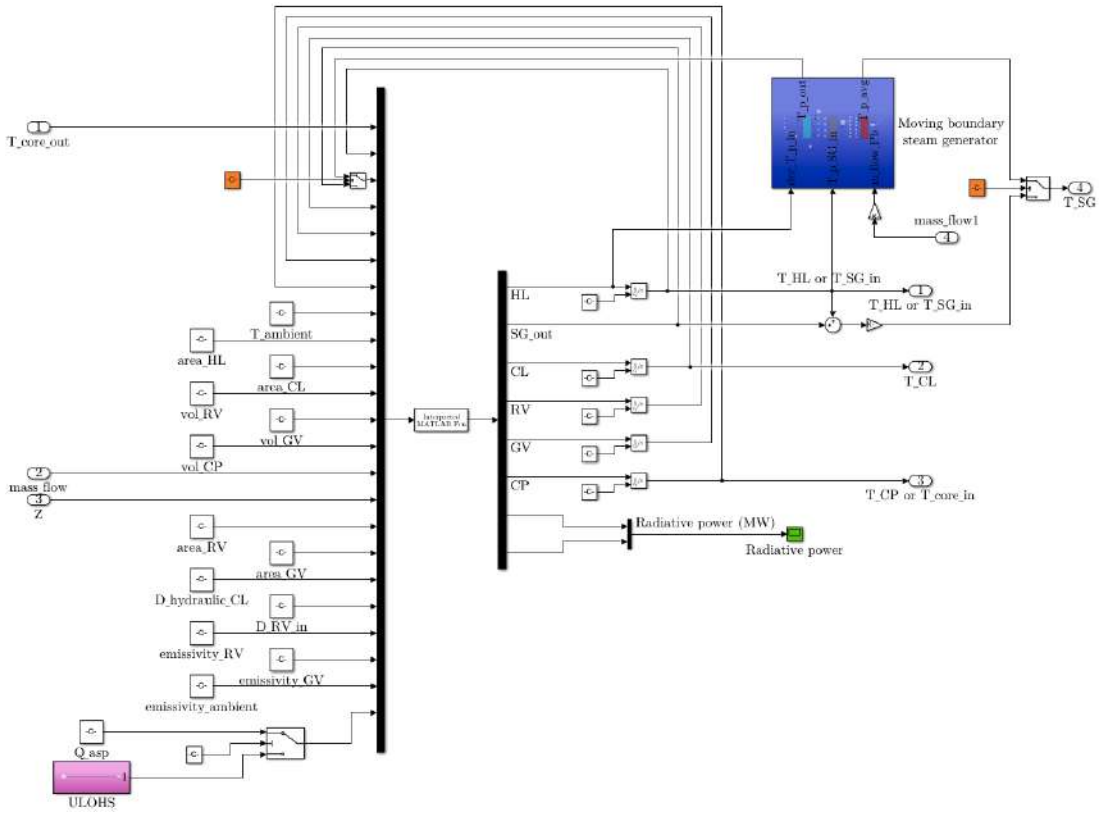

Figure 5.1: Primary system energy balance with moving boundary SG (blue) in Simulink.

Since the SG model is configured for a single tube in a single SG, lead mass flow rate coming from primary circuit is divided by the number of SGs, 10, and by the number of tubes in a SG, 15. All the rest of BELLA and of the moving boundary SG does not change.

5.2. Simulations

As already discussed in Chapter 3, BELLA current capabilities include simulation of unprotected transient over-power (UTOP), loss-of-flow (ULOF), loss-of-heat-sink (ULOHS) scenarios and a combination of ULOF and ULOHS (station blackout). Its coupling with the newly developed SG model is supposed to affect UTOP and ULOF transients because the strong hypothesis of static steam generator is removed. However, any transient which includes ULOHS does not benefit at all from the new SG module because, before the accident is triggered, static model and moving boundary model provide the same result

and, after the accident is triggered, the module is not used anymore. Therefore, ULOHS and ULOF-ULOHS combined are not simulated in this chapter. For their results, the reader is referred to Section 3.4.

This section starts with steady-state conditions of SUNRISE-LFR and then it proceeds by showing simulation results in UTOP and ULOF. It serves both to test the coupling of the codes, to check the differences from previous simulations (with the static SG) in order to assess the limits of the assumed constant SG power removal, and to verify safety margins of the demonstrator reactor under accidental scenarios.

The general Simulink settings adopted in these transients are briefly discussed in Appendix D.

5.2.1. Steady-state conditions

BELLA and SG fully coupled perfectly sustain steady-state conditions. They are set by total power of the reactor, lead temperature at core inlet, lead mass flow rate, total amount of lead inside the primary system, water temperature and mass flow rate at SG inlet. Due to the absence of any transient, only core thermal power and regions lengths are plotted (Figure 5.2). Total simulation time is 4000 s. Nominal values of the most important parameters of SUNRISE-LFR and of the SG are listed in Table 5.1.

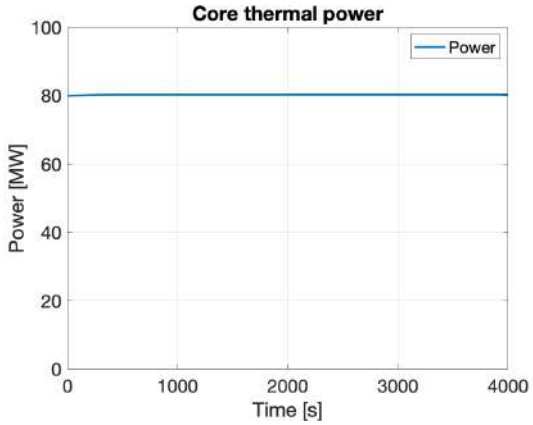

(a) Constant core thermal power.

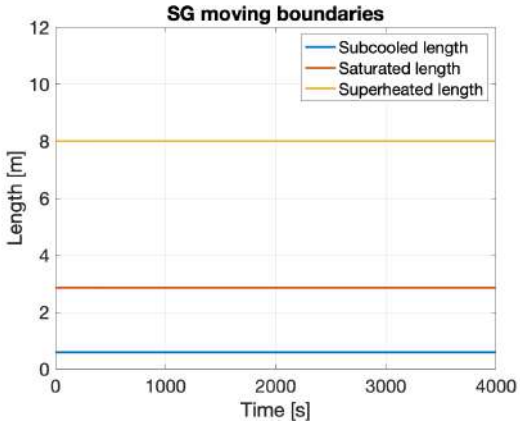

(b) Constant regions lengths.

Figure 5.2: Simulation results adopting BELLA fully coupled with the SG in steady-state conditions.

Quantity	Value	Unit
Core thermal power	80.33	MW
Fuel average temperature*	643.8	°C
Fuel max temperature**	867.8	°C
Clad average temperature*	496.2	°C
Clad max temperature**	559.7	°C
Lead core average temperature	484.8	°C
Lead core inlet temperature	419.6	°C
Lead core outlet temperature	550.0	°C
Lead mass flow rate	4247.2	kg/s
HL free surface level	2.947	m
Radiative power losses from the RV***	328	kW
All SGs thermal power removal	80.00	MW
Subcooled region length	0.591	m
Saturated region length	2.854	m
Superheated region length	8.008	m
Water inlet temperature	340.0	°C
Water outlet temperature	530.0	°C
SG total water mass flow rate	4.461	kg/s

Table 5.1: BELLA-SG steady-state values for the most important quantities. For the starred parameters look at the notes after Table 3.8.

5.2.2. UTOP

It is modeled as a sudden (step-wise) insertion of positive reactivity through the external contribution $\Delta\rho_{ext}$. Its value is 0.2 \$ which corresponds to 133 pcm.

By setting the simulation time to 2000 s and triggering UTOP after 500 s, the major quantities of interest are plotted in Figures 5.3 and 5.4.

The beginning of the transient is identical to Subsection 3.4.2 and here it is just summarized. The insertion of 0.2 \$ of external reactivity increases immediately neutron population, thus core thermal power. Subsequently, all core temperatures (fuel, cladding and lead) grow activating reactivity feedbacks (Doppler, fuel axial expansion and core thermal expansion) which partially counterbalance external reactivity injection. At the

same time, lead temperature increment propagates through the hot leg and arrives at the steam generator. There, lead temperatures in all regions increase and, therefore, lead exchanges more thermal power to the secondary fluid, water, which increases in temperature as well. As a consequence, the SG increments the superheated region length, while subcooled and saturated regions become shorter, even though they continue to exchange the same amount of power (water temperature and mass flow rate at SG inlet are constant throughout the whole transient).

Following lead flow in the primary circuit, cold leg and cold pool increase in temperature, and that allows radial reactivity feedback to enter into play: reactivity is decreased further and reaches negative values around $t = 630$ s. Hence, core thermal power starts decreasing and the same do all system temperatures until steady-state conditions are met: reactivity is null and all temperatures are stabilized.

Differently than the results of BELLA standalone, the moving boundary SG allows the core to increase its thermal power after reactivity injection, as it should be. In fact, after an insertion of 0.2 \$, final core power is approximately 95 MW starting from 80 MW in nominal conditions. At the same time, also the SG modules have increased their total power removal from 80 to 95 MW, although with some delay and without peaking at around 155 MW as the core does. The area between two curves (core power and SG power in Figure 5.3a) corresponds to the energy that is stored inside the system: it explains in another way that the system (fuel, cladding, lead and water) has increased its overall temperature. To be precise, also thermal radiation losses need to be considered, but they are are always less than 700 kW, so they can be neglected in the energy balance at a first rough approximation.

Due to thermal expansion, HL free surface level increases by almost 6%. Moreover, due to the specific dependence of lead mass flow rate derivative on lead temperatures (buoyancy and frictional terms), $\dot{m}_{Pb}$ slightly increases by about 1.6%. However, lead flow velocity never overcomes 0.90 m/s inside the core (the most critical environment due to the small area of flow channels), keeping a good margin to erosion.

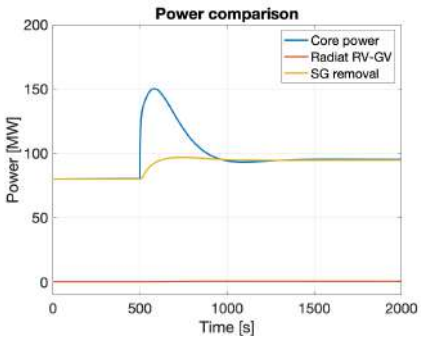

(a) System power comparison.

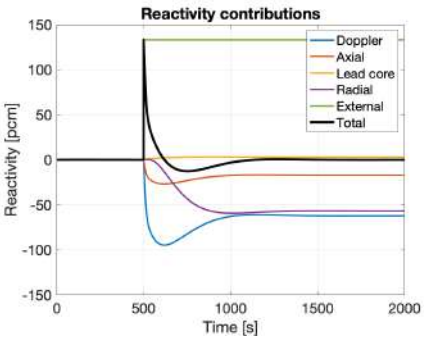

(b) Reactivity contributions.

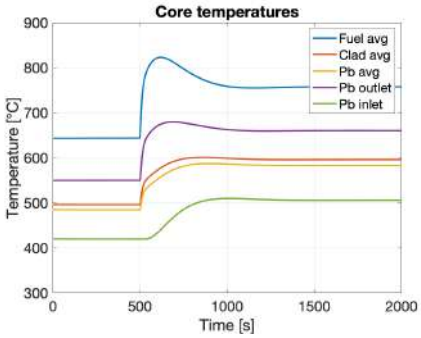

(c) Core temperatures.

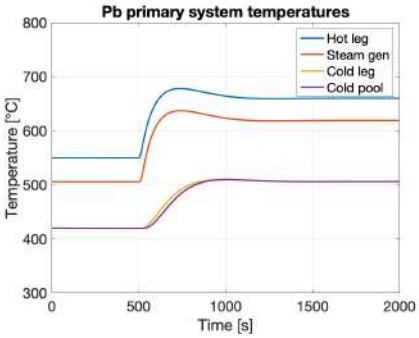

(d) Primary system temperatures.

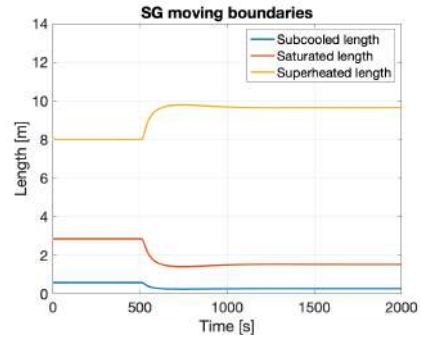

(e) SG regions lengths.

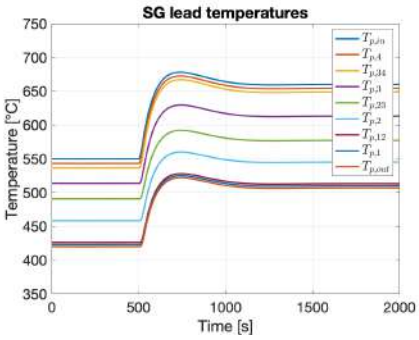

(f) SG lead temperatures.

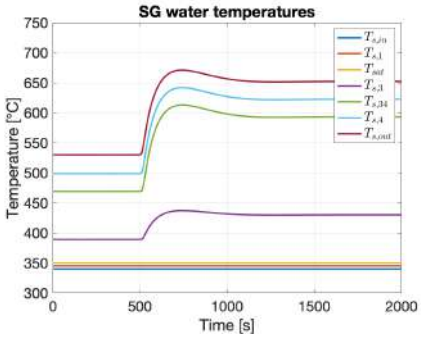

(g) SG water temperatures.

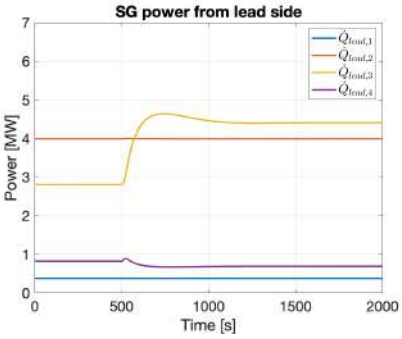

(h) SG power from lead side in regions.

Figure 5.3: Main plots resulting from UTOP simulation.

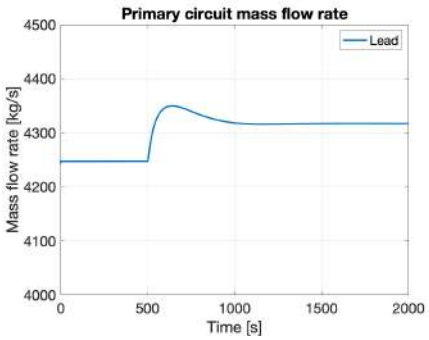

(a) Lead mass flow rate.

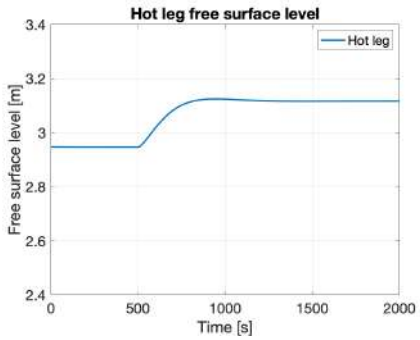

(b) HL free surface level.

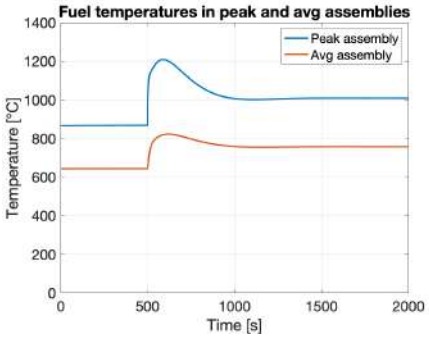

(c) Fuel temperature in the peak** and average* assemblies.

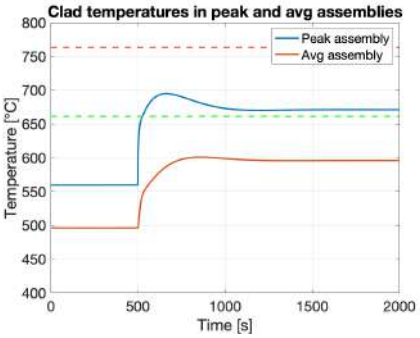

(d) Cladding temperature in the peak** and average* assemblies.

Figure 5.4: Additional plots resulting from UTOP simulation. For the starred parameters look at the notes after Table 3.8.

The last two plots (Figures 5.4c and 5.4d) show the behavior of fuel and cladding in the peak assembly (innermost node at the worst axial position) and in the average assembly (average node at the midplane). This is the meaning of the legend present in the two plots which remains valid for all the other simulations.
As for all scenarios investigated so far, fuel undergoes a significant temperature increase, but stays well distant from the melting point (2850 °C). On the contrary, cladding overcomes the first threshold at 662 °C in the peak assembly, even though by only 9 °C, while the average assembly remains about 65 °C below it. However, the second threshold at 763 °C is never reached.

Table 5.2 lists the value of the main variables of interest after UTOP simulation. It also includes their percentage variation with respect to steady-state values and to BELLA previous version simulation (Subsection 3.4.2).

Quantity (unit)	Value	Variation (S.S.)	Variation (BELLA)
Core thermal power (MW)	95.31	+18.7%	+18.0%
Fuel average temperature* (°C)	757.5	+17.7%	+2.5%
Fuel max temperature** (°C)	1008.6	+16.2%	+5.8%
Clad average temperature* (°C)	596.0	+20.1%	-0.9%
Clad max temperature** (°C)	671.1	+19.9%	+0.8%
Lead core average temperature (°C)	583.0	+20.3%	-1.3%
Lead core inlet temperature (°C)	505.9	+20.6%	-3.6%
Lead core outlet temperature (°C)	660.1	+20.0%	+0.6%
Lead mass flow rate (kg/s)	4316.9	+1.6%	+0.4%
HL free surface level (m)	3.117	+5.8%	-0.9%
Radiative power losses from the RV*** (kW)	646	+103.8%	-11.6%
All SGs thermal power removal (MW)	94.67	+18.3%	-
Subcooled region length (m)	0.277	-53.2%	-
Saturated region length (m)	1.528	-46.5%	-
Superheated region length (m)	9.649	+20.5%	-
Water inlet temperature (°C)	340.0	0%	-
Water outlet temperature (°C)	652.2	+23.1%	-
SG total water mass flow rate (kg/s)	4.461	0%	-

Table 5.2: BELLA-SG steady-state values for the most important quantities. The same notes highlighted in Table 3.8 remain valid here.

Although the adoption of the moving boundary SG model results in some evident changes with respect to UTOP simulated in Subsection 3.4.2, in particular in the new core power level, the overall behavior of the system does not seem to significantly vary. Also the major conclusions in terms of safety margins to fuel melting and cladding creep failure remain unchanged from Subsection 3.4.2.

5.2.3. ULOF

It is the last accidental scenario presented in this chapter. A complete ULOF transient envisages a 100% failure of all the pumps in the system, modeled by an exponential

decrease of the pump pressure head from nominal value to zero with a time constant equal to 10 s.

However, BELLA fully coupled with the moving boundary SG is not capable of simulating such a demanding scenario and the reason is the following. As already discussed in Chapter 4, one of the limits of the new SG model is in simulating scenarios with low power exchanged between the fluids. If the power is lower than a minimum quantity $\dot{Q}_{s,min}$ (Eq. (5.1)), equal to the power required to evaporate all water flow, an error appears and the model fails. This is evident in superheated region's length L_3 or power $\dot{Q}_{superheated}$: they all decrease toward zero and, when the condition of minimum power does not hold anymore, they try to become negative, which is not allowed by the code (Figure 5.5). In that instant the error rises up stopping the simulation from continuing. Another symptom is in water temperatures in superheated region: they all approach the saturation point and try to go below it in case the exchanged power is not enough to complete water flow evaporation.
The minimum exchanged power for one SG unit is:

$$\dot{Q}_{s,min} = \dot{m}_s(h_{s,g} - h_{s,in}) = 4.365 \text{ MW} \tag{5.1}$$

which means 0.291 MW per single tube or 43.65 MW considering all 10 SGs.

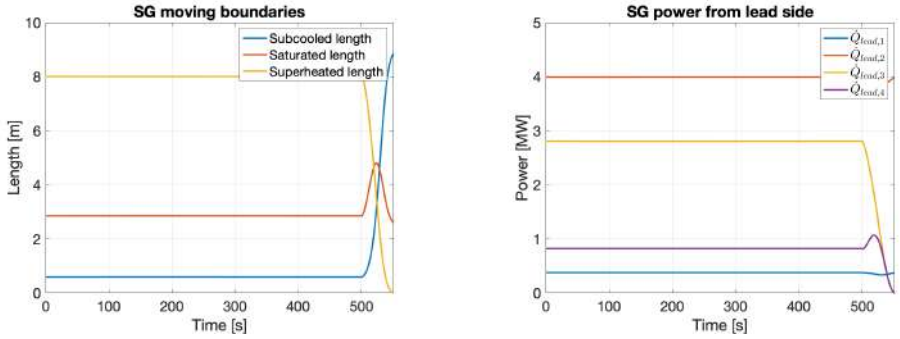

(a) SG regions lengths. (b) SG power from lead side in regions.

Figure 5.5: Error on ULOF scenario: both L_3, Q_{p3} and Q_{p4} arrived at 0.

ULOF is the transient suffering the most from this limit because as soon as the pump stops working, lead mass flow rate decreases inducing a temporary reduction both in core thermal power and in power removed by the SG. If $\dot{Q}_{SG,tot}$ stays above 4.365 MW throughout the whole transient, no problem occurs. But in a complete ULOF this is not the situation. With a total failure of all system pumps, SG thermal power goes temporarily below the threshold and the code fails (again Figure 5.5). The system needs

to keep at least 3% of pump pressure head in order to successfully simulate the scenario.

Because of these reasons, only partial ULOF transients are hereafter presented. In particular, the main discussion is about a ULOF scenario which keeps 3% of pump pressure injection, while at the end of the section some comments are given about ULOF keeping 5%, 10%, 20%, 30% and 50% of pump pressure head. This is how they are named: x% ULOF means a ULOF transient which keeps x% of pump pressure injection.

By setting the simulation time to 3000 s and triggering 3% ULOF after 500 s, the major quantities of interest are plotted in Figures 5.6, 5.7 and 5.8.

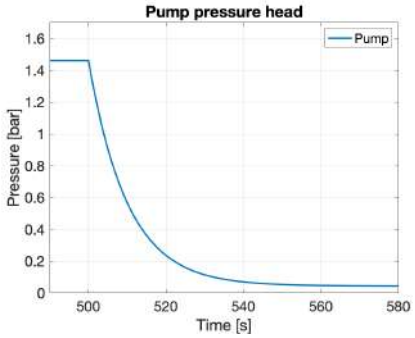

(a) Pump partial failure: exponential decrease of pressure head to 3% of its nominal value.

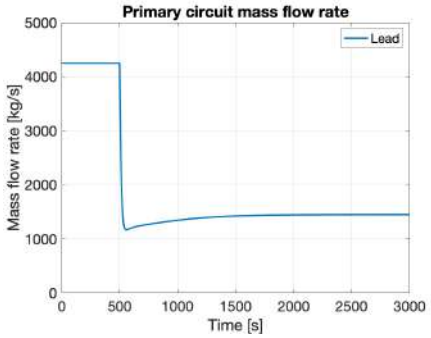

(b) Lead mass flow rate.

Figure 5.6: Pump and mass flow rate in 3% ULOF simulation.

The partial failure of the pumps affects immediately lead mass flow rate (Figure 5.6b), which begins a steep decrease and stops only once natural circulation has established. This has consequences both on core and SG.
At a core level, all temperatures (fuel, cladding and lead) increase activating reactivity feedbacks (Doppler, fuel axial expansion and core thermal expansion) which start to decrease core power level. As a consequence, after an initial peak, core temperatures begin to decrease. In the meantime, hotter lead propagates through the hot leg and arrives at the inlet of the SG.

In the SG the fall of lead mass flow rate has a great impact. Remembering that $\dot{Q}_p = \Gamma c_p \Delta T_p$, power exchanged by lead decreases immediately affecting all SG regions in different ways one to another.
In subcooled and saturated regions, since $\dot{Q}_s$ is almost constant (water conditions at SG inlet do not change), the lower $\dot{Q}_p$ determines a strong decrease of lead temperatures in such a way that ΔT_p across these regions greatly increases and compensates for the loss

of primary flow. Steady-state conditions are met very rapidly with $\dot{Q}_p$ coming back to its initial value.
Conversely, in superheated regions $\dot{Q}_s$ can follow $\dot{Q}_p$ decrease, inducing a strong lowering in all water temperatures down almost to the saturation point (350 °C). Therefore, superheated region's length L_3 strongly decreases (it almost disappears), while L_2 and L_1 raise up with large steep. Due to $\dot{Q}_p$ decrement, also lead temperatures drop, but very shortly hotter lead arrives from the HL and heats up superheated regions on both sides, lead and water. Accordingly, SG lengths change: L_3 increases back to about one half of its initial value, while L_1 decreases to about one half of its peak value and L_2 comes back to approximately its nominal value. $\dot{Q}_p$ and $\dot{Q}_s$ follow.
Eventually this is the effect on the SG: $T_{p,in}$ and $T_{s,out}$ increase while $T_{p,out}$ decreases.

Colder lead at SG outlet flows through the CL and the CP and reaches the core inlet. There, it activates the radial diagrid feedback coefficient which increases reactivity to a positive value. Thus, core power increases and eventually reaches a larger value than the nominal one. The same applies for the SG (due to conservation of energy), which continues to sustain the trends of its temperatures and regions lengths described above.

After smooth oscillations in core temperatures, the final system configuration is the following: higher core and SG thermal power (86 MW), larger ΔT_{Pb} across the core and the SG, an increased water superheating degree ($T_{s,out}$ = 576 °C) and primary coolant flow rate at 1450 kg/s thanks to buoyancy forces.
The net contribution to lead thermal expansion is slightly negative, therefore HL free surface level has slightly decreased.

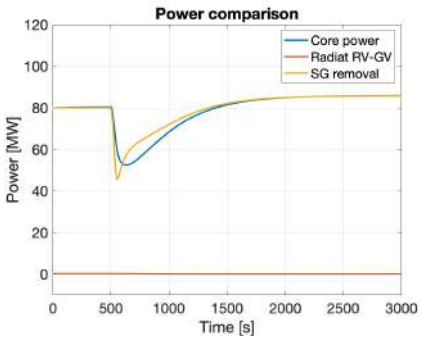

(a) System power comparison.

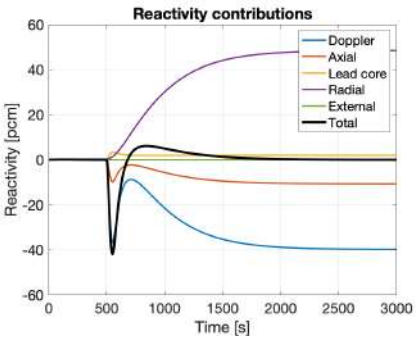

(b) Reactivity contributions.

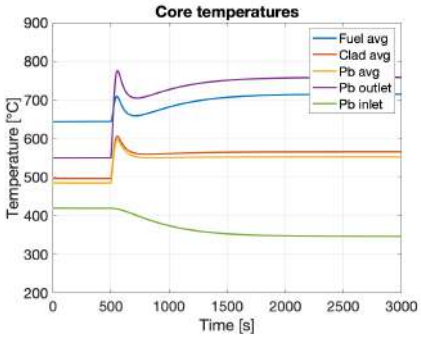

(c) Core temperatures.

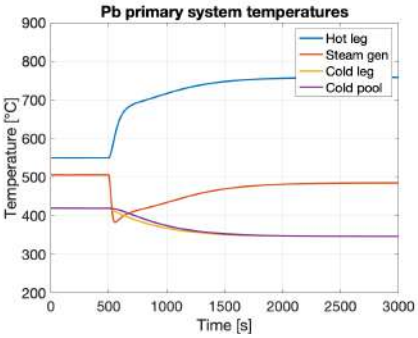

(d) Primary system temperatures.

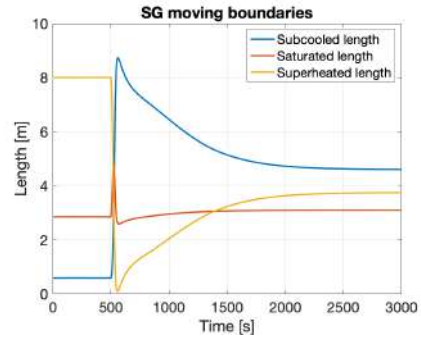

(e) SG regions lengths.

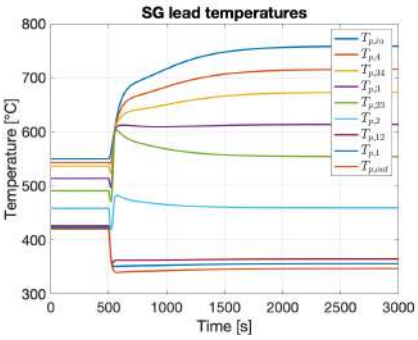

(f) SG lead temperatures.

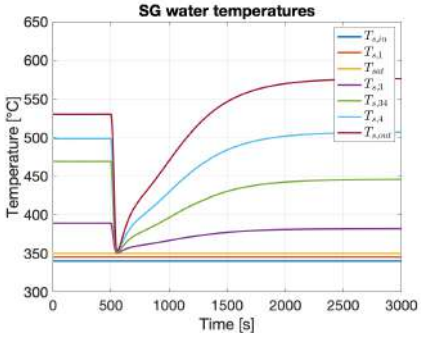

(g) SG water temperatures.

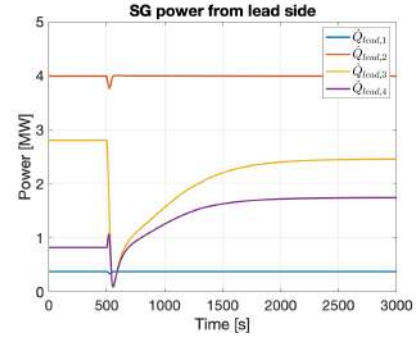

(h) SG power from lead side in regions.

Figure 5.7: Main plots resulting from 3% ULOF simulation.

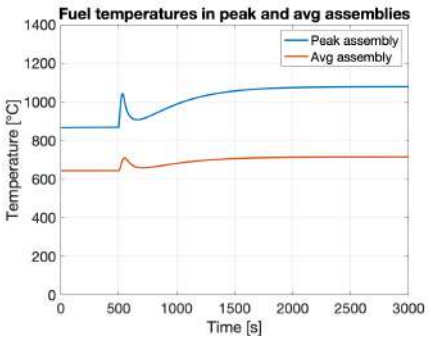

(a) Fuel temperature in the peak** and average* assemblies.

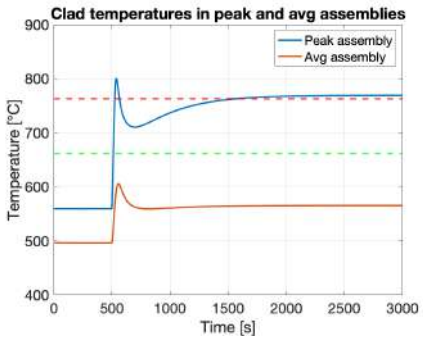

(b) Cladding temperature in the peak** and average* assemblies.

Figure 5.8: Additional plots resulting from 3% ULOF simulation. For the starred parameters look at the notes after Table 3.8.

Focusing on the safety margins, it can be repeated what is written in Subsection 3.4.3. Fuel is always very distant from the melting point; cladding in the average assembly maintains a good margin to creep failure while cladding in the peak assembly overcomes both creep thresholds at final steady-state values. This is a concerning final configuration because the system does not meet the safety requirements for thermal creep, confirming the preliminary conclusions of Subsection 3.4.3. In addition, around $t = 570$ s lead temperature at SG outlet reaches a minimum (340 °C) and then stabilizes at 347 °C, very near to lead melting point (327.5 °C). This increases the coolant freezing risk and adds concerns about liquid metal embrittlement (LME).
The transient needs a better investigation adopting spacial resolving codes (1-d, 2-d or even 3-dimensional tools) to confirm the general results.

Table 5.3 lists the value of the main variables of interest after 3% ULOF simulation. It also includes their percentage variation with respect to steady-state values and to BELLA previous version simulation (retaining 3% pump head).

Quantity (unit)	Value	Variation (S.S.)	Variation (BELLA)
Core thermal power (MW)	85.81	+6.8%	+7.0%
Fuel average temperature* (°C)	714.9	+11.0%	+1.4%
Fuel max temperature** (°C)	1078.7	+24.3%	+2.9%
Clad average temperature* (°C)	565.5	+14.0%	+0.1%
Clad max temperature** (°C)	769.2	+37.4%	+1.5%
Lead core average temperature (°C)	552.4	+14.0%	<-0.1%
Lead core inlet temperature (°C)	346.6	-17.4%	-2.9%
Lead core outlet temperature (°C)	758.2	+37.9%	+1.4%
Lead mass flow rate (kg/s)	1449.6	-65.9%	+1.7%
HL free surface level (m)	2.918	-1.0%	-0.4%
Radiative power losses from the RV*** (kW)	141	-55.4%	-16.6%
All SGs thermal power removal (MW)	85.72	+7.2%	-
Subcooled region length (m)	4.607	+679.4%	-
Saturated region length (m)	3.099	+8.6%	-
Superheated region length (m)	3.747	-53.2%	-
Water inlet temperature (°C)	340.0	0%	-
Water outlet temperature (°C)	576.2	+8.7%	-
SG total water mass flow rate (kg/s)	4.461	0%	-

Table 5.3: BELLA-SG steady-state values for the most important quantities. For the starred parameters look at the notes after Table 3.8.

As it was true for UTOP, also in case of ULOF the adoption of the moving boundary SG confirms the general results obtained with the static SG model. Apart from the different core power level, all temperatures remain within a 3% variation with respect to BELLA standalone simulation, and most of them are within a 2% interval. The same holds for lead mass flow rate.

What is surprising about the system is its response after a loss of flow. The pumps partial failure decreases coolant mass flow rate, but the reactor does not drive toward a lower power configuration. Instead, final thermal power has increased by 7% with respect to nominal value. This behavior is confirmed by the simulation of different amplitudes

ULOF scenarios. Figure 5.9 shows core thermal power trends for ULOF with 50%, 30%, 20%, 10%, 5% and 3% of retained pump pressure head.

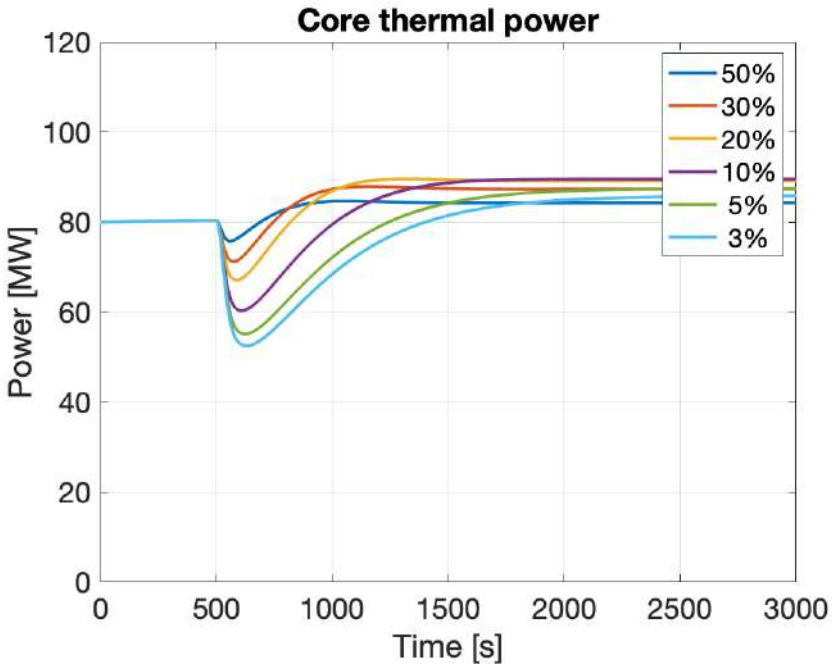

Figure 5.9: Core thermal power in partial ULOF scenarios.

Although the current version of the moving boundary SG does not allow to investigate a complete ULOF, the behavior depicted above suggests that the system is able to keep a large core thermal power, ever higher than in nominal conditions, always removed by an increased SG thermal power. This is accounted by increasing the coolant temperature difference across the core and the SG. Therefore, the system does set on stable, steady-state conditions, but at expense of a worse temperature distribution: hot regions become hotter and cold regions become colder. Table 5.4 lists final core thermal power in the transients shown in Figure 5.9.

Quantity (unit)	**50%**	**30%**	**20%**	**10%**	**5%**	**3%**
Core thermal power (MW)	84.28	87.31	89.15	89.57	87.41	85.81
Variation to S.S. (-)	+4.9%	+8.7%	+11.0%	+11.5%	+8.8%	+6.8%

Table 5.4: Core thermal power after partial ULOF (x% indicates the percentage of retained pump pressure head).

To conclude this subsection, although cladding safety margins mights be compromised

even under a partial (but significant) ULOF, it must be always remembered that this is a severe accident whose likelihood of occurring is known to be very low. Also, it relies on a very conservative, probably even unrealistic, assumption on fission gas release to calculate creep thresholds (Section 2.2).

5.2.4. ULOHS

As already mentioned, the inclusion of the moving boundary SG does not change the simulation of this transient. It results exactly as in Subsection 3.4.4, to which the reader is referred.

5.2.5. ULOF and ULOHS

As already mentioned, the inclusion of the moving boundary SG does not change the simulation of this transient. It results exactly as in Subsection 3.4.5, to which the reader is referred.

5.3. Conclusions

This chapter coupled BELLA with the newly built SG model, exploiting their excellent compatibility both in terms of the general approach (lumped, fast codes) and in terms of the software utilized for their development (MATLAB/Simulink). This final section is meant to give general considerations about Chapter 5, outlining its major achievements, limits and possible future directions of improvement.

As a first general comment, the codes coupling has been successful. The integrated code is able to correctly sustain steady-state conditions and to simulate reference accidental scenarios UTOP and (partial) ULOF, decreasing but not compromising the computational speed of the software. Calculated results are in line with physical expectations and can be reasonably described in terms of the causal relations between input and output variables. This is surely a first important goal of the chapter.

Moreover, the code confirms the overall results obtained by the previous version of BELLA with the static SG, which does not appear to be such an unreasonable assumption, even if it needs to be taken with great attention. Speaking about the static SG, here the reference is only to the constant power removal one modeled by Eq. (3.62).

However, a non-negligible limit of the integrated code raised up. The current version of the SG does not allow to simulate a complete unprotected loss of flow transient. That is the

reason why only partial ULOF scenarios are computed and presented. The causes of that limit are well-known and more than once explained (Section 5.2.3 as well as Chapter 4). They are related to the basic assumption of the moving boundary SG for which the three regions (subcooled, saturated and superheated) need to exist in any working conditions. A possible strategy to remove that hypothesis without abandoning the moving boundary approach leverages on three different sub-models A, B and C coupled together and each representing a SG with a different number of regions: 3, 2 and 1. In this way, transients with low exchanged power, caused by large losses of flow for instance, can be simulated. More details are given in Section 4.6.

Other areas of improvement of the code refer specifically to BELLA on the one side and to the moving boundary SG on the other side. They are described in the dedicated chapters and here only reminded:

- BELLA: neutronics (decay power), structural materials correlations, primary circuit pressure losses, RVACS natural convection, thermomechanical module.
- SG: structural materials correlations, two-phase flow modeling, pressure drops in water side, discretization of subcooled and superheated regions to gain in accuracy and versatility.

Last comments are devoted to the general results of the simulations and to SUNRISE-LFR capability of maintaining safe conditions. Details about each scenario are given in the dedicated subsections. SUNRISE-LFR shows an important capacity of resisting to severe accidents. This is true especially when fuel melting is taking as a reference: excellent properties of uranium nitride and passive safety mechanisms (natural circulation and RVACS) give to the system a high degree of inherent safety which keeps the margin to fuel melting point always very large.
However, a more than concerning situation regards fuel cladding creep rupture. This emerges as the weakness of the current design of SUNRISE-LFR because both in UTOP and ULOF scenarios the safety margin is significantly stressed. In UTOP fuel cladding temperature in the peak assembly consumes more than half of the margin to creep rupture (at 662 °C) when the steady-state final value is considered. In ULOF the situation is even worse because cladding temperature in the peak assembly overcomes also the second threshold (at 763 °C), which means that, if it stays at that temperature assuming a 100% fission gas release, cladding tube breaks after seven days. In any case, it is appropriate to mention that in both transients cladding temperature in the average assembly (at core midplane) does not exhibit any problem at all.
Another issue arising in ULOF is about cold lead pools (CL, CP and core inlet). They

undergo a considerable temperature decrease (final temperature is 347 °C) which poses the attention on coolant freezing risk and on liquid metal embrittlement (LME).

SUNRISE-LFR is designed with the intent of resisting to severe unprotected accidents for seven days before any intervention of the plant operator. One safety requirement is that fuel cladding temperature does not consume more than half of the margin to creep rupture. This does not seem to be respected under the assumptions of the code and under the very conservative hypothesis on thermal creep: as explained in Section 2.2, the safety margins are calculated assuming 100% fission gas release (FGR) in order to be as much conservative as possible. However, a recently published correlation for FGR [55] in uranium nitride fuels calculates that the maximum FGR is less than 10%, even assuming fuel temperatures higher than the ones registered in UTOP and ULOF simulations. This suggests that probably the two thresholds for creep failure adopted in this work are extremely conservative and could be relaxed.
In any case, and without any doubt, ULOF transient requires a deep investigation adopting accurate codes to describe an LFR core with a good spacial resolution.

As a last remark, it has to be remembered that UTOP and ULOF are severe accidental scenarios whose likelihood of occurring is regarded to be extremely low. But this is exactly what design basis accidents are supposed to be and their simulation is extremely important in understanding the behavior of nuclear systems under low-probable but severe events.

6 | Conclusions and future developments

This manuscript presented the thesis work conducted over a seven-month period at Royal Institute of Technology in Stockholm, Sweden. It introduced the state-of-the-art of lead-cooled fast reactors, mentioning the major benefits and challenges that they pose, and described in detail the Swedish demonstrator, SUNRISE-LFR, to which this work is mainly referred. The ultimate goal has been to provide an efficient, accurate but simple zero-dimensional plant simulator oriented to the dynamics and control of LFRs. Chapters 3, 4 and 5 are fully dedicated to it. In particular, leveraging on the already existing BELLA code, which is updated and improved in some parts, a new model for the steam generator (SG) is developed, tested and coupled to BELLA in order to simulate reference accidental scenarios. They are unprotected transient overpower (UTOP), unprotected loss of flow (ULOF), unprotected loss of heat sink (ULOHS) and station blackout modeled as a combination of ULOF and ULOHS.

The choice for the SG module is the moving boundary approach, a lumped model which is able to track efficiently the dynamics of the SG three regions (subcooled, saturated and superheated) without compromising the speed of the overall software. It can be claimed that the results are very satisfying: the integrated code is capable of simulating the reactor normal and off-normal conditions providing physically reasonable results.
However, the complete ULOF transient cannot be simulated due to the biggest limit of this SG model: if the exchanged thermal power decreases below a given threshold (power necessary to evaporate all water flow), the model fails. This is why only partial ULOF are simulated and commented.

The reactor under test is SUNRISE-LFR, whose safety requirements are severely stressed. The demonstrator is designed to withstand an unprotected accidental scenario for seven days without compromising the safety margins to fuel melting and cladding tube creep rupture. In particular, no more than half of the safety margin to creep failure is allowed to be consumed (Section 2.2).

In all simulations, fuel melting is far from being an issue. Its safety margin is always sufficiently large (>1500 °C) to state that it is extremely unlike that it occurs. However, cladding creep failure appears to be of great concern, especially when it comes to UTOP and ULOF: in the first case half of the margin to creep rupture is consumed and in the second case the whole margin is gone. Moreover, under ULOF another issue must be carefully considered: in cold pools (CL, CP and core inlet) lead goes worryingly near the melting point, increasing the freezing risk and liquid metal embrittlement effects. On the other hand, ULOHS and ULOF-ULOHS combined do not suffer from any of these problems; their only concern is an overcooling of the system in the long term that can lead to coolant solidification.
Nevertheless, a critical discussion on simulations outcomes needs always to take into account the assumptions on codes, on transient conditions and on safety margins. In this work, very conservative hypotheses are adopted and, although this might be considered a bit excessive, for instance in terms of the safety margin to creep failure (Section 2.2), it is the standard procedure in design basis accidents safety analysis.

BELLA and the newly developed SG model need an intense benchmark against a reference code for liquid metal fast reactors. That is expected to be done in the near future and the reference code is SAS4A/SASSYS-1.

At the same time some directions of improvement can be pursued, addressing both the primary circuit and the SG models. In particular, about the SG Section 4.6 suggests a strategy to achieve a complete simulation of ULOF while maintaining the general approach adopted. Moreover, another way to significantly improve the code accuracy and versatility is proposed in terms of discretization of subcooled and superheated regions into smaller zones. Regarding BELLA, the thermomechanical module for the fuel (uranium nitride) is currently under development at KTH. Important future works are dedicated to passive auxiliary safety systems (e.g., dip-coolers), secondary circuit and control strategies of the reactor.

Bibliography

[1] European Commission, "EU taxonomy: Commission presents Complementary Climate Delegated Act to accelerate decarbonisation." https://ec.europa.eu/info/publications/220202-sustainable-finance-taxonomy-complementary-climate-delegated-act_en, 2022.

[2] European Commission, "Questions and Answers on the EU Taxonomy Complementary Climate Delegated Act covering certain nuclear and gas activities." https://ec.europa.eu/commission/presscorner/detail/en/qanda_22_712, 2022.

[3] European Commission, "EU taxonomy for sustainable activities." https://ec.europa.eu/info/business-economy-euro/banking-and-finance/sustainable-finance/eu-taxonomy-sustainable-activities_en, 2020.

[4] "Technical assessment of nuclear energy with respect to the "do no significant harm" criteria of Regulation (EU) 2020/852 ("Taxonomy Regulation")," Tech. Rep. JRC124193, European Commission Joint Research Centre, Petten, 2021.

[5] European Commission, "European Green Deal: Commission proposes transformation of EU economy and society to meet climate ambitions." https://ec.europa.eu/commission/presscorner/detail/en/IP_21_3541, 2021.

[6] UNFCCC, "Paris agreement," in *Report of the Conference of the Parties to the United Nations Framework Convention on Climate Change (21st Session, 2015: Paris). Retrieved December*, vol. 4, p. 2017, HeinOnline, 2015.

[7] UNFCCC, "Action on Climate and SDGs." https://unfccc.int/topics/action-on-climate-and-sdgs/action-on-climate-and-sdgs.

[8] G. H. Brundtland, *Report of the World Commission on environment and development: "our common future."*. UN, 1987.

[9] H. Ritchie and M. Roser, "CO2 and Greenhouse Gas Emissions," *Our World in Data*, 2020. https://ourworldindata.org/co2-and-other-greenhouse-gas-emissions.

[10] IEA, "World Energy Outlook 2021." https://www.iea.org/reports/world-energy-outlook-2021, 2021.

[11] C. Frei, A. Wilkinson, H.-W. Schiffer, A. Belostotskaya, J.-M. Dauger, H. Klima, W. D'haeseleer, L. V. d. Souza, G. Campbell, K. Yanbing, *et al.*, "The future of nuclear: diverse harmonies in the energy transition: Report and Executive summary," 2019.

[12] V. Masson-Delmotte, "IPCC, 2021: Climate Change 2021: The Physical Science Basis. Contribution of Working Group I to the Sixth Assessment Report of the Intergovernmental Panel on Climate Change," Cambridge University Press, 2021.

[13] R. K. Pachauri, M. R. Allen, V. R. Barros, J. Broome, W. Cramer, R. Christ, J. A. Church, L. Clarke, Q. Dahe, P. Dasgupta, *et al.*, *Climate change 2014: synthesis report. Contribution of Working Groups I, II and III to the fifth assessment report of the Intergovernmental Panel on Climate Change*. IPCC, 2014.

[14] World Nuclear Association, "Carbon Dioxide Emissions From Electricity." https://www.world-nuclear.org/information-library/energy-and-the-environment/carbon-dioxide-emissions-from-electricity.aspx, 2021.

[15] H. Ritchie, "What are the safest and cleanest sources of energy?," *Our World in Data*, 2020. https://ourworldindata.org/safest-sources-of-energy.

[16] U.S. Energy Information Administration, "Biomass explained: Biomass and the environment." https://www.eia.gov/energyexplained/biomass/biomass-and-the-environment.php, 2020.

[17] U.S. Department of Energy, Office of Nuclear Energy, "What is Generation Capacity?." https://www.energy.gov/ne/articles/what-generation-capacity, 2020.

[18] UNSCEAR, "UNSCEAR 2019 Report to the General Assembly, with scientific annex," 2019.

[19] H. Kamide, G. Rodriguez, P. Guiberteau, N. Kawasaki, B. Hatala, A. Alemberti, S. Bourg, Y. Huang, F. Serre, M. A. Fuetterer, *et al.*, "Generation IV International Forum-GIF, Annual Report 2020," tech. rep., Organisation for Economic Co-Operation and Development, 2021.

[20] U.S. Department of Energy, Office of Nuclear Energy, "Benefits of Small Modular Reactors (SMRs)." https://www.energy.gov/ne/benefits-small-modular-reactors-smrs.

[21] A. Alemberti, M. Frogheri, S. Hermsmeyer, L. Ammirabile, V. Smirnov, M. Taka-

hashi, C. Smith, Y. Wu, and I. Hwang, "Lead-cooled Fast Reactor (LFR) Risk and Safety Assessment White Paper," GEN IV International Forum, 2014.

[22] B. Gromov, Y. S. Belomitcev, E. Yefimov, M. Leonchuk, P. Martinov, Y. I. Orlov, D. Pankratov, Y. G. Pashkin, G. Toshinsky, V. Chekunov, *et al.*, "Use of lead-bismuth coolant in nuclear reactors and accelerator-driven systems," *Nuclear Engineering and Design*, vol. 173, no. 1-3, pp. 207–217, 1997.

[23] K. Tsujimoto, T. Sasa, K. Nishihara, H. Oigawa, and H. Takano, "Neutronics design for lead-bismuth cooled accelerator-driven system for transmutation of minor actinide," *Journal of Nuclear Science and Technology*, vol. 41, no. 1, pp. 21–36, 2004.

[24] G. A. Blengini, C. El Latunussa, U. Eynard, C. T. de Matos, D. M. A. G. Wittmer, K. Georgitzikis, C. C. Pavel, S. Carrara, L. Mancini, M. Unguru, *et al.*, *Study on the EU's List of Critical Raw Materials (2020)*. Publications Office of the European Union, 2020.

[25] A. Elements, "(6N) 99.9999% Bismuth Metal." https://www.americanelements.com/6n-999999-bismuth-metal-7440-69-9.

[26] J. Harrison, R. Leggett, D. Lloyd, A. Phipps, and B. Scott, "Polonium-210 as a poison," *Journal of Radiological Protection*, vol. 27, no. 1, p. 17, 2007.

[27] H. P. Society, "Polonium-210." https://hps.org/documents/po210factsheet.pdf.

[28] N. Chauvin, K. Minato, T. Ogata, C. B. Lee, M. A. Pouchon, K. O. Pasamehmetoglu, Y. J. Choi, J. R. Kennedy, S. Massara, S. Cornet, J. Sommers, and K. McClellan, "State-of-the-art Report on Innovative Fuels for Advanced Nuclear Systems," tech. rep., July 2014.

[29] Y. Yamamoto, M. A. Snead, K. G. Field, and K. A. Terrani, "Handbook of the materials properties of FeCrAl alloys for nuclear power production applications," tech. rep., Oak Ridge National Lab.(ORNL), Oak Ridge, TN (United States), 2017.

[30] J. Ejenstam, M. Halvarsson, J. Weidow, B. Jönsson, and P. Szakalos, "Oxidation studies of Fe10CrAl-RE alloys exposed to Pb at 550 °C for 10,000 h," *Journal of Nuclear Materials*, vol. 443, no. 1-3, pp. 161–170, 2013.

[31] J. Ejenstam and P. Szakálos, "Long term corrosion resistance of alumina forming austenitic stainless steels in liquid lead," *Journal of Nuclear Materials*, vol. 461, pp. 164–170, 2015.

[32] R. Delville, E. Stergar, and M. Verwerft, "Results of a New Production of Nuclear-

Grade 1.4970 '15-15Ti' Stainless Steel Fuel Cladding Tubes for Gen. IV Reactors," in *International Conference on Nuclear Engineering*, vol. 45899, p. V001T02A015, American Society of Mechanical Engineers, 2014.

[33] A. Alemberti, "Lead Cooled Fast Reactors," in *Encyclopedia of Nuclear Energy* (E. Greenspan, ed.), pp. 523–544, Oxford: Elsevier, 2021.

[34] "SUNRISE - Sustainable Nuclear Energy Research in Sweden." https://www.reactor.sci.kth.se/sunrise/sunrise-1.999712.

[35] G. Grasso, C. Petrovich, D. Mattioli, C. Artioli, P. Sciora, D. Gugiu, G. Bandini, E. Bubelis, and K. Mikityuk, "The core design of ALFRED, a demonstrator for the European lead-cooled reactors," *Nuclear Engineering and Design*, vol. 278, pp. 287–301, 2014.

[36] A. Alemberti, M. Caramello, M. Frignani, G. Grasso, F. Merli, G. Morresi, and M. Tarantino, "ALFRED reactor coolant system design," *Nuclear Engineering and Design*, vol. 370, p. 110884, 2020.

[37] Ansaldo Nucleare S.p.A., "Generation IV & SMR - Committed to the future of nuclear energy." https://www.ansaldoenergia.com/Pages/Generation-IV-SMR.aspx.

[38] H. A. Abderrahim, P. Baeten, D. De Bruyn, J. Heyse, P. Schuurmans, and J. Wagemans, "MYRRHA, a multipurpose hybrid research reactor for high-end applications," *Nuclear Physics News*, vol. 20, no. 1, pp. 24–28, 2010.

[39] "About MYRRHA." https://myrrha.be/about-myrrha.

[40] J. Cahalan, F. Dunn, J. Herzog, A. White, and R. Wigeland, "The SAS4A/SASSYS-1 Safety Analysis Code System; Chapter 4 Reactor Point Kinetics, Decay Heat, and Reactivity Feedback," tech. rep., ANL/NE-12/4, Argonne National Laboratory, IL, USA, 2012.

[41] T. H. Fanning, A. J. Brunett, and T. Sumner, "The SAS4A/SASSYS-1 Safety Analysis Code System, Version 5," 1 2017.

[42] S. Bortot, A. Cammi, R. Ghazy, M. E. Ricotti, P. C. Camprini, and C. Artioli, "Transient evaluation of a GEN-IV LFR demonstration plant through lumped parameters analysis of coupled kinetics and thermal-hydraulics," in *Proceedings of the 2010 International Congress on Advances in Nuclear Power Plants-ICAPP'10*, 2010.

[43] S. Bortot, A. Cammi, and C. Artioli, "Dynamic performance assessment of MOX

and metallic fuel core options for a Gen-IV LFR demonstrator," *Progress in Nuclear Energy*, vol. 54, no. 1, pp. 112–122, 2012.

[44] S. Bortot, A. Cammi, S. Lorenzi, R. Ponciroli, A. Della Bona, and N. Juarez, "Stability analyses for the European LFR demonstrator," *Nuclear Engineering and Design*, vol. 265, pp. 1238–1245, 2013.

[45] S. Bortot, E. Suvdantsetseg, and J. Wallenius, "BELLA: a multi-point dynamics code for safety-informed design of fast reactors," *Annals of Nuclear Energy*, vol. 85, pp. 228–235, 2015.

[46] P. Aragon Grabiel, "Implementation of dynamic nuclear fuel thermo-mechanics in transient simulation of lead-cooled reactors," Master's thesis, Universitat Politècnica de Catalunya, 2021.

[47] F. Dehlin, "Progress Report November 2020: Development of passive safety design approaches and self-actuated shut-down systems for an inherently safe, efficient and reliable operation of Gen-IV fast reactors." 2020.

[48] F. Dehlin, J. Wallenius, and S. Bortot, "An analytic approach to the design of passively safe lead-cooled reactors," *Annals of Nuclear Energy*, vol. 169, p. 108971, 2022.

[49] SSF, "Agenda 2030 Research Centers (ARC) 2019." https://strategiska.se/en/research/ongoing-research/ssf-agenda-2030-research-centers-arc-2019/, 2020.

[50] Swedish Energy Agency, "The Swedish Energy Agency supports investments in smart solar parks and lead-cooled reactors." https://www.energimyndigheten.se/nyhetsarkiv/2022/energimyndigheten-stottar-satsning-pa-smarta-solelparker-och-blykylda-reaktorer/, 2022.

[51] LeadCold Reactors (Blykalla Reaktorer), "Uniper, LeadCold and KTH to collaborate on developing the reactor technology of the future." http://www.leadcold.com/collaboration-with-uniper-and-kth.html, 2022.

[52] LeadCold Reactors (Blykalla Reaktorer), "Sealer." http://www.leadcold.com/sealer.html, 2022.

[53] J. Wallenius, S. Bortot, and I. Mickus, "Unprotected transients in SEALER: A small lead-cooled reactor for commercial power production in Arctic regions," in *Proc. PHYSOR*, 2018.

[54] J. Wallenius, S. Qvist, I. Mickus, S. Bortot, P. Szakalos, and J. Ejenstam, "Design

of SEALER, a very small lead-cooled reactor for commercial power production in off-grid applications," *Nuclear Engineering and Design*, vol. 338, pp. 23–33, 2018.

[55] J. Wallenius, "An improved correlation for gas release from nitride fuels," *Journal of Nuclear Materials*, vol. 558, p. 153402, 2022.

[56] P. Dömstedt, M. Lundberg, and P. Szakálos, "Corrosion studies of low-alloyed FeCrAl steels in liquid lead at 750 °C," *Oxidation of Metals*, vol. 91, no. 3, pp. 511–524, 2019.

[57] P. Dömstedt, M. Lundberg, and P. Szakálos, "Corrosion studies of a low alloyed Fe-10Cr-4Al steel exposed in liquid Pb at very high temperatures," *Journal of Nuclear Materials*, vol. 531, p. 152022, 2020.

[58] J. Wallenius and P. Szakalos, "A nuclear reactor comprising a reactor lid and an additional inner lid," 2021.

[59] L. Cinotti, "Nuclear Reactor with Compact Primary Heat Exchanger," 2013.

[60] J. R. Lamarsh, A. J. Baratta, *et al.*, *Introduction to nuclear engineering*, vol. 3. Prentice hall Upper Saddle River, NJ, 2001.

[61] *American National Standard for Decay Heat Power in Light Water Reactors*. American Nuclear Society, 1994.

[62] L. Agee, "RETRAN-3D A Program for Transient Thermal-Hydraulic Analysis of Complex Fluid Flow Systems, NP-7450," *Research Project 889-10 Computer Code Manuals, Prepared by Computer Simulation & Analysis, Inc.*, 1997.

[63] S. Lorenzi, "Development of a control oriented simulator for a lead cooled fast reactor demonstrator," 2011.

[64] K. Mikityuk, "Heat transfer to liquid metal: review of data and correlations for tube bundles," *Nuclear Engineering and Design*, vol. 239, no. 4, pp. 680–687, 2009.

[65] R. A. Seban and T. Shimazaki, "Heat transfer to a fluid flowing turbulently in a smooth pipe with walls at constant temperature," tech. rep., University of California, Berkeley, Institute of Engineering Research, 1949.

[66] N. E. Todreas, M. S. Kazimi, and M. Massoud, *Nuclear systems Volume II: Elements of thermal hydraulic design*. CRC Press, 2021.

[67] H. Blasius, "Das aehnlichkeitsgesetz bei reibungsvorgängen in flüssigkeiten," in *Mitteilungen über Forschungsarbeiten auf dem Gebiete des Ingenieurwesens*, pp. 1–41, Springer, 1913.

[68] S. Chen, Y. Chen, and N. Todreas, "The upgraded Cheng and Todreas correlation for pressure drop in hexagonal wire-wrapped rod bundles," *Nuclear Engineering and Design*, vol. 335, pp. 356–373, 2018.

[69] I. E. Idel'čik, *Handbook of hydraulic resistance: coefficients of local resistance and of friction*. Israel Program for Scientific Translations, 1966.

[70] MathWorks®, "MATLAB® Homepage." https://www.mathworks.com/?s_tid=gn_logo, 2022.

[71] MathWorks®, "PFD Documentation for MATLAB." https://www.mathworks.com/help/pdf_doc/matlab/index.html, 2022.

[72] MathWorks®, "Simulink overview." https://www.mathworks.com/products/simulink.html, 2022.

[73] J. M. Jensen and H. Tummescheit, "Moving boundary models for dynamic simulations of two-phase flows," in *Proc. of the 2nd int. modelica conference*, vol. 3, Oberpfaffhenhofen Germary, 2002.

[74] M. Holmgren, "X steam for matlab," *www.x-eng.com, accessed October*, vol. 21, p. 2006, 2006.

[75] IAPWS, "Revised Release on the IAPWS Industrial Formulation 1997 for the Thermodynamic Properties of Water and Steam." https://www.mathworks.com/matlabcentral/fileexchange/9817-x-steam-thermodynamic-properties-of-water-and-steam, 2022.

[76] W. Wagner and H. J. Kretzschmar, *International Steam Tables-Properties of Water and Steam based on the Industrial Formulation IAPWS-IF97: Tables, Algorithms, Diagrams, and CD-ROM Electronic Steam Tables-All of the equations of IAPWS-IF97 including a complete set of supplementary backward equations for fast calculations of heat cycles, boilers, and steam turbines*. Springer Science & Business Media, 2007.

[77] S. G. Kandlikar, "A general correlation for saturated two-phase flow boiling heat transfer inside horizontal and vertical tubes," 1990.

[78] F. Kreith and R. M. Manglik, *Principles of heat transfer*. Cengage learning, 2016.

[79] A. Žukauskas, "Heat transfer from tubes in crossflow," in *Advances in heat transfer*, vol. 8, pp. 93–160, Elsevier, 1972.

[80] C. Fletcher and R. Schultz, "RELAP5/MOD3 code manual," tech. rep., U.S. Nuclear

Regulatory Commission, Washington, DC (United States). Div. of System Technology, 1992.

[81] C. Fazio, V. Sobolev, A. Aerts, S. Gavrilov, K. Lambrinou, P. Schuurmans, A. Gessi, P. Agostini, A. Ciampichetti, L. Martinelli, *et al.*, "Handbook on lead-bismuth eutectic alloy and lead properties, materials compatibility, thermal-hydraulics and technologies - 2015 edition," tech. rep., Organisation for Economic Co-Operation and Development, 2015.

[82] A. Banerjee, S. Raju, R. Divakar, E. Mohandas, G. Panneerselvam, and M. Antony, "Thermal property characterization of a titanium modified austenitic stainless steel (alloy D9)," *Journal of nuclear materials*, vol. 347, no. 1-2, pp. 20–30, 2005.

[83] L. Leibowitz and R. Blomquist, "Thermal conductivity and thermal expansion of stainless steels D9 and HT9," *International journal of thermophysics*, vol. 9, no. 5, pp. 873–883, 1988.

[84] S. Hayes, J. Thomas, and K. Peddicord, "Material property correlations for uranium mononitride: I. Physical properties," *Journal of Nuclear materials*, vol. 171, no. 2-3, pp. 262–270, 1990.

[85] S. Hayes, J. Thomas, and K. Peddicord, "Material property correlations for uranium mononitride: III. Transport properties," *Journal of nuclear materials*, vol. 171, no. 2-3, pp. 289–299, 1990.

[86] S. Hayes, J. Thomas, and K. Peddicord, "Material property correlations for uranium mononitride: IV. Thermodynamic properties," *Journal of nuclear materials*, vol. 171, no. 2-3, pp. 300–318, 1990.

[87] V. Bobkov, L. Fokin, E. Petrov, V. Popov, V. Rumiantsev, and A. Savvatimsky, "Thermophysical properties of materials for nuclear engineering: a tutorial and collection of data," tech. rep., IAEA, Vienna, 2008.

[88] J. Fink, "Thermophysical properties of uranium dioxide," *Journal of nuclear materials*, vol. 279, no. 1, pp. 1–18, 2000.

[89] V. Krett and J. Cleveland, *Thermophysical Properties of Materials for Water Cooled Reactors*. No. 949 in TECDOC Series, Vienna: IAEA, 1997.

[90] S. Lorenzi, "Development of a control oriented simulator for a lead cooled fast reactor demonstrator," Master's thesis, Politecnico di Milano, 2011.

[91] N. E. Todreas and M. S. Kazimi, *Nuclear systems volume I: Thermal hydraulic fundamentals*. CRC press, 2021.

[92] MathWorks®, "Mathworks Help Center - ode15s." https://www.mathworks.com/help/matlab/ref/ode15s.html, 2022.

[93] MathWorks®, "Mathworks Help Center - ode23s." https://www.mathworks.com/help/matlab/ref/ode23s.html#bu2m56l-1, 2022.

A | Thermo-physical properties correlations

Temperature dependent correlations for coolant, cladding and fuel thermo-physical properties used in the transient analysis are specified below. Units of measure are:

$$\begin{aligned} T &\quad [K] \\ P &\quad [Pa] \\ \rho(T) &\quad \left[\tfrac{kg}{m^3}\right] \\ c_p(T) &\quad \left[\tfrac{J}{kg \cdot K}\right] \\ k(T) &\quad \left[\tfrac{W}{m \cdot K}\right] \\ \mu(T) &\quad [Pa \cdot s] \end{aligned}$$

Some attention must be paid to pressure (Pa) and porosity (-) for which the same letter P is used. Each time it is specified to which quantity a correlation refers.

Lead thermo-physical properties

Lead coolant properties are taken from the handbook on lead and LBE properties released by OECD-NEA in 2015 [81]:

$$\rho(T) = 11441 - 1.2795\ T \tag{A.1}$$

$$c_p(T) = 176.2 - 4.923 \times 10^{-2}\ T + 1.544 \times 10^{-5}\ T^2 - \frac{1.524 \times 10^6}{T^2} \tag{A.2}$$

$$k(T) = 9.2 + 0.011\ T \tag{A.3}$$

$$\mu(T) = 4.55 \times 10^{-4} \exp\left(\frac{1069}{T}\right) \tag{A.4}$$

Cladding thermo-physical properties

Correlations for 15-15Ti density and specific heat capacity are derived from experimental data published for D9 steel by Banerjee and co-workers [82], whereas for thermal conductivity a correlation fitted by Leibowitz and Blomquist to measured conductivity of D9 [83] is adopted:

$$\rho(T) = 8138.6 - 0.24855\ T - 1.02387 \times 10^{-4}\ T^2 + 4.28927 \times 10^{-9}\ T^3 \tag{A.5}$$

$$c_p(T) = 291.9 + 0.3792\ T - \frac{1.345 \times 10^{-4}}{T^2} \tag{A.6}$$

$$k(T) = \begin{cases} 7.598 + 2.391 \times 10^{-2}\ T - 8.899 \times 10^{-6}\ T^2 & T \leq 1030\ K \\ 7.260 + 1.509 \times 10^{-2}\ T & T > 1030\ K \end{cases} \tag{A.7}$$

Fuel thermo-physical properties

Density [84], thermal conductivity [85] and thermal heat capacity [86, 87] for UN fuel in 298 K $\leq T \leq$ 2523 K are:

$$\rho(T) = (14420 - 0.2779\ T - 4.897 \times 10^{-5}\ T^2)\ (1 - P) \tag{A.8}$$

$$k(T) = 1.864\ e^{-2.14P}\ T^{0.361} \tag{A.9}$$

$$c_p(T) = \frac{1}{\mathrm{MM_{UN}}}\left[51.14\left(\frac{\theta_E}{T}\right)^2 \frac{\exp\left(\frac{\theta_E}{T}\right)}{\left[\exp\left(\frac{\theta_E}{T}\right) - 1\right]^2} + 9.491 \times 10^{-3}T + \frac{2.6415 \times 10^{11}}{T^2} \exp\left(\frac{-18081}{T}\right)\right] \tag{A.10}$$

where $P = 0.05$ is the porosity of the fuel, $\theta_E = 365.7$ K is the Einstein temperature and $\mathrm{MM_{UN}}$ $\left(\frac{kg}{mol}\right)$ is uranium nitride molar mass:

$$\mathrm{MM_{UN}} = (0.12 \cdot 235 + 0.88 \cdot 238 + 15) \times 10^{-3}$$

Density [88], thermal heat capacity and thermal conductivity [87] for UO_2 are:

$$\rho(T) = \frac{10963}{9.973 \times 10^{-1} + 9.082 \times 10^{-6}\ T - 2.705 \times 10^{-10}\ T^2 + 4.391 \times 10^{-13}\ T^3} \tag{A.11}$$

$$c_p(T) = 193.238 + 325.7444\ \frac{T}{1000} - 312.0041\ \left(\frac{T}{1000}\right)^2 + 116.8222\ \left(\frac{T}{1000}\right)^3 + \tag{A.12}$$

$$- \ 2.6334\ \left(\frac{T}{1000}\right)^4 - 2.6441\ \left(\frac{T}{1000}\right)^{-2} \tag{A.13}$$

$$k(T) = \frac{100}{7.5408 + 17.692\left(\frac{T}{1000}\right) + 3.6142\left(\frac{T}{1000}\right)^2} + \frac{6400}{\left(\frac{T}{1000}\right)^{5/2}} \exp\left(\frac{-16.35}{\left(\frac{T}{1000}\right)}\right) \tag{A.14}$$

Fuel-cladding gap thermo-physical properties

Helium density and thermal conductivity (IAEA, 1997 [89]):

$$\rho(T) = \frac{P}{R^*_{\mathrm{He}} T} \tag{A.15}$$

$$k(T) = k_0 \cdot \left[1 + 3.2 \times 10^{-3}\ k_1^{3/2}\ \frac{P}{R^*_{\mathrm{He}} T}\right] \tag{A.16}$$

where P is helium pressure, $R^*_{\mathrm{He}} = 2077.3\ \frac{J}{kg \cdot K}$ is helium specific gas constant, while k_0 and k_1 are two quantities dependent on helium temperature T and on a series of correlations coefficients b_i:

$$k_0 = \frac{6.161 \times 10^{-3}\sqrt{T}}{k_1} \tag{A.17}$$

$$k_1 = \exp\left\{\sum_{i=1}^{5} b_i \left[\ln\left(\frac{T}{10.4}\right)\right]^{i-1}\right\} \tag{A.18}$$

Validity range is $300\ K < T < 2500\ K$ and $0.1 < P < 6\ MPa$.

T91 steel thermo-physical properties

Since at the time of writing it was difficult to find tabulated data and peer-reviewed correlations for Fe-10Cr-4Al-RE adopted in SUNRISE-LFR, here it is proposed a set of correlations for T91 steel [90]:

$$\rho(T) = 7799 - 0.201\ T - 1.102 \times 10^{-4}\ T^2 \tag{A.19}$$

$$k(T) = 17.94 + 0.0251\ T - 1.45 \times 10^{-5}\ T^2 \tag{A.20}$$

$$c_p(T) = -3.979 \times 10^{-9}\ T^4 + 1.151 \times 10^{-5}\ T^3 - 1.103 \times 10^{-2}\ T^2 + 4.677\ T - 244.0 \tag{A.21}$$

They have been temporarily adopted for the SG walls modeling.

B | Derivation of the coolant mass flow rate dynamical equation

This appendix shows the step-by-step derivation of primary fluid (lead) mass flow rate dynamical equation starting from first principle momentum balance. It is based on Todreas and Kazimi's book [66], chapter 3.

Momentum balance equation (3-dimensional):

$$\rho\frac{D\vec{v}}{Dt} = \frac{\partial\rho\vec{v}}{\partial t} + \nabla\cdot\rho\vec{v}\vec{v} = -\nabla P + \nabla\cdot\overline{\overline{\tau}} + \rho\vec{g} \tag{B.1}$$

where ρ is density $\left(\frac{kg}{m^3}\right)$, $\vec{v}$ velocity $\left(\frac{m}{s}\right)$, P pressure (Pa), $\overline{\overline{\tau}}$ shear stress tensor (Pa) and $\vec{g}$ gravitational acceleration $\left(\frac{m}{s^2}\right)$.

By scalarly multiplying Eq. (B.1) by $\hat{e}_l$, the versor of the curvilinear coordinate l, and introducing the Darcy-Weisbach expression for the shear term, 1-dimensional momentum balance equation is obtained:

$$\frac{\partial G}{\partial t} + \frac{\partial}{\partial l}\left(\frac{G^2}{\rho}\right) = -\frac{\partial P}{\partial l} - \frac{f|G|G}{2\rho D_h} - \rho g cos\theta \tag{B.2}$$

where $G = \rho v$ is the mass flux $\left(\frac{kg}{m^2\cdot s}\right)$, f the single-phase Darcy friction factor (-) and θ the angle formed by vertical axis z and direction l.

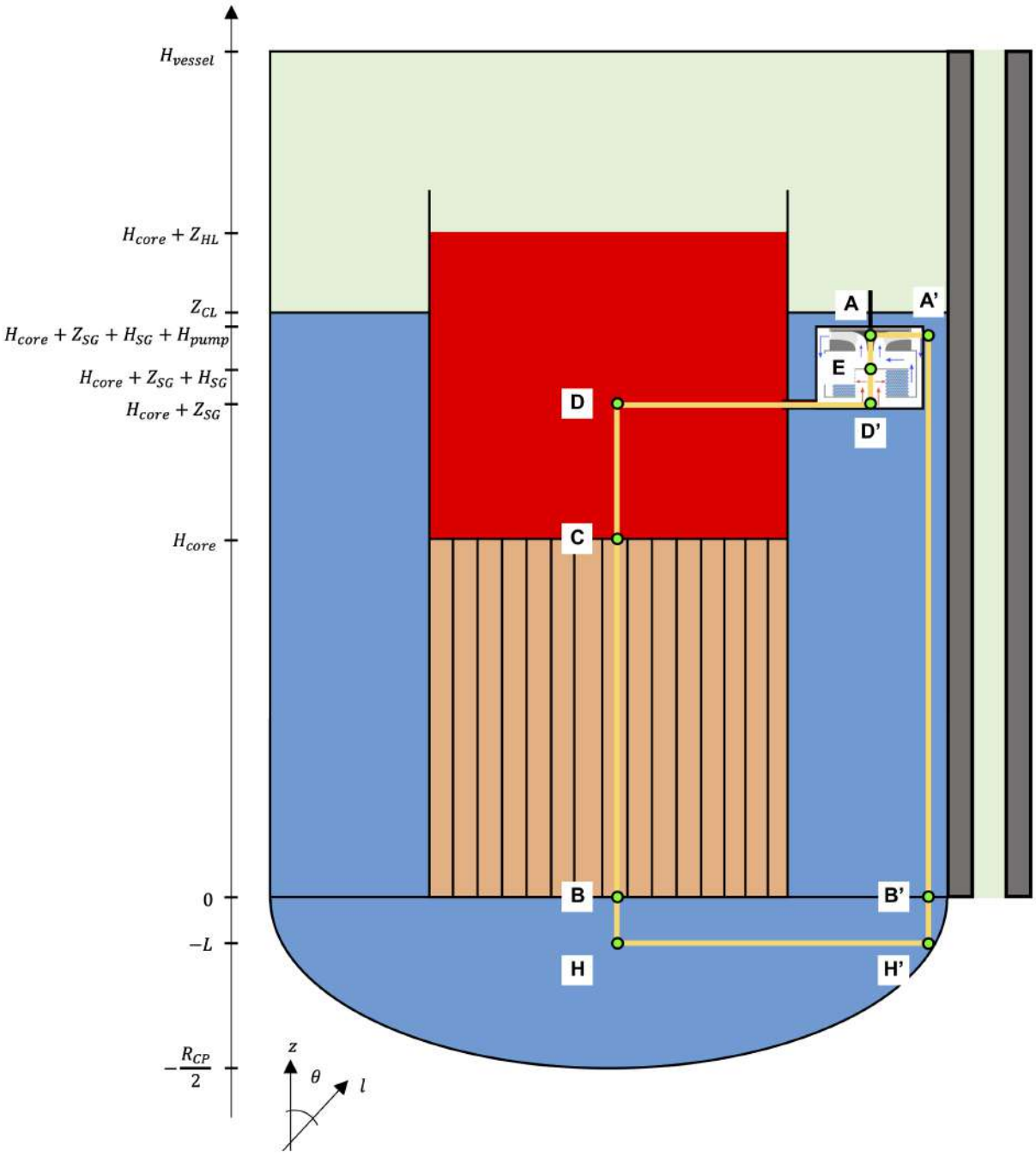

Figure B.1: Sketch of the loop (in yellow with green points) for the integration of momentum balance equation in SUNRISE-LFR.

To derive the dynamical equation for the lead mass flow rate $\dot{m}_{Pb}$ $\left(\frac{kg}{s}\right)$, momentum balance equation (B.2) has to be integrated around the loop of Figure B.1 from node A to node E clockwise. One by one, each term is considered starting from right hand side.

Static pressure:

$$\int_A^E -\frac{\partial P}{\partial l}dl = -\int_A^E dP = -\Delta P_{A,E} = \Delta P_{E,A} = \Delta P_{pump} - \Delta P_{fr}^{pump} + g\rho^{SG,out}H^{pump} \tag{B.3}$$

where ΔP_{pump} is the pump pressure head, positive under operating conditions and null when pump is failed.
Friction term:

$$\begin{aligned}\int_A^E -\frac{f|G|G}{2\rho D_h}dl &= \int_A^{B'} -\frac{f|G|G}{2\rho D_h}dl + \int_{B'}^{B} -\frac{f|G|G}{2\rho D_h}dl + \int_B^C -\frac{f|G|G}{2\rho D_h}dl + \\ &+ \int_C^D -\frac{f|G|G}{2\rho D_h}dl + \int_D^{D'} -\frac{f|G|G}{2\rho D_h}dl + \int_{D'}^E -\frac{f|G|G}{2\rho D_h}dl = \\ &= -\Delta P_{fr}^{CL} - \Delta P_{fr}^{annular} - \Delta P_{fr}^{core} - \Delta P_{fr}^{HL} - \Delta P_{fr}^{annular} - \Delta P_{fr}^{SG}\end{aligned} \tag{B.4}$$

with each ΔP_{fr} usually split into distributed and concentrated contributions:

$$\Delta P_{fr} = \Delta P_{fr,distr} + \Delta P_{fr,conc} \tag{B.5}$$

Gravity term:

$$\int_A^E -\rho g cos\theta dl = \int_A^{A'} + \int_{A'}^{B'} + \int_{B'}^{H'} + \int_{H'}^{H} + \int_H^B + \int_B^C + \int_C^D + \int_D^{D'} + \int_{D'}^E \tag{B.6}$$

However, considering that $\int_A^{A'} = \int_{H'}^{H} = \int_D^{D'} = 0$ because elevation does not change and that $\int_{B'}^{H'} = \int_H^B$ since density does not change, gravity term becomes:

$$\begin{aligned}\int_A^E -\rho g cos\theta dl &= \int_{A'}^{B'} \rho^{CL} g dl - \int_B^C \rho^{core} g dl - \int_C^D \rho^{HL} g dl - \int_{D'}^E \rho^{SG} g dl = \\ &= \overline{\rho}^{CL} g(H^{core} + Z^{SG} + H^{SG} + H^{pump}) - \overline{\rho}^{core} g H^{core} - \overline{\rho}^{HL} g Z^{SG} - \overline{\rho}^{SG} g H^{SG}\end{aligned} \tag{B.7}$$

Coming to the left hand side, temporal acceleration term:

$$\begin{aligned}\int_A^E \frac{\partial G}{\partial t}dl &= \sum_{k=A}^{E}\int_k^{k+1}\frac{\partial G_k}{\partial t}dl = \sum_{k=A}^{E}\frac{\partial G_k}{\partial t}L_k = \sum_{k=A}^{E}\frac{L_k}{A_k}\frac{\partial \dot{m}_{Pb}}{\partial t} = \\ &= \sum_{k=A}^{E}\frac{L_k}{A_k}\frac{d\dot{m}_{Pb}}{dt} = \frac{d\dot{m}_{Pb}}{dt}\left(\sum_{k=A}^{E}\frac{L_k}{A_k}\right)\end{aligned} \tag{B.8}$$

where L_k is the length of k-th flow section of uniform flow area A_k:

$$\sum_{k=A}^{E} \frac{L_k}{A_k} = \frac{H^{core}}{A^{core}} + \frac{Z^{SG}}{A^{HL}} + \frac{H^{SG}}{A^{SG}} + \frac{Z^{CL}}{A^{CL}} \tag{B.9}$$

All the different flow areas of the fuel assembly (foot, excan, rail, etc.) are here neglected. Flow area of the SG needs to be improved once the CAD model of the module is available. Other contribution (e.g., CP) are neglected because hard to estimate at this point. It is worth to note that in principle these approximations do not affect the steady-state value of the mass flow rate $\dot{m}_{Pb}$ but only its time constant.

Lastly, spacial acceleration term:

$$\int_A^E \frac{\partial}{\partial l}\left(\frac{G^2}{\rho}\right) dl = \int_A^E d\left(\frac{G^2}{\rho}\right) = \left(\frac{G^2}{\rho}\right)_E - \left(\frac{G^2}{\rho}\right)_A \simeq 0 \tag{B.10}$$

under the assumptions that flow area in A and E are the same and that density ρ does not change (the contribution coming from pump pressure injection is negligible).

Rearranging the terms and naming

$$\Delta P_{buoyancy} = \overline{\rho}^{CL} g(H^{core} + Z^{SG} + H^{SG}) - \overline{\rho}^{core} g H^{core} - \overline{\rho}^{HL} g Z^{SG} - \overline{\rho}^{SG} g H^{SG} \tag{B.11}$$

$$\Delta P_{friction} = \Delta P_{fr}^{core} + \Delta P_{fr}^{SG} + \Delta P_{fr}^{HL} + \Delta P_{fr}^{CL} + \Delta P_{fr}^{pump} + 2\Delta P_{fr}^{annular} \tag{B.12}$$

the final equation is:

$$\frac{d\dot{m}_{Pb}}{dt} = \frac{\Delta P_{buoyancy} - \Delta P_{friction} + \Delta P_{pump}}{\sum_{k=A}^{E} \frac{L_k}{A_k}} \tag{B.13}$$

where pump term is calculated from steady-state nominal conditions and kept fixed:

$$\Delta P_{pump} = \Delta P_{pump}(0) = \Delta P_{friction}(0) - \Delta P_{buoyancy}(0) \tag{B.14}$$

In steady-state conditions and assuming that $\overline{T}^{core} = \overline{T}^{SG} = \frac{\overline{T}^{HL} + \overline{T}^{CL}}{2}$, buoyancy term can be simplified to

$$\Delta P_{buoyancy} = g(\overline{\rho}^{CL} - \overline{\rho}^{HL}) H_{th} = g\beta(\overline{T}^{HL} - \overline{T}^{CL}) H_{th} \tag{B.15}$$

with $\beta = -\frac{\partial \rho}{\partial T}$ (lead thermo-physical properties are listed in Appendix A) and $H_{th} =$

$\frac{1}{2}H^{core} + Z^{SG} + \frac{1}{2}H^{SG}$ (distance between core and SG thermal centers).

C | Two-phase flows modeling

This appendix briefly presents different approaches to describe two-phase flow systems and focuses on the one adopted in the SG model. The reference is Todreas and Kazimi's book [91], chapter 5.

The SG saturated region is a single-component, two-phase system with liquid water and vapor as co-existing phases. Neglecting chemical reactions, existing models are divided into two main categories:

- Mixture models, which describe the two-phase flow in terms of a pseudo single-phase flow (the mixture) with averaged properties. The approach is macroscopic.
- Multifluid models, which take into account also (microscopical) interface interactions between liquid water and vapor. They can describe the formation of liquid film, vapor, droplets.

The simplest mixture model, called homogeneous equilibrium model (HEM), assumes there is no relative velocity between the two phases, i.e. homogeneous flow (HF), and that vapor and liquid are in thermodynamic equilibrium. In this case mass, momentum and energy balance equations of the mixture are sufficient to describe the flow.
Extensions of HEM to include relative velocity (slip) between the two phases or thermal non-equilibrium (e.g., subcooled boiling) effects are possible using externally supplied, usually empiric, constitutive relations. A well-known example for such mixture models is thermal equilibrium drift flux model, which introduces a slip ratio different than unity.

In a two-fluid model, three conservation equations are written both for liquid and vapor phases. Hence, the model is often called the six-equation model. It requires a larger number of constitutive equations, among which the most important are on transfer of mass (Γ), energy ($\dot{Q}$) and momentum ($\vec{F}$) across liquid-vapor interfaces.
Extensions to multifluid models are also possible but have not been applied as widely as the simpler two-fluid model. They are capable of describing vapor bubbles, continuous liquid, continuous vapor and liquid droplets at the same time by means of separate sets of conservation equations.

Among the alternative models the choice depends on the nature of the problem to be solved. Once a model is selected, constitutive relations are needed to describe the exchange rate of mass, momentum and energy.

The saturated region of the moving boundary steam generator is modeled adopting HEM.

Homogeneous equilibrium model (HEM)

It asks for three conservation equations − mass, momentum and energy − of the mixture and two constitutive laws − wall momentum and energy. Water and steam are at thermodynamic equilibrium (same temperature, same chemical potential, while pressures are related by the Young-Laplace equation) and flow with the same velocity.

In order to describe average properties some equilibrium mixture quantities are introduced:

$$\overline{\gamma} = \frac{1}{L}\int_0^L \frac{A_g(z)}{A}dz = \frac{V_g}{V_g+V_l} \tag{C.1}$$

$$\overline{x}_{st} = \frac{M_g}{M_g+M_l} \tag{C.2}$$

$$\overline{x} = \frac{\Gamma_g}{\Gamma_g+\Gamma_l} \tag{C.3}$$

$$\overline{x}_{vol} = \frac{\dot{V}_g}{\dot{V}_g+\dot{V}_l} \tag{C.4}$$

$$\overline{x}_{th} = \frac{h-h_l}{h_g-h_l} \tag{C.5}$$

$$\rho_{mix} = \overline{\gamma}\rho_g + (1-\overline{\gamma})\rho_l \tag{C.6}$$

$\overline{\gamma}$ is the (volumetric) average void fraction, $\overline{x}_{st}$ the average static quality, $\overline{x}$ the average mass quality (or dryness fraction), $\overline{x}_{vol}$ the average volumetric quality, $\overline{x}_{th}$ the thermodynamic equilibrium quality and ρ_{mix} the mixture density.

The very general relations between $\overline{\gamma}$, $\overline{x}$ and $\overline{x}_{vol}$ are:

$$\frac{1-\overline{\gamma}}{\overline{\gamma}} = \overline{s}\,\frac{1-\overline{x}_{vol}}{\overline{x}_{vol}} = \overline{s}\,\frac{\rho_g}{\rho_l}\frac{1-\overline{x}}{\overline{x}} \tag{C.7}$$

being $\overline{s} = \frac{\overline{v}_g}{\overline{v}_l}$ the average slip ratio.

Considering HEM:

- Homogeneous flow (HF): average slip ratio equal to unity ($\overline{s} = 1$) which in turn means $\overline{\gamma} = \overline{x}_{vol}$ from Eq. (C.7).

- Thermodynamic equilibrium: average mass quality and thermodynamic average quality coincide ($\overline{x} = \overline{x}_{th}$).

Then a formula for average volumetric void fraction can be derived [90]:

$$\overline{\gamma} = (1+\eta)\left[1 - \eta \ln\left(1 + \frac{1}{\eta}\right)\right] \tag{C.8}$$

$$\text{with} \quad \eta = \frac{\rho_{s,g}}{\rho_{s,l} - \rho_{s,g}} \tag{C.9}$$

the saturated density ratio.

D | Simulink® settings in simulations

This appendix shows the Simulink settings of the simulated transients. It serves both as a way to motivate them and as a reference to those who want to replicate the simulations using BELLA and the SG model.

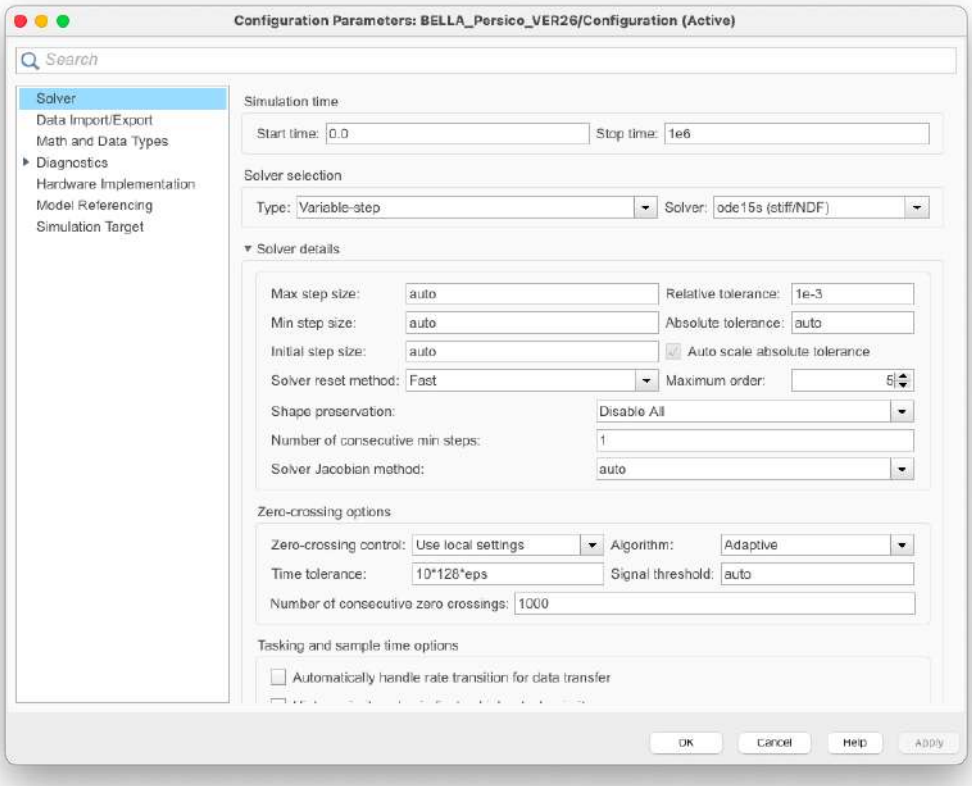

Figure D.1: Solver settings window in Simulink.

Figure D.1 shows the Simulink window for solver settings. Apart from the *Start time*, always set to zero, and the *Stop time*, decided according to the simulation's dynamics and the interested time scale, the parameters that were utilized are:

- *Solver*
- *Max step size*
- *Relative tolerance*

The solver *Type* was always maintained on *Variable-step* to let Simulink adjust the time-step dynamically according to the specified accuracy requirements. It is way more efficient than the alternative *Fixed-step*, whose time-step is chosen by the user and kept fixed, especially for those dynamical systems or scenarios that have conditional events or different components in the dynamics.

Simulink offers a wide list of solvers, but due to the stiffness characterizing BELLA and the SG model only implicit methods were efficient in keeping numerical stability without using impractically small time-steps. Among those implicit solvers listed by Simulink, two resulted to be very reliable: *ode15s* and *ode23s*. Ode15s [92] is a variable-order solver based on the numerical differentiation formulas (NDFs) of orders 1 to 5. Ode23s [93] is a fixed-order solver based on a modified Rosenbrock formula of order 2. It can solve some kinds of stiff problems for which ode15s is not effective.
Ode15s seemed to be the most efficient (the fastest with the same accuracy requirements) and it allowed to simulate with success all scenarios. Ode23s was not as good as ode15s but it permitted the simulation of most of the transients with sufficiently small computational effort.

Max step size sets the maximum allowed time-step size and in most of the cases it was left to the default *auto*, i.e. Simulink itself computes it according to simulation's conditions. In some demanding simulations, in particular with ULOF, it was necessary to set it to a very low value to obtain an acceptable result. In case of BELLA coupled with the SG model, it has been necessary to set it to 1 or even to 0.5 to avoid errors in the numerical convergence of the simulation. That came with the downside of longer computational times.

Relative tolerance, together with the *Absolute tolerance*, sets the accuracy requirements for the simulation to converge. It was kept most of the times on its default value 10^{-3} but during the work different options have been considered. For instance lower values, such as 10^{-5} and 10^{-7}, were tried with the aim of increasing the level of accuracy but without always obtaining the hoped results. The default value seemed to be the most suitable for all the simulations.

The following Tables D.1, D.2 and D.3 list the solver configuration of each simulated transient presented in Chapters 3, 4 and 5, respectively.

Transient	Simulation sime (s)	Solver	RTOL	Max step size
Steady-state	4000	ode15s	10^{-3}	auto
UTOP	2000	ode15s	10^{-3}	auto
ULOF	3000	ode15s	10^{-3}	1
ULOHS	4000	ode15s	10^{-3}	auto
ULOHS	10^{6}	ode15s	10^{-3}	auto
ULOF-ULOHS	4000	ode15s	10^{-3}	auto
ULOF-ULOHS	10^{6}	ode15s	10^{-3}	auto

Table D.1: Solver settings in BELLA simulations.

Transient	Simulation sime (s)	Solver	RTOL	Max step size
Steady-state	4000	ode15s	10^{-3}	auto
$T_{p,in}$ surge	50	ode23s	10^{-3}	auto
Γ loss	100	ode23s	10^{-3}	1
$T_{s,in}$ decrease	40	ode15s	10^{-3}	auto
$\dot{m}_s$ loss	40	ode15s	10^{-3}	auto

Table D.2: Solver settings in SG standalone simulations.

Transient	Simulation sime (s)	Solver	RTOL	Max step size
Steady-state	4000	ode15s	10^{-3}	auto
UTOP	2000	ode15s	10^{-3}	auto
ULOF 50%	3000	ode15s	10^{-3}	1
ULOF 30%	3000	ode15s	10^{-3}	1
ULOF 20%	3000	ode15s	10^{-3}	1
ULOF 10%	3000	ode15s	10^{-3}	1
ULOF 5%	3000	ode15s	10^{-3}	0.5
ULOF 3%	3000	ode15s	10^{-3}	2

Table D.3: Solver settings in BELLA fully coupled with SG simulations.

List of Figures

List of Tables

Acknowledgements

It is actually very difficult to find the right words to express my gratitude to all the people that stood by my side during this long journey. Undoubtedly, these few lines are not even sufficient to do it, but they might be a fair beginning.

I would like to start from the person that made my Swedish experience possible by accepting my candidacy to work in SUNRISE, Prof. J. Wallenius. Not only an incredible man of science but also a clever teacher in the nuclear sector. Thank you very much for all the patience and trust you put in me. At the same time, a sincere gratitude goes also to F. Dehlin, PhD student, who helped me in solving various doubts throughout my work. And I would like to extend this to all the colleagues at the Nuclear Engineering Division, starting from G. Sanchez and G. Wang, with whom I shared the office for seven months, and ending with Prof. S. Bortot, who I first contacted in the early February 2021, and Prof. P. Olsson, coordinator of SUNRISE.

I must also acknowledge all the precious contribution and the continuous support of my thesis supervisor Prof. A. Cammi. Thanks to his knowledge and practical expertise it has been a lot easier for me to complete this work with success. My thankfulness goes also to all the other professors of the Energy Department, Politecnico di Milano: I learned a lot from all your courses.

Then, an important role in the whole journey has been covered by all my longtime friends. We have grown up together and I am really proud of the bonds that keep us really close even when in different countries. I want to send a grateful thank also to my friends from Politecnico, always ready to support each other in the best way and to whom I wish their best career. And to my newest friends, Italian and international, that made my Swedish period something special: it would have been totally different without you, thanks!

The last part is dedicated to my big family, starting from my grandma Natalina, who decided to improve her technological skills in using smartphones in order to keep in contact with me while living in Sweden. Even my aunt Giulia and my cousins Linda and Gabriele have been able to make me feel at home with their deep affection and encouragement.

But for sure there is only one reason why all this has been possible. And this is my family. It is thank to your constant trust, motivation and love that I successfully achieved my goals, both as a student and as a young man. Thank you mamma Loretta, papà Ernesto and brother Emanuele. It is even hard to understand how important this has been, from the very beginning.

Thank you all.